

Computational study of structural and optical properties of two-dimensional transition-metal dichalcogenides with implanted defects

Stefan Hermann Rost

Information

Band / Volume 92

ISBN 978-3-95806-682-3

Forschungszentrum Jülich GmbH
Peter Grünberg Institut (PGI)
Quanten-Theorie der Materialien (PGI-1/IAS-1)

Computational study of structural and optical properties of two-dimensional transition-metal dichalcogenides with implanted defects

Stefan Hermann Rost

Schriften des Forschungszentrums Jülich
Reihe Information / Information

Band / Volume 92

ISSN 1866-1777

ISBN 978-3-95806-682-3

Bibliografische Information der Deutschen Nationalbibliothek.
Die Deutsche Nationalbibliothek verzeichnet diese Publikation in der
Deutschen Nationalbibliografie; detaillierte Bibliografische Daten
sind im Internet über <http://dnb.d-nb.de> abrufbar.

Herausgeber und Vertrieb: Forschungszentrum Jülich GmbH
Zentralbibliothek, Verlag
52425 Jülich
Tel.: +49 2461 61-5368
Fax: +49 2461 61-6103
zb-publikation@fz-juelich.de
www.fz-juelich.de/zb

Umschlaggestaltung: Grafische Medien, Forschungszentrum Jülich GmbH

Druck: Grafische Medien, Forschungszentrum Jülich GmbH

Copyright: Forschungszentrum Jülich 2023

Schriften des Forschungszentrums Jülich
Reihe Information / Information, Band / Volume 92

D 82 (Diss. RWTH Aachen University, 2023)

ISSN 1866-1777
ISBN 978-3-95806-682-3

Vollständig frei verfügbar über das Publikationsportal des Forschungszentrums Jülich (JuSER)
unter www.fz-juelich.de/zb/openaccess.



This is an Open Access publication distributed under the terms of the [Creative Commons Attribution License 4.0](https://creativecommons.org/licenses/by/4.0/), which permits unrestricted use, distribution, and reproduction in any medium, provided the original work is properly cited.

Abstract

Single photons are expected to play an essential role in the transfer of quantum information in modern quantum technology. Monolayers of transition-metal dichalcogenides (TMDs) with implanted defects are promising candidates for single photon sources that allow us to control the polarization of the emitted photons due to their unique spin-valley locking property. This work provides a computational study of a variety of possible materials for implantation, which could possibly be used to confine the photon emission in real space allowing for single photon emission. Several of the tools necessary to carry out the study have been developed and implemented in the course of this work. Here, the focus is on the prediction of electron energy loss spectra and band structure calculations for crystals including a defect. The latter is not straight forward, since the calculation of such defects is done in a supercell consisting of multiple pristine unit cells. The band structure for a supercell is completely different from the pristine one unless the developed unfolding method is applied. This method reveals the defect as a small perturbation to the pristine system, allowing to calculate band structures of defect systems that are comparable to experiments. Experimental electron energy loss spectroscopy (EELS) measurements have a finite \mathbf{k} resolution due to the finite size of the collection aperture in the transition electron microscope. This spectrum deviates significantly from the EELS spectrum for zero \mathbf{k} momentum, as it is commonly calculated using the theoretical dielectric function. Here, a stable method for integrating the theoretical spectra over \mathbf{k} is developed that solves the added difficulty of the integrand varying over several (typically six) orders of magnitude around $k = 0$. This scheme is extended by an extrapolation method for a fast convergence of the introduced vacuum, necessary for calculating monolayers in the context of 3D periodic boundary conditions. The combination of both shows a very favorable agreement with experimental spectra, when applied to three prototypical two-dimensional systems. Density-functional theory (DFT) studies of structural relaxations, band structures, and EELS spectra are carried out for a variety of TMDs (MoS_2 , MoSe_2 , WSe_2) with defects (P, Cr, S, Se, vacancy), applying the developed methods. The investigated system of MoSe_2 +S turns out to lower the conduction band state at the direct band gap compared to the pristine MoSe_2 while preserving the spin-valley locking property. The optical transition in a small island of this material surrounded by MoSe_2 is therefore a promising candidate for single photon emission. Also doping with chromium, which introduces an addition state within the band gap, is a promising candidate to localize the photon emission.

Zusammenfassung

Einzelne Photonen könnten in der Zukunft eine essenzielle Rolle in der Übertragung von Quanteninformation für moderne Quantentechnologie spielen. Monolagen aus Übergangsmetalldichalkogeniden (TMDs) mit implantierten Defekten sind vielversprechende Kandidaten für Einzelphotonenquellen, die es ermöglichen, dank ihrer besonderen „spin-valley locking“ Eigenschaft, die Polarisation der emittierten Photonen zu kontrollieren. Diese Arbeit behandelt eine rechnerische Analyse einer Vielzahl möglicher Materialien zur Implantierung, die dazu genutzt werden könnten, die Photonenemission im Realraum einzuschränken, um die Erzeugung einzelner Photonen zu ermöglichen. Im Verlauf dieser Arbeit wurden die hierfür nötigen Programme entwickelt und implementiert. Das Augenmerk liegt an dieser Stelle auf der Vorhersage von Bandstrukturen der Defektsysteme und deren Elektronenenergieverlustspektren. Rechnerisch werden solche Defektsysteme in Superzellen dargestellt, die aus einer Vielzahl ungestörter Einheitszellen bestehen. Deren Bandstruktur lässt sich nur mit Hilfe der entwickelten Rückfaltungsmethode in Bezug zu der Bandstruktur der ungestörten Einheitszelle setzen. Hierbei wird der Defekt als eine Störung des ursprünglichen Materials dargestellt und kann somit mit der entsprechend experimentellen Messung verglichen werden. In der experimentellen Elektronenenergieverlustspektroskopie (EELS) haben die gemessenen Spektren eine begrenzte \mathbf{k} Auflösung, aufgrund des begrenzten Einsammelwinkels des Spektrometers im Elektronenmikroskop. Dieses Spektrum unterscheidet sich deutlich von dem üblicherweise berechneten EELS Spektrum basierend auf der dielektrischen Funktion ohne Beachtung eines möglichen Impuls Übertrags. Im Folgenden wird eine Methode zur Integration der theoretischen Spektren über \mathbf{k} entwickelt, die, trotz der zusätzlichen Schwierigkeit eines um bis zu sechs Größenordnungen schwankenden Integranden bei $k = 0$, stabil ist. Diese wird erweitert um eine Extrapolationsmethode zur schnellen Konvergenz des zusätzlich hinzugefügten Vakuums, um die Berechnung von Monolagen mit 3D periodischen Randbedingungen zu ermöglichen. Angewendet auf drei typische zweidimensionale Systeme hat die Kombination aus beiden Methoden eine hervorragende Übereinstimmung mit dem Experiment gezeigt. Für eine Vielzahl von TMDs (MoS_2 , MoSe_2 , WSe_2) mit Defekten (P, Cr, S, Se, Fehlstelle) wurde die Bandstruktur und räumliche Relaxation mit Dichtefunktionaltheorie (DFT) sowie die EELS Spektren, unter Anwendung der entwickelten Methoden, studiert. Es konnte gezeigt werden, dass $\text{MoSe}_2 + \text{S}$ ein niedrigeres Leitungsband bei der direkten Bandlücke hat als das störstellenfreie MoSe_2 und dennoch die „spin-valley locking“ Eigenschaft behält. Somit ist die optische Anregung in einer kleinen Insel dieses Materials umgeben von reinem MoSe_2 ein vielversprechender Kandidat für die Emission einzelner Photonen. Das Dotieren mit Chrom ist durch einen zusätzlichen Zustand in der Bandlücke ebenfalls ein vielversprechender Kandidat zur Lokalisierung der Photonenemission.

Contents

List of Figures	viii
Abbreviations and Acronyms	xvii
1 Introduction	1
2 Theoretical background	7
2.1 Density-functional theory (DFT)	7
2.2 FLAPW method	9
2.3 Random-phase approximation (RPA)	12
2.4 The dielectric function	13
2.4.1 The microscopic dielectric function	13
2.4.2 The macroscopic dielectric function	14
2.5 Model description of defect states	15
2.5.1 The effective mass model	15
2.5.2 Deep defects	18
2.6 Observation techniques	19
2.6.1 TEM	19
2.6.2 Photoluminescence spectroscopy	20
2.6.3 Angle-resolved photoemission spectroscopy	20
3 Revealing hidden features in supercell calculations	23
3.1 Theory for unfolding the band structure	25
3.2 Implementation	29
3.2.1 Calculations within the Fleur code	29
3.2.2 Unfolding in the case of SOC (2nd variation)	33
3.2.3 Visualization	34
3.3 Features of unfolded band structure	36
3.3.1 Coupling between two bands	37
3.3.2 Relevance of the supercell size (MoS ₂ +Cr)	40

3.4	Band structures of monolayers with isoelectronic substitutional atoms	41
3.4.1	Interplay of structure and electronic properties for the pristine material	41
3.4.2	MoS ₂ +Se	43
3.4.3	MoSe ₂ +S	48
3.4.4	WSe ₂ +S	52
3.5	Band structures of monolayers with implanted atomic defects	54
3.5.1	MoS ₂ +P	55
3.5.2	MoS ₂ +Cr (@ Mo)	56
3.5.3	MoS ₂ +Cr (@ S)	58
3.5.4	MoS ₂ +Cr+S	60
3.5.5	MoS ₂ +vacancy	62
3.5.6	MoSe ₂ +P	63
3.5.7	MoSe ₂ +Cr (@ Mo)	64
3.5.8	MoSe ₂ +Cr (@ Se)	66
3.5.9	MoSe ₂ +Cr+Se	66
3.5.10	MoSe ₂ +vacancy	67
3.5.11	MoSe ₂ +Cr (interstitial)	68
3.6	Unfolding of the band structure for other types of supercells and systems	70
3.6.1	Surface states of simple unit cell	70
3.6.2	Rotated supercells and general surface states	70
4	Phenomena in low-energy electron energy loss spectroscopy (EELS)	73
4.1	Introduction to EELS	74
4.1.1	Theoretical scattering cross section	74
4.1.2	Electron energy loss	75
4.2	Dielectric layer model	77
4.2.1	Theoretical description of the layer model	78
4.2.2	Different MoS ₂ layer distances within the model	81
4.2.3	Influence of vacuum within the layer model	86
4.2.4	Classical derivation of the plasma frequency	96
4.3	Calculating EELS spectra for 2D systems	98
4.3.1	Treatment of vacuum in supercell calculations	98
4.3.2	Material response in quasi 2D crystals	100
4.3.3	Extrapolating to infinite layer distance	107
4.4	Momentum dependent EELS	112
4.4.1	Momentum summation EELS	113
4.4.2	EELS for pristine MoS ₂ monolayer with momentum summation	119
4.4.3	Application to other 2D materials	128
5	EELS calculation for implanted systems	131
5.1	The dielectric function in the supercell approach	131
5.2	Tool for visualization	133

5.3	EELS signature of defect states	133
5.3.1	MoS ₂ +P	134
5.3.2	MoS ₂ +Cr+S	136
5.3.3	MoSe ₂ +Cr in several configurations	137
5.4	Optical transition elements	139
6	Conclusions	141
A	Tool for plotting band structures	145
B	Tool for plotting EELS	147
C	Computational parameters	149
C.1	Self-consistent DFT calculations	150
C.1.1	Crystal structure of pristine systems	150
C.2	EELS calculations	151
C.3	List of materials (supercells)	153
C.3.1	MoS ₂ +P	153
C.3.2	MoS ₂ +Cr (@ Mo)	154
C.3.3	MoS ₂ +Cr (@ S)	157
C.3.4	MoS ₂ +Cr+S	159
C.3.5	MoS ₂ +vacancy	162
C.3.6	MoS ₂ rotated supercell	163
C.3.7	MoSe ₂ +P	163
C.3.8	MoSe ₂ +Cr (@ Mo)	164
C.3.9	MoSe ₂ +Cr (@ S)	167
C.3.10	MoSe ₂ +Cr+Se	169
C.3.11	MoSe ₂ +vacancy	172
C.3.12	MoSe ₂ +Cr (interstitial)	173
C.3.13	MoS ₂ +Se	175
C.3.14	MoSe ₂ +S	177
C.3.15	WSe ₂ +S	179
C.4	Using quantities within the Fleur code	181
C.4.1	Reciprocal lattice vectors	181
D	Additional Remarks	183
D.1	Fourier transform	183
D.2	Additional figures	183
E	List of scientific contributions	187
	Bibliography	191

List of Figures

1.1	The most evident difference between the MoSe ₂ bulk and MoSe ₂ monolayer band structure is the change from an indirect band gap semiconductor (bulk) to a direct band gap semiconductor (monolayer).	4
2.1	Visualization of the atomic potential landscape in a crystal. As an example a localized core state, an extended valence band state, and a semi-core state are drawn. Adapted from [23].	10
2.2	Visualization of the LAPW basis with the interstitial region (white) and the muffin-tin spheres (blue). The drawing is 2D, even though the basis is in 3D.	11
2.3	Visualization of the Kronig–Penney model with changed potential barriers due to a "deep" defect.	18
3.1	Schematic drawing of a quadratic dispersion calculated in a two unit cell large supercell (1D case) in comparison to the same band structure path in the primitive reciprocal cell. An example for possible unfolding weights (spectral weights) is shown.	25
3.2	Schematic drawing of a 2×2 supercell in reciprocal space (red) and the corresponding primitive reciprocal cell (blue). A k point and its periodic images belonging to the primitive unit cell (g_1, g_2) are marked (crosses) in comparison to the same K point of the reciprocal supercell (G_1, G_2) with the according periodic images (circles).	26
3.3	Unfolded band structure for the case of a pristine 2×2×2 silicon supercell. The supercell band structure contains the bands that are shown in blue and the ones plotted in grey. The blue highlighted band structure is the one of the primitive cell, identified by the unfolding weights. This plot is done using the automatically created gnuplot script.	30
3.4	Unfolded diamond band structure with A-nitrogen-center defect (blue). Additionally, the defect states within the band gap are highlighted. This plot is done using the developed graphical MATLAB tool.	32

3.5	Unfolded MoS ₂ band structure in a 3 × 3 supercell including spin-orbit coupling in 2nd variation. The spin-valley locking property is clearly visible.	34
3.6	Screenshot of the GUI for visualization of unfolded band structures. A plotting process of MoS ₂ with a P defect is shown. In the upper area a plot of the atom groups helps to select a projection onto one.	35
3.7	Unfolded band structure of 3×3×1 MoSe ₂ +P (right) in comparison to the pristine MoSe ₂ (left). Spin up is plotted in blue and spin down in red. Wherever a defect level (from the phosphorus atom) crosses a state of MoSe ₂ , the Hamiltonian can have interaction terms and therefore an avoided crossing may appear (hybridization). An additional band is visible crossing the Fermi energy. The same state is observed in the density of states at the phosphorus atom. This plot is done for demonstrational purpose only. The band structure for the relaxed system is found in Sec. 3.5.6	36
3.8	2 band model: The model resembles the situation of a defect band close to a host material band. From left to right the interaction strength increases. From top to bottom the distance between the two bands is decreased. The line width corresponds to the amount of "host" band ("defect" band) character, except for the first column.	38
3.9	Comparison of the two different supercell sizes demonstrates that a 5×5×1 supercell is necessary for the defect to have very little dispersion, as one would expect for a single defect . The smaller supercell size shows a system where the concentration of defect atoms is high enough for them to interact.	40
3.10	Influence of the structure parameter (z) on the band gap at K and Q for a pristine MoS ₂ monolayer.	42
3.11	Effect of strain on the lattice of MoS ₂ . Negative values correspond to compression. Positive values mean tensile stress. The band gap change is shown as well as the relaxed position of the sulfur layer. The relaxed position can be expressed in terms of the z -parameter.	43
3.12	Atomic structure of MoS ₂ with implanted selenium showing the relaxed position of the defect atom, shifted out of the metal layer. The exact atomic positions can be found in the appendix (Sec. C.3).	44
3.13	Comparison of the pristine material with a low concentrations of selenium implantation in MoS ₂ in the top layer of a 3×3×1 supercell.	44
3.14	Comparison of two different low concentrations of selenium implantation in MoS ₂ in the top layer of a 3×3×1 supercell.	45
3.15	Comparison of two different high concentrations of selenium implantation in MoS ₂ in the top layer of a 3×3×1 supercell.	46
3.16	Overview of the band gap size for different concentrations of selenium in MoS ₂ . The concentration is given with respect to the amount of sulfur atoms in the pristine material.	47

3.17	Influence of the Hilbert energy mesh on the imaginary part of the dielectric function. The label "Hilbert" refers to the SPEX input file [17], where the first number defines the amount of mesh points up to 5 Htr and the second number the exponential growth of the distance between the mesh points.	47
3.18	Imaginary part of the dielectric function (MoS_2) for different selenium concentrations on a $8 \times 8 \times 1$ k-point grid in reciprocal space.	48
3.19	Atomic structure of MoSe_2 with implanted sulfur showing the relaxed position of the defect, shifted towards the metal layer. The exact atomic positions can be found in the appendix (Sec. C.3).	49
3.20	Unfolded band structure of a 3×3 supercell MoSe_2 with substitutional implantation of one sulfur atom in the chalcogen layer (5.5% sulfur considering both chalcogen layers). The pristine band structure of MoSe_2 is shown in turquoise for comparison. The calculation is done without SOC. The direct band gap at K is reduced by 20 meV due to the sulfur.	50
3.21	Unfolded band structure of a 3×3 supercell MoSe_2 with substitutional implantation of three sulfur atoms in the chalcogen layer (16.7% sulfur considering both chalcogen layers). The pristine band structure of MoSe_2 is shown in turquoise for comparison. The calculation is done without SOC. The direct band gap at K is reduced by 43.5 meV due to the sulfur.	51
3.22	Pristine monolayer WSe_2 showing the effect of SOC when comparing the K and $-K$ valley. The layers are separated by a vacuum of 12.98 Å. The two spins are shown in red and blue.	52
3.23	Unfolded band structure of a 3×3 supercell WSe_2 with substitutional implantation of one sulfur atom in the chalcogen layer (5.5% sulfur). The pristine band structure of WSe_2 is shown in turquoise for comparison. The calculation is done with SOC.	53
3.24	Unfolded band structure of a 3×3 supercell WSe_2 with substitutional implantation of three sulfur atoms in the chalcogen layer (16.7% sulfur). The pristine band structure of WSe_2 is shown in turquoise for comparison. The calculation is done with SOC.	54
3.25	Atomic structure of MoS_2 with phosphorus showing the relaxed position of the defect, slightly shifted towards the metal layer in comparison to the other chalcogen atoms. The exact atomic positions can be found in the appendix (Sec. C.3). Plotted using XCrySDen [41].	55
3.26	Unfolded band structure for MoS_2+P , calculated in a 3×3 supercell. The state slightly above the Fermi level for one spin state is clearly visible.	56
3.27	Atomic structure of MoS_2 with implanted chromium at a metal atom showing the relaxed position of the defect and neighbouring chalcogen atoms, slightly shifted towards the defect atom. The exact atomic positions can be found in the appendix (Sec. C.3). Plotted using XCrySDen [41].	57

3.28	Unfolded band structure for MoS_2+Cr , calculated in a 5×5 supercell. The defect state within the band gap is clearly visible. The calculation includes two spins, which are degenerate due to the lack of SOC.	57
3.29	Atomic structure of MoS_2 with implanted chromium at a chalcogen atom showing the relaxed position of the defect, shifted out of the layer. The exact atomic positions can be found in the appendix (Sec. C.3). Plotted using XCrySDen [41].	59
3.30	Unfolded band structure for MoS_2+Cr (@ S), calculated in a 5×5 supercell. The defect state within the band gap is clearly visible.	60
3.31	Atomic structure (relaxed) of MoS_2 with chromium implantation at the chalcogen atom plus an additional chalcogen atom on top. The exact atomic positions can be found in the appendix (Sec. C.3). Plotted using XCrySDen [41].	61
3.32	Unfolded band structure for $\text{MoS}_2+\text{Cr}+\text{S}$, calculated in a 5×5 supercell. The defect state within the band gap is clearly visible. The calculation includes two spins, which are degenerate due to the lack of SOC.	61
3.33	Atomic structure (relaxed) of MoS_2 with a missing chalcogen atom. The exact atomic positions can be found in the appendix (Sec. C.3). Plotted using XCrySDen [41].	62
3.34	Unfolded band structure for MoS_2 with a vacancy in the chalcogen layer, calculated in a 3×3 supercell. The defect state within the band gap is clearly visible. The calculation includes two spins, which are degenerate due to the lack of SOC.	63
3.35	Unfolded band structure for MoSe_2+P , calculated in a 3×3 supercell. The state slightly above the Fermi level is clearly visible.	63
3.36	Unfolded band structure for MoSe_2+Cr , calculated in a 5×5 supercell. The defect state within the band gap is clearly visible. The calculation includes two spins, which are degenerate due to the lack of SOC.	65
3.37	Unfolded band structure for MoSe_2+Cr (@ Se), calculated in a 5×5 supercell. The defect states within the band gap are clearly visible. The calculation includes 2 spins but no SOC.	66
3.38	Unfolded band structure for $\text{MoSe}_2+\text{Cr}+\text{Se}$, calculated in a 5×5 supercell. The defect state within the band gap is clearly visible. The calculation includes two spins, which are degenerate due to the lack of SOC.	67
3.39	Unfolded band structure for MoSe_2 with a vacancy in the chalcogen layer, calculated in a 3×3 supercell. The defect state within the band gap is clearly visible. The calculation includes two spins, which are degenerate due to the lack of SOC.	68
3.40	Atomic structure of MoSe_2 with implanted chromium at an interstitial position showing the relaxed position of the defect atom. The exact atomic positions can be found in the appendix (Sec. C.3). Plotted using XCrySDen [41].	68

3.41	Unfolded band structure for MoSe ₂ with a chromium defect atom at an interstitial position, calculated in a 5×5 supercell. The calculation includes two spins, but does not include SOC.	69
3.42	Unfolded band structure for twisted MoS ₂ . The band structure without unfolding is shown in grey. This demonstrates the possibility to obtain the primitive unit cell band structure from the rotated unit cell.	71
4.1	Representation of a TMD slab system with effective dielectric constant $\epsilon_{\parallel}, \epsilon_{\perp}$, and ϵ_{vac} . d_{eff} denotes the effective layer thickness, which is determined in Sec. 4.2.2.	78
4.2	Illustration of the fictitious capacitors in the homogeneous layer model for the case of the dielectric constant in parallel and in perpendicular direction	79
4.3	Imaginary part of the effective dielectric function perpendicular to the layer compared for different vacuum distances (MoS ₂). The convergence with a vacuum spacing of 34.9 Å and 49.2 Å can be clearly seen . The comparison to the unchanged dielectric function (out-of-plane direction), plotted as dotted lines (axis label on the right), makes the convergence behavior obvious.	83
4.4	Imaginary part of the effective dielectric function parallel to the layer compared for different vacuum distances (MoS ₂). The convergence with a larger vacuum spacing can be clearly seen . The comparison to the unchanged dielectric function (in-plane direction), plotted as dotted lines, makes the convergence behavior obvious.	84
4.5	Effective EELS spectrum for 12.3 Å to 49.2 Å compared with the original EELS. The original EELS refers to the EELS based on the calculated dielectric function including vacuum without any model considerations.	85
4.6	Effective EELS spectrum for 12.3 Å to 49.2 Å compared with the original EELS. The original EELS refers to the EELS based on the calculated dielectric function including vacuum without any model considerations.	86
4.7	Comparison of different layer distances with and without scaling by the vacuum size for MoS ₂ . Here the imaginary part of the in-plane component with and without LFE is shown.	92
4.8	Comparison of different layer distances with and without scaling by the vacuum size for MoS ₂ . Here the imaginary part of the out-of-plane component with and without LFE is shown.	93
4.9	Comparison of different layer distances without scaling by the vacuum size for MoS ₂ . Here EELS for the in-plane component with and without LFE is shown.	94
4.10	Comparison of different layer distances with and without scaling by the vacuum size for MoS ₂ . Here EELS for the out-of-plane component with and without LFE is shown.	95
4.11	Infinite stack of layers with distance d used in a slab system.	102

4.12	Loss function of MoS ₂ calculated by extrapolation using Eq. (4.3.58) for different layer distances. A very fast convergence is visible, independent of the momentum transfer (in-plane).	110
4.13	Fig. 4.12 shows the explicit convergence of the extrapolated loss function, whereas here the convergence of the the two limiting cases towards the extrapolated loss function with increasing layer distance is shown.	111
4.14	Momentum resolved EELS spectra for MoS ₂ with a momentum transfer between 0 (Γ) and a momentum transfer of $K = (1/3, 1/3, 0)$. The color darkness (white-blue-green) corresponds to the extrapolated EELS intensity. A layer distance of 24.6 Å is used.	112
4.15	Visualization of the prefactor for the in-plane and the out-of-plane component of the dielectric function.	117
4.16	EELS spectrum and absorption spectrum of MoS ₂ without momentum transfer	120
4.17	EELS spectrum and absorption spectrum of MoS ₂ with $0.23 \frac{1}{\text{Å}}$ momentum transfer	121
4.18	EELS spectrum and absorption spectrum of MoS ₂ with $0.023 \frac{1}{\text{Å}}$ momentum transfer	122
4.19	Comparison and convergence of different k-point grids with the Γ point treated explicitly (MoS ₂). The summation over the full Brillouin zone for a 20×20 (orange), 60×60 (blue), 100×100 (purple) and 180×180 (green) grid are shown.	123
4.20	Comparison of the experimental spectrum of MoS ₂ (orange) recorded by our collaborators from the University of Limerick [53] and the EELS summation (blue) using a 100×100 grid of k-points summed for the full Brillouin zone.	124
4.21	Comparison of the experimental spectrum of MoS ₂ (orange) recorded by our collaborators from Limerick [53] and the EELS summation (blue) using a combined dataset for different vacuum distances. 100×100 grid of k-points summed for the full Brillouin zone.	125
4.22	Comparison of experimental EELS Data for MoS ₂ [53] and the extrapolated and summed loss function for 24.6 Å as well as the absorption function ($\text{Im}(\varepsilon)$) without momentum transfer.	126
4.23	Impact of (convergence) quantities on the summed and extrapolated loss spectrum of MoS ₂	127
4.24	Influence of the speed of the electrons on the summed up spectrum — prefactor of $\frac{1}{v^2}$ is left out to focus on the peak structure.	128
4.25	Comparison of experimental EELS Data for hBN [54] and the extrapolated and summed loss function as well as the absorption function ($\text{Im}(\varepsilon)$) without momentum transfer.	129
4.26	Comparison of experimental EELS Data for graphene [55] and the extrapolated and summed loss function as well as the absorption function ($\text{Im}(\varepsilon)$) without momentum transfer.	130

5.1	Comparison of calculated EELS for MoS ₂ in a simple unit cell (dark orange) and in a 3×3 supercell (blue). Special care was taken to converge all computational parameters and the mesh for summation so that the results are comparable. Also, the maximum momentum transfer included in the integration is the same for both cases.	132
5.2	Screenshot of the GUI for visualization of EELS spectra. A plotting process of the integrated EELS spectrum of MoS ₂ in comparison to the experimental spectrum is shown. In the upper area, a plot of the irreducible wedge (red) and the integration maximum (grey) is visualized.	133
5.3	Comparison of calculated EELS for MoS ₂ +P and the pristine MoS ₂ , both including the extrapolation and integration scheme. Both calculations are done in a 3×3 supercell. The metallic character of the phosphorus implantation is clearly visible.	134
5.4	Comparison of calculated absorption function for MoS ₂ +P and the pristine MoS ₂ . Both calculation are done in a 3×3 supercell. The metallic character of the phosphorus implantation is clearly visible. . .	135
5.5	Comparison of calculated EELS for MoS ₂ +S+Cr (5×5 supercell) and the pristine MoS ₂ (3×3 supercell). The influence of the defect is clearly visible.	136
5.6	Comparison of calculated absorption function for MoS ₂ +S+Cr (5×5 supercell) and the pristine MoS ₂ (3×3 supercell). The influence of the defect is clearly visible.	137
5.7	Comparison of calculated absorption function for pristine MoSe ₂ (5×5 supercell) and MoSe ₂ +Cr (5×5 supercell) in various positions of the crystal structure (interstitial, Se substitutional, Mo substitutional, and Se substitutional with additional Se). The influence of the different defects is clearly visible.	138
5.8	The Kohn-Sham band structure of the pristine monolayer MoS ₂ is shown in blue. The additional color represents the energy of the transition element. The thickness represents the size of the matrix element (likelihood for this transition). It can be clearly seen that the highest transition probability is at the <i>K</i> point.	140
A.1	Screenshot of the GUI for visualization of unfolded band structures. A plotting process of MoS ₂ with a P defect is shown. In the upper area, a plot of the atom groups helps to select a projection onto one.	146
B.1	Screenshot of the GUI for visualization of EELS spectra. A plotting process of the integrated EELS spectrum of MoS ₂ in comparison to the experimental spectrum is shown. In the upper area a plot of the irreducible wedge (red) and the integration maximum (grey) is visualized.	147
D.1	Convergence behavior with interlayer distance and with momentum transfer (including LFE)	184

D.2	Convergence behavior with interlayer distance and with momentum transfer (without LFE)	185
D.3	Unfolded band structure for MoSe ₂ +Cr+Se, calculated in a 5×5 supercell with a similar DFT parameter set as MoSe ₂ +Cr (interstitial). The defect state within the band gap is clearly visible and not effected by the underconverged parameter set. The calculation includes two spins, which are degenerate due to the lack of SOC. This DFT calculation is used as a starting point for the absorption spectrum of MoSe ₂ +Cr+Se in Fig. 5.7	186

Abbreviations and Acronyms

ARPES	angle-resolved photoemission spectroscopy
BSE	Bethe–Salpeter equation
DFT	density-functional theory
EELS	electron energy loss spectroscopy
eff	effective
ext	external
FLAPW	full-potential linearized augmented plane-wave
GGA	generalized gradient approximation
Htr	Hartree
KS	Kohn–Sham
LDA	local-density approximation
LFE	local field effects
MPB	mixed product basis

RPA	random-phase approximation
SOC	spin-orbit coupling
TDDFT	time-dependent density-functional theory
TEM	transmission electron microscopy
TMD	transition-metal dichalcogenide
tot	total
XC	exchange-correlation

Introduction

We are at the transition to a new quantum age. Quantum technology in the form of quantum computing, quantum annealing and quantum communication is evolving from a theoretical quantum mechanical concept to working machines. Unprecedented computational abilities through new devices on the basis of quantum technology will lead to advances in materials design, artificial intelligence, and health care [1]. The development of materials to meet the requirements of these devices is a key field of research. Quantum information has to be transferred from and to a stationary "qubit" system. Specially prepared photons can be used for this purpose. This thesis is concerned with the search for materials that could be used to create photons for this and many more applications in the context of quantum technology. In recent years, transition-metal dichalcogenides (TMDs) have gained more and more attention in this context, where they are promising candidates for novel semiconductor devices [2]. Monolayer-thick samples have remarkable physical properties due to their two-dimensional structure making them an exciting platform for the development of photonic devices with new functionalities.

Motivation

Methods in quantum computing, quantum research, and quantum cryptography, like the BB84 algorithm [3], rely on single photons with known polarization. Electrically driven photon emission with these properties [4] is a key requirement to make these methods available for widespread practical applications. In TMDs a combination of the hexagonal lattice symmetry with massive atoms that introduce a spin splitting of energy levels due to their strong spin-orbit-coupling (SOC) results in a spin-valley locking. Here, the energetically most favorable state of an excited electron within the symmetry of the crystal is connected to its spin. Exploiting this spin-valley locking property of the TMDs allows controlling the polarization of the emitted photon by

the spin of the electron introduced into the system [5]. A suitable defect in the TMD monolayer could localize the emission of photons in real space and therefore allow for electrically driven single photon emission [6, 7].

Aim of this work

The aim of this work is to identify suitable materials for implantation in MoSe₂ or MoS₂ for optical experiments, aiming to achieve single photon emission. These defects should reflect the symmetry of the host lattice and preserve the spin-valley locking property. The defects are mainly located in the chalcogen layer because here the experimental realization of the implantation process is more feasible and introduces less strain on the structure as a whole [2]. To verify the suitability, the electronic structure is analyzed with ab-initio methods in this thesis. This analysis includes structural relaxations, calculations of valence band electron energy loss spectra [8, 9], and band structures within the Jülich DFT code package [10–12].

This work is embedded in a project together with three experimental groups: The group of Prof. Beata Kardynal at PGI-9, Forschungszentrum Jülich doing photoluminescence (PL) experiments, the group of Prof. Ursel Bangert at the University of Limerick doing investigations using transition electron microscopy (TEM) and performing electron energy loss spectroscopy (EELS), as well as the group of Prof. Hans Hofsäss, Universität Göttingen, implanting defect atoms into the samples. This work supports the planning process, measurement, and interpretation of results by theoretical developments and modeling of material properties.

Supercell unfolding

In order to perform calculations including a defect atom, this defect atom has to be embedded in a pristine environment. A supercell consisting of multiple pristine unit cells has to be constructed for this purpose. This results in an accordingly smaller reciprocal cell. The band structure of a supercell appears very different from the pristine band structure even though it describes the same (or a slightly distorted) system. Since the band structure of a supercell (with a defect) is not straightforward to interpret, a method for unfolding the bands is implemented using an algorithm based on the one by Rubel and coworkers [13]. The result is a band structure that looks similar to the one of the primitive unit cell but contains additional information on the defect states.

EELS for 2D Systems

EELS spectra are used to characterize the possible electron excitations within a system. EELS is an important tool to distinguish pristine and defected regions in a sample. With fine enough resolution, it may even be possible to distinguish different

types of defects. For this purpose, it is important to compare the measured spectra with theoretically simulated spectra. The calculation of these spectra can be done using many-body perturbation theory. Using the random-phase approximation (RPA) (Sec. 2.3) the results turn out to be different from experimental loss spectra obtained from EELS. The reason for this could be either the inadequacy of the RPA or the interpretation of the inverse dielectric function as the EELS spectrum, which might be too simplistic for a direct comparison to experimental spectra. In the scope of this thesis the latter will be demonstrated. Furthermore, it is shown that computing electron energy loss spectra for comparison to experiment requires a methodological extension in order to include multiple momentum transfers, which turns out to be necessary for a typical transition electron microscope (TEM) setup. This methodology is derived and applied to pristine and defect systems. For prototypical pristine 2D systems (hBN, graphene and MoS₂) a very favorable agreement with experimental measurements is found. The calculation of monolayer material properties requires a much larger computational effort than the treatment of a bulk material, since the former requires larger unit cells due to the additional vacuum to be included. For theoretical methods that require 3D periodic boundary conditions a large vacuum has to be placed in between the periodic images of the slabs to effectively decouple them. Especially for the case of RPA the long range screening effects cause a slow convergence with respect to the added vacuum, making supercell calculations including a defect atom practically impossible due to limited computational resources. In this work a method for extrapolating to infinite layer distance is developed, drastically reducing the required vacuum in the computational unit cell.

The study of monolayer materials is very interesting, since their properties can be significantly different from the bulk material due to a different structure, surface states, and less screening. Besides the very well known graphene, TMDs form another class of materials that can be exfoliated into two-dimensional materials down to monolayer systems. Like graphene, TMDs also show very different material properties in the monolayer configuration than in the bulk configuration. In Fig. 1.1 the band structure of a MoSe₂ monolayer is shown in comparison to the band structure of bulk MoSe₂. Comparing the band gap the K point, it becomes obvious that the monolayer has a direct band gap whereas the bulk material has an indirect one. This makes the monolayer material very interesting for optical applications. Photons carry very little (nearly no) momentum, therefore a direct band gap is needed for their emission (unless

Monolayer
properties

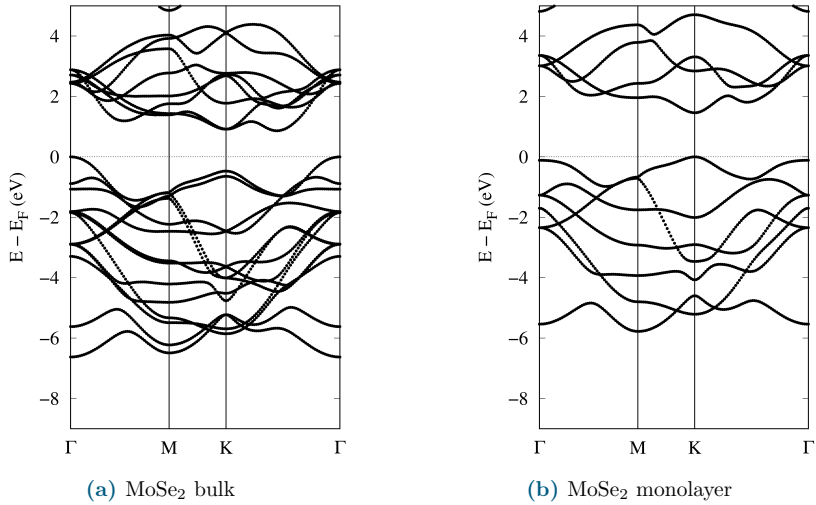


Figure 1.1: The most evident difference between the MoSe₂ bulk and MoSe₂ monolayer band structure is the change from an indirect band gap semiconductor (bulk) to a direct band gap semiconductor (monolayer).

multi-scattering events with a phonon are taken into account). The same property is found for other TMDs like MoS₂, WS₂, and WSe₂.

Functionalization of defects

Introducing defects into the crystal structure of the material breaks the translation symmetry and changes its properties. Clear diamonds obtain a red colour from nitrogen-vacancy defects, transistors would not work without controlled doping and there are countless more examples. There is a complete description and classification of defect states in [Sec. 2.5](#), at this point the emphasis is on the motivation for introducing defect atoms into the system. Defect atoms can have many effects on the crystal. Three of them that are of relevance at this point are: changing the atomic structure, changing the electric properties, and changing the optical properties (additional energy levels).

Introducing a change of the structure (phase) is for example used in new types of nonvolatile memory [14]. Changing the charge of the system is used in the design of P-doped or N-doped semiconductors by introducing an electron into the system or taking one out. But in general, introducing a defect to the system breaks the translational symmetry of the lattice, therefore lifting the degeneracy of certain states.

Or the defect atom introduces additional defect levels due to its electronic configuration. If these defect states lie within the band gap of a semiconductor they can change the optical emission spectrum drastically. They can also be used to trap an electron-hole pair (exciton) at them if it is energetically more favorable for the exciton to be located at the defect atom. A localization of the excited state in real-space corresponds to emission (due to recombination of the electron-hole pair) only at that point, which means only a single excitation at a time - a requirement for single photon emission. Implantation in the case of a monolayer TMD is only possible with very low ion energy [15, 16].

This work is mainly based on the Fleur code and the SPEX code developed at the Forschungszentrum Jülich. The Fleur code [10] is an open-source community code that is an implementation of density-functional theory in the linearized augmented plane-wave (LAPW) basis (Sec. 2.2), allowing for an all-electron treatment. The implemented full-potential linearized augmented plane-wave method is widely considered the most precise electronic structure method. Its basic workflow is the self-consistent solution of the Kohn-Sham equations (Sec. 2.1). It includes a large variety of features with a focus on non-collinear magnetism. In this work the main use is the structure optimization through force relaxation, the calculation of band structures, and in the case of defect systems, their unfolding in reciprocal space. The DFT result of Fleur provides a starting point for applying RPA.

SPEX [17] is an independent part of the Jülich FLAPW code family. It uses the self-consistent solution from Fleur to calculate theoretical spectra and quasiparticle properties employing the *GW* approximation. It is based on many-body perturbation theory and also uses the FLAPW method with the addition of the mixed product basis (MPB) [12]. It is a feature rich software that allows for the calculation of "EELS and optical spectra as well as total energies in the RPA approximation, and spin-wave and optical (experimental) spectra from the Bethe-Salpeter equation, Hubbard U parameters, Wannier interpolation, and more" [17]. In this work it is used to calculate the dielectric function based on RPA (Sec. 2.3). The dielectric function is the main ingredient for calculating the EELS spectrum.

Bringing together the results of the EELS spectrum and unfolded band structure for a defect system allows for a thorough understanding of the electronic properties of the defect and an assumption of the experimental results to be expected. The unfolded band structure helps to evaluate the type of defect state introduced and its interplay

Computational
methods

Using the
combined
finding

with the spin-valley locking property. Whereas the EELS spectrum delivers information on the transitions that can actually be excited. This knowledge is on the one hand important for the decision on the kind of defect to be investigated in order to achieve single photon emission. On the other hand, it is indispensable to the analysis of the measured data. Without predictions of the expected result, the interpretation of PL spectra and EELS experiments is very difficult.

Organization of this thesis

Before diving into the main topics of this thesis, the first chapter gives a motivation for this work as well as an overview of the techniques involved. In the following chapter the theoretical background is build up to lay the foundation for the developments within this work. It is meant to be a compact easy to follow summary of the essential points to understand the following work, rather giving the main idea and reference to relevant literature than repeating complete derivations available from the original sources. The main content is organized in the following three chapters. First hidden features of band structures for supercells are discussed by introducing an unfolding scheme and its application to defect systems. Then the calculation of EELS spectra for monolayers is extended to include effects inherent to the experimental method that have been neglected before. To effectively reduce the vacuum needed in the calculation of monolayers an extrapolation scheme is introduced. This developed methodology makes prediction of EELS spectra for monolayers including defect atoms possible which is shown in the following using the systems from the first part. The work will conclude with a summery, outlook, and a set of additional information and descriptions on the developed tools.

Theoretical background

2.1	Density-functional theory (DFT)	7
2.2	FLAPW method	9
2.3	Random-phase approximation (RPA)	12
2.4	The dielectric function	13
2.4.1	The microscopic dielectric function	13
2.4.2	The macroscopic dielectric function	14
2.5	Model description of defect states	15
2.5.1	The effective mass model	15
2.5.2	Deep defects	18
2.6	Observation techniques	19
2.6.1	TEM	19
2.6.2	Photoluminescence spectroscopy	20
2.6.3	Angle-resolved photoemission spectroscopy	20

2.1 Density-functional theory (DFT)

Density-functional theory (DFT) is a widely spread method in theoretical condensed matter physics to determine the ground-state properties of a many-body systems of electrons in a crystal. Taking into account the Born-Oppenheimer approximation, the atom cores can be considered fixed for the observation of the electron movement. DFT is applied in theoretical chemistry and physics in different kind of approximations and implementations specialized for specific cases and systems. It is based on the finding that relevant properties of a system can be extracted from its position dependent

density [18]. P. Hohenberg and W. Kohn showed that the ground state of an electronic system is uniquely determined by its electron density. Additionally, they proved that the ground-state density $n_0(\mathbf{r})$ minimizes the total energy functional $E[n(\mathbf{r})]$.

$$E[n(\mathbf{r})] = T[n(\mathbf{r})] + W[n(\mathbf{r})] + V[n(\mathbf{r})] \quad (2.1.1)$$

with the kinetic energy $T[n(\mathbf{r})]$, the electron-electron interaction energy $W[n(\mathbf{r})]$, and the external potential energy $V[n(\mathbf{r})] = \int n(\mathbf{r})V(\mathbf{r})d\mathbf{r}$ where $V(\mathbf{r})$ is the external potential created by the positive charges of the nuclei. Unfortunately they did not describe how to obtain the universal functional $T[n(\mathbf{r})]+W[n(\mathbf{r})]$, which is an ongoing field of research as more and more sophisticated approximations are still being developed.

W. Kohn and L. J. Sham introduced a fictitious non-interacting system with an effective potential [19]. This non-interacting system is much easier to compute than the interacting system. The Kohn-Sham system is designed to have the exact same ground-state density $n_0(\mathbf{r})$ as the interacting many-body system, so that the ground-state properties of the interacting system can be extracted, given the exact functional. Strictly speaking excited states of the interacting system cannot be determined from the Kohn-Sham system.

The Kohn-Sham wave functions can be found by solving the stationary Schrödinger equation and diagonalizing the Kohn-Sham Hamiltonian.

$$\left(-\frac{\hbar^2}{2m}\nabla^2 + V_{KS}(\mathbf{r}) \right) \phi_i(\mathbf{r}) = \epsilon_i \phi_i(\mathbf{r}) \quad (2.1.2)$$

All equations are given in atomic units where $e = m_e = \hbar = \frac{1}{4\pi\epsilon_0} = 1 a.u.$ but the constants are included nevertheless as a reminder to the well known form in SI units. The electron density is then given by the sum over the orbital densities of the occupied states $n(\mathbf{r}) = \sum_i \int \phi_i(\mathbf{r})\phi_i^*(\mathbf{r})d\mathbf{r}$. This density is identical to the density of the interacting system. Unfortunately the Kohn-Sham potential depends itself on the density

$$V_{KS}(\mathbf{r}) = V(\mathbf{r}) + \int \frac{e^2 n(\mathbf{r}')}{|\mathbf{r} - \mathbf{r}'|} d\mathbf{r}' + \frac{\delta E_{XC}}{\delta n(\mathbf{r})} \quad (2.1.3)$$

and therefore this system of equations can only be solved self-consistently. Here E_{XC} is the exchange-correlation energy in correspondence with the Kohn-Sham total energy:

$$E[n(\mathbf{r})] = T_{KS}[n(\mathbf{r})] + W_H[n(\mathbf{r})] + V[n(\mathbf{r})] + E_{XC}[n(\mathbf{r})] \quad (2.1.4)$$

Here E_{XC} accounts for the difference between the many-body electron-electron interaction energy and the Hartree energy $W_H = \iint \frac{e^2}{2} \frac{n(\mathbf{r})n(\mathbf{r}')}{|\mathbf{r}-\mathbf{r}'|} d\mathbf{r}' d\mathbf{r}$ as well as a correction to the Kohn-Sham kinetic energy of the non-interacting system in comparison to the interacting one. One of the first approximations for an ab-initio functional to calculate E_{XC} , the local-density approximation (LDA), already delivers surprisingly precise results. It depends only on the electron density at each point in space and gives the exchange-correlation energy according to the homogeneous electron gas with the same density. To achieve higher accuracy, needed for example for the prediction of chemical bonds, one has to use more accurate approximations for E_{XC} . The generalized gradient approximation [20, 21] (GGA) is not only using the density but also the density gradient. Both approaches deliver very good results for the ground-state properties. In theory the Kohn-Sham system describes the ground state of a system correctly and delivers eigenvalues also for the excited states, though these eigenvalues have, strictly speaking, no meaning for the real interacting system. Therefore, the band structure is quantitatively wrong for the excited states and the resulting band gap is usually underestimated. To overcome this shortcoming more computationally demanding methods like time-dependent density-functional theory (TDDFT) and *GW* have to be used. There are also attempts to lift the shortcomings of the LDA and GGA functional by further extensions like hybrid functionals, metaGGA, and hyperGGA (improving the precision according to "Jacob's ladder" [22]).

Walter Kohn got the Nobel Prize in chemistry in 1998 for his work on DFT, because his theory revolutionized the ability of modeling material properties.

2.2 FLAPW method

The potential $V(\mathbf{r})$ of a crystal consists of regions around the atom cores that experience predominantly the Coulomb potential of the nuclei and areas in between the atoms where the potential is only slowly varying. A code based on the plane-wave basis can only model well the regions with relatively flat potential and therefore has to adopt some kind of pseudo-potential around the atom cores (unless infinitely many basis functions

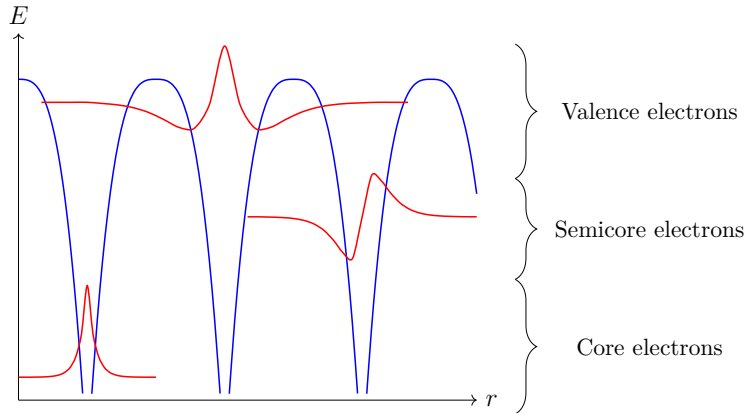


Figure 2.1: Visualization of the atomic potential landscape in a crystal. As an example a localized core state, an extended valence band state, and a semi-core state are drawn. Adapted from [23].

are used, which is computationally impossible). The aim of the full-potential linearized augmented plane-wave (FLAPW) method is to lift this limitation and consider all electron wave functions of the crystal without the assumption of a pseudo-potential. Therefore, the crystal is divided into areas around the atom core, where the basis functions already incorporate the $1/r$ potential and areas in between where the wave functions are modeled by plane waves. These two basis sets have to be matched at the so called muffin-tin boundary. In Fig. 2.1 the atom landscape is pictured. In addition to the described treatment of the valence electrons the core electrons are treated separately. To increase the flexibility of the basis set and allow for a better matching at the muffin-tin boundary additional local orbitals are included within the muffin-tin sphere that help to describe the semicore electrons. These electrons have an energy in between the valence band electrons and core electrons but are mostly confined to the muffin-tin sphere. The treatment of these semicore electrons is one of the difficulties of the LAPW basis set and can be addressed by introducing local orbital basis functions [24].

The construction of the electron wave functions in the LAPW basis can be summarized

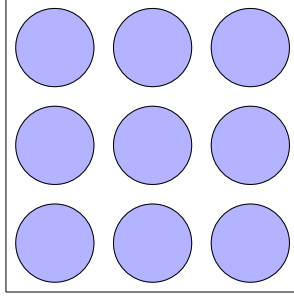


Figure 2.2: Visualization of the LAPW basis with the interstitial region (white) and the muffin-tin spheres (blue). The drawing is 2D, even though the basis is in 3D.

as the following, with basis functions $\chi_{\mathbf{k},\mathbf{G}}(\mathbf{r})$ (Fig. 2.2).

$$\chi_{\mathbf{k},\mathbf{G}}(\mathbf{r}) = \begin{cases} \frac{1}{\sqrt{\Omega}} e^{i(\mathbf{k}+\mathbf{G})\mathbf{r}} & \text{interstitial region} \\ \sum_{l,m} (a_{lm}^{\alpha,\mathbf{G}}(\mathbf{k})u_l^\alpha(\mathbf{r}^\alpha) + b_{lm}^{\alpha,\mathbf{G}}(\mathbf{k})\dot{u}_l^\alpha(\mathbf{r}^\alpha)) Y_{lm}(\hat{\mathbf{r}}^\alpha) & \text{muffin-tin } \alpha \end{cases} \quad (2.2.1)$$

Here \mathbf{G} are the reciprocal crystal basis vectors, Ω is the unit cell volume, u_l^α and $\dot{u}_l^\alpha(r^\alpha)$ are solutions for the spherical potential (and the corresponding derivatives), Y_{lm} denote the spherical harmonics and $a_{lm}^{\alpha,\mathbf{G}}(\mathbf{k})$ as well as $b_{lm}^{\alpha,\mathbf{G}}(\mathbf{k})$ are matching coefficients to make sure the transition between the muffin-tin area and the interstitial region with plane wave basis functions is smooth.

Using the FLAPW method, the stationary Schrödinger equation (Eq. (2.1.2)) can be expressed as an eigenvalue problem using the basis functions $\chi_{\mathbf{k},\mathbf{G}}(\mathbf{r})$ [11]. The electron wave functions $\Psi_{\mathbf{k}}^n(\mathbf{r})$ with a Bloch vector \mathbf{k} and a band index n can be formulated in the expansion coefficients $c_n^{\mathbf{k},\mathbf{G}}$.

$$\Psi_{\mathbf{k}}^n(\mathbf{r}) = \sum_{\mathbf{G}} c_n^{\mathbf{k},\mathbf{G}} \chi_{\mathbf{k},\mathbf{G}}(\mathbf{r}) \quad (2.2.2)$$

The Hamiltonian used for the stationary Schrödinger equation can be expressed in the basis of the functions $\chi_{\mathbf{k},\mathbf{G}}(\mathbf{r})$. Together with the overlap matrix ($S_{\mathbf{G}',\mathbf{G}}^k = \int_{\Omega} \chi_{\mathbf{k},\mathbf{G}'}^*(\mathbf{r}) \chi_{\mathbf{k},\mathbf{G}}(\mathbf{r}) d^3\mathbf{r}$) the generalized eigenvalue problem can be set up [11].

$$\sum_{\mathbf{G}} H_{\mathbf{G}',\mathbf{G}}^k c_n^{\mathbf{k},\mathbf{G}} = \epsilon_n^{\mathbf{k}} \sum_{\mathbf{G}} S_{\mathbf{G}',\mathbf{G}}^k c_n^{\mathbf{k},\mathbf{G}} \quad (2.2.3)$$

Here, ϵ_n^k are the eigenvalues that give the Kohn-Sham band structure of the system.

2.3 Random-phase approximation (RPA)

In the random-phase approximation [25, 26] the polarizability of a system is calculated by taking into account that an excitation will cause a change of potential that itself introduces a small perturbation, thus inducing an infinite series of excitations. This can be visualized in an infinite series of excitation diagrams, where each circle denotes an electron-hole excitation and the dashed lines bare Coulomb interactions.

$$\begin{aligned} \chi(\mathbf{q}, \omega) = & \text{Diagram 1} + \text{Diagram 2} + \text{Diagram 3} \\ & + \text{Diagram 4} + \text{Diagram 5} + \text{Diagram 6} + \dots \end{aligned} \quad (2.3.1)$$

In reciprocal space of a periodic system this can be summarized in the following microscopic response function $\chi_{\mathbf{G}, \mathbf{G}'}(\mathbf{q}, \omega)$:

$$\chi_{\mathbf{G}, \mathbf{G}'}(\mathbf{q}, \omega) = P_{\mathbf{G}, \mathbf{G}'}(\mathbf{q}, \omega) + \sum_{\mathbf{G}_1} P_{\mathbf{G}, \mathbf{G}_1}(\mathbf{q}, \omega) v_{\mathbf{G}_1} \chi_{\mathbf{G}_1, \mathbf{G}'}(\mathbf{q}, \omega) \quad (2.3.2)$$

where $P_{\mathbf{G}, \mathbf{G}'}(\mathbf{q}, \omega)$ denotes the polarizability and v the Coulomb potential. The polarizability can be calculated using the Kohn-Sham eigensolutions with the wave functions $\varphi_n(\mathbf{r})$ and the eigenvalues ϵ_n . n is the index for each state (or in reciprocal space to the band index) (atomic units).

$$\begin{aligned} P(\mathbf{r}, \mathbf{r}'; \omega) = & 2 \sum_n^{\text{occ.}} \sum_{n'}^{\text{unocc.}} \varphi_n^*(\mathbf{r}) \varphi_n(\mathbf{r}') \varphi_{n'}(\mathbf{r}) \varphi_{n'}^*(\mathbf{r}') \\ & \times \left[\frac{1}{\omega + \epsilon_n - \epsilon_{n'} + i\eta} - \frac{1}{\omega - \epsilon_n + \epsilon_{n'} - i\eta} \right] \end{aligned} \quad (2.3.3)$$

Here η is a positive infinitesimal which reflects the time ordering of the response function. Furthermore, the Bloch vector is suppressed for simplicity and a non-spin-polarized system is assumed, which leads to a factor of two instead of an explicit spin summation [12]. The summation over band index n' for the unoccupied states is in theory up to infinity. In practice the number of included states in the summation is a convergence parameter of the calculation.

2.4 The dielectric function

The response of a material to an external electric field is described by the dielectric function $\varepsilon(\mathbf{q}, \omega)$. The external perturbation can have the form of light, an incoming charged particle, or an electric field. The dielectric function itself is determined by the possible excitations (single excitations and collective excitations) within the crystal. These are not only determined by the components of the crystal but also by its electronic structure, crystal shape, and the interface to the surrounding.

In condensed matter physics there is a wealth of theories that aim at a model description of this dielectric function like the Drude model or Lorentz model. In the macroscopic Maxwell equations the dielectric function relates the electric field with the displacement field. In this work the dielectric function is determined by ab-initio calculations based on density-functional theory (DFT) and the random-phase approximation (RPA).

2.4.1 The microscopic dielectric function

In general the microscopic dielectric function $\varepsilon(\mathbf{r}, \mathbf{r}', \omega)$, as it is used in linear response theory, is dependent on the place of interest in real space \mathbf{r} , all other positions \mathbf{r}' , and the frequency of the excitation ω . With this, the total potential due to some arbitrary external potential can be written as:

$$\Phi^{\text{tot}}(\mathbf{r}, \omega) = \int \varepsilon^{-1}(\mathbf{r}, \mathbf{r}', \omega) \Phi^{\text{ext}}(\mathbf{r}', \omega) d\mathbf{r}' \quad (2.4.1)$$

The microscopic dielectric function can be calculated from the polarizability (Eq. (2.3.3)) found within the framework of the random-phase approximation and the Coulomb potential $v(\mathbf{r} - \mathbf{r}'')$ by:

$$\varepsilon(\mathbf{r}, \mathbf{r}'; \omega) = \delta(\mathbf{r} - \mathbf{r}') - \int v(\mathbf{r} - \mathbf{r}'') P(\mathbf{r}'', \mathbf{r}'; \omega) d^3 r'' \quad (2.4.2)$$

In a periodic system with lattice vectors \mathbf{G} , \mathbf{G}' and using a plane-wave representation, the microscopic function reads:

$$\varepsilon_{\mathbf{G}\mathbf{G}'}(\mathbf{k}, \omega) = \frac{1}{V} \iint e^{-i(\mathbf{k}+\mathbf{G})\mathbf{r}} \varepsilon(\mathbf{r}, \mathbf{r}'; \omega) e^{i(\mathbf{k}+\mathbf{G}')\mathbf{r}'} d^3 r d^3 r' \quad (2.4.3)$$

The normalization of the plane waves $e^{i(\mathbf{k}+\mathbf{G})\mathbf{r}}/\sqrt{V}$ results in a prefactor of $1/V$, where V is the crystal volume. The dielectric function is here shown for the plane-wave representation, whereas the used code frameworks (Fleur and SPEX) rely on the

FLAPW method. As described in the [Sec. 2.2](#) the LAPW basis is different in the area around the atom cores, but it can be treated analogously to the plane-wave basis with simple changes. The same holds for the mixed product basis (MPB) [12] additionally used within the SPEX code. For simplicity, it is sufficient to show the physical quantities for the plane-wave basis.

2.4.2 The macroscopic dielectric function

The microscopic dielectric function plane-wave representation is connected to the macroscopic one, describing the system on a large scale, by [25, 27]:

$$\varepsilon_M(\mathbf{q}, \omega) = \frac{1}{\varepsilon_M^{-1}(\mathbf{q}, \omega)} = \frac{1}{\varepsilon_{\mathbf{0}\mathbf{0}}^{-1}(\mathbf{q}, \omega)} \quad (2.4.4)$$

Here $\varepsilon_{\mathbf{0}\mathbf{0}}(\mathbf{q}, \omega)$ is the long wavelength part of the microscopic dielectric function in reciprocal space ($\mathbf{G} = \mathbf{G}' = \mathbf{0}$ component of $\varepsilon_{\mathbf{G}\mathbf{G}'}(\mathbf{q}, \omega)$). The macroscopic dielectric function is the one that is used in classical electrodynamics (real or reciprocal space - whichever is useful at the time) relating the displacement field \mathbf{D} and the electric field \mathbf{E} .

$$\mathbf{D} = \varepsilon_M \mathbf{E}$$

For the complete characterization of the dielectric function in reciprocal space it is important to note the angular dependence around $\mathbf{q} = \mathbf{0}$. Depending on the direction $\hat{\mathbf{q}}$ from which one approaches $\mathbf{q} = \mathbf{0}$ the limit $\lim_{\mathbf{q} \rightarrow \mathbf{0}} \varepsilon_{\mathbf{0}\mathbf{0}}(\mathbf{q}, \omega)$ has in general a different value. It can therefore be formulated in vector form by $\varepsilon(\mathbf{q}, \omega) \sim \hat{\mathbf{q}}^T \varepsilon(\omega) \hat{\mathbf{q}}$. The 3×3 dielectric tensor has the following form, that can be simplified depending on the symmetries of the system.

$$\varepsilon(\omega) = \begin{pmatrix} \varepsilon_{q_x, q_x}(\omega) & \varepsilon_{q_x, q_y}(\omega) & \varepsilon_{q_x, q_z}(\omega) \\ \varepsilon_{q_y, q_x}(\omega) & \varepsilon_{q_y, q_y}(\omega) & \varepsilon_{q_y, q_z}(\omega) \\ \varepsilon_{q_z, q_x}(\omega) & \varepsilon_{q_z, q_y}(\omega) & \varepsilon_{q_z, q_z}(\omega) \end{pmatrix}. \quad (2.4.5)$$

The "inverse" tensor $\varepsilon^{-1}(\omega)$, that is used for the macroscopic relation therefore has to be understood as the tensor approximating $\hat{\mathbf{q}}^T \varepsilon^{-1}(\omega) \hat{\mathbf{q}} \approx 1/(\hat{\mathbf{q}}^T \varepsilon(\omega) \hat{\mathbf{q}})$. For a system that does not have a diagonal and isotropic dielectric tensor, this does not simplify to $\varepsilon^{-1}(\omega) = [\varepsilon(\omega)]^{-1}$ [12] but is rather identical to the second order in the components of $\hat{\mathbf{q}}$.

2.5 Model description of defect states

Any irregularity in a perfect crystal structure is a defect. First of all, one can differentiate the type of defect by its spatial extent. There are line defects (whole lines or planes of dislocation) and there are point defects (small groups of atoms or single atoms). Single atom point defects are the only ones discussed in this work.

They can be further classified by their position within the crystal structure. There are interstitial defects, where an atom sits in between two lattice sites, substitutional impurities, where a different atom sits at the same site as the replaced host lattice atom and there are vacancies.

Furthermore, a defect can either be a donor, an acceptor or isoelectronic. This differentiation is done by whether the defect donates an electron to the system, accepts an electron from the system or does not change the electronic configuration at all. This can be determined from the position in the periodic table in relation to the host atom being replaced.

If the defect is considered within a semiconductor material, the type can be further differentiated by the defect states it introduces in the band gap. If the additional defect states are located close enough to the conduction band minimum (CBM), in the case of a donor, or close enough to the valence band maximum (VBM), in the case of a acceptor, to be ionized at room temperature, they are considered "shallow" defects. Defects in the middle of the band gap are considered "deep" defects.

For the treatment of defects within a crystal there exists a variety of model approaches. Here two of them are introduced that help to understand the role of a defect atom within a crystal and allow for an interpretation of calculated electronic band structures. The "effective mass model" can treat defect states that are very shallow and only show a small perturbation in comparison to the host lattice state. On the other hand "deep defects" result in electronic states that have more in common with a single atom than with a host lattice state.

2.5.1 The effective mass model

To gain an understanding of the effects a defect atom has onto the crystal and its electronic properties (band structure) it is instructive to study a very reduced model. The effective mass model is only valid for shallow dopants (hydrogenic defects), that add a small perturbation to the system.

The starting point is the Schrödinger equation of an undisturbed crystal. This derivation

is guided by the lecture of Akiko Natori [28]. SI units are used in this chapter, to give explicit results in the end.

$$H_{\text{crys}}\psi(r) = E\psi(r) \quad (2.5.1)$$

H_{crys} is the undisturbed Hamiltonian of the pristine crystal. The solutions to this Hamiltonian are given by the eigenfunctions $\phi_{nk}(r)$ and eigenenergies ε_{nk} . An additional perturbation $V(r)$ is added to the crystal (that could be a defect).

$$(H_{\text{crys}} + V(r))\psi(r) = E\psi(r) \quad (2.5.2)$$

The solutions to this new Schrödinger-equation will be expressed using the former eigenfunctions as a basis. This is useful because one can assume that a single shallow defect will only slightly alter the wave functions. This is not true for deep defects, which will be considered in [Sec. 2.5.2](#).

$$\psi(r) = \sum_m \int \chi_m(k) \phi_{mk}(r) \frac{dk}{(2\pi)^3} \quad (2.5.3)$$

For this derivation we are only interested in the conduction band minimum, which we assume to have band index n and to be located at the Γ point ($k = 0$). The eigenfunctions is $\phi_{nk}(r) = u_{nk}(r)e^{ikr}$, $u_{nk}(r)$ being the lattice periodic part of the Bloch function. At $k = 0$ the planewave part vanishes $\phi_{n0}(r) = u_{n0}(r)e^{i0r} = u_{n0}(r)$. So in the present case the following approximation is true for the states around the conduction band minimum:

$$\phi_{nk}(r) \approx u_{n0}(r)e^{ikr} = \phi_{n0}(r)e^{ikr} \quad (2.5.4)$$

Therefore, the new wave function is:

$$\psi(r) \approx \phi_{n0}(r) \int \chi_n(k) e^{ikr} \frac{dk}{(2\pi)^3} \quad (2.5.5)$$

Performing the Fourier transform delivers:

$$\psi(r) = \phi_{n0}(r)\chi_n(r). \quad (2.5.6)$$

Now using this, the effect of the unperturbed Hamiltonian on the new wave function will be investigated.

$$H_{\text{crys}}\psi(r) = H_{\text{crys}} \int \chi_n(k) \phi_{nk}(r) \frac{dk}{(2\pi)^3} \quad (2.5.7)$$

$$= \int \chi_n(k) \varepsilon_{nk} \phi_{nk}(r) \frac{dk}{(2\pi)^3} \quad (2.5.8)$$

$$\approx \phi_{n0}(r) \int \chi_n(k) \varepsilon_{nk} e^{ikr} \frac{dk}{(2\pi)^3} \quad (2.5.9)$$

Each band n can be represented by an infinite series of polynomials k^m (with prefactors a_{mn}): $\varepsilon_{nk} = \sum_m a_{mn} k^m$

$$H_{\text{crys}}\psi(r) \approx \phi_{n0}(r) \sum_m a_{mn} \int \chi_n(k) k^m e^{ikr} \frac{dk}{(2\pi)^3} \quad (2.5.10)$$

$$= \phi_{n0}(r) \sum_m a_{mn} \int \chi_n(k) (-i\nabla)^m e^{ikr} \frac{dk}{(2\pi)^3} \quad (2.5.11)$$

$$= \phi_{n0}(r) \sum_m a_{mn} (-i\nabla)^m \chi_n(r) \quad (2.5.12)$$

$$= \phi_{n0}(r) \varepsilon_n (-i\nabla) \chi_n(r) \quad (2.5.13)$$

Reintroducing the energy eigenvalues instead of the infinite series was now useful. But instead of the discrete eigenvalues used before, the "Effective mass approximation" is used, where the local change of the curvature determines the effective mass ($m^* = \hbar^2 \left(\frac{d^2\varepsilon}{dk^2}\right)^{-1}$). The energy eigenvalues for the conduction band around Γ are in this case:

$$\varepsilon_n(k) \approx \varepsilon_c + \frac{\hbar^2 k^2}{2m^*} \quad (2.5.14)$$

The next step is to solve the Schrödinger equation for the envelope function $\chi(r)$. The connection between the envelope function and the wave function is given by the Bloch eigenfunctions, that serve as a basis $\psi(r) \approx \phi_{n0}(r) \chi_n(r)$

$$(\varepsilon_n(-i\nabla) + V(r))\chi(r) = E\chi(r) \quad (2.5.15)$$

$$\left(-\frac{\hbar^2}{2m^*}\nabla^2 + V(r)\right)\chi(r) = (E - \varepsilon_c)\chi(r) \quad (2.5.16)$$

All the effects of the defect are included in ε_c and the effective mass m^* . With the Coulomb potential from a donor ion in the electrostatic screening environment of the crystal:

$$V(r) = -\frac{e^2}{4\pi\varepsilon_0\varepsilon_s r} \quad (2.5.17)$$

the solution of the Schrödinger equation is analogous to the unperturbed system:

$$E = \varepsilon_c - \frac{e^4 m^*}{8h^2 \varepsilon_0^2 \varepsilon_s^2} = \varepsilon_c - Ry \frac{m^*}{m_0 \varepsilon_s^2} \quad (2.5.18)$$

The final energy of the defect state is only determined by the Rydberg constant ($Ry = 13.6 \text{ eV}$), the dielectric environment, and the effective mass. This emphasizes that in the case of a shallow dopant the defect state will appear similar to the host state (also when analyzing the band structure).

2.5.2 Deep defects

One possible definition of "deep" defect states is purely based on their position within the band gap, but it is also possible to distinguish "deep" and "shallow" defects by their interaction distance within the crystal [29]. Shallow defects act similar to the host lattice wave function and are spatially very extended whereas the influence of deep defects is concentrated on one atom side. In the picture of a simple Kronig–Penney model this means that one of the potential wells has increased height of the barriers 2.3. In contrast a shallow defect would correspond to the modulation of one valley. For a deep defect this is often connected to a local structure change making spatial relaxation highly important [30]. Their localization in real space means that they are delocalized

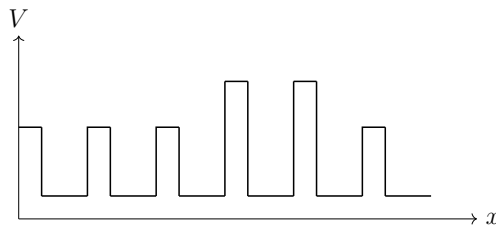


Figure 2.3: Visualization of the Kronig–Penney model with changed potential barriers due to a "deep" defect.

in reciprocal space. This delocalization enables them to interact with a variety of

momentum vectors or phonons, also allowing for non-radiative recombination [31]. Their treatment requires therefore not only the focus on the minimum of one single band (like in the effective mass theory) but rather the treatment of the whole band structure [31].

2.6 Observation techniques

To understand the purpose of the methods developed and tools used in the following it is important to give a short overview of the experimental techniques involved in characterizing monolayer-thick TMDs.

2.6.1 TEM

Transmission electron microscopy (TEM) is a very powerful and versatile technique. It functions somewhat similarly to light microscopy but with fast electrons and magnetic lenses that change their trajectory [32]. At the top of the microscope an electron gun, based on a Schottky-field emitter, produces a coherent electron beam. These electrons are then accelerated to up to 300 keV. There are two main modes how the electron beam can be focused on the probe:

1. A focused beam that can be used for scanning the probe (Scanning Transmission Electron Microscopy (STEM))
2. A parallel broad beam, by which a larger area can be investigated with collinear electrons

Since the probe is thin enough for the electrons to be transmitted, they can be detected underneath the probe. Here is a second system of lenses allowing to operate the TEM in two modes (depending on the incoming electron beam):

1. Real space imaging
2. Momentum space imaging

The real space imaging allows us to picture single atoms, their position, distance to other atoms, and using their intensity some information on the type of atom. In momentum space the electrons are scattered after interaction with the material. They

are then collected inside some aperture, effectively limiting the maximum scattering angle detected. By detection with a pixelated detector or limiting the detection to a certain scattering angle it is also possible to obtain information about the transferred momentum during interaction with the probe.

Additionally, it is possible to analyze the energy of the electrons detected. The result is a loss spectrum specific to the excitation within the probe. This electron energy loss spectroscopy (EELS) gives a wealth of information on the material and its properties. There is a variety of developments combining EELS with momentum resolution or spatial resolution. To add spatial resolution it is either possible to use a focused electron beam or to record an image in real space and analyze the EELS spectrum at each pixel. Even combination of spatial resolution and momentum resolution are possible but in the end one is limited by the Heisenberg uncertainty principle [33], even though the experimental limit due to the number of available electrons is reached at much lower resolution [34, 35]. Especially for the monolayer materials of interest to this work the intensity of the electron beam has to be carefully limited in fluence and energy to not destroy the probe before it is imaged.

2.6.2 Photoluminescence spectroscopy

Photoluminescence spectroscopy allows us to investigate the optical and electronic properties of the direct band gap. Electrons from the valence band are excited with photons to the conduction band, where they relax to the lowest conduction band state before recombination with the vacancy left in the valence band. During this relaxation process a photon is emitted that can be detected. This method is sensitive to exciton binding energies (also trions etc.) and can also detect very low concentration of defect atoms.

An extension of this experiment can be used to proof single photon emission [36]. For this the emitted light is analyzed behind a beam splitter with two photodetectors ensuring that there is only one single photon emission within a certain very short delay.

2.6.3 Angle-resolved photoemission spectroscopy

Another widely used technique that enables us to directly measure the band structure is the angle-resolved photoemission spectroscopy (ARPES). Here high energy photons

(35 – 100 eV) are used to extract electrons from the material. These electrons are then measured with energy and angular resolution [37]. This allows for the determination of all occupied energy levels within the full Brillouin zone including the according momentum information. MoS₂ has already been measured in high quality [38]. The unfolded band structures show what would be expected in an ARPES measurement for a defect systems.

Revealing hidden features in supercell calculations

3.1	Theory for unfolding the band structure	25
3.2	Implementation	29
3.2.1	Calculations within the Fleur code	29
3.2.2	Unfolding in the case of SOC (2nd variation)	33
3.2.3	Visualization	34
3.3	Features of unfolded band structure	36
3.3.1	Coupling between two bands	37
3.3.2	Relevance of the supercell size (MoS ₂ +Cr)	40
3.4	Band structures of monolayers with isoelectronic substitutional atoms	41
3.4.1	Interplay of structure and electronic properties for the pristine material	41
3.4.2	MoS ₂ +Se	43
3.4.3	MoSe ₂ +S	48
3.4.4	WSe ₂ +S	52
3.5	Band structures of monolayers with implanted atomic defects	54
3.5.1	MoS ₂ +P	55
3.5.2	MoS ₂ +Cr (@ Mo)	56
3.5.3	MoS ₂ +Cr (@ S)	58
3.5.4	MoS ₂ +Cr+S	60
3.5.5	MoS ₂ +vacancy	62
3.5.6	MoSe ₂ +P	63
3.5.7	MoSe ₂ +Cr (@ Mo)	64

3.5.8	MoSe ₂ +Cr (@ Se)	66
3.5.9	MoSe ₂ +Cr+Se	66
3.5.10	MoSe ₂ +vacancy	67
3.5.11	MoSe ₂ +Cr (interstitial)	68
3.6	Unfolding of the band structure for other types of supercells and systems	70
3.6.1	Surface states of simple unit cell	70
3.6.2	Rotated supercells and general surface states	70

In the calculation of a pristine lattice one chooses the smallest possible unit cell, reflecting the symmetry of the pristine lattice. In reciprocal space the energy values and wave functions are calculated in the whole Brillouin zone but then a path along a few of the high symmetry points is chosen, and the energy values are only plotted along this path — this is the well known band structure. There is no useful representations of the full Brillouin zone including the relevant energy levels at each point in reciprocal space, unless one restricts the plot to a certain energy, for example the Fermi energy. For most materials the minima and maxima do appear at, or close to, high symmetry points. So it is sufficient to analyze the band structure instead of the full Brillouin zone.

To calculate a single defect one has to build a supercell made up of multiple pristine unit cells. The defect atom is put in one of the primitive cells, but is embedded in a pristine surrounding. If the aim is to calculate a single defect the supercell has to be chosen large enough so that its periodic images, due to the periodic boundary conditions, don't interact. The reciprocal cell of such a supercell is much smaller than the original primitive reciprocal cell. Consequently, also the high symmetry points and path are different from the primitive reciprocal cell. This implies that for a system without any defect the calculated supercell band structure changes depending on the supercell size, even though the same pristine "physical" system is calculated. In an experimental context a constructed supercell is not visible as a supercell — rather it is shown as the primitive system (and in the case of a defect with a small perturbation). Instead of calculating a new system (the supercell system), one would like to relate the results back to the primitive reciprocal cell. This unfolding to the primitive cell is done through the technique that is presented in the following.

3.1 Theory for unfolding the band structure

Relating the band structure of the supercell to the band structure of the primitive cell consists of two steps. First the band structure of the supercell has to be calculated, not along the high symmetry path in the reciprocal supercell, the reciprocal cell of the supercell, but along the band structure path of the primitive unit cell. This path can cross multiple of Brillouin zones of the reciprocal supercell (depending on the size of the supercell). At each k -point of this path some kind of weight has to be found to

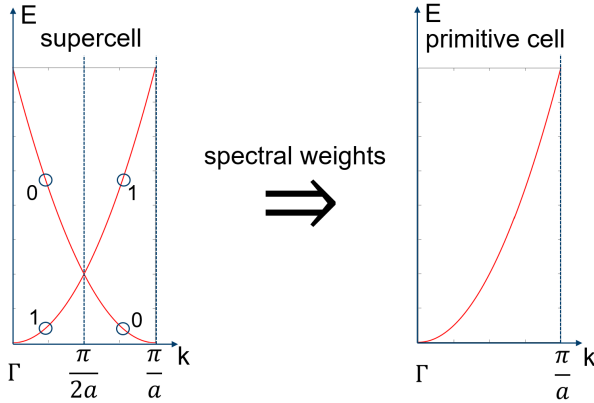


Figure 3.1: Schematic drawing of a quadratic dispersion calculated in a two unit cell large supercell (1D case) in comparison to the same band structure path in the primitive reciprocal cell. An example for possible unfolding weights (spectral weights) is shown.

differentiate between the energy levels that are also visible in the band structure of the primitive cell and energy levels that exist due to the supercell construction. In Fig. 3.1 a schematic drawing of the expected weights for a two unit cell large supercell in 1D is shown. The derivation for a plane wave basis follows the idea from [13].

Starting from Bloch plane waves in a unit cell of volume Ω with the according coefficients $C_{n,\mathbf{K}}(\mathbf{G})$

$$\Psi_{n,\mathbf{K}}(\mathbf{r}) = \frac{1}{\sqrt{\Omega}} \sum_{\mathbf{G}} C_{n,\mathbf{K}}(\mathbf{G}) e^{i(\mathbf{K}+\mathbf{G})\cdot\mathbf{r}} \quad (3.1.1)$$

the wave functions are normalized with the condition $\langle \Psi_{n,\mathbf{K}} | \Psi_{n,\mathbf{K}} \rangle = 1$. Therefore the coefficients fulfill the condition:

$$\sum_{\mathbf{G}} C_{n,\mathbf{K}}(\mathbf{G}) \cdot C_{n,\mathbf{K}}^*(\mathbf{G}) = 1 \quad (3.1.2)$$

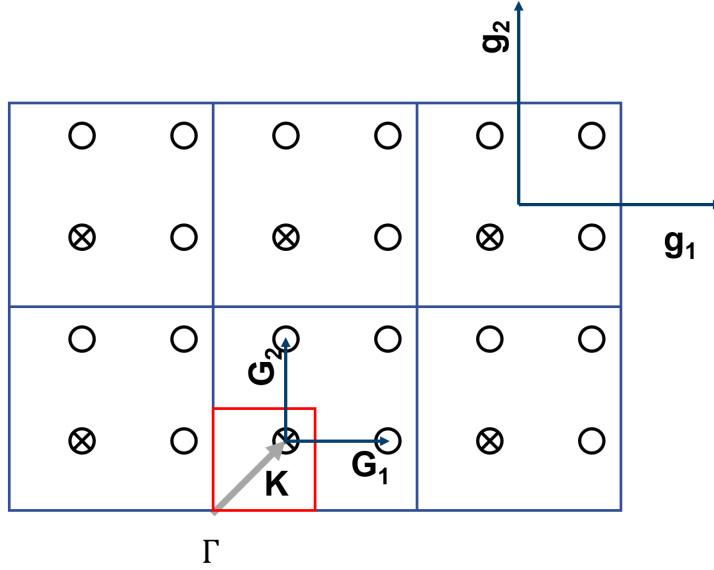


Figure 3.2: Schematic drawing of a 2×2 supercell in reciprocal space (red) and the corresponding primitive reciprocal cell (blue). A \mathbf{k} point and its periodic images belonging to the primitive unit cell ($\mathbf{g}_1, \mathbf{g}_2$) are marked (crosses) in comparison to the same \mathbf{K} point of the reciprocal supercell ($\mathbf{G}_1, \mathbf{G}_2$) with the according periodic images (circles).

When calculating a supercell it is possible to find the \mathbf{k} points of the primitive unit cell that correspond to one \mathbf{K} point of the supercell with the following condition:

$$\mathbf{k} = \mathbf{K} + m_1 \mathbf{G}_1 + m_2 \mathbf{G}_2 + m_3 \mathbf{G}_3 \quad (3.1.3)$$

with $m_i = \{0, 1, \dots, n_i - 1\}$ and n_i being the size of the supercell (in multiples of the primitive unit cell) along the i 's direction. For each set of $\mathbf{k} + \{\mathbf{g}\}$ there is a subset of $\mathbf{K} + \{\mathbf{G}\}$ that fulfills $\mathbf{k} + \mathbf{g} = \mathbf{K} + \mathbf{G}$. This subset of \mathbf{G} vectors can be used to calculate an individual weight between 0 and 1 for each state at \mathbf{K} . The subgroup of these \mathbf{G} vectors fulfilling the condition is called $\tilde{\mathbf{G}}$. Here the selected \mathbf{K} and the selected group of $\tilde{\mathbf{G}}$ are both dependent on the \mathbf{k} , so strictly speaking one would have to write $\mathbf{K}(\mathbf{k})$ and $\tilde{\mathbf{G}}(\mathbf{k})$. The sum of plane wave coefficients ($w_n(\mathbf{k})$) has a value between 0 and 1, since it is restricted to a subset $\tilde{\mathbf{G}}$ of \mathbf{G} vectors. Without this restriction, so summing over the full set of \mathbf{G} vectors, it would be 1.

$$w_n(\mathbf{k}) = \sum_{\tilde{\mathbf{G}}} |C_{n,\mathbf{K}}(\tilde{\mathbf{G}})|^2 \quad (3.1.4)$$

In the FLAPW method this is a little different. Here the LAPW basis functions are given by

$$\Psi_{n,\mathbf{K}}(\mathbf{r}) = \sum_{\mathbf{G}} C_{n,\mathbf{K}}(\mathbf{G}) \cdot \chi_{\mathbf{K},\mathbf{G}}(\mathbf{r}) \quad (3.1.5)$$

with $\chi_{\mathbf{K},\mathbf{G}}(\mathbf{r})$ being the complete set of basis functions of interstitial plane waves and spherical harmonics. In this case the normalization condition $\langle \Psi_{n,\mathbf{K}} | \Psi_{n,\mathbf{K}} \rangle = 1$ corresponds to:

$$1 = \int \left(\sum_{\mathbf{G}} C_{n,\mathbf{K}}^*(\mathbf{G}) \cdot \chi_{\mathbf{K},\mathbf{G}}^*(\mathbf{r}) \right) \cdot \left(\sum_{\mathbf{G}'} C_{n,\mathbf{K}}(\mathbf{G}') \cdot \chi_{\mathbf{K},\mathbf{G}'}(\mathbf{r}) \right) d\mathbf{r} \quad (3.1.6)$$

$$1 = \sum_{\mathbf{G}} \sum_{\mathbf{G}'} C_{n,\mathbf{K}}^*(\mathbf{G}) \cdot C_{n,\mathbf{K}}(\mathbf{G}') \int \chi_{\mathbf{K},\mathbf{G}}^*(\mathbf{r}) \cdot \chi_{\mathbf{K},\mathbf{G}'}(\mathbf{r}) d\mathbf{r} \quad (3.1.7)$$

The overlap matrix of the basis functions is known and can be written as $S_{\mathbf{K},\mathbf{G},\mathbf{G}'}$

$$S_{\mathbf{K},\mathbf{G},\mathbf{G}'} = \langle \chi_{\mathbf{K},\mathbf{G}} | \chi_{\mathbf{K},\mathbf{G}'} \rangle = \int \chi_{\mathbf{K},\mathbf{G}}^*(\mathbf{r}) \cdot \chi_{\mathbf{K},\mathbf{G}'}(\mathbf{r}) d\mathbf{r} \quad (3.1.8)$$

$$1 = \sum_{\mathbf{G}} \sum_{\mathbf{G}'} C_{n,\mathbf{K}}^*(\mathbf{G}) \cdot C_{n,\mathbf{K}}(\mathbf{G}') \cdot S_{\mathbf{K},\mathbf{G},\mathbf{G}'} \quad (3.1.9)$$

So the ‘‘spectral weights’’ can be defined exactly the way they were written before.

$$w_n(\mathbf{k}) = \sum_{\tilde{\mathbf{G}}(\mathbf{k})} \sum_{\mathbf{G}'} C_{n,\mathbf{K}(\mathbf{k})}^*(\tilde{\mathbf{G}}(\mathbf{k})) \cdot C_{n,\mathbf{K}(\mathbf{k})}(\mathbf{G}') \cdot S_{\mathbf{K}(\mathbf{k}),\tilde{\mathbf{G}}(\mathbf{k}),\mathbf{G}'} \quad (3.1.10)$$

Another option is to use a representation of the LAPW basis in-plane waves. Despite the fact, that this representation has a very slow convergence, I want to show that it is possible to apply. Starting from a representation for

$$\chi_{\mathbf{K},\mathbf{G}}(\mathbf{r}) = \sum_{\mathbf{Z}} D_{n,\mathbf{K},\mathbf{G}}(\mathbf{Z}) e^{i(\mathbf{K}+\mathbf{Z})\mathbf{r}} \quad (3.1.11)$$

and replacing the LAPW basis functions

$$\Psi_{n,\mathbf{K}}(\mathbf{r}) = \sum_{\mathbf{G}} C_{n,\mathbf{K}}(\mathbf{G}) \cdot \chi_{\mathbf{K},\mathbf{G}}(\mathbf{r}) \quad (3.1.12)$$

$$= \sum_{\mathbf{G}} C_{n,\mathbf{K}}(\mathbf{G}) \cdot \left(\sum_{\mathbf{Z}} D_{n,\mathbf{K},\mathbf{G}}(\mathbf{Z}) \cdot e^{i(\mathbf{K}+\mathbf{Z})\mathbf{r}} \right) \quad (3.1.13)$$

$$= \sum_{\mathbf{G},\mathbf{Z}} C_{n,\mathbf{K}}(\mathbf{G}) \cdot D_{n,\mathbf{K},\mathbf{G}}(\mathbf{Z}) \cdot e^{i(\mathbf{K}+\mathbf{Z})\mathbf{r}} \quad (3.1.14)$$

the norm becomes a little more complicated $\langle \Psi_{n,\mathbf{K}} | \Psi_{n,\mathbf{K}} \rangle = 1$

$$\langle \Psi_{n,\mathbf{K}} | \Psi_{n,\mathbf{K}} \rangle = \int \sum_{\mathbf{G},\mathbf{Z}} \sum_{\mathbf{G}',\mathbf{Z}'} C_{n,\mathbf{K}}^*(\mathbf{G}) \cdot D_{n,\mathbf{K},\mathbf{G}}^*(\mathbf{Z}) \cdot e^{-i(\mathbf{K}+\mathbf{Z})\mathbf{r}} \cdot C_{n,\mathbf{K}}(\mathbf{G}') \cdot D_{n,\mathbf{K},\mathbf{G}'}(\mathbf{Z}') \cdot e^{i(\mathbf{K}+\mathbf{Z}')\mathbf{r}} \mathbf{d}\mathbf{r} \quad (3.1.15)$$

$$\langle \Psi_{n,\mathbf{K}} | \Psi_{n,\mathbf{K}} \rangle = \sum_{\mathbf{G},\mathbf{G}'} \sum_{\mathbf{Z}} C_{n,\mathbf{K}}^*(\mathbf{G}) \cdot D_{n,\mathbf{K},\mathbf{G}}^*(\mathbf{Z}) \cdot C_{n,\mathbf{K}}(\mathbf{G}') \cdot D_{n,\mathbf{K},\mathbf{G}'}(\mathbf{Z}). \quad (3.1.16)$$

Now the “spectral weights” can be defined the same way like before again implying that $\mathbf{K}(\mathbf{k})$ and $\tilde{\mathbf{G}}(\mathbf{k})$ are \mathbf{k} dependent due to the selection of the subgroup of \mathbf{G}

$$w_n(\mathbf{k}) = \sum_{\tilde{\mathbf{G}},\mathbf{G}'} \sum_{\mathbf{Z}} C_{n,\mathbf{K}}^*(\tilde{\mathbf{G}}) \cdot D_{n,\mathbf{K},\tilde{\mathbf{G}}}^*(\mathbf{Z}) \cdot C_{n,\mathbf{K}}(\mathbf{G}') \cdot D_{n,\mathbf{K},\mathbf{G}'}(\mathbf{Z}). \quad (3.1.17)$$

Given the overlap matrix in the plane wave representation:

$$S_{\mathbf{K},\mathbf{G},\mathbf{G}'} = \langle \chi_{\mathbf{K},\mathbf{G}} | \chi_{\mathbf{K},\mathbf{G}'} \rangle \quad (3.1.18)$$

$$= \int \sum_{\mathbf{Z},\mathbf{Z}'} D_{n,\mathbf{K},\mathbf{G}}^*(\mathbf{Z}) e^{-i(\mathbf{K}+\mathbf{Z})\mathbf{r}} D_{n,\mathbf{K},\mathbf{G}'}(\mathbf{Z}') e^{i(\mathbf{K}+\mathbf{Z}')\mathbf{r}} \mathbf{d}\mathbf{r} \quad (3.1.19)$$

$$= \sum_{\mathbf{Z}} D_{n,\mathbf{K},\mathbf{G}}^*(\mathbf{Z}) D_{n,\mathbf{K},\mathbf{G}'}(\mathbf{Z}) \quad (3.1.20)$$

Using this result the “spectral weight” can be rewritten, giving the same result like before.

$$w_n(\mathbf{K}) = \sum_{\tilde{\mathbf{G}}, \mathbf{G}'} C_{n, \mathbf{K}}^*(\tilde{\mathbf{G}}) \cdot C_{n, \mathbf{K}}(\mathbf{G}') \cdot S_{\mathbf{K}, \tilde{\mathbf{G}}, \mathbf{G}'} \quad (3.1.21)$$

The band structure along the reciprocal path of the primitive unit cell is then calculated with an additional “plotting weight” for each state.

In principle the unfolding technique is not limited to the case of stretched unit cells (see Eq. (3.1.3)). The supercell can also be rotated (and stretched) as long as the transformation matrix between the lattice vectors contains only integer values. For the reciprocal lattice vectors the condition ($i = 1, 2, 3$)

$$\mathbf{g}_i = \mathbf{n} \cdot \mathbf{G}_i \quad (3.1.22)$$

with the transformation matrix

$$\mathbf{n} = \begin{pmatrix} n_{1,1} & n_{1,2} & n_{1,3} \\ n_{2,1} & n_{2,2} & n_{2,3} \\ n_{3,1} & n_{3,2} & n_{3,3} \end{pmatrix}. \quad (3.1.23)$$

has to exist. For the selection of the subset of \mathbf{G} , which fulfills $\mathbf{k} + \mathbf{g} = \mathbf{K} + \mathbf{G}$, it is required that each entry of the matrix \mathbf{n} has an integer value. By using a general transformation matrix it is possible to unfold from rotated cells. This is interesting in the case of surface state calculations. For the here investigated case of TMDs a supercell is just a stretched primitive cell, meaning the transformation matrix is diagonal.

3.2 Implementation

The unfolding mechanism is implemented within the Fleur code. Performing the calculation as a post processing tool would require large files to be written out to hard disk, since the full \mathbf{G} dependence of the wave functions is needed.

3.2.1 Calculations within the Fleur code

The necessary routines for the unfolding mechanism are implemented in the Fleur routine “Fleur/kpoints/unfoldBandKPTS.f90”. The routine is executed within the

main eigenvalue procedure of Fleur, directly after the diagonalization. The implementation is parallelized for multiple MPI-threads (regarding the k-point loop) with the requirement that the number of k-points is a multiple of the number of MPI-threads. In the publication by O. Rubel et al. [13] only the plane-wave part was used to calculate

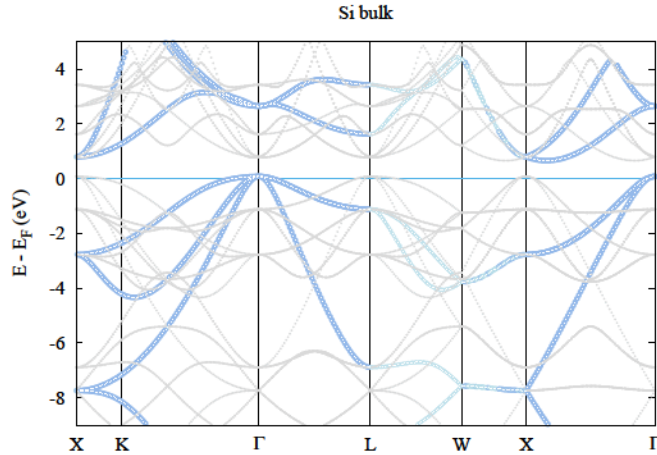


Figure 3.3: Unfolded band structure for the case of a pristine $2 \times 2 \times 2$ silicon supercell. The supercell band structure contains the bands that are shown in blue and the ones plotted in grey. The blue highlighted band structure is the one of the primitive cell, identified by the unfolding weights. This plot is done using the automatically created gnuplot script.

the unfolding weights. In the present implementation it is possible to switch between using only the plane-wave part of the wave functions or the full LAPW basis function set including the overlap matrix necessary. This feature is controlled by the flag `useOverlap="F"` in the input file. Even though the including of the full LAPW basis is more precise, there was no significant difference for any of the tested systems.

The k-point path in the reciprocal supercell can be automatically given in terms of the primitive reciprocal cell, if the supercell is constructed as a multiple of the primitive cell. Within the code there are two possibilities for this. First one could fold the path into the first Brillouin zone before the calculation, the other is to compute a k-point path stretching over several supercell Brillouin zones. Both ways were tested, delivering the same results. The latter one is used in the final implementation. This

is especially helpful for an easy calculation when using a rotated supercell because it spares the identification of the corresponding \mathbf{K} point in the first Brillouin zone of the reciprocal supercell. The subset of \mathbf{G} can then be found by using the transformation matrix \mathbf{n} (Eq. (3.1.22)) and checking whether $\mathbf{n}^{-1}\mathbf{G}$ gives an integer valued result in the reciprocal lattice vector basis.

A test case showing silicon in a pristine $2 \times 2 \times 2$ silicon supercell is shown in Fig. 3.3. It is impressive to see that the supercell calculation would have suggested silicon as a direct band gap semiconductor (grey and blue band structure), whereas the unfolding correctly reveals the band gap as being indirect (only blue band structure).

The usage within the Fleur input file is well described in the online available manual www.flapw.de/Max-5.1/documentation/bandUnfolding/ [10]. For completeness a copy of my description from the manual is given in the following.

Description of unfolding in the Fleur manual

This feature is controlled by a separate flag within the output section. In this section the size of the supercell has to be specified (in multiples of the primitive unit cell). Unfolding the band structure can only be used when the flag for a band structure calculation (`/output/@band`) is set. When the Boolean flag `/output/unfoldingBand/@unfoldBand` is set to `T`, two band structures are calculated. The band structure of the provided cell (supercell) and a band structure for the primitive cell, meaning the unfolded band structure, is written out. Fleur then creates additional output files (`band_sc.1`, `band_sc.2` and `band_sc.gp`) with the same usage as described for the normal band structure calculation. The gnuplot file can be used directly to plot the unfolded band structure. Additionally, the information is also written to the `banddos.hdf` file. There it can be used for other plotting tools. This allows for additional analysis, for example the combination of band unfolding and band character weight is then possible to plot. The calculation can only run with a number of k-points for the band structure that is a multiple of the number of MPI threads. This is checked at the beginning of the calculation, if the associated error message is displayed, please adapt your parallelization or number of k-points accordingly.

It follows an example for a $4 \times 4 \times 4$ diamond supercell with a single A-nitrogen-center defect. The band unfolding specification in the input file for such a calculation is:

```
<unfoldingBand unfoldBand="T" supercellX="4" supercellY="4" supercellZ="4"/>
```

Fig. 3.4 shows the supercell band structure along the high symmetry path of the primitive unit cell with the obtained unfolding weights. The visualization of the weights makes the unfolded band structure clearly identifiable while the supercell band structure is very faint. In addition to this visualization the two defect states due to the A-nitrogen-center are highlighted in the band gap (yellow). Additionally, the

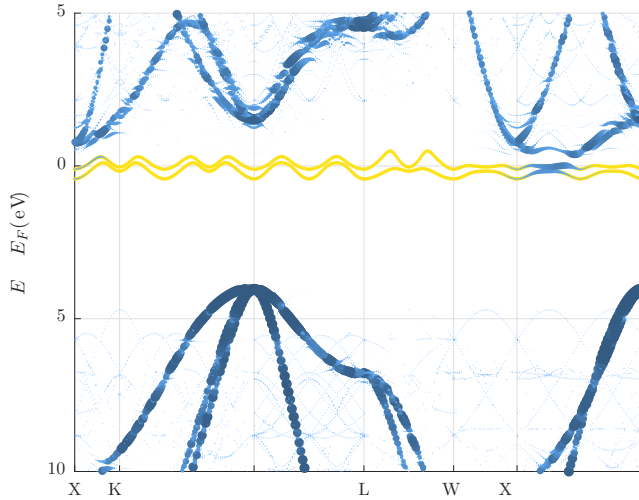


Figure 3.4: Unfolded diamond band structure with A-nitrogen-center defect (blue). Additionally, the defect states within the band gap are highlighted. This plot is done using the developed graphical MATLAB tool.

ability to use a rotated supercell is available. This can be useful for surfaces. The full transformation matrix between the primitive cell and the supercell can be given below the unfolding input (example: hexagonal lattice (MoS_2) scaled by $\sqrt{3}$ and twisted — the resulting band structure is shown in Fig. 3.42). It has to consist of integer values for the unfolding to work. Should one use the entries `supercell...` in addition to the full matrix, then both are combined.

```
<unfoldingBand unfoldBand="T" supercellX="1" supercellY="1"
  supercellZ="1">
<transMat>
  <row-1>-1 2 0</row-1>
  <row-2> 2 -1 0</row-2>
```

```

    <row-3> 0 0 1</row-3>
  </transMat>
</unfoldingBand>

```

It is important to note that the k-point path is not adapted automatically to the supercell when using the full transformation matrix. This means the path has to be given in terms of the supercell coordinates.

In the case of using the entries `supercellX`, `supercellY`, and `supercellZ` it is not necessary to adapt the k-point path to the supercell, rather the path of the primitive cell can be given as an input. If the supercell has the same ratio of basis vectors as the primitive cell the path is found automatically by the input generator.

The unfolding method is also of high interest for the calculation of film systems and surface states. In this case the unfolding is either performed purely in the z-direction or combined with a transformation matrix to allow the setup of an efficient surface cell. To simplify the setup the flag `&expert primCellZ=6.854 /` in the input generator can be used. This flag has two different functionalities. In the case of a true film system `film=T` the vacuum is set accordingly, so that the unfolding works (an integer multiple of the primitive cell is required). For the case of a pseudo film system (3D periodic system with additional vacuum) the input generator checks if the cell is a multiple of the size of the primitive cell in z-direction. The size of the primitive cell is to be given in atomic units.

3.2.2 Unfolding in the case of SOC (2nd variation)

The Fleur code has the ability to treat spin-orbit coupling (SOC) in 2nd variation. This gives a significant speedup compared to the treatment in 1st variation. In this context a treatment in 2nd variation means that SOC is handled as a variational treatment to the before diagonalized scalar-relativistic Hamiltonian. This treatment requires an implementation of the unfolding after the inclusion of SOC, which is also done. Additionally, the combination of the unfolding weights with the spin weights along a certain quantization axis has to be handled for the plotting. The usage within the Fleur input file is explained at the end of the previous section. An example for MoS₂ in a 3 × 3 supercell is shown in Fig. 3.5, where the splitting between the two spin channels (projection onto the z-direction) with opposite ordering at *K* and $-K$ is easy to identify.

As a side note, it can be mentioned that the basis functions in 2nd variation are

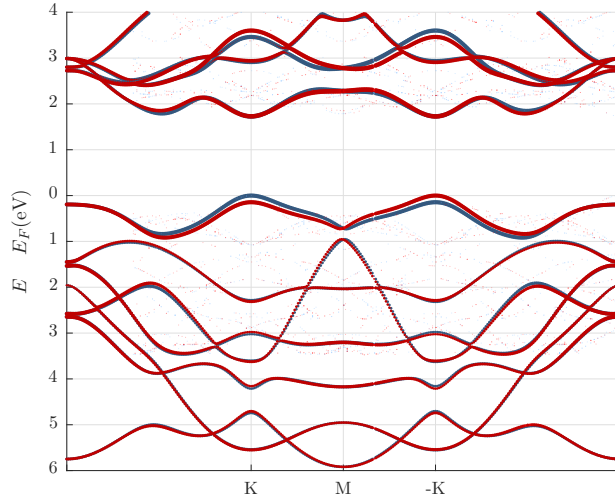


Figure 3.5: Unfolded MoS₂ band structure in a 3 × 3 supercell including spin-orbit coupling in 2nd variation. The spin-valley locking property is clearly visible.

the wave functions calculated in 1st variation. These are then used to calculate the unfolding weights.

Unfolding with SOC in the Fleur manual

It is also possible to use the unfolding method for the case of spin-orbit coupling in 2nd variation (`l_soc="T"`). In this case a second variation eigenvalue problem is solved and the resulting wave functions are used. The switch `use0lap` allows us to control whether the overlap matrix for the basis functions is used or not. In the case of unfolding for the second variation wave functions this switch has to be set to false (`use0lap="F"`).

```
<unfoldingBand unfoldBand="T" supercellX="4" supercellY="4" supercellZ
="4" use0lap="F"/>
```

3.2.3 Visualization

A GUI (graphical user interface) tool based on MATLAB has been designed to automate the plotting of the `banddos.hdf` file. Band structures are vastly used to show the properties of a material, plotting them is a very repetitive task in some sense and for

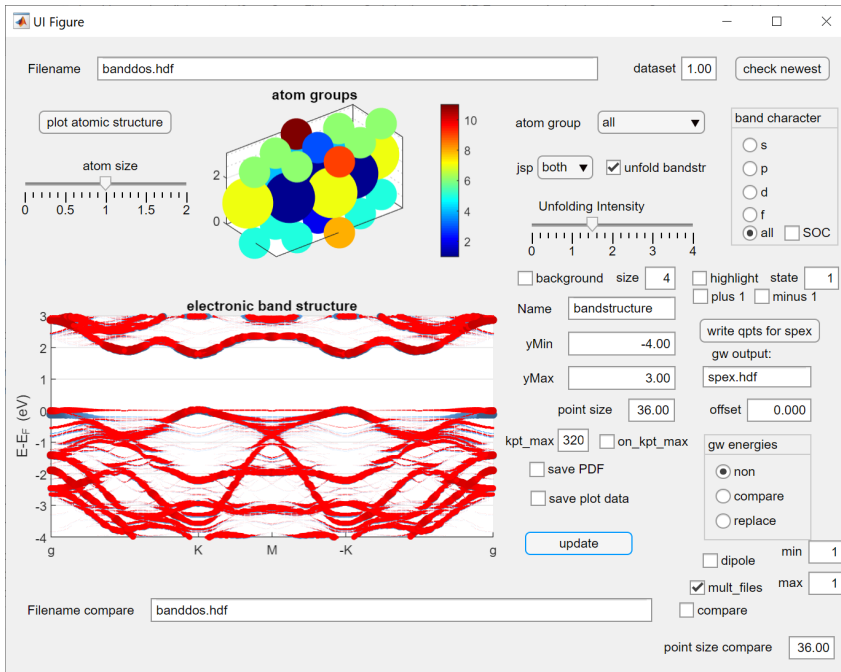


Figure 3.6: Screenshot of the GUI for visualization of unfolded band structures. A plotting process of MoS₂ with a P defect is shown. In the upper area a plot of the atom groups helps to select a projection onto one.

this Fleur already creates an automatized gnuplot script. But it becomes much more insightful to combine this information with the projection onto a certain atomic orbital or a certain orbital character or in the case of SOC with the projected spin weight. Combining a band structure with the information on the atomic orbital allows us to connect a certain state with its position in real space (if it is localized), for example in the case of a MoS₂ defect system the real space origin of the defect state. Combinations with the orbital character allow for an understanding of the states involved and are crucial to construct Wannier orbitals. In the case of a supercell this has to be combined with the calculated unfolding weight.

This is easily possible with the developed GUI, as including additional information in the band structure is just one click. Additionally, it is possible to export the plot as a publishable PDF and also as a raw text file that can be used for other plotting tools. It also allows us to combine the unfolding weights from Fleur with energy values from SPEX. A detailed description with directions to the download can be found in

the Appendix (Appx. A).

The major advantage of such a GUI is that trying out different projections or combinations is very fast and easy. So gaining an intuitive understanding of the system is possible.

3.3 Features of unfolded band structure

In this section different features of unfolded band structures are discussed. The coupling between two bands, avoided crossings and defect levels are well visible in the band structure of MoSe_2+P , shown as an example in Fig. 3.7. The comparison to the pristine

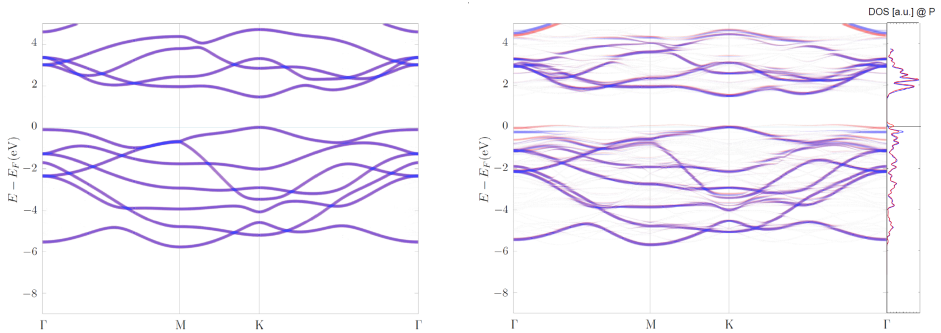


Figure 3.7: Unfolded band structure of $3\times 3\times 1$ MoSe_2+P (right) in comparison to the pristine MoSe_2 (left). Spin up is plotted in blue and spin down in red. Wherever a defect level (from the phosphorus atom) crosses a state of MoSe_2 , the Hamiltonian can have interaction terms and therefore an avoided crossing may appear (hybridization). An additional band is visible crossing the Fermi energy. The same state is observed in the density of states at the phosphorus atom. This plot is done for demonstrational purpose only. The band structure for the relaxed system is found in Sec. 3.5.6.

structure demonstrates how the defect introduces a perturbation to the whole system. Unfolding the band structure allows the results of a supercell calculation to be related to the results of the primitive unit cell of the pristine material. This means that the defect can actually be seen in the band structure as a small perturbation to the pristine system.

In the following the coupling between two bands, which is responsible for the avoided crossings, will be analyzed. Also, the relevance of the supercell size for calculations involving defects will be discussed.

3.3.1 Coupling between two bands

Depending on the energy difference and the symmetry two bands can couple to each other. The aim is to set up a model to analyze and visualize this behaviour. The model is based on the following plot (MATLAB). It recreates the situation of two interacting states.

```
clear;
close all;
k = linspace(-pi,pi,300);
E=0;
t=0;
figure(10)
hold on
for i=1:5
    E=(i-2)*2;
    for j=0:4
        t=j*0.3;
        lambda_1=(k.^2+E)./2+sqrt((k.^2-E).^2./4+t^2);
        lambda_2=(k.^2+E)./2-sqrt((k.^2-E).^2./4+t^2);
        w=sqrt(t^2./(t^2+(k.^2-lambda_2).^2));
        w_host=sqrt(t^2./(t^2+(k.^2-lambda_1).^2));
        subplot(5,5,5*(i-1)+1+j);
        hold on
        ylim([-5 10])
        scatter(k,lambda_1,2*w_host.^4+0.0001)
        scatter(k,lambda_2,2*w.^4+0.0001)
        hold off
        xticks([-pi 0 pi])
        xticklabels({'-\pi','0','\pi'})
    end
end
end
hold off
```

The model is constructed of 2 bands. One band has a quadratic dispersion (similar to a delocalized host band). The other resembles a defect band without any dispersion (localized) at energy ε . The two bands are interacting with the parameter t . This

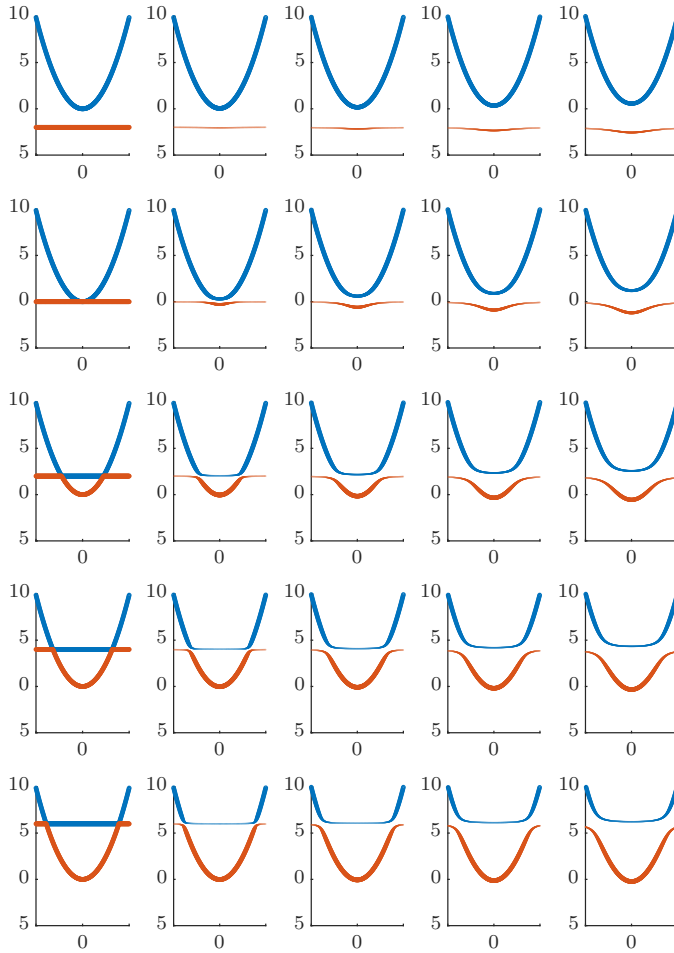


Figure 3.8: 2 band model: The model resembles the situation of a defect band close to a host material band. From left to right the interaction strength increases. From top to bottom the distance between the two bands is decreased. The line width corresponds to the amount of "host" band ("defect" band) character, except for the first column.

interaction causes them to avoid one another. The Hamiltonian for this system is:

$$\begin{pmatrix} k^2 & t \\ t & \varepsilon \end{pmatrix} \begin{pmatrix} x \\ y \end{pmatrix} = \lambda \begin{pmatrix} x \\ y \end{pmatrix} \quad (3.3.1)$$

The solution to this eigenvalue problem with eigenvectors $v_{1,2} = \begin{pmatrix} x_{1,2} \\ y_{1,2} \end{pmatrix}$ and eigenvalues $\lambda_{1,2}$ is found by diagonalization.

$$\lambda_{1,2} = \frac{k^2 + \varepsilon}{2} \pm \sqrt{\frac{(k^2 - \varepsilon)^2}{4} + t^2} \quad (3.3.2)$$

$$v_1 = \begin{pmatrix} 1 \\ -\frac{k^2 - \lambda_1}{t} \end{pmatrix} \text{ and } v_2 = \begin{pmatrix} 1 \\ -\frac{k^2 - \lambda_2}{t} \end{pmatrix} \quad (3.3.3)$$

The corresponding weights that attribute the amount of "host" band character (and the amount of "defect" band character) for each eigenvector is corresponding to its normalization prefactor (reciprocal length):

$$w_1 = \sqrt{\frac{t^2}{t^2 + (k^2 - \lambda_1)^2}} \quad (3.3.4)$$

$$w_2 = \sqrt{\frac{t^2}{t^2 + (k^2 - \lambda_2)^2}} \quad (3.3.5)$$

These "energy eigenvalues" are plotted together with the corresponding weights in the Fig. 3.8. It can be seen how the influence between the two bands increases on one another with a growing interaction constant.

Now, when analyzing unfolded band structures it is important to keep this interpretation in mind because the thickness could be interpreted as a electron density or a probability to find an electron at a certain momentum and energy. Both is not wrong in the context of a supercell but cannot be interpreted directly from the thickness. A high unfolding weight (thick line in the band structure plot) only implies that this certain state has a symmetry that corresponds to the one of the primitive cell. This can also be fulfilled by an extended defect state. The number of electrons in a certain state can only be understood from the original (supercell) band structure (not unfolded) - also in the unfolded one it is possible to identify the number of electrons, if a state is known to be non-degenerate (for example a certain defect state).

3.3.2 Relevance of the supercell size (MoS₂+Cr)

If the aim is to simulate a single defect the supercell size has to be chosen large enough. Depending on the type of defect a different size can be required to suppress the interaction between periodic images of the defect atom (due to the 3D periodic boundary condition). For instance, in the following example of a substitutional atom in the metal layer a 5×5 supercell is needed instead of the 3×3 one, which is used for the phosphorous defect. This is visible in Fig. 3.9 where the defect state has a well visible

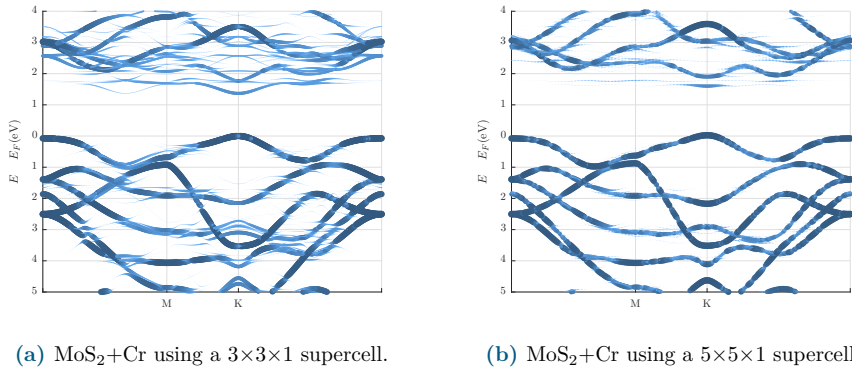


Figure 3.9: Comparison of the two different supercell sizes demonstrates that a $5 \times 5 \times 1$ supercell is necessary for the defect to have very little dispersion, as one would expect for a single defect. The smaller supercell size shows a system where the concentration of defect atoms is high enough for them to interact.

dispersion for the case of a $3 \times 3 \times 1$ supercell (Fig. 3.9a), which implies an interaction between the periodic images of the chromium atom. For the larger $5 \times 5 \times 1$ supercell the defect state has barely any dispersion making it appear like a localized atomic state — spread out in reciprocal space and therefore localized in real space. Thus, the larger $5 \times 5 \times 1$ supercell is necessary in order to calculate an isolated chromium defect.

3.4 Band structures of monolayers with isoelectronic substitutional atoms

There are two approaches for determining the crystal structure when performing calculations in computational physics. Either one uses an experimentally given structure and position of the atoms or one calculates the positions of the atoms by minimizing the force between them (sometimes under certain constraints).

But also the experimental structure can depend on many factors like sample preparation, temperature, impurities and the substrate. These can introduce strain (locally or globally), accidentally changing the properties of the material. On the other hand, strain can also be used on purpose as a tool to tailor the properties of a material.

In the following the interplay between the atomic structure and resulting electronic properties will be investigated. The results are then used to explain the influence of isoelectronic substitutional atoms in TMD monolayers.

3.4.1 Interplay of structure and electronic properties for the pristine material

The pristine TMD monolayer is for computational purposes defined by 4 main quantities: The in-plane lattice constant (a), the out-of-plane lattice constant (c), the vacuum in the cell, and the z -parameter. The in-plane lattice constant is well known by experimental crystallographic methods (the lattice constant without strain). The vacuum included in the supercell is rather a computational parameter and should be chosen so that periodic images of the layer do not interact. The out-of-plane lattice constant gives, in combination with the z -parameter, the position of the chalcogen atoms with respect to the metal layer. To be precise, it defines the distance between the metal and the chalcogen layer. The atom positions in the hexagonal unit cell are given by (this depends on the basis-vectors (a and c)):

$$\text{Mo} : (1/3, 2/3, 0)$$

$$\text{S} : (2/3, 1/3, \pm z)$$

In the following the influence of the lattice constant and the z -parameter on the band structure will be analyzed. Therefore, the structure parameter z is artificially set to a value which results in a position that does not minimize the forces. Thus, it creates a

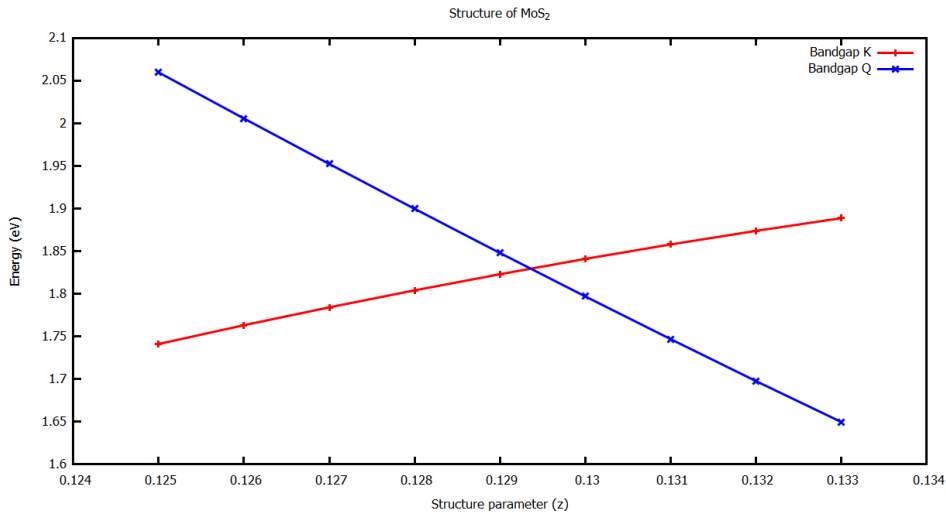


Figure 3.10: Influence of the structure parameter (z) on the band gap at K and Q for a pristine MoS_2 monolayer.

structure that is not relaxed. The resulting band gap for MoS_2 at K and the indirect band gap between K and Q (midpoint between K and Γ) are shown in Fig. 3.10. For a very compressed system the valence band maximum shifts from the K point to the Γ point, making it an indirect band gap. Here, the focus is on a small compression and the band gap at the K point and at the Q point. A direct connection between the size of the band gap and the z -parameter is obvious in Fig. 3.10. For a compressed layer (in z -direction) (small z) MoS_2 has a direct band gap, whereas for a stretched layer (large z) the band gap becomes indirect. The relaxed position (PBE) for the sulfur layer is at $z = 0.128$. The relation between the size of the band gap and the z -parameter is nearly linear. This calculation highlights the importance of finding the relaxed position of the chalcogen layer before calculating any electronic properties because these are strongly dependent on the position of the atoms. Changing the z -parameter is somewhat artificial and experimentally not possible to do, but introducing strain into the layer by stretching or compressing along the in-plane direction is possible (for example by bending the substrate [39]). This will also lead to a repositioning of the chalcogen layers. If the layer is stretched it leaves more room for the chalcogen atoms, allowing them to move closer. The opposite is true for compression. The relaxed position (residual force $5 \cdot 10^{-4} \text{ eV/\AA}$) can be expressed in terms of a corresponding

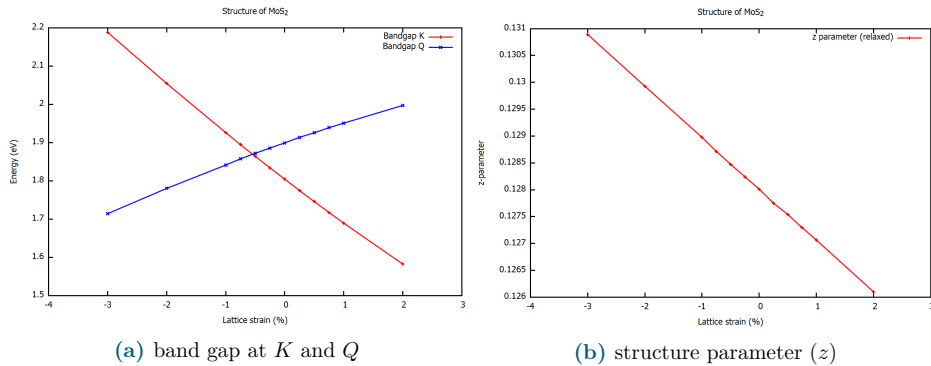


Figure 3.11: Effect of strain onto the lattice of MoS₂. Negative values correspond to compression. Positive values mean tensile stress. The band gap change is shown as well as the relaxed position of the sulfur layer. The relaxed position can be expressed in terms of the z -parameter.

z -parameter (Fig. 3.11b). The band gap change (Fig. 3.11a) is stronger than compared to just changing the z -parameter, but shows exactly the same behaviour.

This investigation implies that for the calculation of defect atoms the relaxation of the atomic positions is crucial. Especially for defect atoms from the same group of the periodic table this is important, as the electronic configuration is similar (compared to the host atom) and only the size of the defect atom is significantly different.

3.4.2 MoS₂+Se

Motivated by an experimental observation done by Minh Bui and Beata Kardynal, different concentrations of selenium implantation are investigated. They observed that at low temperature and for high concentrations of selenium implantation the photoluminescence is quenched [40]. A possible explanation could be that the band gap becomes indirect for high selenium concentrations. The fact that this behaviour of the photoluminescence is only visible at low temperature suggests that the difference between the fundamental indirect band gap and the direct band gap cannot be large compared with the thermal energy at room temperature. Otherwise, the photoluminescence would also be quenched at higher temperature at the same concentration — this is not observed. In the following, different concentrations of selenium in a 3×3 supercell of MoS₂ will be studied. The top chalcogen layer contains 9 atoms, all compounds with zero to four sulfur atoms replaced by selenium atoms are tested as well as the

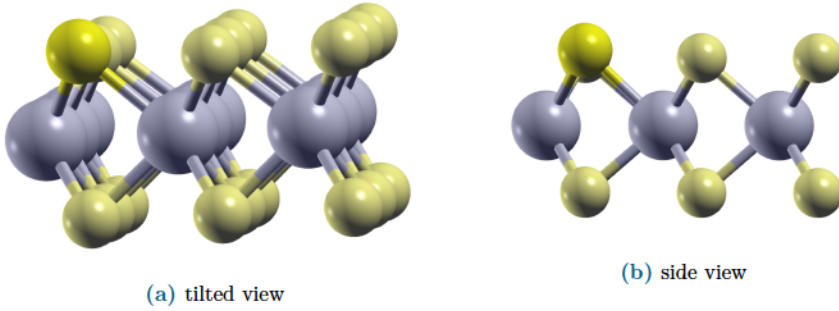
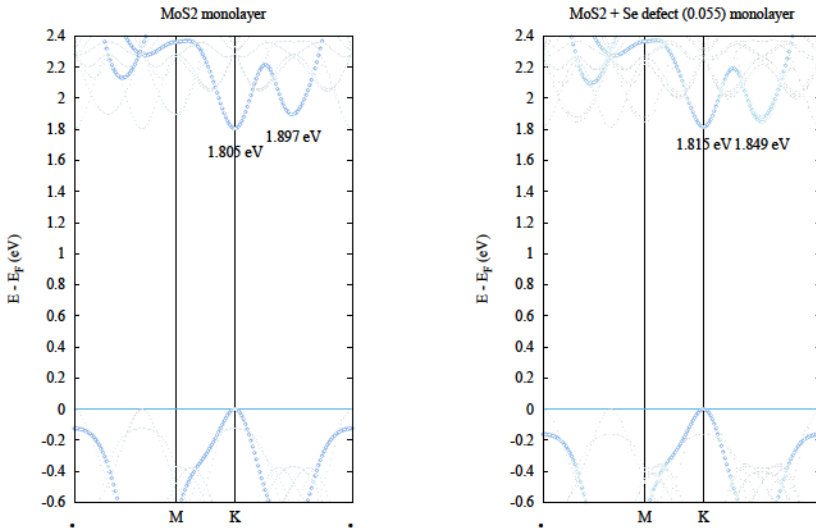


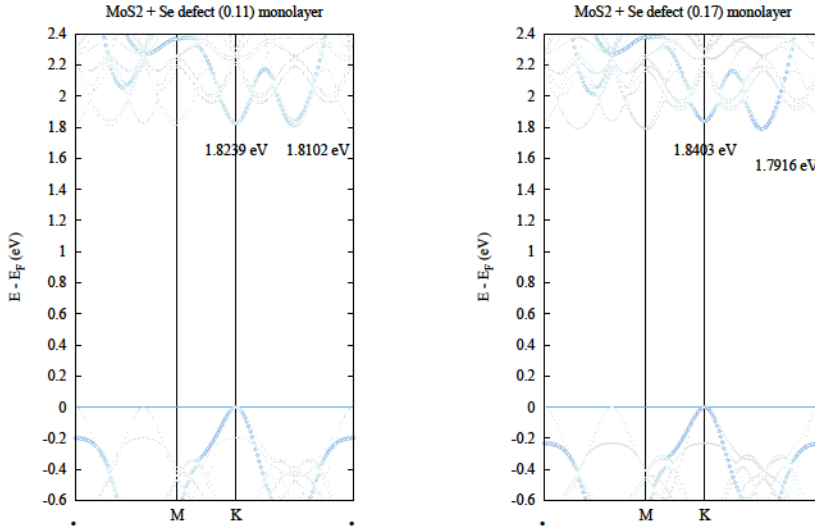
Figure 3.12: Atomic structure of MoS_2 with implanted selenium showing the relaxed position of the defect atom, shifted out of the metal layer. The exact atomic positions can be found in the appendix (Sec. C.3).



(a) The pristine MoS_2 structure is shown — no selenium implantation. The calculation is done in a $3 \times 3 \times 1$ supercell. (b) One sulfur atom of the top layer is replaced by selenium, which moved 0.156 Angstrom out-of-plane.

Figure 3.13: Comparison of the pristine material with a low concentrations of selenium implantation in MoS_2 in the top layer of a $3 \times 3 \times 1$ supercell.

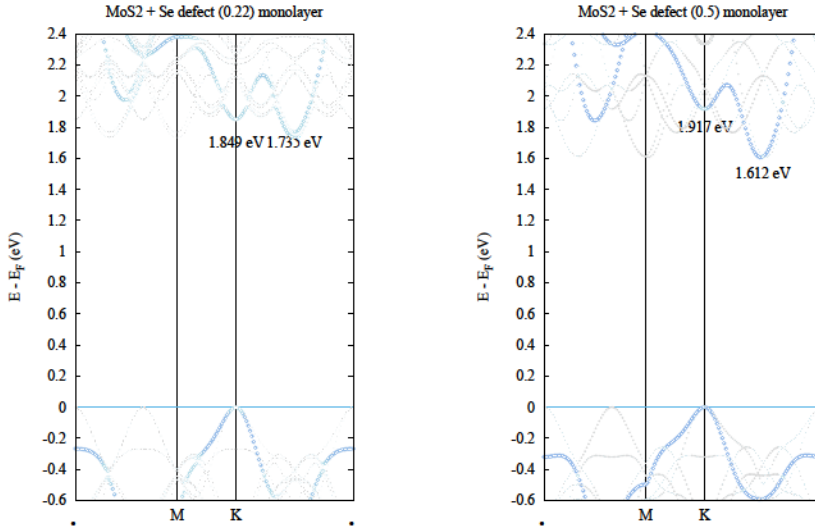
Janus compound in which all sulfur atoms (top layer) are replaced by selenium.



(a) Two sulfur atoms of the top layer are replaced by selenium, which moved 0.148 Angstrom out of the plane. (b) Three sulfur atoms of the top layer are replaced by selenium, which moved 0.140 Angstrom out of the plane.

Figure 3.14: Comparison of two different low concentrations of selenium implantation in MoS_2 in the top layer of a $3 \times 3 \times 1$ supercell.

Before being able to calculate the band structure, one has to carefully relax the atom positions. This is very important, since the distance and angle between the metal layer and the chalcogen layer significantly determine whether the band gap is direct or indirect by altering the dispersion of the conduction band (also partly of the valence band). During the spatial relaxation, mostly the selenium atom moves out of the plane which is not surprising as it is larger than the sulfur atom. The other atoms in the unit cell only change their position slightly. By comparing Fig. 3.13 and Fig. 3.14 the predicted transition between a direct band gap and an indirect band gap can be observed. As the concentration increases (Fig. 3.15) the conduction band minimum at the K point increases in energy and the conduction band minimum at the Q point decreases. The whole transition is summarized in Fig. 3.16. All calculations are carried out with exactly the same parameters and without SOC.



- (a) Four sulfur atoms of the top layer are replaced by selenium, which moved 0.133 Angstrom out of the plane. (b) Nine sulfur atoms of the top layer are replaced by selenium, which moved 0.09 Angstrom out of the plane.

Figure 3.15: Comparison of two different high concentrations of selenium implantation in MoS_2 in the top layer of a $3 \times 3 \times 1$ supercell.

In Sec. 3.4.1 the influence of the structure parameter z on the band gap is studied. The selenium position being slightly outward of the sulfur plane is corresponding to a larger z parameter. Therefore, Fig. 3.10 connects the origin of the band gap change observed for an increasing concentrations of selenium (Fig. 3.16) with the spatial position of the selenium atom.

To analyze the possibility for photon emission further, the imaginary part of the dielectric function, showing the possible transitions in the material, is plotted for the different concentrations. While calculating the dielectric function (based on the polarization function) within the SPEX code, it is important to use a fine enough energy mesh for the frequency integration to depict the small energy changes between the different band gaps. In the case shown here, a small band gap change is of high interest, therefore different meshes for the frequency integration were tested. The convergence behavior is shown in Fig. 3.17. It turns out that a setting of "HILBERT

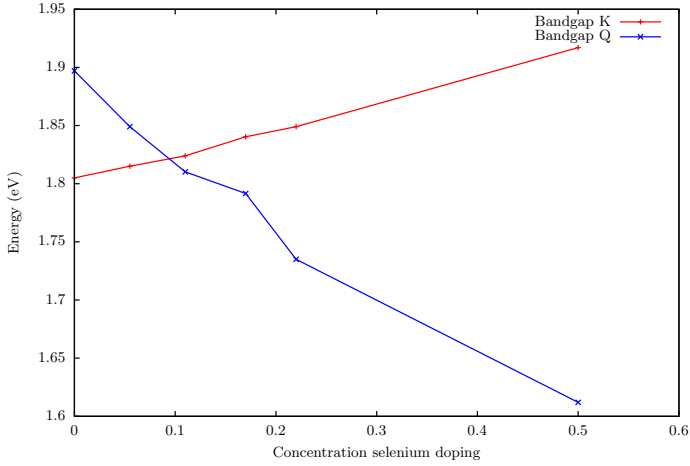
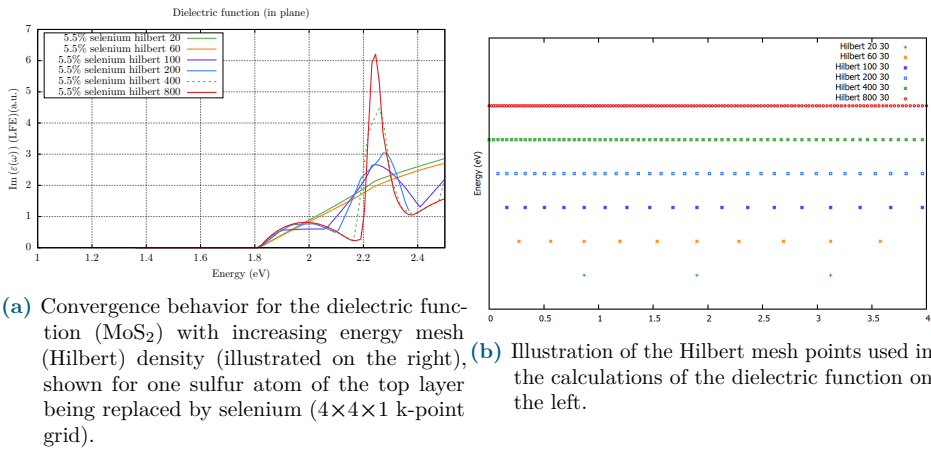


Figure 3.16: Overview of the band gap size for different concentrations of selenium in MoS_2 . The concentration is given with respect to the amount of sulfur atoms in the pristine material.



(a) Convergence behavior for the dielectric function (MoS_2) with increasing energy mesh (Hilbert) density (illustrated on the right), shown for one sulfur atom of the top layer being replaced by selenium ($4 \times 4 \times 1$ k-point grid). (b) Illustration of the Hilbert mesh points used in the calculations of the dielectric function on the left.

Figure 3.17: Influence of the Hilbert energy mesh on the imaginary part of the dielectric function. The label "Hilbert" refers to the SPEX input file [17], where the first number defines the amount of mesh points up to 5 Htr and the second number the exponential growth of the distance between the mesh points.

400 30" is sufficient to clearly distinguish the different excitations. The first number "400" refers to the number of mesh points up to 5 Htr and the second number "30"

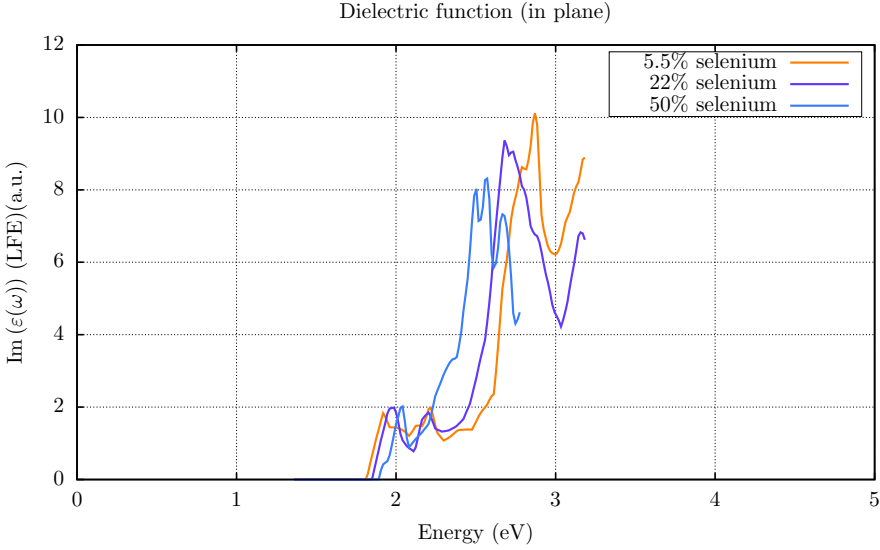


Figure 3.18: Imaginary part of the dielectric function (MoS_2) for different selenium concentrations on a $8 \times 8 \times 1$ k-point grid in reciprocal space.

to the exponential growth of the distance between the mesh points up to 5 Htr. The resulting dielectric functions are shown in Fig. 3.18. The change of the band gap, which corresponds to the onset of the spectrum, is clearly visible for the different concentrations of selenium.

3.4.3 $\text{MoSe}_2 + \text{S}$

The investigation in Sec. 3.4.2 shows that $\text{MoS}_2 + \text{Se}$ is not useful as a potential single photon emitter, because the band gap at K is increased by the dopant rather than reduced, as it is needed for a localized photon emission. Consequently, the open question is if the opposite change could be achieved, meaning a decrease of the direct band gap. If implantation with a larger atom (selenium replacing sulfur) forces the implanted atom out of the layer, making the material an indirect band gap semiconductor, then implantation with a smaller atom (sulfur instead of selenium) maybe has the opposite effect. This idea is supported by the observations made for the effect of strain on the pristine material (Fig. 3.10 and Fig. 3.11a).

In a similar setup as in Sec. 3.4.2 MoSe_2 is implanted with different concentrations of sulfur. Performing the spatial relaxation immediately shows a large force on the

sulfur atom pushing it into the layer. Fig. 3.19 shows the final relaxed position (0.17 Å

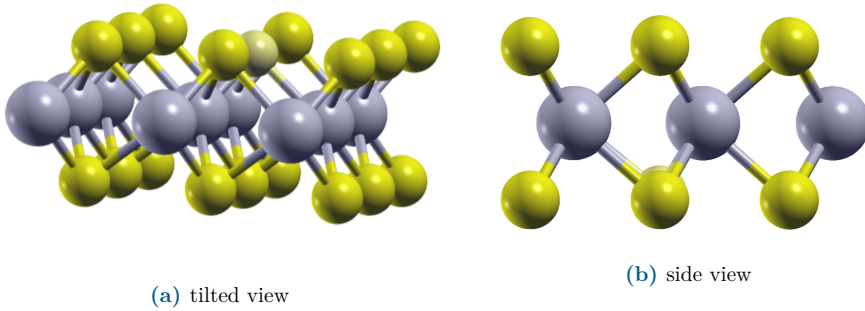


Figure 3.19: Atomic structure of MoSe₂ with implanted sulfur showing the relaxed position of the defect, shifted towards the metal layer. The exact atomic positions can be found in the appendix (Sec. C.3).

into the layer) for one out of nine selenium atoms replaced by a sulfur atom. Fig. 3.20 shows the band structure of MoSe₂ with one sulfur atom in the chalcogen layer after relaxation. The direct band gap decreases by about 20 meV compared to the pristine system. The change is mainly due to the conduction band shift. For the case of three sulfur atoms replaced in the chalcogen layer the shift of each of the atoms is a little smaller (0.003 Å less than in the case of one sulfur) but the decrease of the band gap is more than doubled with the increased concentration (43.5 meV) (Fig. 3.21). The indirect band gap (between *Q* point and *K* point) is in both cases increased. For a higher concentration also more distortion of the band structure is visible. Additional bands with low intensity (low unfolding weight) appear both in the conduction bands and in the valence bands. In photoluminescence experiments it should be possible to measure the decrease of the band gap. Now the question is, if this type of implantation can be used for single photon emission. Since this type of implantation rather changes the overall band structure than introducing a defect state (like for phosphorus), it seems that the defect state is very spread out in real space. A small dispersion of a band in reciprocal space (very flat band) is connected to a localization of the electron wave functions in real space and vice versa. Nevertheless, having a cluster of this "alloy" could be assumed to limit the effect of a reduced band gap to a confined area and trap an exciton, given the size of the area is limited to the size of an exciton in this material.

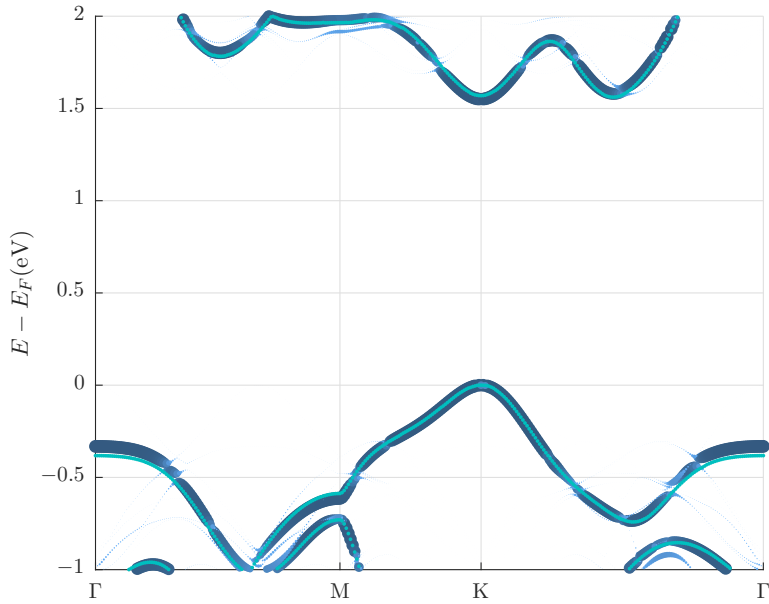


Figure 3.20: Unfolded band structure of a 3×3 supercell MoSe_2 with substitutional implantation of one sulfur atom in the chalcogen layer (5.5% sulfur considering both chalcogen layers). The pristine band structure of MoSe_2 is shown in turquoise for comparison. The calculation is done without SOC. The direct band gap at K is reduced by 20 meV due to the sulfur.

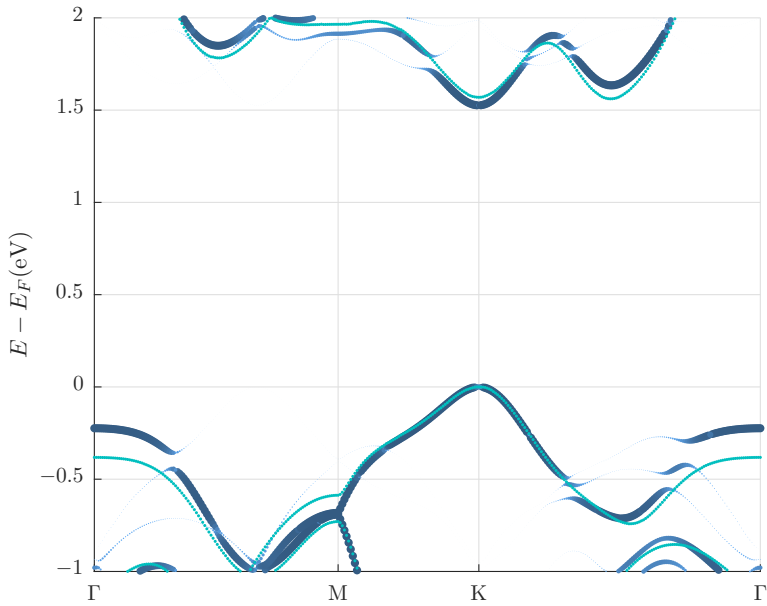


Figure 3.21: Unfolded band structure of a 3×3 supercell MoSe_2 with substitutional implantation of three sulfur atoms in the chalcogen layer (16.7% sulfur considering both chalcogen layers). The pristine band structure of MoSe_2 is shown in turquoise for comparison. The calculation is done without SOC. The direct band gap at K is reduced by 43.5 meV due to the sulfur.

3.4.4 WSe₂+S

For WSe₂+S a similar effect should be observable as for MoSe₂+S, since the structural and electronic properties are similar. The largest difference is the stronger spin orbit coupling in tungsten compared to molybdenum. Therefore, the following calculations treat the full SOC. The unfolding of the wave functions from the supercell to the primitive cell is here performed using the wave function found in 2nd variation treatment for SOC (Sec. 3.2.2).

Here one full band structure of the pristine WSe₂ is included to show the strong effect of SOC in the conduction band (Fig. 3.22). The spin-valley locking property is well visible. The spin splitting of the valence band at +*K* (and -*K*) point is 0.5 eV. Replacing one out of nine atoms in the chalcogen layer delivers the result shown in

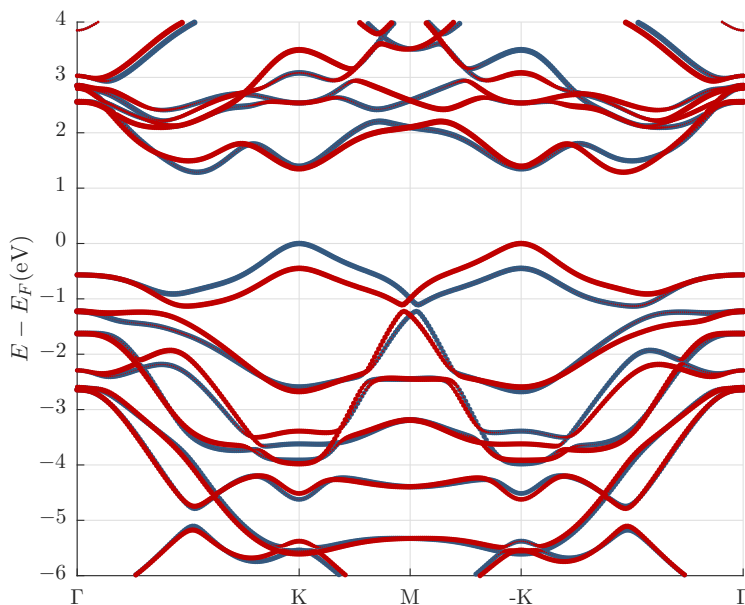


Figure 3.22: Pristine monolayer WSe₂ showing the effect of SOC when comparing the *K* and -*K* valley. The layers are separated by a vacuum of 12.98 Å. The two spins are shown in red and blue.

Fig. 3.23. The structural relaxation causes the sulfur atom to be moved by 0.166 Å into the layer. This is done before introducing SOC in 2nd variation. The exact atomic

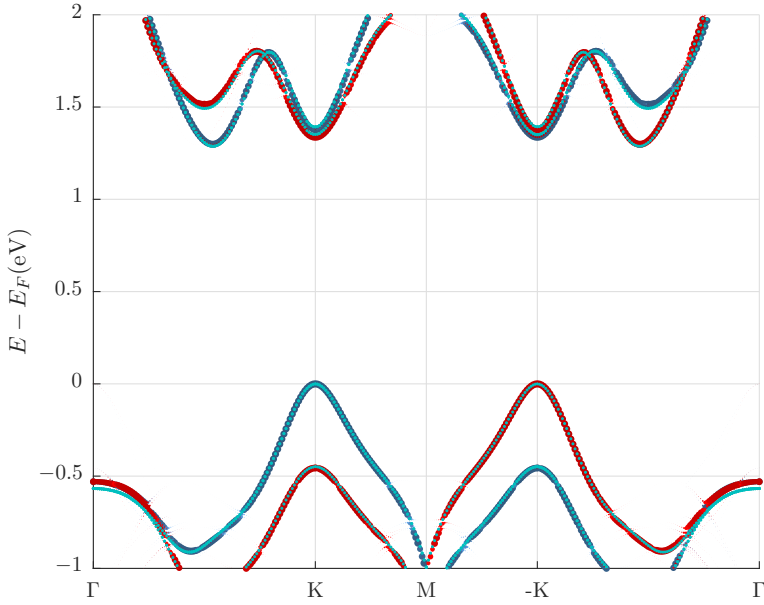


Figure 3.23: Unfolded band structure of a 3×3 supercell WSe_2 with substitutional implantation of one sulfur atom in the chalcogen layer (5.5% sulfur). The pristine band structure of WSe_2 is shown in turquoise for comparison. The calculation is done with SOC.

positions can be found in the appendix (Sec. C.3). The shift of the conduction band and the resulting closing of the direct band gap is 15 meV. Here, the spin ordering in the valence and conduction band are opposite, as usual for any TMD showing with spin-valley locking. Therefore, the smallest direct band gap includes a spin-flip. For a higher concentration of three out of the nine selenium atoms in the top layer being replaced by sulfur, the changes due to the increased concentration are comparable to MoSe_2 (Fig. 3.24). At the same time as the conduction band is reduced at the K point, it increases in energy at the Q point.

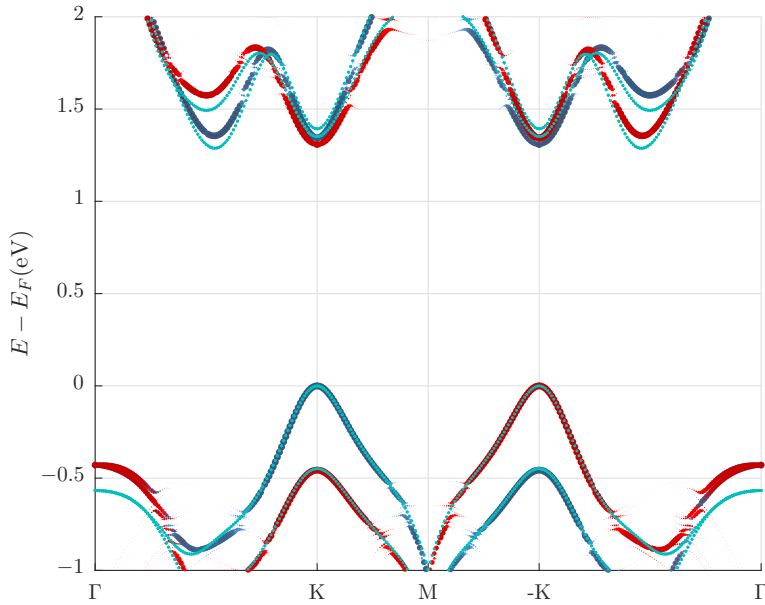


Figure 3.24: Unfolded band structure of a 3×3 supercell WSe_2 with substitutional implantation of three sulfur atoms in the chalcogen layer (16.7% sulfur). The pristine band structure of WSe_2 is shown in turquoise for comparison. The calculation is done with SOC.

3.5 Band structures of monolayers with implanted atomic defects

Since this work is part of a project together with experimental groups from the University of Limerick, the University of Göttingen, and the Forschungszentrum Jülich, the aim is to apply the developed methods to a range of different host materials and implants that are of high interest to these groups. For the conducted experiments the defect atoms (ions) are implanted into the monolayer with ultralow energy. This implantation process can introduce a large range of defects which are not thermodynamically allowed, but at the same time the use of the low implantation energy limits the number of possible implantation sites e.g. selenium will replace only sulfur in the top layer. Here MoS_2 and MoSe_2 with phosphorus doping, chromium doping and a vacancy defect will be investigated. Phosphorus is a prototypical dopant from group

V with one valence electron less than selenium or sulfur. Chromium as a transition metal has many oxidation states. It is from the same group as molybdenum and is predicted to form a defect state. However, during the implantation process it can end up in different position of the lattice and therefore one needs to know the effect of each of them on the band structure. It is possible to find chromium atoms at the metal site, at the chalcogen site, or at the chalcogen site with an additional chalcogen atom on top. Doping with phosphorus or chromium is substantially different compared to the exchanging of sulfur and selenium (isoelectronic) as they introduce donor or acceptor levels in the band structure rather than a change of the overall dispersion.

3.5.1 MoS₂+P

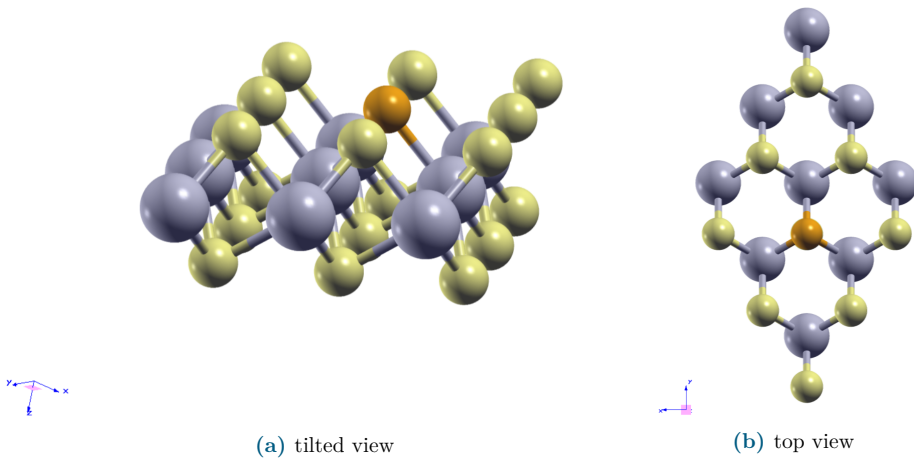


Figure 3.25: Atomic structure of MoS₂ with phosphorus showing the relaxed position of the defect, slightly shifted towards the metal layer in comparison to the other chalcogen atoms. The exact atomic positions can be found in the appendix (Sec. C.3). Plotted using XCrySDen [41].

Replacing one chalcogen atom by a phosphorus atom is likely to leave an open bond due to the missing electron and therefore introduce a defect state. The calculation is performed in a 3×3 supercell. During the force relaxation process the phosphorus atom does not move by much. The relaxation is first done for the pristine material, then the defect is introduced for another relaxation within the supercell. The final positions after all forces are converged up to a maximum of $5 \cdot 10^{-2}$ eV/Å can be found in the appendix (Sec. C.3). The calculation shown here does not include SOC,

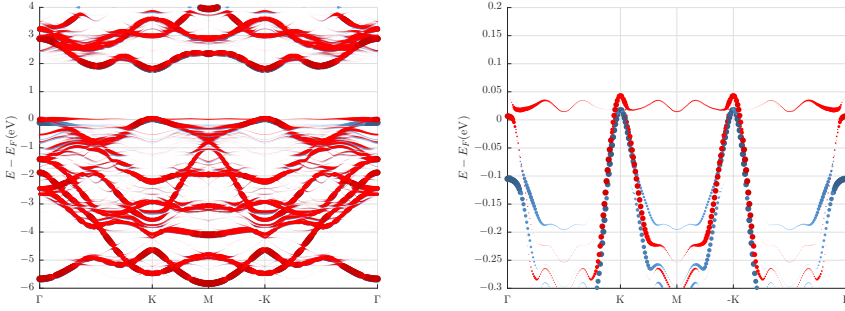


Figure 3.26: Unfolded band structure for MoS₂+P, calculated in a 3×3 supercell. The state slightly above the Fermi level for one spin state is clearly visible.

therefore does not show the splitting at the K and -K valley.

Fig. 3.26 shows the unfolded band structure of the defect system. The most prominent defect state is evident right at the Fermi energy. Here, the host material band structure is clearly visible and not shifted compared to the pristine band structure, but an additional state is visible shortly above the Fermi energy. This state is actually spin-polarized, which seems likely, since phosphorus is a group-V element with one missing electron compared to sulfur (group-VI) that was replaced. The additional states introduce transitions with very low energy, or to be more precise in this case it is even crossing the Fermi energy — making the material metallic. Its capability to possibly trap excitons for single photon emission is not very high, as it does not lower the band gap directly at the *K* point. Overall this defect band right at the Fermi level is a characteristic single atom defect and does not seem to interact much with the host system, since its dispersion is very low (spread out in reciprocal space) suggesting a high localization in real space.

3.5.2 MoS₂+Cr (@ Mo)

Implantation of chromium into a molybdenum substitutional site requires higher energy than implantation of chromium into other sites of the lattice. Therefore during the process of implantation of chromium into the molybdenum sub-lattice, the following configurations have to be considered: substitutional implantation at the molybdenum site, substitutional implantation at the sulfur site, and substitutional implantation at the sulfur site with an additional sulfur atom on top.

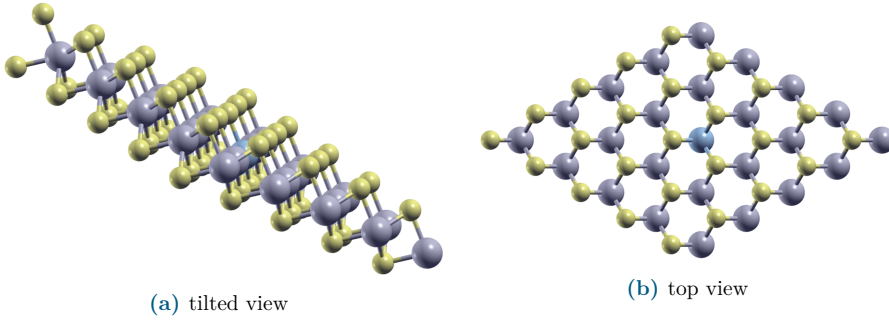


Figure 3.27: Atomic structure of MoS₂ with implanted chromium at a metal atom showing the relaxed position of the defect and neighbouring chalcogen atoms, slightly shifted towards the defect atom. The exact atomic positions can be found in the appendix (Sec. C.3). Plotted using XCrySDen [41].

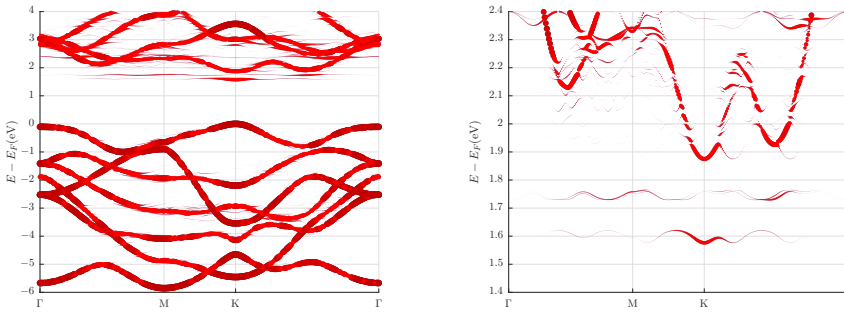


Figure 3.28: Unfolded band structure for MoS₂+Cr, calculated in a 5×5 supercell. The defect state within the band gap is clearly visible. The calculation includes two spins, which are degenerate due to the lack of SOC.

First the substitutional implantation of molybdenum will be investigated, since it seems most intuitive to replace one metal atom with another. It should be mentioned that implantation into the metal layer by low energy ions is in general more difficult than implantation into the chalcogen layer, since the probability of creating a vacancy in the chalcogen layer is higher than for implantation into the latter.

The spatial relaxation of the structure with chromium replacing one molybdenum atom in a 5×5 supercell is only causing a marginal shift within the layer of the sulfur atoms towards the chromium defect (Fig. 3.27). Also the molybdenum sub-lattice does not show a significant movement. It turns out (see Sec. 3.3.2) that a large supercell of 5×5 primitive unit cells is needed to decrease the interaction between periodic images of the

defect. The Fermi level remains unchanged in the following band structure calculation (Fig. 3.28). The well visible defect states (spin degenerate) appear right below the conduction band minimum (about 300 meV and 110 meV). This means that chromium introduces acceptor-like states, as they can be unoccupied or capture one electron. The lower defect state has a high unfolding weight around the K point. This means it reflects the symmetry of the host lattice quite well, which could be due to coupling to neighbouring states of the host lattice (see Sec. 3.3.1). This state could be well suited for single photon emission as the spin-valley locking property of the host material is not influenced by any defect state and should therefore be preserved (Fig. 3.28 is without SOC). The energy gap between the host state and the defect level is suitable to bind the electron-hole pair. Furthermore, the small dispersion of the defect states suggests a high localization in real space.

3.5.3 MoS₂+Cr (@ S)

The doping with chromium is also possible at the position of sulfur, replacing one chalcogen atom. This type of doping introduces a high strain onto the lattice. Therefore, a 5×5 supercell is used to allow for larger movement in the relaxation process and minimize the interaction between periodic images of the defect. During the spatial relaxation shown in Fig. 3.29 the chromium atom moves out of the plane by 0.427 Å. This type of defect introduces multiple defect states within the band gap and shifts the Fermi energy, meaning some of the states are donors. Furthermore, it introduces a spin-splitting of the defect states. Since the calculation is done without SOC, there is no definition of which spin corresponds to spin up or spin down, but nevertheless the blue bands of Fig. 3.30 can only be occupied by one spin and the red bands by the other (for most of the band structure they are on top of one another — spin degenerate). Note that the chromium atom is slightly magnetic. None of the defect states within the band gap seem to show a strong interaction with a host state, since the unfolding weight is spread nearly evenly over the whole band structure path. This is true even for the states close to the valence band and conduction band edge. For photon emission this defect is most likely unsuitable, since the possible transitions are significantly different for the two spins. For the one spin (blue) a possible transitions is between the two defect states without involving the valence band of the host material and therefore the spin-valley locking property is lost. For the other spin the band gap is significantly changed due to the additional donor state in the middle of the

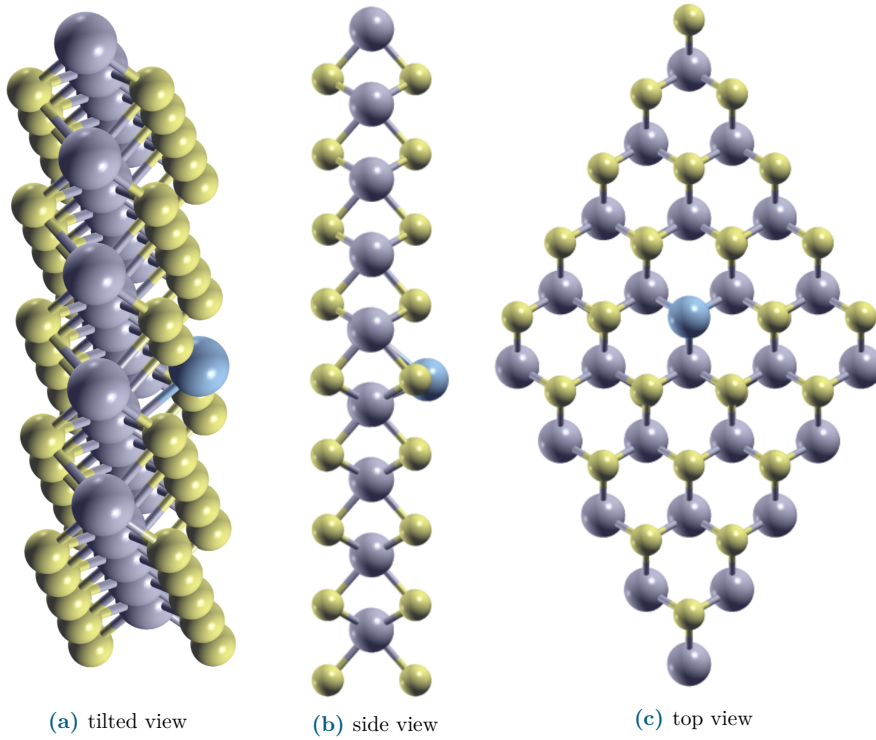


Figure 3.29: Atomic structure of MoS_2 with implanted chromium at a chalcogen atom showing the relaxed position of the defect, shifted out of the layer. The exact atomic positions can be found in the appendix (Sec. C.3). Plotted using XCrySDen [41].

band gap. Furthermore, a small spin splitting of the original valence band maximum (now located at about -1 eV) is visible.

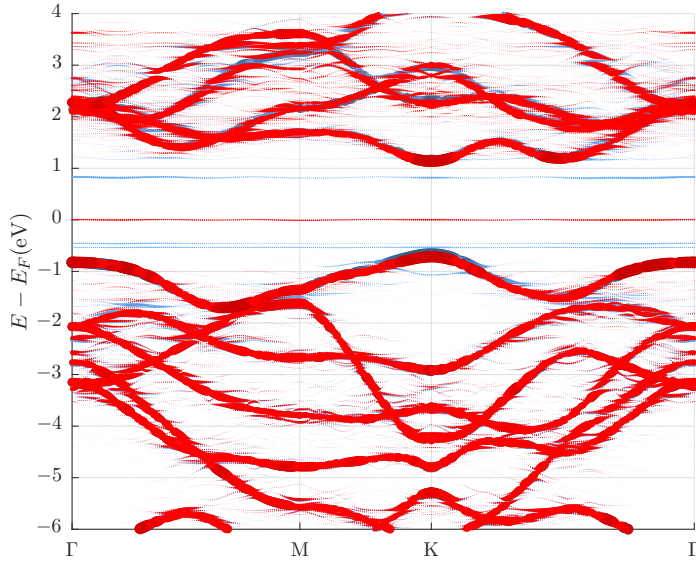


Figure 3.30: Unfolded band structure for MoS_2+Cr (@ S), calculated in a 5×5 supercell. The defect state within the band gap is clearly visible.

3.5.4 $\text{MoS}_2+\text{Cr}+\text{S}$

When implanting chromium into MoS_2 (substitutional implantation of chromium at the sulfur site), it is possible that the sulfur atom that has been released from the lattice does not have enough energy to escape and binds as an adatom to the chromium atom that replaced it in the lattice. This fills the open bond from the chromium atom, creating a very stable defect. The configuration is shown in Fig. 3.31. The spatial relaxation in this case only moves the chromium atom a little inwards. The overall Fermi energy is not changed (unlike the same implantation without an additional sulfur atom). Also, there is no spin-splitting. The state within the band gap is a deep defect level, which is "atomic-like" without any dispersion or concentration of unfolding weights. The other defect states around 2 eV cause an avoided crossing close to the K point with a high concentration of the unfolding weight. Here, the defect state seems to couple with the host state, just like it can be observed in the 2-band model (Sec. 3.3.1). This type of defect could be a promising candidate for photon emission if it had only one state and if the state right in the middle of the band gap wouldn't exist.

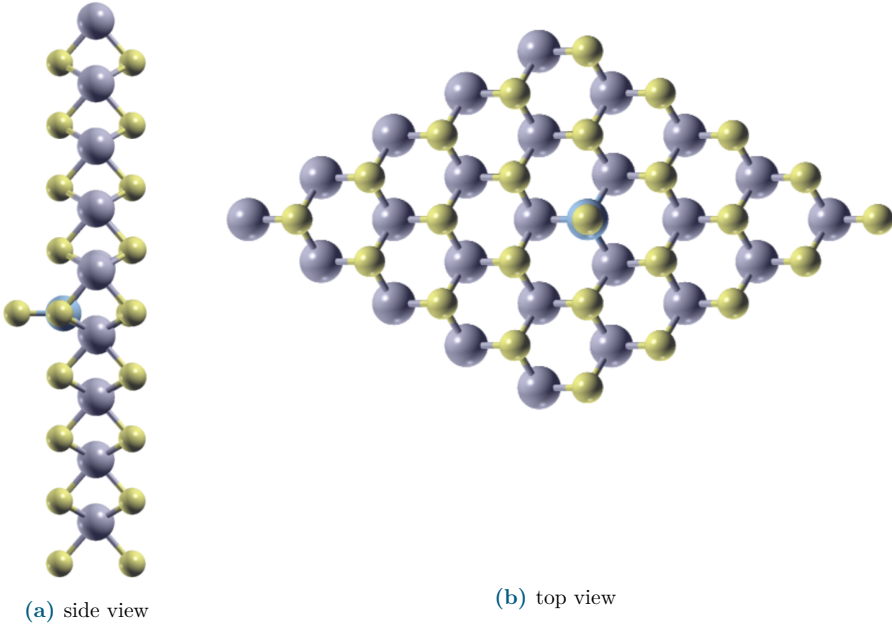


Figure 3.31: Atomic structure (relaxed) of MoS₂ with chromium implantation at the chalcogen atom plus an additional chalcogen atom on top. The exact atomic positions can be found in the appendix (Sec. C.3). Plotted using XCrySDen [41].

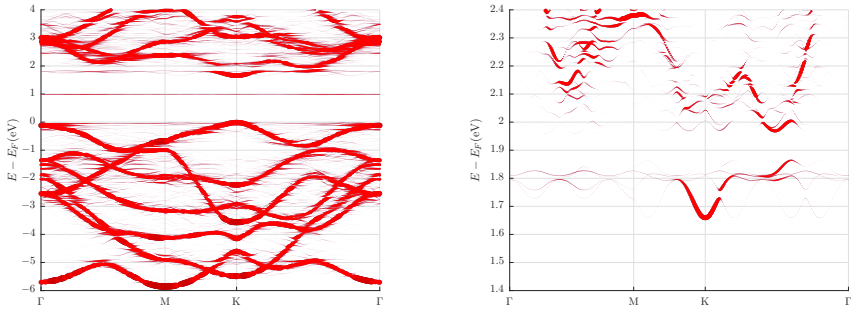


Figure 3.32: Unfolded band structure for MoS₂+Cr+S, calculated in a 5×5 supercell. The defect state within the band gap is clearly visible. The calculation includes two spins, which are degenerate due to the lack of SOC.

Possible transitions will have a completely different energy than the ones of pristine

MoS₂. This is only true if the transition is allowed (transition element not zero). This is investigated later in this work (Sec. 5.3). The results will show that this is the case.

3.5.5 MoS₂+vacancy

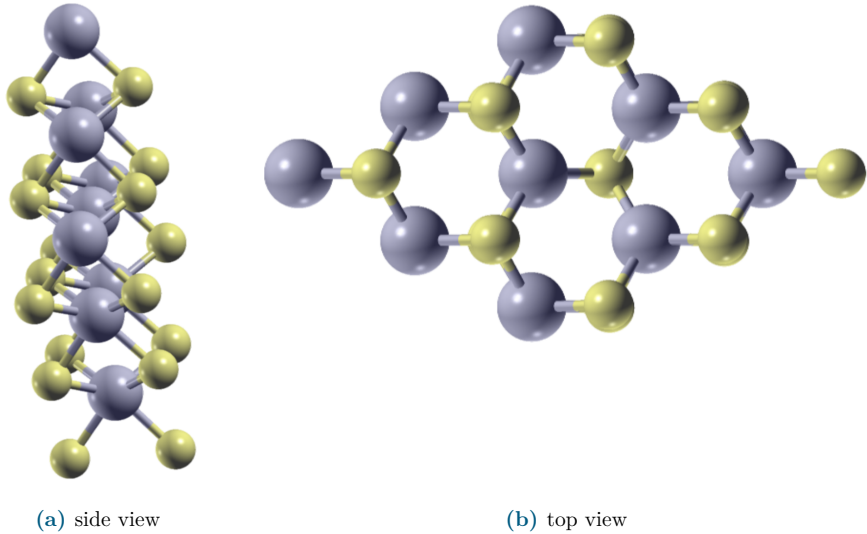


Figure 3.33: Atomic structure (relaxed) of MoS₂ with a missing chalcogen atom. The exact atomic positions can be found in the appendix (Sec. C.3). Plotted using XCrySDen [41].

During the implantation process it is also possible to create vacancies in the chalcogen layer. Therefore, the investigation of such defects is important in order to differentiate them from the others in experimental observations. Experimentally these can be realized by implantation of a noble gas atom that will not dislodge the lattice atom (metal sub-lattice), nor will it bind to any host atom. Probably, also implantation with any ion can result in vacancies as a side effect. During the relaxation process the neighbouring atoms move a little towards the vacancy, filling up a bit of the available space. The resulting band structure seems to be quite distorted with a small shift of the Fermi energy. Additionally in Fig. 3.34, there is a defect state in the middle of the band gap, showing only small dispersion. Energetically this defect state is in the same region as the defect state for MoS₂+S+Cr. In other materials clusters of vacancies are used as photon sources [42].

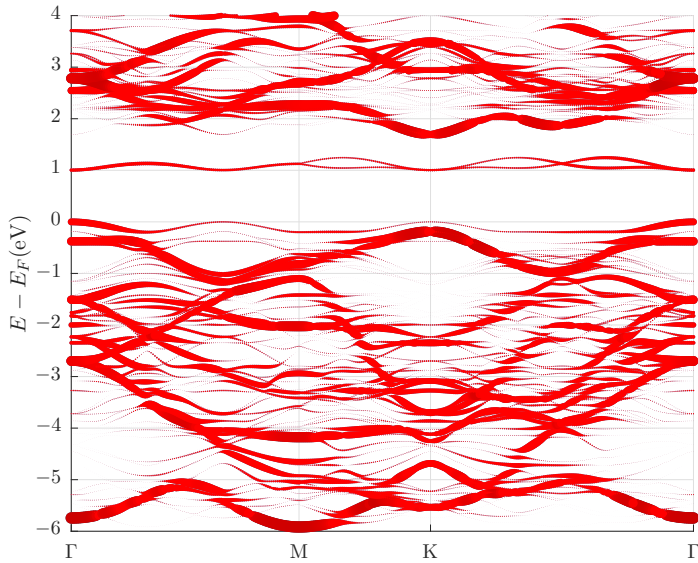


Figure 3.34: Unfolded band structure for MoS₂ with a vacancy in the chalcogen layer, calculated in a 3×3 supercell. The defect state within the band gap is clearly visible. The calculation includes two spins, which are degenerate due to the lack of SOC.

3.5.6 MoSe₂+P

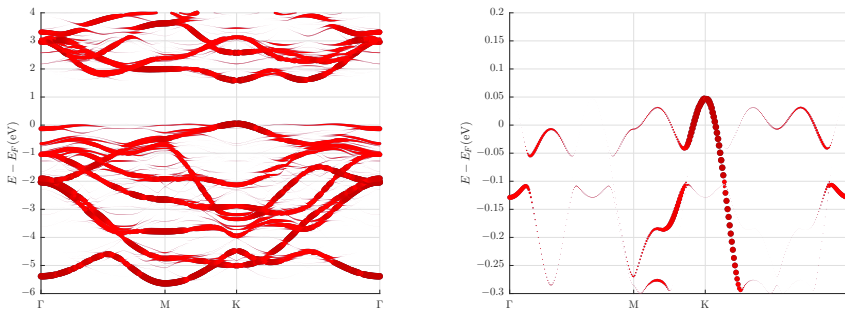


Figure 3.35: Unfolded band structure for MoSe₂+P, calculated in a 3×3 supercell. The state slightly above the Fermi level is clearly visible.

The structure of MoSe_2+P looks similar to the structure of MoS_2+P , just with a small difference in the relaxed positions. Just like for MoS_2+P , the calculation is performed in a 3×3 supercell. The phosphorus is pressed towards the metal layer by 0.18 \AA in comparison to the selenium atoms. This is closer to the metal layer than in the case of MoS_2+P . The exact atomic positions can be found in the appendix (Sec. C.3). This is not very surprising, since the selenium atoms are larger than the sulfur atoms. The same has been observed when replacing selenium with sulfur. A very interesting marginal difference in the band structure is the appearance of the defect state at the Fermi energy (Fig. 3.35). At the K point this defect state seems to actually bend away from the valence band edge, so the highest state is not the defect state but the host state. This was much less pronounced for MoS_2 , but it is also visible, just much closer in energy. It is very surprising that the resulting band structure is not spin-polarized (both spins (blue and red) are overlaid). The starting point for the charge distribution was chosen to be spin-polarized (the same as for MoS_2), so it is unclear how this behavior can be understood in comparison to MoS_2 .

3.5.7 MoSe_2+Cr (@ Mo)

The configuration of MoSe_2+Cr (@ Mo) is very similar to MoS_2+Cr (@ Mo), here also a 5×5 supercell is used. The exact atomic positions for the spatial relaxation can be found in the appendix (Sec. C.3). It is interesting to note that the defect states close to the conduction band minimum actually have the same relative distance as from the conduction band of MoS_2+Cr (@ Mo). Since MoSe_2 has a smaller band gap, this implies that the defect state also has to shift in energy. For a pure single atom state one would rather expect that the energy level is independent of the host material. This supports the fact that the defect state is bound with the host conduction band state, which is to be assumed from the strong unfolding weight close to the K point (showing that the defect state shares some of its symmetries with the host state).

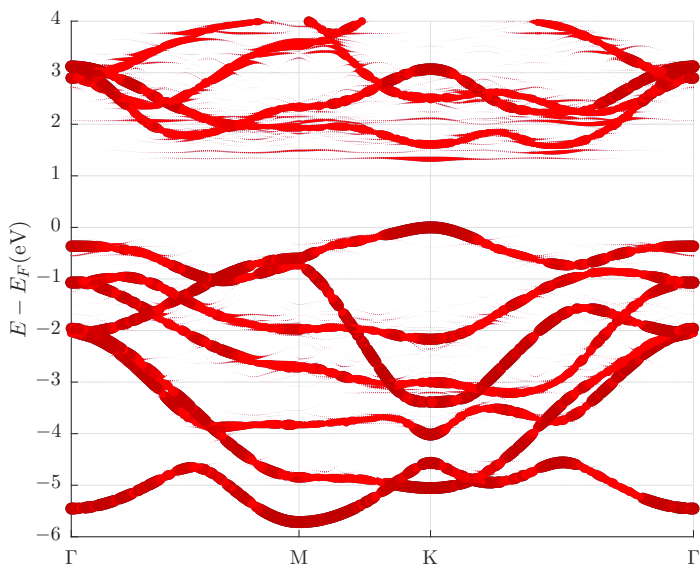


Figure 3.36: Unfolded band structure for MoSe₂+Cr, calculated in a 5×5 supercell. The defect state within the band gap is clearly visible. The calculation includes two spins, which are degenerate due to the lack of SOC.

3.5.8 MoSe₂+Cr (@ Se)

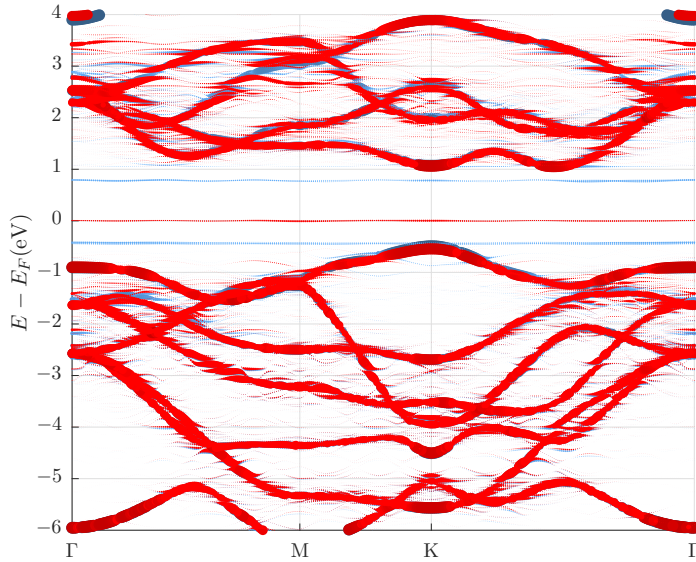


Figure 3.37: Unfolded band structure for MoSe₂+Cr (@ Se), calculated in a 5×5 supercell. The defect states within the band gap are clearly visible. The calculation includes 2 spins but no SOC.

The configuration is similar to the one of MoS₂+Cr (@ S), but during the spatial relaxation process chromium moved only half the distance (compared to MoS₂+Cr (@ S)) out of the layer (0.26 Å). The exact atomic positions can be found in the appendix (Sec. C.3). All observations for the band structure are equivalent to MoS₂+Cr (@ S), due to the shift of the Fermi energy even the band gap is similar to MoS₂+Cr (@ S). The only difference is within the valence band, where the host states (and the connected defect state) are closer to the Fermi energy. Here the defect states were also shifted according to the host material even though they look very much like independent particle bands due to their tiny dispersion and no concentration of the unfolding weight.

3.5.9 MoSe₂+Cr+Se

The atomic configuration is similar to MoS₂+Cr+S (5×5 supercell), but with small

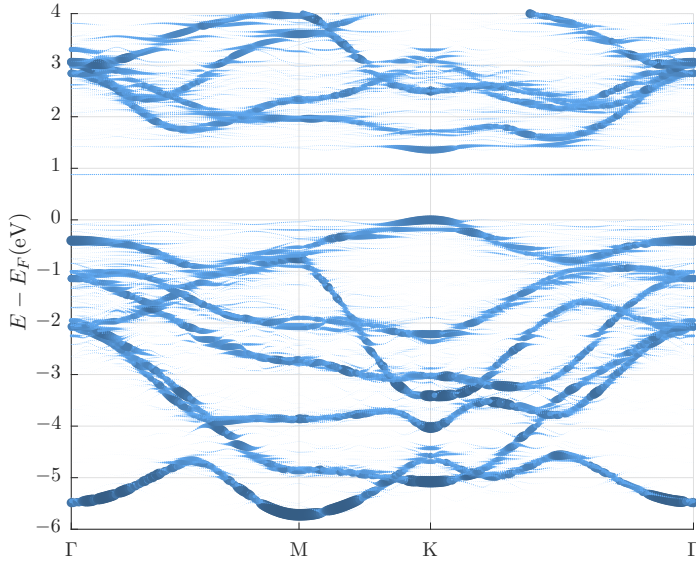


Figure 3.38: Unfolded band structure for $\text{MoSe}_2+\text{Cr}+\text{Se}$, calculated in a 5×5 supercell. The defect state within the band gap is clearly visible. The calculation includes two spins, which are degenerate due to the lack of SOC.

differences in the spatial relaxation. The exact atomic positions can be found in the appendix (Sec. C.3). The band structure is similar, except for the smaller band gap due to the host material. Also, the defect band in the middle of the band gap is moved by a little — from 0.96 eV for $\text{MoS}_2+\text{Cr}+\text{S}$ to 0.88 eV for $\text{MoSe}_2+\text{Cr}+\text{Se}$.

3.5.10 $\text{MoSe}_2+\text{vacancy}$

Also in the case of MoSe_2 , it is important to calculate the effect of a vacancy defect, to be able to differentiate it from the other type of defects in experimental observations. Vacancies can occur at any step during the sample preparation process but most likely during the implantation. During the relaxation process the neighbouring atoms move a little towards the vacancy, filling up a bit of the available space. The resulting band structure seems to be quite distorted. Additionally, there is a defect state in the middle of the band gap, showing only small dispersion. Energetically this defect state is in the same region as the defect state for $\text{MoSe}_2+\text{Se}+\text{Cr}$.

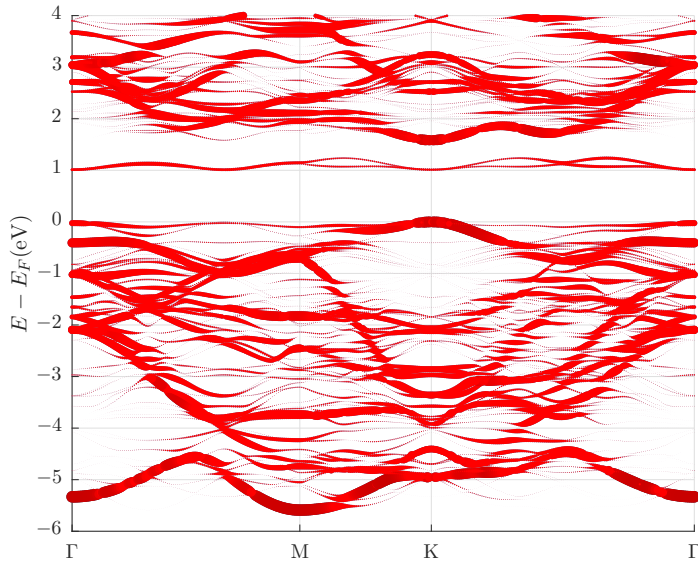


Figure 3.39: Unfolded band structure for MoSe₂ with a vacancy in the chalcogen layer, calculated in a 3×3 supercell. The defect state within the band gap is clearly visible. The calculation includes two spins, which are degenerate due to the lack of SOC.

3.5.11 MoSe₂+Cr (interstitial)

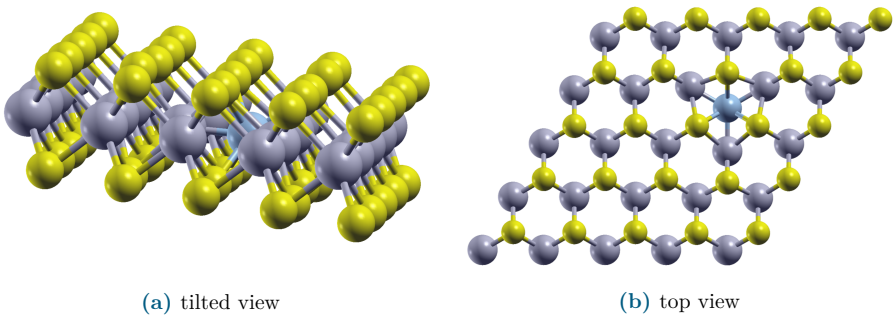


Figure 3.40: Atomic structure of MoSe₂ with implanted chromium at an interstitial position showing the relaxed position of the defect atom. The exact atomic positions can be found in the appendix (Sec. C.3). Plotted using XCrySDen [41].

MoSe₂ has a larger lattice constant than MoS₂ (3.28 Å and 3.15 Å), therefore it is more likely to have a chromium defect in the interstitial position between the molybdenum atoms in the metal layer. This configuration is shown in Fig. 3.40 where it is clear that the neighboring molybdenum atoms (and connected selenium atoms) drift away from the introduced chromium defect (the exact atom positions can be found in Sec. C.3). The final positions of the atoms turned out to be stable. The resulting band structure (Fig. 3.40) shows a spin polarization for the defect states. The introduced donor states shift the Fermi energy to the upper half of the host material band gap. In order to analyze further which (optical) transition are possible the absorption function of a range of different chromium defects, including this one, is shown in Sec. 5.3.3.

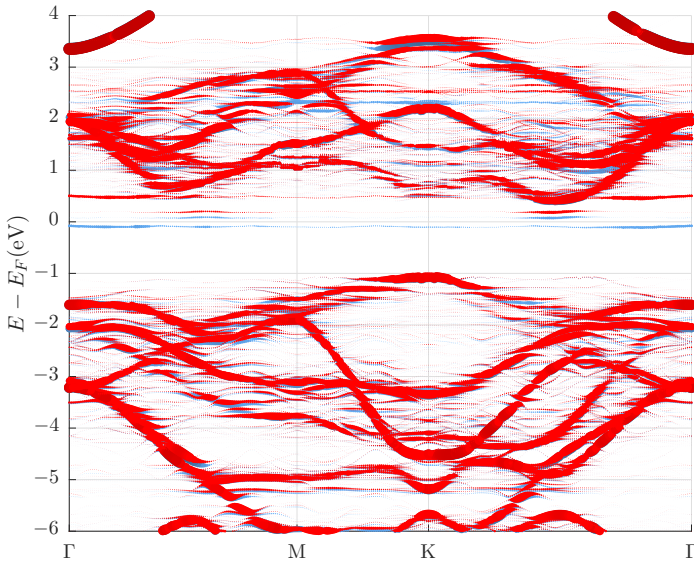


Figure 3.41: Unfolded band structure for MoSe₂ with a chromium defect atom at an interstitial position, calculated in a 5×5 supercell. The calculation includes two spins, but does not include SOC.

3.6 Unfolding of the band structure for other types of supercells and systems

The unfolding mechanism can also be applied to other types of supercells, also those requiring the unfolding only in one or two spatial directions. Furthermore, it is even possible to treat rotated supercells as long as the transformation matrix consists only of integer values.

3.6.1 Surface states of simple unit cell

Simply including additional vacuum in the z-direction and calculating additional surface states being created is a straightforward application for the unfolding algorithm. There is only one requirement — the supercell has to be an integer multiple of the bulk unit cell. Therefore, Fleur includes the option to ensure this by setting the height (z-direction) of the bulk unit cell. Fleur is then calculating/checking for the requirement of being an integer multiple itself. Unfortunately, the interesting surface states are often constructed in a different type of crystal symmetry than the bulk unit cell. This makes it impossible to use the unfolding, unless a special type of surface cell is constructed.

3.6.2 Rotated supercells and general surface states

For example bismuth tellurides have a rhombohedral bulk unit cell, but when constructing a surface cell the preferred construction is in a hexagonal unit cell. Therefore, there is no integer valued transformation possible between the two cells. In this case a new surface unit cell can be found that is transformable to the bulk unit cell by an integer valued matrix that includes rotations.

This option to include the full transformation matrix is implemented. Therefore all types of unit cells, including rotated ones, can be calculated using Fleur and the implementation done as part of this work.

Before being able to use the unfolding, one has to construct the surface cell that is connected with the primitive bulk cell by an integer transformation. There is published work on this by S. Yang et al. [43] including a code to perform the construction of the surface cell automatically. But it is also possible to come up with the special surface cell "by hand".

Here an example of twisted MoS₂ is shown (Fig. 3.42). A supercell is scaled by a factor of $\sqrt{3}$ in each in-plane direction and twisted by 120°. The exact coordinates of the used supercell can be found in the appendix (Sec. C.3). The according unfolding input is used as an example in the description of the unfolding implementation (Sec. 3.2.1). This example demonstrates convincingly that the unfolded band structure is the same as for a stretched unit cell (compare Fig. 3.13a).

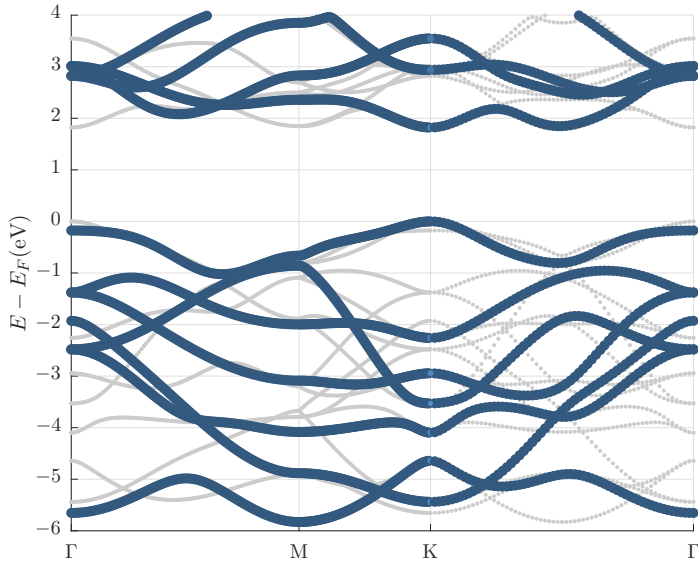


Figure 3.42: Unfolded band structure for twisted MoS₂. The band structure without unfolding is shown in grey. This demonstrates the possibility to obtain the primitive unit cell band structure from the rotated unit cell.

Phenomena in low-energy electron energy loss spectroscopy (EELS)

- 4.1 Introduction to EELS 74
 - 4.1.1 Theoretical scattering cross section 74
 - 4.1.2 Electron energy loss 75
- 4.2 Dielectric layer model 77
 - 4.2.1 Theoretical description of the layer model 78
 - 4.2.2 Different MoS₂ layer distances within the model 81
 - 4.2.3 Influence of vacuum within the layer model 86
 - 4.2.4 Classical derivation of the plasma frequency 96
- 4.3 Calculating EELS spectra for 2D systems 98
 - 4.3.1 Treatment of vacuum in supercell calculations 98
 - 4.3.2 Material response in quasi 2D crystals 100
 - 4.3.3 Extrapolating to infinite layer distance 107
- 4.4 Momentum dependent EELS 112
 - 4.4.1 Momentum summation EELS 113
 - 4.4.2 EELS for pristine MoS₂ monolayer with momentum summation 119
 - 4.4.3 Application to other 2D materials 128

Electron energy loss spectroscopy (EELS) allows us to gain a wealth of information on the electronic structure of the crystal. In comparison to optical methods, transitions including momentum transfer are possible. The method was so successful that measuring instruments were especially built for EELS. Later the measurement procedure was established inside a transmission electron microscope (Sec. 2.6.1).

4.1 Introduction to EELS

An intuitive starting point for the discussion on EELS is the energy loss of an electron when traveling through a probe. Energy is lost due to inelastic scattering processes that can be described by the dielectric response of the material. Initially, this was derived by P. Nozières and D. Pines [44]. It has been summarized in multiple reviews [45, 46] and many PhD theses [47, 48]. Here, I will follow the derivation by P. Schattschneider [9].

4.1.1 Theoretical scattering cross section

The EELS experiment can be understood in a semi-classical approach, where an incoming electron interacts with some effective field, losing energy along the trajectory. In this approach, the relevant quantities have a simple physical interpretation. First, the theoretical scattering cross section of EELS will be calculated. The electron beam given by the current $j(\mathbf{r}, t)$ experiences a decelerating field $E(\mathbf{r}, t)$ created by the electrons of the material. The loss of energy (energy dissipation) per unit volume at point \mathbf{r} and time t is given by [9].

$$L(\mathbf{r}, t) = \mathbf{E}(\mathbf{r}, t) \mathbf{j}(\mathbf{r}, t) \quad (4.1.1)$$

For an electron travelling in z direction the energy loss per unit path length is given by the following integration with $d^2\mathbf{x}_\perp$ being the in-plane integration, perpendicular to the z direction.

$$p = \int d^2\mathbf{x}_\perp \int dt L(\mathbf{r}, t) \quad (4.1.2)$$

The corresponding in-plane Fourier transform of the energy loss is dependent on z .

$$L_z(\mathbf{q}_\perp, \omega) = \int d^2\mathbf{x}_\perp \int dt L(\mathbf{x}_\perp, z, t) e^{-i(\mathbf{q}_\perp \mathbf{x}_\perp - \omega t)} \quad (4.1.3)$$

In $(\mathbf{q}_\perp, \omega)$ space Eq. (4.1.1) is a convolution with z as a parameter.

$$L_z(\mathbf{q}_\perp, \omega) = \frac{1}{(2\pi)^3} \mathbf{E}_z(\mathbf{q}_\perp, \omega) \star \mathbf{j}_z(\mathbf{q}_\perp, \omega) \quad (4.1.4)$$

Now rewriting the energy loss per distance (Eq. (4.1.2)).

$$p = \frac{1}{(2\pi)^3} \int d^2\mathbf{q}_\perp \int_{-\infty}^{\infty} d\omega \mathbf{E}_z(-\mathbf{q}_\perp, -\omega) \mathbf{j}_z(\mathbf{q}_\perp, \omega) \quad (4.1.5)$$

Using the Fourier space representations of the real quantities E and j , it becomes clear that they obey the following: $\mathbf{E}_z(-\mathbf{q}_\perp, -\omega) = \mathbf{E}_z^*(\mathbf{q}_\perp, \omega)$ and $\mathbf{j}_z(-\mathbf{q}_\perp, -\omega) = \mathbf{j}_z(\mathbf{q}_\perp, \omega)$. Using this and exploiting the symmetry of the integral gives:

$$p = \frac{1}{(2\pi)^3} \int d^2\mathbf{q}_\perp \int_0^\infty d\omega (\mathbf{E}_z^* \mathbf{j}_z + \mathbf{E}_z \mathbf{j}_z^*) \quad (4.1.6)$$

The energy loss per unit length can also be written in terms of the energy loss $\hbar\omega$ and the differential scattering probability $\frac{\partial^3 P}{\partial^2 \mathbf{q}_\perp \partial \omega}$. Here the energy loss P is written per momentum transfer and per frequency.

$$p = \int d^2\mathbf{q}_\perp \int_0^\infty d\omega \hbar\omega \frac{\partial^3 P}{\partial^2 \mathbf{q}_\perp \partial \omega} \quad (4.1.7)$$

This leads to the final scattering probability.

$$\frac{\partial^3 P}{\partial^2 \mathbf{q}_\perp \partial \omega} = \frac{1}{(2\pi)^3 \hbar\omega} (\mathbf{E}_z^* \mathbf{j}_z + \mathbf{E}_z \mathbf{j}_z^*) \quad (4.1.8)$$

4.1.2 Electron energy loss

In this derivation, the electron is considered as a point charge traveling at speed \mathbf{v} at normal incidence, creating a plasmon in the probe. The velocity component in the direction of this plasmon is \mathbf{v}_\parallel . The momentum of this plasmon is split up into $q_z = \frac{\omega}{v}$ (will be a result later) parallel to the incident electron and \mathbf{q}_\perp perpendicular to the incident electron. The electron is described by [9]¹:

$$\tilde{j}_\parallel(\mathbf{r}, t) = -v_\parallel e \delta(\mathbf{r} - \mathbf{v}t) \longleftrightarrow j_\parallel(\mathbf{q}, \omega) = -2\pi e v_\parallel \delta(\omega - q_z v) \quad (4.1.9)$$

with the representation in terms of $\mathbf{q}_\perp, \omega, z$ [9]:

$$j_\parallel(\mathbf{q}_\perp, z, \omega) = \frac{1}{2\pi} \int dq_z j_\parallel e^{iq_z z} \quad (4.1.10)$$

using the geometric relation $v_\parallel/v = q_z/q = q_z/\sqrt{q_z^2 + q_\perp^2}$ and integrating ($\int dx \delta(ax) = \frac{1}{|a|}$) the current is described as [9]:

$$j_\parallel(\mathbf{q}_\perp, z, \omega) = -e \frac{\omega}{v \sqrt{(\omega/v)^2 + q_\perp^2}} e^{i \frac{\omega}{v} z} \quad (4.1.11)$$

¹ With the Fourier transforms (Sec. D.1): $-j_\parallel(\mathbf{q}, \omega) = \int dt \int d\mathbf{r} v_\parallel e \delta(\mathbf{r} - \mathbf{v}t) e^{-i\mathbf{q}\mathbf{r}} e^{i\omega t} = v_\parallel e \int dt \int d\mathbf{r} e^{-i\mathbf{q}\mathbf{v}t} e^{i\omega t} = \frac{1}{2\pi} 2\pi v_\parallel e \int dt e^{-i(q_z v - \omega)t} = 2\pi e v_\parallel \delta(\omega - q_z v)$

The electric field is found using the Maxwell equations (cgs units).[9]

$$\nabla \mathbf{D}(\mathbf{r}, t) = 4\pi\rho(\mathbf{r}, t) \quad (4.1.12)$$

The Fourier transform of both sides of the equation is performed. The charge on the right side can be replaced similarly to the current defined before ($\rho(\mathbf{r}, t) = -e\delta(\mathbf{r} - \mathbf{v}t) \longleftrightarrow \rho(\mathbf{q}, \omega) = -2\pi e\delta(\omega - q_z v)$):

$$i\mathbf{q}\mathbf{D}(\mathbf{q}, \omega) = -8\pi^2 e\delta(\omega - q_z v) \quad (4.1.13)$$

The dielectric function is introduced via $\varepsilon(\mathbf{q}, \omega)\mathbf{E}(\mathbf{q}, \omega) = \mathbf{D}(\mathbf{q}, \omega)$.

$$i\varepsilon(\mathbf{q}, \omega)\mathbf{q}\mathbf{E}(\mathbf{q}, \omega) = -8\pi^2 e\delta(\omega - q_z v) \quad (4.1.14)$$

The electric field is rotation-free, since it is created from a potential ($\mathbf{E}(\mathbf{r}) = -\nabla\Phi(\mathbf{r})$). The electric field is parallel to \mathbf{q} ($\mathbf{E}(\mathbf{q}) = -i\mathbf{q}\Phi(\mathbf{q})$ (Fourier transform)). To calculate the energy lost, the component parallel to the current is of interest. Here again, the in-plane Fourier transform is performed (z -direction is left unchanged). This is analogue to the Fourier transform used for the current.

$$E_{\parallel}(\mathbf{q}_{\perp}, z, \omega) = \frac{1}{2\pi} \int dq_z E_{\parallel} e^{iq_z z} = \frac{4\pi e}{ivq} \frac{e^{i\frac{\omega}{v}z}}{\varepsilon(\mathbf{q}, \omega)} \quad (4.1.15)$$

with \mathbf{q} :

$$q^2 = q_{\perp}^2 + q_z^2 = q_{\perp}^2 + \left(\frac{\omega}{v}\right)^2 \quad (4.1.16)$$

The energy loss due to the dissipation in this field, created by the response from the material to the external field, $\int dt \int d^3r \mathbf{E}(\mathbf{r}, t)\mathbf{j}(\mathbf{r}, t)$ can then be found. Using the result for the scattering cross section (Eq. (4.1.8)) the energy loss probability per energy and per momentum is (\mathbf{q}_{\perp} denotes the possible momentum transfers in-plane (perpendicular to the incident electron)):

$$\frac{\partial^3 P}{\partial^2 \mathbf{q}_{\perp} \partial \omega} = \frac{4\pi e^2}{(2\pi)^3 \hbar \omega} \frac{\omega}{v^2 \mathbf{q}^2} \left(\frac{1}{i\varepsilon(\mathbf{q}, \omega)} - \frac{1}{i\varepsilon^*(\mathbf{q}, \omega)} \right) \quad (4.1.17)$$

Simplification leads to the final differential scattering cross section:

$$\frac{\partial^3 P}{\partial^2 q_{\parallel} \partial \omega} = -\frac{8\pi e^2}{(2\pi)^3 \hbar v^2 q^2} \text{Im} \frac{1}{\varepsilon(\mathbf{q}, \omega)} \quad (4.1.18)$$

The energy loss derived from the differential scattering cross section is dependent on the frequency ω (or energy $\hbar\omega$). If the detector is placed at different angles from normal incidence, one can also record EELS spectra for different in-plane wave vectors \mathbf{q}_{\perp} . For a fixed \mathbf{q}_{\perp} , there are two ω -dependent functions that contribute to the spectrum. The inverse macroscopic dielectric function $\varepsilon^{-1}(\mathbf{q}, \omega)$ and the prefactor $\frac{1}{q^2} = \frac{1}{q_{\perp}^2 + (\omega/v)^2}$. The dielectric function is responsible for the peak structure of the spectrum, whereas the prefactor acts as a weight function. This prefactor gives low energies a higher weight than high energies [49].

To further assess the relative importance of the two terms, it is helpful to estimate the orders of magnitude of the different quantities. The prefactor to the momentum dependent loss function contains the momentum as well as the speed of the electron. The momentum can be separated into the contribution perpendicular to the electron and in the direction of the electron. Due to the high speed of the electron, assuming all energy loss in the direction of the electron is a very good approximation. Therefore, this momentum component can be expressed via the energy loss and the frequency $q_{\perp} = \omega/v$. This means the prefactor does not only vary with the momentum transferred to the plasmon (or excitation of the material) and the speed of the electron but also with the energy lost. The significance of this dependence varies with the energy range and momentum range studied. Commonly only the term dependent on the dielectric function is used as the energy loss $-\text{Im} \varepsilon^{-1}(\mathbf{q}, \omega)$ [49]. A detailed discussion and evaluation of the energy loss will follow in [Sec. 4.4](#).

4.2 Dielectric layer model

Van-der-Waals bound layered materials like MoS₂ can be separated into two effective dielectric environments. An effective dielectric material inside the slab and a vacuum area in between the slabs are combined in the full dielectric function. The areas can be seen as separate capacitors which are combined by Kirchhoff's law ([Fig. 4.1](#)).

4.2.1 Theoretical description of the layer model

The layered structure in Fig. 4.1 can be considered as a set of capacitors. Perpendicular to the layers it is a series of capacitors with dielectric constants of ε and ε_{vac} . In the direction of the layers these are capacitors in parallel. Inside the material ε_{\parallel} is considered identical to ε_{\perp} . By Kirchhoff's laws two capacitors in series have a total capacitance C_{total} of:

$$\frac{1}{C_{\text{total}}} = \frac{1}{C_1} + \frac{1}{C_2} \quad (4.2.1)$$

The capacitance of a parallel plate capacitor can be calculated by:

$$C_1 = \varepsilon_0 \varepsilon_1 \frac{A}{d} \quad (4.2.2)$$

assuming $A \gg d$. Here A stands for the area of the capacitor and d for the thickness. Considering a unit cell size of L and an effective thickness of d_{eff} . This can be written as:

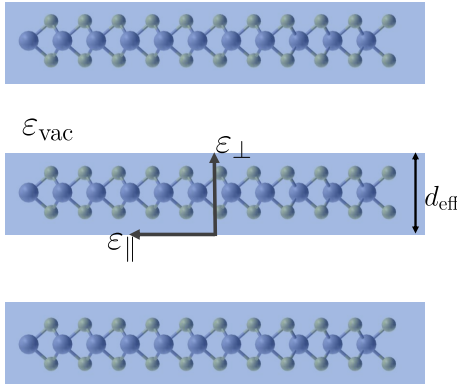


Figure 4.1: Representation of a TMD slab system with effective dielectric constant $\varepsilon_{\parallel}, \varepsilon_{\perp}$, and ε_{vac} . d_{eff} denotes the effective layer thickness, which is determined in Sec. 4.2.2.

$$\frac{1}{\varepsilon_0 \varepsilon_{\text{total}} \frac{A}{L}} = \frac{1}{\varepsilon_0 \frac{A}{L - d_{\text{eff}}}} + \frac{1}{\varepsilon_0 \varepsilon \frac{A}{d_{\text{eff}}}} \quad (4.2.3)$$

The effective dielectric constant is therefore:

$$\varepsilon_{\text{total}} = \frac{1}{1 + \frac{d_{\text{eff}}}{L} \left(\frac{1}{\varepsilon} - 1 \right)} \quad (4.2.4)$$

The similar consideration can be made for the parallel case.

$$C_{\text{total}} = C_1 + C_2 \quad (4.2.5)$$

Here the capacitors are placed as shown in Fig. 4.2a with a depth of T and a cell size in parallel direction of L_x . Therefore, d equals L_x and A is calculated by $T \cdot d_{\text{eff}}$ (respectively $T \cdot (L - d_{\text{eff}})$). In this case the

total dielectric constant is given by

$$\varepsilon_0 \varepsilon_{\text{total}} \frac{L \cdot T}{L_x} = \varepsilon_0 \frac{(L - d_{\text{eff}}) \cdot T}{L_x} + \varepsilon_0 \varepsilon \frac{d_{\text{eff}} \cdot T}{L_x} \quad (4.2.6)$$

This simplifies to:

$$\varepsilon_{\text{total}} = \left(1 - \frac{d_{\text{eff}}}{L}\right) + \varepsilon \frac{d_{\text{eff}}}{L} \quad (4.2.7)$$

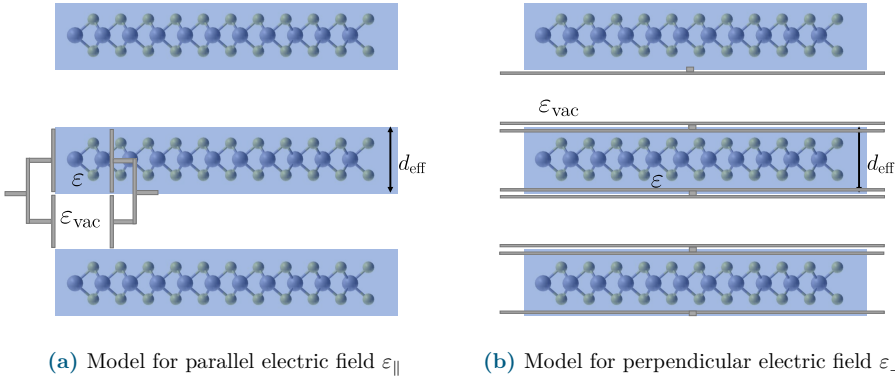


Figure 4.2: Illustration of the fictitious capacitors in the homogeneous layer model for the case of the dielectric constant in parallel and in perpendicular direction

Alternative derivation in a model crystal

A thorough derivation for a mixed material assuming a grid of independent dipoles by D. E. Aspnes can be found in [50] and is analogously done in the following. A heterogeneous dielectric medium can be modeled as a cubic lattice with points of known polarizability α in front of a vacuum background. Each of the points produces a dipole field of

$$\mathbf{E}_{\text{dip}}(\mathbf{r}) = \frac{3(\mathbf{p} \cdot \mathbf{r})\mathbf{r} - \mathbf{p}r^2}{r^5}, \quad (4.2.8)$$

where \mathbf{p} is the dipole vector. This allows us to write down the full electric field at every point (\mathbf{R}_n labels the lattice sites):

$$\mathbf{e}(\mathbf{r}) = \mathbf{E} + \sum_{\mathbf{R}_n} \mathbf{E}_{\text{dip}}(\mathbf{r} - \mathbf{R}_n) \quad (4.2.9)$$

$$\mathbf{p}(\mathbf{r}) = \sum_{\mathbf{R}_n} \alpha \mathbf{e}(\mathbf{0}) \delta(\mathbf{r} - \mathbf{R}_n) \quad (4.2.10)$$

The local field $\mathbf{e}(\mathbf{0}) = \mathbf{E} + \sum_{\mathbf{R}_n \neq 0} \mathbf{E}_{\text{dip}}(\mathbf{R}_n)$ is simple for full cubic symmetry, since in that case the sum vanishes so that $\mathbf{E} = \mathbf{e}(\mathbf{0}) = \mathbf{E}_{\text{loc}}$. With a volume density of n and the volume integral of a dipole field $-4\pi\mathbf{p}/3$, the average macroscopic field and dipole moment can be found.

$$\mathbf{P} = n\alpha\mathbf{E}_{\text{loc}} \text{ and } \mathbf{E} = \mathbf{E}_{\text{loc}} \left(1 - \frac{4\pi}{3}n\alpha \right) \quad (4.2.11)$$

Including the dielectric function $\mathbf{D} = \varepsilon\mathbf{E} = \mathbf{E} + 4\pi\mathbf{P}$ allows us to find the Clausius-Mossotti expression and extend it for two different types of dielectric response.

$$\frac{\varepsilon - 1}{\varepsilon + 2} = \frac{4\pi}{3}n\alpha = \frac{4\pi}{3}(n_a\alpha_a + n_b\alpha_b) \quad (4.2.12)$$

This can be reformulated using the macroscopic quantity ε rather than (the microscopic) α so that the equation becomes (f_a being the volume fraction):

$$\frac{\varepsilon - 1}{\varepsilon + 2} = f_a \frac{\varepsilon_a - 1}{\varepsilon_a + 2} + f_b \frac{\varepsilon_b - 1}{\varepsilon_b + 2} \quad (4.2.13)$$

Now using a self consistent approach of an average host medium with dielectric constant of ε rather than the vacuum, the effective medium approximation (EMA) is found.

$$f_a \frac{\varepsilon_a - \varepsilon}{\varepsilon_a + 2\varepsilon} + f_b \frac{\varepsilon_b - \varepsilon}{\varepsilon_b + 2\varepsilon} = 0 \quad (4.2.14)$$

For a layered material this can be simplified further. Instead of using spherical dipoles two cases can be looked at.

For a parallel field, the electric field \mathbf{E} is uniform everywhere and by simply averaging the dielectric displacement $\mathbf{D} = f_a\mathbf{D}_a + f_b\mathbf{D}_b$ one finds:

$$\varepsilon = f_a\varepsilon_a + f_b\varepsilon_b \quad (4.2.15)$$

In perpendicular direction to the layers, \mathbf{D} is uniform and therefore averaging \mathbf{E} leads to $\mathbf{E} = f_a \mathbf{E}_a + f_b \mathbf{E}_b$:

$$\frac{1}{\varepsilon} = f_a \frac{1}{\varepsilon_a} + f_b \frac{1}{\varepsilon_b} \quad (4.2.16)$$

This is equivalent to the case of parallel and perpendicular capacitors. These equations are called Wiener absolute bounds. Nevertheless, this is based on macroscopic quantities, assuming the microstructure is small (compared to the wavelength of light). For an excitation with momentum transfer, the electric field is changing on the microscopic scale, therefore the full microscopic treatment is needed in that case and the layer model is only an approximation.

4.2.2 Different MoS₂ layer distances within the model

By assigning an effective layer thickness, an effective material dielectric function can be calculated for different layer distances. This quantity should then be independent of the vacuum distance between the layers.

Calculating the effective layer thickness

Combining the two formulations for the parallel and the perpendicular oriented dielectric function, the effective layer thickness (d) can be calculated (Eq. (4.2.7) and Eq. (4.2.4)). In the following, ε_{\parallel} refers to the total dielectric constant parallel to the layers and ε_{\perp} to the total perpendicular dielectric constant. The dielectric constant (ε) is the dielectric function ($\varepsilon(\omega)$) for $\omega = 0$. Solving the two equations for ε , the effective dielectric constant inside the material, gives:

$$\varepsilon = \varepsilon_{\perp} \cdot \frac{\varepsilon_{\parallel} - 1}{\varepsilon_{\perp} - 1} \quad (4.2.17)$$

Also the effective layer thickness d_{eff} can be calculated with the same formulas.

$$d_{\text{eff}} = L \cdot \frac{(\varepsilon_{\perp} - 1)(\varepsilon_{\parallel} - 1)}{\varepsilon_{\perp}(\varepsilon_{\parallel} - 2) + 1} \quad (4.2.18)$$

For different vacuum distances of MoS₂, these quantities have been calculated. It is important to notice that the results only match up with the here described theory in the case of the renormalized dielectric function. The results are summarized in [Tab. 4.1](#)

layer distance in Å	ε_{\perp}	ε_{\parallel}	ε	d_{eff}
12.30	1.67898	7.42119	15.88	5.308
24.60	1.25406	4.20543	15.82	5.320
36.90	1.15631	3.13396	15.79	5.325
49.20	1.11285	2.59826	15.76	5.327
123.0	1.04220	1.63486	15.68	5.319

Table 4.1: Effective layer thickness and effective dielectric constant for MoS₂ layer distances with A-A stacking.

Effective layer dielectric function

In the following, the effective dielectric function for a monolayer of MoS₂, calculated from the dielectric function of a slab system, will be analyzed for different vacuum spacings. Using an effective layer thickness of 5.3 Å (Sec. 4.2.2) the effective dielectric function within the material can be calculated by rearranging Eq. (4.2.4).

$$\varepsilon = \frac{1}{\frac{L}{d}(\frac{1}{\varepsilon_{\perp}} - 1) + 1} \quad (4.2.19)$$

This dielectric function should converge with larger distance between the layers, since it is constructed to describe only the response of the material slab and compensates for the vacuum spacing used. For a larger vacuum gap, the interaction in between the layers is reduced. Therefore, it can be observed that the dielectric function perpendicular to the material layers for 34.9 Å and 49.2 Å is nearly identical (Fig. 4.3). Consequently, it is necessary to use at least a spacing of 34.9 Å to model a monolayer within the layer model.

The same analysis is also possible for the parallel dielectric function by rearranging Eq. (4.2.7):

$$\varepsilon = 1 - \frac{L}{d} + \varepsilon_{\parallel} \frac{L}{d} \quad (4.2.20)$$

Here, the convergence with larger vacuum spacings is very fast. To calculate the optical absorption (imaginary part of the dielectric function) in the in-plane case a vacuum distance of 12.3 Å is sufficient.

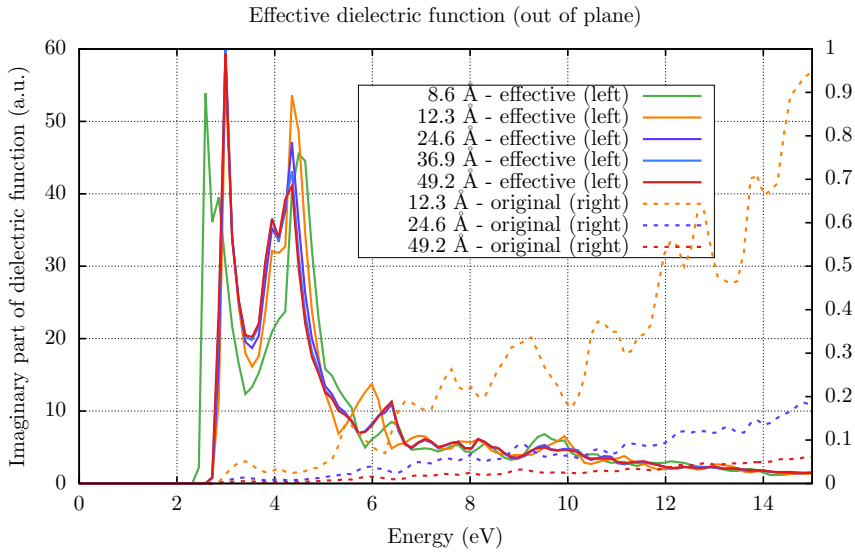


Figure 4.3: Imaginary part of the effective dielectric function perpendicular to the layer compared for different vacuum distances (MoS_2). The convergence with a vacuum spacing of 34.9 \AA and 49.2 \AA can be clearly seen. The comparison to the unchanged dielectric function (out-of-plane direction), plotted as dotted lines (axis label on the right), makes the convergence behavior obvious.

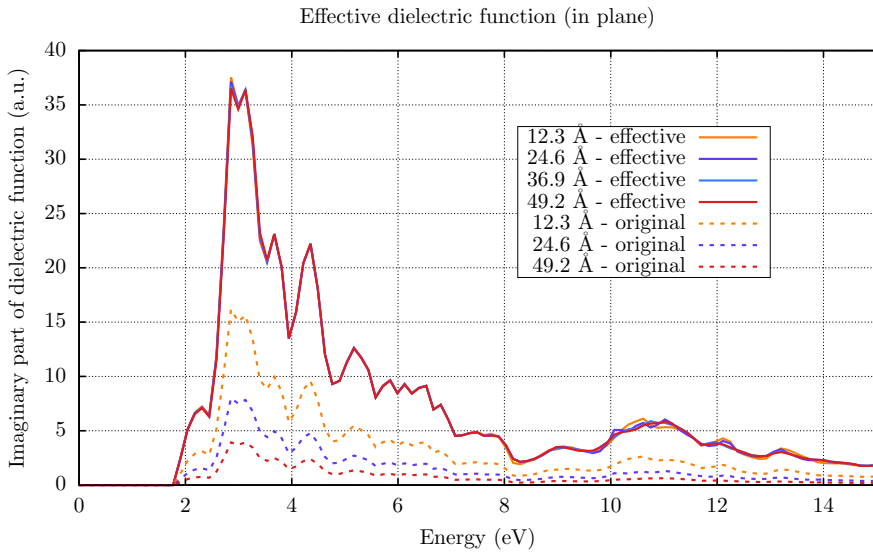


Figure 4.4: Imaginary part of the effective dielectric function parallel to the layer compared for different vacuum distances (MoS_2). The convergence with a larger vacuum spacing can be clearly seen. The comparison to the unchanged dielectric function (in-plane direction), plotted as dotted lines, makes the convergence behavior obvious.

Effective EELS spectrum

In the previous section, the effective dielectric function was calculated. Now, from this, an effective EELS spectrum ($\text{Im} \frac{1}{\epsilon}$ (Eq. (4.1.18))) can be found and compared to the EELS spectrum with vacuum (the one of the slab system). Surprisingly, this

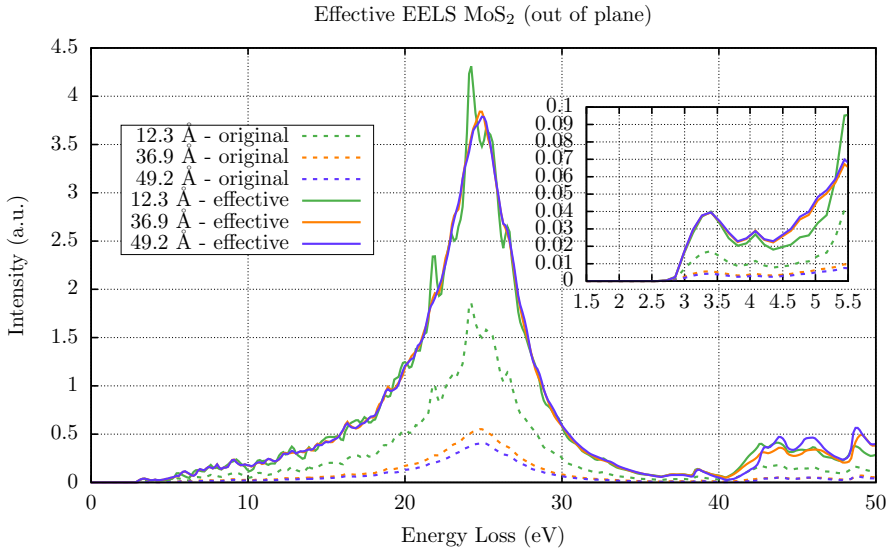


Figure 4.5: Effective EELS spectrum for 12.3 Å to 49.2 Å compared with the original EELS. The original EELS refers to the EELS based on the calculated dielectric function including vacuum without any model considerations.

effective EELS (Fig. 4.6) changes the peak position compared to the EELS spectrum with vacuum (Fig. 4.9). In both cases (out-of-plane and in-plane), there are significant differences between the effective EELS and the calculated EELS including vacuum. But the effective EELS seems to converge very fast with the layer distance. This is to be expected as the effective dielectric function based on the layer model also converged very quickly with the layer distance. Using this effective dielectric function to calculate EELS is assuming it would give the correct response. But it is rather a result of a model calculation assuming the material slab is isotropic — the different results for the effective dielectric function, comparing the one in the in-plane direction and the one in the out-of-plane direction, show that this is clearly not the case. Therefore, it is clear that these results show just a model system, but this model system is not sufficient to treat the anisotropic MoS₂ system. Also, these considerations only focus

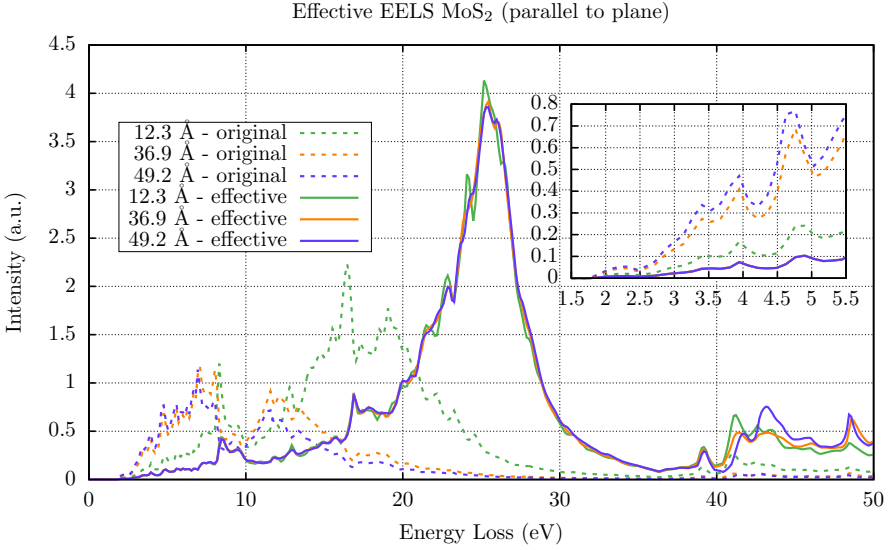


Figure 4.6: Effective EELS spectrum for 12.3 Å to 49.2 Å compared with the original EELS. The original EELS refers to the EELS based on the calculated dielectric function including vacuum without any model considerations.

on a static homogeneous charge distribution in the material layer — this is not the case in reality. Nevertheless, the layer model is very helpful to understand the overall behavior of these layered materials and to estimate an effective layer thickness. But overall, a more sophisticated model is needed to calculate the effective spectra.

4.2.3 Influence of vacuum within the layer model

In Sec. 4.2.1, an effective medium theory is described where a system of homogeneous layers resembles the real slab system with quasi 2D monolayers and vacuum in between. Even though this effective theory does not describe the EELS spectrum in a realistic way, it is very useful for gaining understanding. Using this model the influence of increasing vacuum on certain quantities can be modeled and understood. Within the model, the horizontal component of the dielectric function ε_{\parallel} , the vertical component ε_{\perp} and a theoretical dielectric function within the homogeneous slab ε are used. This effective dielectric function is, as previously shown, (Fig. 4.4 and Fig. 4.3) nearly independent of the distance between the layers. In Sec. 4.2.1 the following equations

were found:

$$\varepsilon_{\perp} = \frac{1}{1 + \frac{d}{L}(\frac{1}{\varepsilon} - 1)} \quad (4.2.21)$$

$$\varepsilon_{\parallel} = \left(1 - \frac{d}{L}\right) + \varepsilon \frac{d}{L} \quad (4.2.22)$$

From this, optical excitations (the imaginary part of the dielectric function) or EELS spectra ($\text{Im}(\varepsilon^{-1}(\omega))$) can be calculated for each component. Since the vacuum included should not have an influence on the final result (it does not contribute to the dielectric properties of the layer (except the states at the surface)), scaling with the amount of introduced vacuum L/d is necessary so that a convergence with increasing layer distance can be found. A detailed discussion of the quantities involved can be found in [Sec. 4.3.1](#). The relevant quantities for the optical excitations and the EELS spectra will be analyzed in the following. The model dielectric function will be used to understand the speed of convergence with increasing layer distance.

$$\frac{L}{d} \text{Im}(\varepsilon_{\perp}^{-1}(\omega)) = \frac{L}{d} \text{Im}\left(1 + \frac{d}{L}\left(\frac{1}{\varepsilon(\omega)} - 1\right)\right) \quad (4.2.23)$$

$$= \text{Im}\left(\frac{L}{d}\left(1 + \frac{d}{L}\left(\frac{1}{\varepsilon(\omega)} - 1\right)\right)\right) \quad (4.2.24)$$

$$= \text{Im}\left(\frac{L}{d} + \frac{1}{\varepsilon(\omega)} - 1\right) \quad (4.2.25)$$

Only the imaginary part is of interest, therefore all purely real quantities can be left out.

$$= \text{Im}\left(\frac{1}{\varepsilon(\omega)}\right) \quad (4.2.26)$$

One is left with a result that is independent of L , since $\varepsilon(\omega)$ is the dielectric function inside the material slab and thus independent of L . So for the perpendicular direction, the EELS result should, if scaled properly, be approximately independent of the chosen layer distance. This is only true under the assumption of the layer model that considers the charge distribution as homogeneous. Since the non-homogeneous part of the inter-layer interaction is not taken into account, there is a visible (but fast) convergence with interlayer distance in [Fig. 4.10](#) as the non-homogeneous part of the inter-layer interaction decreases. This is only true for the case of LFE being included.

Next, EELS for the parallel case ($\text{Im}(\varepsilon_{\parallel}^{-1}(\omega))$) is considered.

$$\frac{L}{d} \text{Im}(\varepsilon_{\parallel}^{-1}(\omega)) = \frac{L}{d} \text{Im}\left(\frac{1}{1 - \frac{d}{L} + \varepsilon(\omega)\frac{d}{L}}\right) \quad (4.2.27)$$

$$= \frac{L}{d} \text{Im}\left(\frac{1 - \frac{d}{L} + \frac{d}{L} \text{Re}(\varepsilon(\omega)) - i \text{Im}(\varepsilon(\omega))\frac{d}{L}}{\left(1 - \frac{d}{L} + \frac{d}{L} \text{Re}(\varepsilon(\omega))\right)^2 + \left(\text{Im}(\varepsilon(\omega))\frac{d}{L}\right)^2}\right) \quad (4.2.28)$$

Now that the denominator is purely real, eliminating all terms that have no imaginary contribution is possible.

$$= -\text{Im}\left(\frac{\varepsilon(\omega)}{\left(1 - \frac{d}{L} + \frac{d}{L} \text{Re}(\varepsilon(\omega))\right)^2 + \left(\text{Im}(\varepsilon(\omega))\frac{d}{L}\right)^2}\right) \quad (4.2.29)$$

For large layer distances this simplifies to:

$$\lim_{L \rightarrow \infty} \frac{L}{d} \text{Im}(\varepsilon_{\parallel}^{-1}(\omega)) = -\text{Im}(\varepsilon(\omega)) \quad (4.2.30)$$

This suggests that scaling by the vacuum distance delivers a result independent of the layer distance for large layer distances.

Contrary to this, in [Fig. 4.9](#) it seems like scaling is not necessary. It rather can be observed that one part of the structure gradually disappears as the interlayer distance is being increased. A possible explanation for this can be found in the very slow convergence with respect to the layer distance. Approximating Eq. (4.2.29) leads to:

$$\begin{aligned} & -\text{Im}\left(\frac{\varepsilon(\omega)}{\left(1 - \frac{d}{L} + \frac{d}{L} \text{Re}(\varepsilon(\omega))\right)^2 + \left(\text{Im}(\varepsilon(\omega))\frac{d}{L}\right)^2}\right) \\ & \approx -\text{Im}(\varepsilon(\omega)) - \text{Im}(\varepsilon(\omega))\frac{d}{L}(2 - 2\text{Re}(\varepsilon(\omega))) \\ & \quad - \text{Im}(\varepsilon(\omega))\left(\frac{d}{L}\right)^2[3(\text{Re}(\varepsilon(\omega)) - 1)^2 - (\text{Im}(\varepsilon(\omega)))^2] + \dots \end{aligned} \quad (4.2.31)$$

Compared to the case of EELS based on the dielectric function in perpendicular direction to the surface, it takes much higher L in order to achieve convergence. [Fig. 4.10](#) does not even show a converged result. The required layer distance seems to be much larger than the here calculated distances.

The next case that is considered, is the absorption function for the perpendicular part

of the dielectric function.

$$\frac{L}{d} \text{Im} (\varepsilon_{\perp}(\omega)) = \frac{L}{d} \text{Im} \left(\frac{1}{1 - \frac{d}{L} + \frac{d}{L} \frac{1}{\varepsilon(\omega)}} \right) \quad (4.2.32)$$

$$= \frac{L}{d} \text{Im} \left(\frac{1 - \frac{d}{L} + \frac{d}{L} \text{Re}(\frac{1}{\varepsilon(\omega)}) - i \text{Im}(\frac{1}{\varepsilon(\omega)}) \frac{d}{L}}{\left(1 - \frac{d}{L} + \frac{d}{L} \text{Re}(\frac{1}{\varepsilon(\omega)})\right)^2 + \left(\text{Im}(\frac{1}{\varepsilon(\omega)}) \frac{d}{L}\right)^2} \right) \quad (4.2.33)$$

Now eliminating all terms that are only real gives:

$$= - \text{Im} \left(\frac{\frac{1}{\varepsilon(\omega)}}{\left(1 - \frac{d}{L} + \frac{d}{L} \text{Re}(\frac{1}{\varepsilon(\omega)})\right)^2 + \left(\text{Im}(\frac{1}{\varepsilon(\omega)}) \frac{d}{L}\right)^2} \right) \quad (4.2.34)$$

For large layer distances, this simplifies to:

$$\lim_{L \rightarrow \infty} \frac{L}{d} \text{Im} (\varepsilon_{\perp}(\omega)) = - \text{Im} \left(\frac{1}{\varepsilon(\omega)} \right) \quad (4.2.35)$$

The result suggest that by scaling with a factor of L/d there should be convergence visible. In Fig. 4.8, exactly this can be seen for the physically meaningful case including LFE. Looking at the speed of convergence also in this case, like in the case of EELS for the parallel component, a quite slow convergence behavior with increasing layer distance L is evident in the following expression:

$$\begin{aligned} & - \text{Im} \left(\frac{\frac{1}{\varepsilon(\omega)}}{\left(1 - \frac{d}{L} + \frac{d}{L} \text{Re}(\frac{1}{\varepsilon(\omega)})\right)^2 + \left(\text{Im}(\frac{1}{\varepsilon(\omega)}) \frac{d}{L}\right)^2} \right) \\ & \approx - \text{Im} \left(\frac{1}{\varepsilon(\omega)} \right) - \text{Im} \left(\frac{1}{\varepsilon(\omega)} \right) \frac{d}{L} (2 - 2 \text{Re}(\frac{1}{\varepsilon(\omega)})) \\ & - \text{Im} \left(\frac{1}{\varepsilon(\omega)} \right) \left(\frac{d}{L} \right)^2 [3 \text{Re}(\frac{1}{\varepsilon(\omega)}) - 1]^2 - \left(\text{Im} \frac{1}{\varepsilon(\omega)} \right)^2 + \dots \end{aligned} \quad (4.2.36)$$

Now investigating the fourth and last case — the absorption function for the parallel component of the dielectric function:

$$\frac{L}{d} \text{Im} (\varepsilon_{\parallel}(\omega)) = \frac{L}{d} \text{Im} \left(\left(1 - \frac{d}{L}\right) + \varepsilon(\omega) \frac{d}{L} \right) \quad (4.2.37)$$

$$= \text{Im} (\varepsilon(\omega)) \quad (4.2.38)$$

This result is independent of the layer distance, therefore the observation in Fig. 4.7 can be explained. Scaling with L/d compensates the added vacuum.

Calculations for MoS₂ with increasing layer distance

In Sec. 4.2.3, predictions were made on the dependence of optical excitations and EELS spectra on the interlayer distances. In the following, calculations for MoS₂ are shown for different layer distances. The graphs are grouped per component, similar to the considerations in the previous section. There is always one plot with and one without local field effects (LFE) — where useful, also the scaling by L/d is shown. For experimental predictions, only the figures including LFE are of interest, since the real physical system is not homogeneous. Without LFE the effect of local charge distribution changes, as they appear in the real system, are not correctly shown. The

$\text{Im}(\varepsilon)$	nLFE	LFE
\parallel	√	√
\perp	√	X

Table 4.2: Does scaling $\text{Im}(\varepsilon)$ by L/d deliver results that converge quickly? "√" stands for yes, "X" for no.

$-\text{Im}(\varepsilon^{-1})$	nLFE	LFE
\parallel	X	X
\perp	X	√

Table 4.3: Does scaling $-\text{Im}(\varepsilon^{-1})$ by L/d deliver results that converge quickly? "√" stands for yes, "X" for no.

figures without LFE are only interesting for comparison with the before discussed model and to understand the influence of LFE.

Before showing all the plots, the two tables (Tab. 4.2 and Tab. 4.3) summarize the

results, giving an overview of the overall behavior. From this overview it is already clear that scaling according to the vacuum is not enough to correct the influence of the vacuum on the calculated spectra. The convergence is sometimes not even visible, even though a layer distance of up to 123 \AA was used.

The following overview of plots is not supposed to be a final result — it is to highlight the influence of the included vacuum (slab system) onto the two components of the dielectric function (in-plane and out-of-plane).

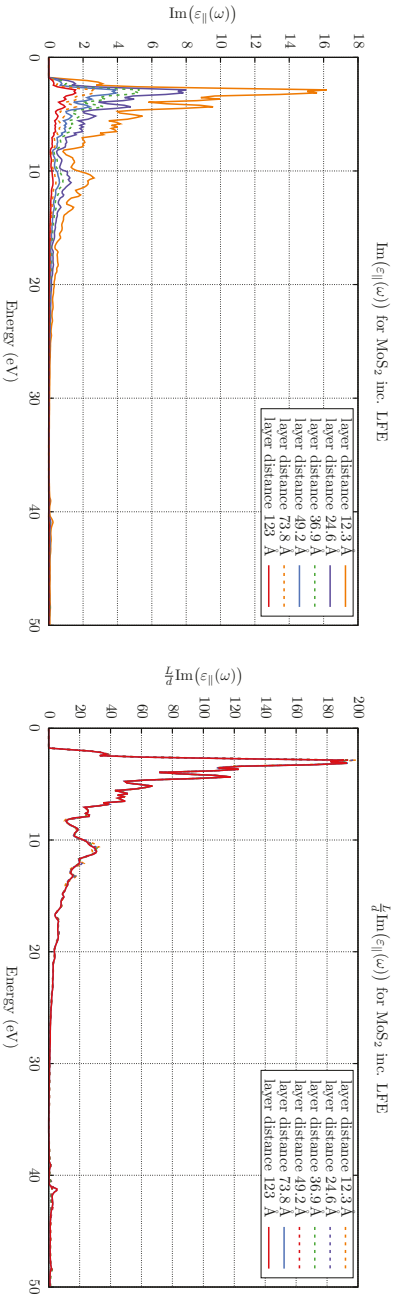
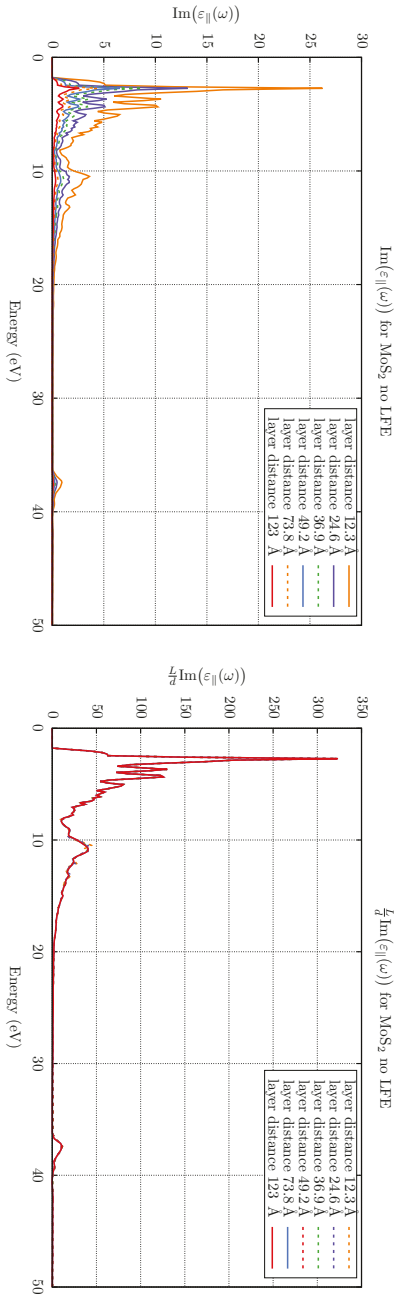


Figure 4.7: Comparison of different layer distances with and without scaling by the vacuum size for MoS₂. Here the **imaginary part of the in-plane component with and without LFE** is shown.

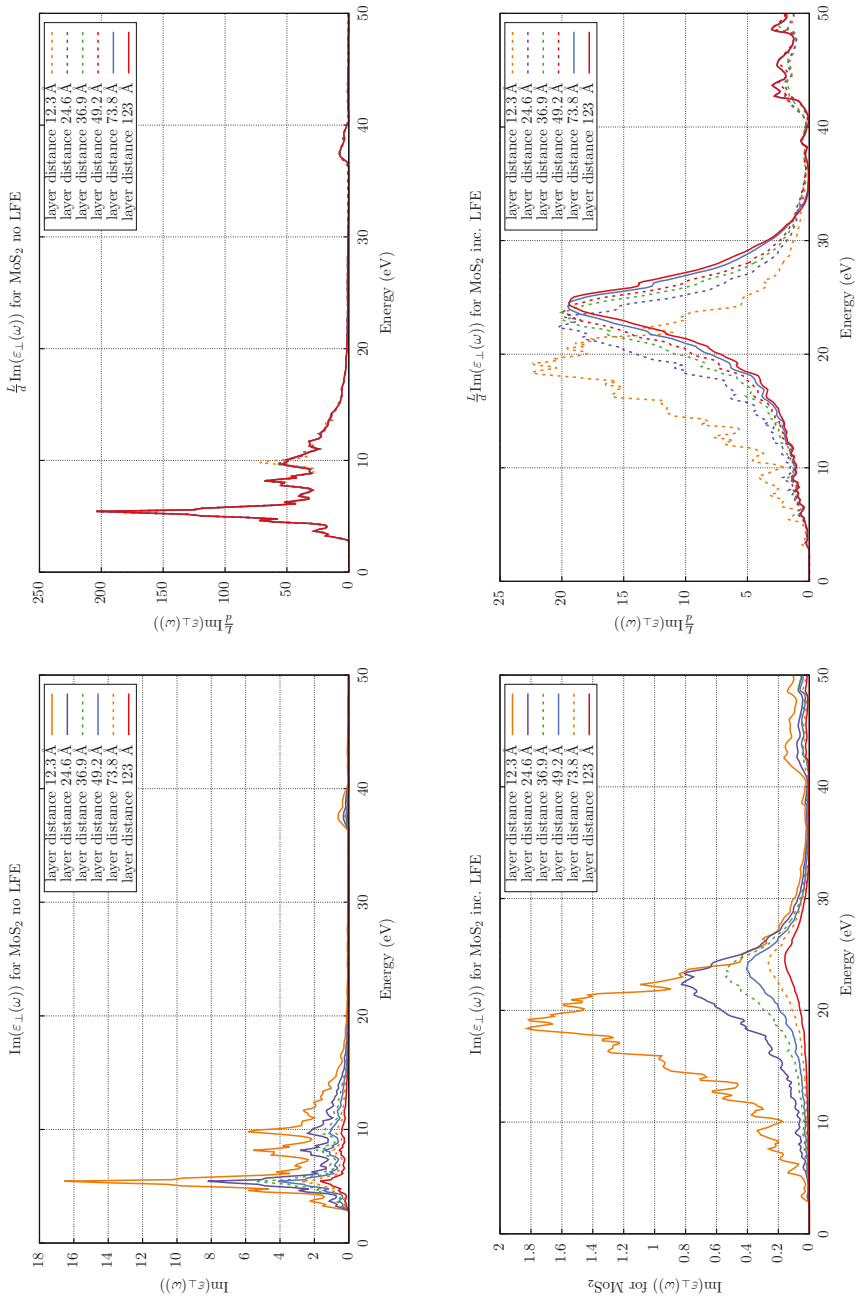


Figure 4.8: Comparison of different layer distances with and without scaling by the vacuum size for MoS₂. Here the **imaginary part** of the **out-of-plane** component with and without LFE is shown.

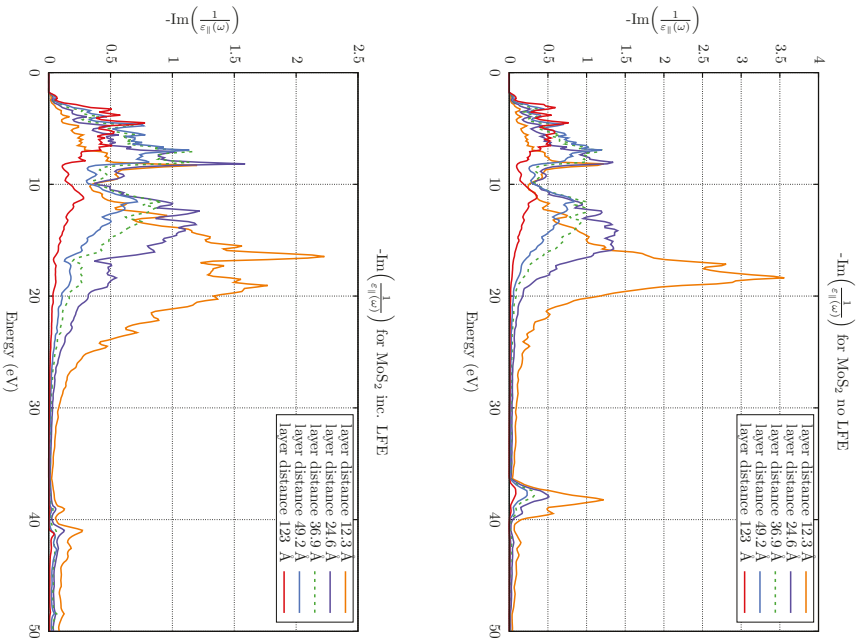


Figure 4.9: Comparison of different layer distances without scaling by the vacuum size for MoS_2 . Here **EELS** for the **in-plane** component with and without LFE is shown.

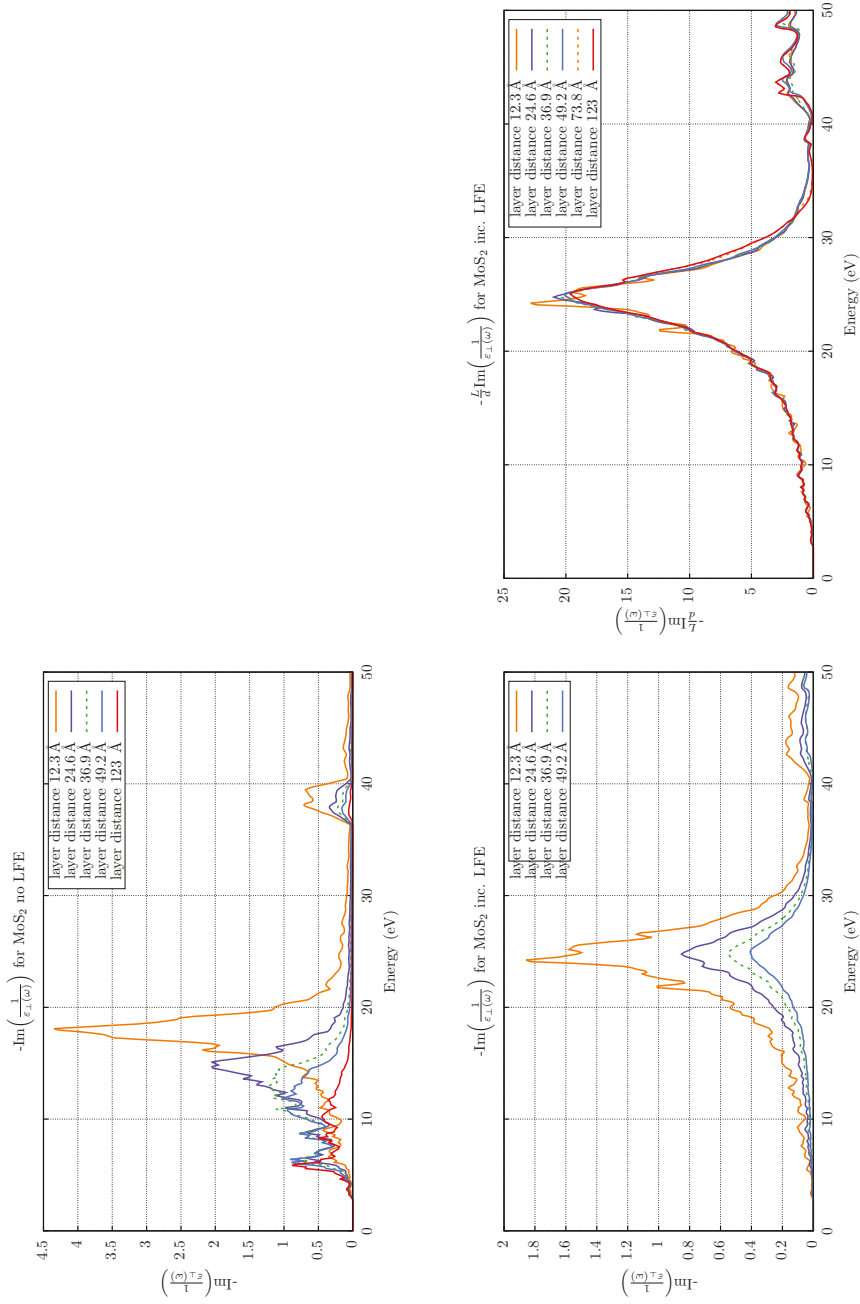


Figure 4.10: Comparison of different layer distances with and without scaling by the vacuum size for MoS₂. Here **EELS** for the **out-of-plane** component with and without LFE is shown.

4.2.4 Classical derivation of the plasma frequency

In Fig. 4.10 the EELS spectrum for the out-of-plane component of the dielectric function (inc. LFE) (MoS₂) shows the main peak around 25 eV. It can be observed that the peak position is independent of the interlayer distance. The similar plot for the in-plane component (Fig. 4.9) shows a completely different behavior. Here, again looking at the physically meaningful case including LFE, the peak position of the first excitation changes depending on the included vacuum. It shifts from around 8 eV for a layer separation of 12.3 Å to around 5 eV for a layer distance of 123 Å.

This shifting of the main excitation can maybe be explained with the shifting of the plasma frequency. Using the values from Tab. 4.1 it is possible to calculate the plasma frequency in the in-plane and in the out-of-plane direction for different layer distances. The results will then be compared to the described observations for the peak positions. The plasma frequency can be derived using only the Poisson equation, the continuity equation and an approximation for only small density changes.

Starting with the Poisson equation, where Φ is the potential, q the charge and ρ the density

$$\Delta\Phi(\mathbf{r}, t) = -q \frac{\rho(\mathbf{r}, t)}{\varepsilon} \quad (4.2.39)$$

and the continuity equation, where \mathbf{j} is the current

$$q \frac{\partial \rho(\mathbf{r}, t)}{\partial t} + \text{div}(\mathbf{j}(\mathbf{r}, t)) = 0 \quad (4.2.40)$$

one can use Newton's laws, where \mathbf{v} is the speed and m the mass,

$$\mathbf{F}(\mathbf{r}, t) = m \frac{\partial \mathbf{v}(\mathbf{r}, t)}{\partial t} \quad (4.2.41)$$

expressing the force via the electric field $\mathbf{E}(\mathbf{r}, t)$,

$$\mathbf{F}(\mathbf{r}, t) = q\mathbf{E}(\mathbf{r}, t) = -q \cdot \text{grad}(\Phi(\mathbf{r}, t)) \quad (4.2.42)$$

to substitute the expression for the current. Thereby the differential equation for a harmonic oscillator is found.

$$\mathbf{j}(\mathbf{r}, t) = q \cdot \rho(\mathbf{r}, t)\mathbf{v}(\mathbf{r}, t) \quad (4.2.43)$$

For small density changes this can be approximated to

$$\mathbf{j}(\mathbf{r}, t) \approx q \cdot \rho_0 \mathbf{v}(\mathbf{r}, t) \quad (4.2.44)$$

deriving the whole equation by time allows for substitution into Newton's law.

$$\frac{1}{q \rho_0} \frac{\partial \mathbf{j}(\mathbf{r}, t)}{\partial t} = \frac{\partial \mathbf{v}(\mathbf{r}, t)}{\partial t} \quad (4.2.45)$$

$$\frac{1}{q \rho_0} \frac{\partial \mathbf{j}(\mathbf{r}, t)}{\partial t} = -\frac{q}{m} \text{grad}(\Phi(\mathbf{r}, t)) \quad (4.2.46)$$

Applying the Nabla operator to both sides allows for substitution of the Poisson Eq. (4.2.39) and the continuity Eq. (4.2.40).

$$\frac{1}{q \rho_0} \frac{\partial \nabla \mathbf{j}(\mathbf{r}, t)}{\partial t} = -\frac{q}{m} \Delta(\Phi(\mathbf{r}, t)) \quad (4.2.47)$$

$$\frac{\partial^2 \rho(\mathbf{r}, t)}{\partial t^2} = -\frac{q^2 \rho_0}{m \varepsilon} \rho(\mathbf{r}, t) \quad (4.2.48)$$

This is a harmonic oscillator with the eigenfrequency ω_p called the plasma frequency.

$$\omega_p^2 = \frac{q^2 \rho_0}{m \varepsilon} \quad (4.2.49)$$

Let us do an estimate for the here studied case of a MoS₂ monolayer, calculated as a slab system. q is the charge of an electron. m is the mass of an electron. The density can be approximated by the amount of valence electrons in the system and the system size (here 12.3 Å layer spacing is used). For the dielectric constant, the in-plane value

of 7.4 can be used (Tab. 4.1).

$$\omega_p^2 = \frac{q^2 \rho_0}{m \varepsilon} = \frac{(1.602 \cdot 10^{-19} \text{C})^2 \cdot 26 \cdot \frac{1}{12.3 \text{Å} \cdot 8.593 \text{Å}^2}}{9.109 \cdot 10^{-31} \text{kg} \cdot 8.854 \cdot 10^{-12} \frac{\text{C}}{\text{V m}} \cdot 7.4} \quad (4.2.50)$$

$$\omega_p = 1.02 \cdot 10^{16} \frac{1}{\text{s}} \quad (4.2.51)$$

This is equivalent to an energy of 6.77 eV. For a layer distance of 123 Å this is a little different. With a dielectric constant of 1.63 and a lower electron density, the energy corresponding to the plasma frequency is at 4.56 eV. This shift roughly corresponds to the observed shift of the first excitation in Fig. 4.9. For the out-of-plane direction the same procedure cannot be applied because the slab structure prevents a hopping of electrons from one layer to another. Therefore, the structure cannot be seen as an overall system (as for the in-plane case) but rather as an individual layer. Consequently, the plasma frequency should be independent of the layer distance. Exactly this can be observed in Fig. 4.10 (inc. LFE), showing the same peak position for all layer distances. Only the peak height is scaled depending on the included vacuum. Using the results from Tab. 4.1 one finds a dielectric constant of 1.68 (12.3 Å) for the out-of-plane case. This corresponds to a plasma frequency of 14.2 eV, which does not exactly match the before shown plot, but nevertheless is in the same order of magnitude.

4.3 Calculating EELS spectra for 2D systems

The aim of the following section is to describe the electron energy loss function including the momentum dependence and compare it to experimentally measured spectra. The understanding gained in the layer model will help with a correct understanding of the results. First, a formal derivation for the response function in a 2D system will be presented followed by a method for extrapolating to infinite layer distance (a true monolayer) based on the ideas for a 2D response function. The main aim is to cancel all interlayer interactions and effects due to the supercell construction.

4.3.1 Treatment of vacuum in supercell calculations

The effect of an increasing amount of vacuum in one unit cell for an increasing interlayer distance has to be corrected. Otherwise, the observables of the material would become smaller the larger the distance between the layers L is chosen.

As a brief reminder before going through the full derivation, the dependence between

the physical quantities and the included vacuum will be repeated. In the thesis of Ralf Hambach [47] it was formulated in the following way. d is the effective material thickness, one possibility to determine it is using layer model (Sec. 4.2).

$$\chi(\mathbf{q}, \mathbf{q}') \propto \Omega^{-1} \quad P(\mathbf{q}, \mathbf{q}') \propto \Omega^{-1} \quad \Omega \propto L/d \quad (4.3.1)$$

Energy loss function for large supercells

The energy loss in the material is described in a simplified way by (real space representation of Eq. (4.1.18)):

$$L(\mathbf{r}, \mathbf{r}', \omega) \propto -\text{Im} \left(\frac{1}{\varepsilon(\mathbf{r}, \mathbf{r}', \omega)} \right) \quad (4.3.2)$$

In the framework of *GW* the screened interaction W and dielectric functions ε are formulated as the following (here matrix notation is used for better readability, so $\varepsilon(\mathbf{r}, \mathbf{r}', \omega)$ is written as $\varepsilon(\omega)$) [12, 51]. $\mathbf{1}$ is to be understood as the identity matrix where necessary.

$$\varepsilon(\omega) = \mathbf{1} - \mathbf{vP}(\omega) \quad (4.3.3)$$

\mathbf{v} denotes the Coulomb interaction $v(\mathbf{r}, \mathbf{r}') = \frac{1}{|\mathbf{r}-\mathbf{r}'|}$ and \mathbf{P} the polarization function. The connection between the polarization function and the independent-particle polarizability χ^0 is given by $P = \chi^0 + \chi^0 f_{XC} P$, where f_{XC} is the exchange-correlation kernel [47] (p. 42). For RPA $f_{XC} = 0$ is true, therefore $P = \chi^0$.

$$\mathbf{W}(\omega) = \mathbf{v} + \mathbf{vP}(\omega)\mathbf{W}(\omega) \quad (4.3.4)$$

$$\mathbf{W}(\omega) = \varepsilon^{-1}(\omega)\mathbf{v} \quad (4.3.5)$$

Here ε^{-1} means the inverse of ε , this can be calculated using the Neumann series ($(\mathbf{1} - A)^{-1} = \sum_{k=0}^{\infty} A^k$ (within the convergence radius)) but also by combining Eq. (4.3.4) and 4.3.5:

$$\varepsilon^{-1}(\omega) = \mathbf{1} + \mathbf{vP}(\omega) + \mathbf{vP}(\omega)\mathbf{vP}(\omega) + \dots \quad (4.3.6)$$

This means the following statement can be made for the energy loss function, including local field effects:

$$-\text{Im}(\varepsilon^{-1}(\omega)) = -\text{Im}(1 + \mathbf{vP}(\omega) + \mathbf{vP}(\omega)\mathbf{vP}(\omega) + \dots) \quad (4.3.7)$$

$$= -\text{Im}(\mathbf{vP}(\omega) + \mathbf{vP}(\omega)\mathbf{vP}(\omega) + \dots) \quad (4.3.8)$$

The polarization function is inversely proportional to the size of the supercell [47]. Therefore, when scaling the loss function by the volume of the supercell and increasing the vacuum to infinity, higher terms can be neglected giving:

$$-\text{Im}(\varepsilon^{-1}(\omega)) \xrightarrow{\Omega \rightarrow \infty} -\text{Im}(\mathbf{vP}(\omega)) = \text{Im}(\varepsilon(\omega)) \quad (4.3.9)$$

This implies that one can use $-\text{Im}(\varepsilon^{-1}(\omega))$ or $\text{Im}(\varepsilon(\omega))$, given that the spectrum is converged. The layer distances needed to achieve a converged result can be very different for the loss ($-\text{Im}(\varepsilon^{-1}(\omega))$) and the absorption spectrum ($\text{Im}(\varepsilon(\omega))$). Therefore, it is helpful to use whichever one converges faster.

4.3.2 Material response in quasi 2D crystals

Calculating material response for quasi 2D crystals is very different compared to the continuous bulk crystal. Using the common techniques to evaluate the whole supercell (slab system including vacuum) leads to a wrong interpretation of the monolayer, since the additional vacuum and interlayer interaction of the slab system (supercell) should not be included in the true monolayer. Therefore, the results for the slab system without additional adjustment do not allow for precise predictions and comparisons to the experiment (that uses a monolayer). This derivation follows the work done by V. Nazarov [52] and shows a way to obtain the response of the monolayer system from the response of the slab system.

The induced charge due to an external field can be written as:

$$\rho(\mathbf{r}, \omega) = \int \chi(\mathbf{r}, \mathbf{r}', \omega) \Phi^{\text{ext}}(\mathbf{r}', \omega) d\mathbf{r}' \quad (4.3.10)$$

The induced potential, due to a charge density, is defined as follows:

$$\Phi^{\text{ind}}(\mathbf{r}, \omega) = \int_{\mathbb{R}^3} \frac{\rho(\mathbf{r}', \omega)}{|\mathbf{r} - \mathbf{r}'|} d^3r' \quad (4.3.11)$$

For the 2D case and for the 3D case the Fourier transformation can be performed to find the according expression in reciprocal space.

$$3\text{D: } \Phi_{\mathbf{G}_{\parallel}}^{\text{ind}}(\mathbf{q}, \omega) = \frac{4\pi}{|\mathbf{q} + \mathbf{G}|^2} \rho_{\mathbf{G}}(\mathbf{q}, \omega) \quad 2\text{D: } \Phi_{\mathbf{G}_{\parallel}}^{\text{ind}}(\mathbf{q}, \omega) = \frac{2\pi}{|\mathbf{q} + \mathbf{G}|} \rho_{\mathbf{G}}(\mathbf{q}, \omega) \quad (4.3.12)$$

Using cylindrical coordinates this can be rewritten using \mathbf{r} as 2D in-plane coordinate, with the aim to find a mixed real space and reciprocal space representation:

$$\Phi^{\text{ind}}(\mathbf{r}, z, \omega) = \int_{\mathbb{R}^2} \int_{-\infty}^{\infty} \frac{\rho(\mathbf{r}', z', \omega)}{\sqrt{(z - z')^2 + (\mathbf{r} - \mathbf{r}')^2}} dz' d^2 r' \quad (4.3.13)$$

Performing the 2D Fourier transformation only in-plane ($e^{-i\mathbf{k}_{\parallel}\mathbf{r}d^2r}$) leads to the following result:

$$\Phi^{\text{ind}}(\mathbf{k}_{\parallel}, z, \omega) = \int_{\mathbb{R}^2} \int_{\mathbb{R}^2} \int_{-\infty}^{\infty} \frac{\rho(\mathbf{r}', z', \omega)}{\sqrt{(z - z')^2 + (\mathbf{r} - \mathbf{r}')^2}} dz' d^2 r' e^{-i\mathbf{k}_{\parallel}\mathbf{r}d^2r} \quad (4.3.14)$$

Substituting $\mathbf{r} - \mathbf{r}' = \mathbf{y}$ and $d^2r = d^2y$ leads to:

$$\Phi^{\text{ind}}(\mathbf{k}_{\parallel}, z, \omega) = \int_{\mathbb{R}^2} \int_{\mathbb{R}^2} \int_{-\infty}^{\infty} \frac{\rho(\mathbf{r}', z', \omega)}{\sqrt{(z - z')^2 + (\mathbf{y})^2}} e^{-i\mathbf{k}_{\parallel}(\mathbf{y}+\mathbf{r}')} dz' d^2 r' d^2 y \quad (4.3.15)$$

The integration can now be split up into a part for \mathbf{r}' and one for \mathbf{y} :

$$\Phi^{\text{ind}}(\mathbf{k}_{\parallel}, z, \omega) = \int_{-\infty}^{\infty} \int_{\mathbb{R}^2} \rho(\mathbf{r}', z', \omega) e^{-i\mathbf{k}_{\parallel}\mathbf{r}'} d^2 r' \cdot \int_{\mathbb{R}^2} \frac{e^{-i\mathbf{k}_{\parallel}\mathbf{y}}}{\sqrt{(z - z')^2 + (\mathbf{y})^2}} d^2 y dz' \quad (4.3.16)$$

In each integral, the coordinate system is changed to polar coordinates, with \mathbf{r} and θ being the angle between \mathbf{k}_{\parallel} and \mathbf{r}' (\mathbf{k}_{\parallel} and \mathbf{y}). In the local density ($\rho(\mathbf{r}', z', \omega)$), the vector \mathbf{r}' is left unchanged, even though it could also be formulated in polar coordinates.

$$\begin{aligned} \Phi^{\text{ind}}(\mathbf{k}_{\parallel}, z, \omega) = & \int_{-\infty}^{\infty} \int_0^{2\pi} \int_0^{\infty} \rho(\mathbf{r}', z', \omega) e^{-i|\mathbf{k}_{\parallel}|r_1 \cos(\theta_1)} r_1 dr_1 d\theta_1 \\ & \cdot \int_0^{2\pi} \int_0^{\infty} \frac{e^{-i|\mathbf{k}_{\parallel}|r_2 \cos(\theta_2)}}{\sqrt{(z - z')^2 + (r_2)^2}} r_2 dr_2 d\theta_2 dz' \end{aligned} \quad (4.3.17)$$

The first integral is the Fourier transformed density. The second integral can be solved using the first order Bessel function $J_0(x) = \frac{1}{2\pi} \int_{-\pi}^{\pi} e^{ix \sin(\phi)} d\phi = \frac{1}{2\pi} \int_0^{2\pi} e^{-ix \cos(\phi)} d\phi$.

$$\Phi^{\text{ind}}(\mathbf{k}_{\parallel}, z, \omega) = \int_{-\infty}^{\infty} \rho(\mathbf{k}_{\parallel}, z', \omega) \cdot \int_0^{\infty} \frac{2\pi J_0(|\mathbf{k}_{\parallel}|r_2)}{\sqrt{(z-z')^2 + (r_2)^2}} r_2 dr_2 dz' \quad (4.3.18)$$

Substituting $r = |\mathbf{k}_{\parallel}|r_2$ and therefore $dr_2 = \frac{dr}{|\mathbf{k}_{\parallel}|}$ leads to:

$$\Phi^{\text{ind}}(\mathbf{k}_{\parallel}, z, \omega) = \int_{-\infty}^{\infty} \rho(\mathbf{k}_{\parallel}, z', \omega) \cdot \int_0^{\infty} \frac{2\pi J_0(r)}{\sqrt{(z-z')^2 + |\mathbf{k}_{\parallel}|^2 + (r)^2}} \frac{r}{|\mathbf{k}_{\parallel}|} dr dz' \quad (4.3.19)$$

Solving the integral and replacing \mathbf{k}_{\parallel} with $\mathbf{G}_{\parallel} + \mathbf{q}_{\parallel}$, to adjust the situation to a crystal with translation symmetry, leads to:

$$\Phi_{\mathbf{G}_{\parallel}}^{\text{ind}}(\mathbf{q}_{\parallel}, z, \omega) = \int_{-\infty}^{\infty} \rho_{\mathbf{G}_{\parallel}}(\mathbf{q}_{\parallel}, z', \omega) \frac{2\pi}{|\mathbf{G}_{\parallel} + \mathbf{q}_{\parallel}|} e^{-|z-z'|\|\mathbf{G}_{\parallel} + \mathbf{q}_{\parallel}\|} dz' \quad (4.3.20)$$

In the calculation, a stack of layers is used with layer distance d , as seen in Fig. 4.11,

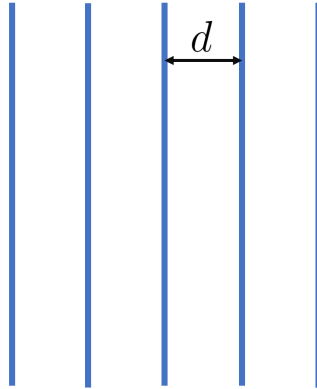


Figure 4.11: Infinite stack of layers with distance d used in a slab system.

so that in the following it is possible to differentiate between the density response of the whole system to an external field $\tilde{\chi}$ and the density response of only one layer to the external field χ . The latter one is a mixture of the response to the external field and the induced field of the other layers in the stack that act onto one layer.

The result in Eq. (4.3.20) can be rewritten as a sum over an infinite stack of layers (indexed m) with distance d .

$$\Phi_{\mathbf{G}_{\parallel}}^{\text{ind}}(\mathbf{q}_{\parallel}, z, \omega) = \frac{2\pi}{|\mathbf{G}_{\parallel} + \mathbf{q}_{\parallel}|} \sum_m \int_{-d/2}^{d/2} \rho_{\mathbf{G}_{\parallel}}(\mathbf{q}_{\parallel}, z', \omega) e^{-|z-z'-md||\mathbf{G}_{\parallel} + \mathbf{q}_{\parallel}|} dz' \quad (4.3.21)$$

The effective field acting on one layer is the combination of the external field with the induced field of all other layers. Therefore, the $m = 0$ contribution of the induced field has to be left out.

$$\Phi_{\mathbf{G}_{\parallel}}^{\text{eff}}(\mathbf{q}_{\parallel}, z, \omega) = \Phi_{\mathbf{G}_{\parallel}}^{\text{ext}}(\mathbf{q}_{\parallel}, z, \omega) + \frac{2\pi}{|\mathbf{G}_{\parallel} + \mathbf{q}_{\parallel}|} \sum_{m \neq 0} \int_{-d/2}^{d/2} \rho_{\mathbf{G}_{\parallel}}(\mathbf{q}_{\parallel}, z', \omega) e^{-|z-z'-md||\mathbf{G}_{\parallel} + \mathbf{q}_{\parallel}|} dz' \quad (4.3.22)$$

For this consideration z is confined to $\frac{d}{2} > z > -\frac{d}{2}$. Therefore, the sum over m can be split up into a negative part and a positive part which then can be simplified.

$$\begin{aligned} \Phi_{\mathbf{G}_{\parallel}}^{\text{eff}}(\mathbf{q}_{\parallel}, z, \omega) &= \Phi_{\mathbf{G}_{\parallel}}^{\text{ext}}(\mathbf{q}_{\parallel}, z, \omega) + \frac{2\pi}{|\mathbf{G}_{\parallel} + \mathbf{q}_{\parallel}|} \int_{-d/2}^{d/2} \rho_{\mathbf{G}_{\parallel}}(\mathbf{q}_{\parallel}, z', \omega) \\ &\cdot \sum_{m=1}^{\infty} e^{(z-z'-md)|\mathbf{G}_{\parallel} + \mathbf{q}_{\parallel}|} + e^{-(z-z'+md)|\mathbf{G}_{\parallel} + \mathbf{q}_{\parallel}|} dz' \end{aligned} \quad (4.3.23)$$

$$\begin{aligned} \Phi_{\mathbf{G}_{\parallel}}^{\text{eff}}(\mathbf{q}_{\parallel}, z, \omega) &= \Phi_{\mathbf{G}_{\parallel}}^{\text{ext}}(\mathbf{q}_{\parallel}, z, \omega) + \frac{2\pi}{|\mathbf{G}_{\parallel} + \mathbf{q}_{\parallel}|} \int_{-d/2}^{d/2} \rho_{\mathbf{G}_{\parallel}}(\mathbf{q}_{\parallel}, z', \omega) \\ &\cdot \sum_{m=1}^{\infty} e^{-md|\mathbf{G}_{\parallel} + \mathbf{q}_{\parallel}|} \cdot \left(e^{(z-z')|\mathbf{G}_{\parallel} + \mathbf{q}_{\parallel}|} + e^{-(z-z')|\mathbf{G}_{\parallel} + \mathbf{q}_{\parallel}|} \right) dz' \end{aligned} \quad (4.3.24)$$

With the $\cosh(x) = \frac{e^x + e^{-x}}{2}$ and the geometric series $\sum_{m=1}^{\infty} q^m = \frac{q}{q-1}$, this can be simplified to:

$$\begin{aligned} \Phi_{\mathbf{G}_{\parallel}}^{\text{eff}}(\mathbf{q}_{\parallel}, z, \omega) &= \Phi_{\mathbf{G}_{\parallel}}^{\text{ext}}(\mathbf{q}_{\parallel}, z, \omega) + \frac{2\pi}{|\mathbf{G}_{\parallel} + \mathbf{q}_{\parallel}|} \cdot \frac{2}{e^{d|\mathbf{G}_{\parallel} + \mathbf{q}_{\parallel}|} - 1} \\ &\cdot \int_{-d/2}^{d/2} \rho_{\mathbf{G}_{\parallel}}(\mathbf{q}_{\parallel}, z', \omega) \cosh((z-z')|\mathbf{G}_{\parallel} + \mathbf{q}_{\parallel}|) dz' \end{aligned} \quad (4.3.25)$$

Now the Fourier series expansion for cosh in the regime $\frac{d}{2} > z > -\frac{d}{2}$ can be used to find the full 3D reciprocal space representation. The potentials are also replaced by the corresponding Fourier series expansion without renaming [52]

$$\begin{aligned} \sum_{G_z} \Phi_{\mathbf{G}_{\parallel}, G_z}^{\text{eff}}(\mathbf{q}_{\parallel}, \omega) e^{iG_z z} &= \sum_{G_z} \Phi_{\mathbf{G}_{\parallel}, G_z}^{\text{ext}}(\mathbf{q}_{\parallel}, \omega) e^{iG_z z} + \frac{4\pi}{|\mathbf{G}_{\parallel} + \mathbf{q}_{\parallel}|(e^{d|\mathbf{G}_{\parallel} + \mathbf{q}_{\parallel}|} - 1)} \\ &\cdot \int_{-d/2}^{d/2} \sum_{G_{z'}} \rho_{\mathbf{G}_{\parallel}, G_{z'}}(\mathbf{q}_{\parallel}, \omega) e^{iG_{z'} z'} \\ &\sum_{G_z} \sum_{G_{z'}} D_{G_z, G_{z'}}(|\mathbf{G}_{\parallel} + \mathbf{q}_{\parallel}|) e^{iG_z z - iG_{z'} z'} dz' \end{aligned} \quad (4.3.26)$$

where [52]

$$D_{G_z, G_{z'}}(p) = \frac{4(p^2 - G_z G_{z'})}{d^2(p^2 + G_z^2)(p^2 + G_{z'}^2)} \cos\left(\frac{(G_z + G_{z'})d}{2}\right) \sinh^2\left(\frac{pd}{2}\right) \quad (4.3.27)$$

The sum and integral can be exchanged and summarized. When doing so, one summation has to be renamed to $G_{z'}$:

$$\begin{aligned} \sum_{G_z} \Phi_{\mathbf{G}_{\parallel}, G_z}^{\text{eff}}(\mathbf{q}_{\parallel}, \omega) e^{iG_z z} &= \sum_{G_z} \Phi_{\mathbf{G}_{\parallel}, G_z}^{\text{ext}}(\mathbf{q}_{\parallel}, \omega) e^{iG_z z} + \frac{4\pi}{|\mathbf{G}_{\parallel} + \mathbf{q}_{\parallel}|(e^{d|\mathbf{G}_{\parallel} + \mathbf{q}_{\parallel}|} - 1)} \\ &\cdot \sum_{G_{z'}} \sum_{G_z} \sum_{G_{z'}} \rho_{\mathbf{G}_{\parallel}, G_{z'}}(\mathbf{q}_{\parallel}, \omega) D_{G_z, G_{z'}}(|\mathbf{G}_{\parallel} + \mathbf{q}_{\parallel}|) \\ &\int_{-d/2}^{d/2} e^{iG_{z'} z'} e^{iG_z z - iG_{z'} z'} dz' \end{aligned} \quad (4.3.28)$$

Solving the integral gives $d \cdot \delta_{G_{z'}, G_{z'}}$. Therefore, one sum can be neglected.

$$\begin{aligned} \sum_{G_z} \Phi_{\mathbf{G}_{\parallel}, G_z}^{\text{eff}}(\mathbf{q}_{\parallel}, \omega) e^{iG_z z} &= \sum_{G_z} \Phi_{\mathbf{G}_{\parallel}, G_z}^{\text{ext}}(\mathbf{q}_{\parallel}, \omega) e^{iG_z z} + \frac{4\pi d}{|\mathbf{G}_{\parallel} + \mathbf{q}_{\parallel}|(e^{d|\mathbf{G}_{\parallel} + \mathbf{q}_{\parallel}|} - 1)} \\ &\cdot \sum_{G_z} \sum_{G_{z'}} \rho_{\mathbf{G}_{\parallel}, G_{z'}}(\mathbf{q}_{\parallel}, \omega) D_{G_z, G_{z'}}(|\mathbf{G}_{\parallel} + \mathbf{q}_{\parallel}|) e^{iG_z z} \end{aligned} \quad (4.3.29)$$

Due to the orthogonality of the plane wave basis, comparing the sum is equivalent to comparing the components. This leaves us with the following expression in 3D reciprocal space.

$$\Phi_{\mathbf{G}_{\parallel}, G_z}^{\text{eff}}(\mathbf{q}_{\parallel}, \omega) = \Phi_{\mathbf{G}_{\parallel}, G_z}^{\text{ext}}(\mathbf{q}_{\parallel}, \omega) + \sum_{G_{z'}} \frac{4\pi d \rho_{\mathbf{G}_{\parallel}, G_{z'}}(\mathbf{q}_{\parallel}, \omega) D_{G_z, G_{z'}}(|\mathbf{G}_{\parallel} + \mathbf{q}_{\parallel}|)}{|\mathbf{G}_{\parallel} + \mathbf{q}_{\parallel}| (e^{d|\mathbf{G}_{\parallel} + \mathbf{q}_{\parallel}|} - 1)} \quad (4.3.30)$$

The density-response function of just one slab, taking into account the induced field from all other slabs, is given by:

$$\rho_{\mathbf{G}}(\mathbf{q}_{\parallel}, \omega) = \sum_{\mathbf{G}'} \chi_{\mathbf{G}, \mathbf{G}'}(\mathbf{q}_{\parallel}, \omega) \Phi_{\mathbf{G}'}^{\text{eff}}(\mathbf{q}_{\parallel}, \omega) \quad (4.3.31)$$

The density-response function of the whole stacked system, as calculated, on the other hand is defined as:

$$\rho_{\mathbf{G}}(\mathbf{q}_{\parallel}, \omega) = \sum_{\mathbf{G}'} \tilde{\chi}_{\mathbf{G}, \mathbf{G}'}(\mathbf{q}_{\parallel}, \omega) \Phi_{\mathbf{G}'}^{\text{ext}}(\mathbf{q}_{\parallel}, \omega) \quad (4.3.32)$$

Since the density change for both formulations is the same, one can relate the two different density-response functions to one another.

$$\begin{aligned} \sum_{\mathbf{G}'} \tilde{\chi}_{\mathbf{G}, \mathbf{G}'}(\mathbf{q}_{\parallel}, \omega) \Phi_{\mathbf{G}'}^{\text{ext}}(\mathbf{q}_{\parallel}, \omega) &= \sum_{\mathbf{G}'} \chi_{\mathbf{G}, \mathbf{G}'}(\mathbf{q}_{\parallel}, \omega) \\ &\cdot \left(\Phi_{\mathbf{G}'}^{\text{ext}}(\mathbf{q}_{\parallel}, \omega) + \sum_{G_{z'}} \frac{4\pi d \rho_{\mathbf{G}'_{\parallel}, G_{z'}}(\mathbf{q}_{\parallel}, \omega) D_{G_{z'}, G_{z'}}(|\mathbf{G}'_{\parallel} + \mathbf{q}_{\parallel}|)}{|\mathbf{G}'_{\parallel} + \mathbf{q}_{\parallel}| (e^{d|\mathbf{G}'_{\parallel} + \mathbf{q}_{\parallel}|} - 1)} \right) \end{aligned} \quad (4.3.33)$$

The density included in the induced potential can be replaced by the response to the external field (Eq. (4.3.32)). $\rho_{\mathbf{G}'_{\parallel}, G_{z'}}(\mathbf{q}_{\parallel}, \omega) = \sum_{\mathbf{G}''} \tilde{\chi}_{\mathbf{G}'_{\parallel}, G_{z'}, \mathbf{G}''}(\mathbf{q}_{\parallel}, \omega) \Phi_{\mathbf{G}''}^{\text{ext}}(\mathbf{q}_{\parallel}, \omega)$

$$\begin{aligned} \sum_{\mathbf{G}'} \tilde{\chi}_{\mathbf{G}, \mathbf{G}'}(\mathbf{q}_{\parallel}, \omega) \Phi_{\mathbf{G}'}^{\text{ext}}(\mathbf{q}_{\parallel}, \omega) &= \sum_{\mathbf{G}'} \chi_{\mathbf{G}, \mathbf{G}'}(\mathbf{q}_{\parallel}, \omega) \Phi_{\mathbf{G}'}^{\text{ext}}(\mathbf{q}_{\parallel}, \omega) \\ &+ \sum_{\mathbf{G}'} \chi_{\mathbf{G}, \mathbf{G}'}(\mathbf{q}_{\parallel}, \omega) \sum_{G_{z'}} \frac{4\pi d D_{G_{z'}, G_{z'}}(|\mathbf{G}'_{\parallel} + \mathbf{q}_{\parallel}|)}{|\mathbf{G}'_{\parallel} + \mathbf{q}_{\parallel}| (e^{d|\mathbf{G}'_{\parallel} + \mathbf{q}_{\parallel}|} - 1)} \sum_{\mathbf{G}''} \tilde{\chi}_{\mathbf{G}'_{\parallel}, G_{z'}, \mathbf{G}''}(\mathbf{q}_{\parallel}, \omega) \Phi_{\mathbf{G}''}^{\text{ext}}(\mathbf{q}_{\parallel}, \omega) \end{aligned} \quad (4.3.34)$$

Renaming \mathbf{G}'' and \mathbf{G}' as well as reordering the sums helps to get the term in a similar structure.

$$\begin{aligned} \sum_{\mathbf{G}'} \tilde{\chi}_{\mathbf{G},\mathbf{G}'}(\mathbf{q}_{\parallel}, \omega) \Phi_{\mathbf{G}'}^{\text{ext}}(\mathbf{q}_{\parallel}, \omega) &= \sum_{\mathbf{G}'} \chi_{\mathbf{G},\mathbf{G}'}(\mathbf{q}_{\parallel}, \omega) \Phi_{\mathbf{G}'}^{\text{ext}}(\mathbf{q}_{\parallel}, \omega) \\ &+ \sum_{\mathbf{G}'} \sum_{\mathbf{G}''} \sum_{G_z'} \chi_{\mathbf{G},\mathbf{G}''}(\mathbf{q}_{\parallel}, \omega) \frac{4\pi d D_{G_z'', G_z'}(|\mathbf{G}_{\parallel}'' + \mathbf{q}_{\parallel}|)}{|\mathbf{G}_{\parallel}'' + \mathbf{q}_{\parallel}|(e^{d|\mathbf{G}_{\parallel}'' + \mathbf{q}_{\parallel}|} - 1)} \tilde{\chi}_{\mathbf{G}_{\parallel}'', G_z', \mathbf{G}'}(\mathbf{q}_{\parallel}, \omega) \Phi_{\mathbf{G}'}^{\text{ext}}(\mathbf{q}_{\parallel}, \omega) \end{aligned} \quad (4.3.35)$$

Since the external field is fully arbitrary, the equation can be rewritten as:

$$\tilde{\chi}_{\mathbf{G},\mathbf{G}'}(\mathbf{q}_{\parallel}, \omega) = \chi_{\mathbf{G},\mathbf{G}'}(\mathbf{q}_{\parallel}, \omega) + \sum_{\mathbf{G}''} \sum_{G_z'} \chi_{\mathbf{G},\mathbf{G}''}(\mathbf{q}_{\parallel}, \omega) \frac{4\pi d D_{G_z'', G_z'}(|\mathbf{G}_{\parallel}'' + \mathbf{q}_{\parallel}|)}{|\mathbf{G}_{\parallel}'' + \mathbf{q}_{\parallel}|(e^{d|\mathbf{G}_{\parallel}'' + \mathbf{q}_{\parallel}|} - 1)} \tilde{\chi}_{\mathbf{G}_{\parallel}'', G_z', \mathbf{G}'}(\mathbf{q}_{\parallel}, \omega) \quad (4.3.36)$$

In the attempt to express the whole summation as matrix-products, first a new matrix is introduced.

$$\frac{4\pi d D_{G_z'', G_z'}(|\mathbf{G}_{\parallel}'' + \mathbf{q}_{\parallel}|)}{|\mathbf{G}_{\parallel}'' + \mathbf{q}_{\parallel}|(e^{d|\mathbf{G}_{\parallel}'' + \mathbf{q}_{\parallel}|} - 1)} \hat{=} \frac{4\pi d D_{G_z'', G_z''}(|\mathbf{G}_{\parallel}'' + \mathbf{q}_{\parallel}|)}{|\mathbf{G}_{\parallel}'' + \mathbf{q}_{\parallel}|(e^{d|\mathbf{G}_{\parallel}'' + \mathbf{q}_{\parallel}|} - 1)} \delta_{\mathbf{G}_{\parallel}'', \mathbf{G}_{\parallel}''} = C_{\mathbf{G}'', \mathbf{G}''}(\mathbf{q}_{\parallel}) \quad (4.3.37)$$

This allows us to rewrite the sum. Due to $\delta_{\mathbf{G}_{\parallel}'', \mathbf{G}_{\parallel}''}$, the sum can be generalized.

$$\tilde{\chi}_{\mathbf{G},\mathbf{G}'}(\mathbf{q}_{\parallel}, \omega) = \chi_{\mathbf{G},\mathbf{G}'}(\mathbf{q}_{\parallel}, \omega) + \sum_{\mathbf{G}''} \sum_{\mathbf{G}'''} \chi_{\mathbf{G},\mathbf{G}''}(\mathbf{q}_{\parallel}, \omega) C_{\mathbf{G}'', \mathbf{G}'''}(\mathbf{q}_{\parallel}) \tilde{\chi}_{\mathbf{G}'', \mathbf{G}'''}(\mathbf{q}_{\parallel}, \omega) \quad (4.3.38)$$

This is equivalent to the following short form in matrix notation.

$$\tilde{\chi}(\mathbf{q}_{\parallel}, \omega) = \chi(\mathbf{q}_{\parallel}, \omega) + \chi(\mathbf{q}_{\parallel}, \omega) C(\mathbf{q}_{\parallel}) \tilde{\chi}(\mathbf{q}_{\parallel}, \omega) \quad (4.3.39)$$

This can be inverted to find an expression for χ .

$$\tilde{\chi}(\mathbf{q}_{\parallel}, \omega) \left[1 + C(\mathbf{q}_{\parallel}) \tilde{\chi}(\mathbf{q}_{\parallel}, \omega) \right]^{-1} = \chi(\mathbf{q}_{\parallel}, \omega) \quad (4.3.40)$$

With $C_{\mathbf{G},\mathbf{G}'}(\mathbf{q}_{\parallel})$ simplified to:

$$C_{\mathbf{G},\mathbf{G}'}(\mathbf{q}_{\parallel}) = \delta_{\mathbf{G}_{\parallel},\mathbf{G}'_{\parallel}} \frac{((|\mathbf{G}_{\parallel} + \mathbf{q}_{\parallel}|)^2 - G_z G'_z)}{((|\mathbf{G}_{\parallel} + \mathbf{q}_{\parallel}|)^2 + G_z^2)((|\mathbf{G}_{\parallel} + \mathbf{q}_{\parallel}|)^2 + G_z'^2)} \cos\left(\frac{(G_z + G'_z)d}{2}\right) \left(1 - e^{-d(|\mathbf{G}_{\parallel} + \mathbf{q}_{\parallel}|)}\right) \frac{4\pi|\mathbf{G}_{\parallel} + \mathbf{q}_{\parallel}|}{d|\mathbf{G}_{\parallel} + \mathbf{q}_{\parallel}|} \quad (4.3.41)$$

4.3.3 Extrapolating to infinite layer distance

In Sec. 4.3.2, the effects of the repeated slab systems were discussed. In the following derivation, the aim is to extrapolate from the repeated slab system to the monolayer including the effects of momentum transfer. This will allow for a very fast convergence with respect to the interlayer distance in the repeated slab system.

The starting point is Eq. (4.3.20) written for only one layer.

$$\Phi_{\mathbf{G}_{\parallel}}^{\text{intra}}(\mathbf{q}_{\parallel}, z, \omega) = \int_{-d/2}^{d/2} \rho_{\mathbf{G}_{\parallel}}(\mathbf{q}_{\parallel}, z', \omega) \frac{2\pi}{|\mathbf{G}_{\parallel} + \mathbf{q}_{\parallel}|} e^{-|z-z'|\|\mathbf{G}_{\parallel} + \mathbf{q}_{\parallel}\|} dz' \quad (4.3.42)$$

Approximating it for a thin layer ($z - z' \approx 0$) and introducing the average charge per layer $\bar{\rho}_{\mathbf{G}_{\parallel}}(\mathbf{q}_{\parallel}, \omega)$ yields:

$$\approx \int_{-d/2}^{d/2} \rho_{\mathbf{G}_{\parallel}}(\mathbf{q}_{\parallel}, z', \omega) \frac{2\pi}{|\mathbf{G}_{\parallel} + \mathbf{q}_{\parallel}|} dz' \quad (4.3.43)$$

$$= \bar{\rho}_{\mathbf{G}_{\parallel}}(\mathbf{q}_{\parallel}, \omega) \frac{2\pi d}{|\mathbf{G}_{\parallel} + \mathbf{q}_{\parallel}|} \quad (4.3.44)$$

Equation (4.3.22) is used with an additional distinguishment between the layer thickness for integration d and the distance between the layers L .

$$\Phi_{\mathbf{G}_{\parallel}}^{\text{inter}}(\mathbf{q}_{\parallel}, z, \omega) = \frac{2\pi}{|\mathbf{G}_{\parallel} + \mathbf{q}_{\parallel}|} \sum_{m \neq 0} \int_{-d/2}^{d/2} \rho_{\mathbf{G}_{\parallel}}(\mathbf{q}_{\parallel}, z', \omega) e^{-|z-z'-mL|\|\mathbf{G}_{\parallel} + \mathbf{q}_{\parallel}\|} dz' \quad (4.3.45)$$

Equivalent to [Sec. 4.3.2](#), this can be solved ($d < L$) (Eq. (4.3.25)) and also approximated for a thin layer ($z - z' \approx 0$) with an average charge.

$$\Phi_{\mathbf{G}_{\parallel}}^{\text{inter}}(\mathbf{q}_{\parallel}, z, \omega) = \frac{2\pi}{|\mathbf{G}_{\parallel} + \mathbf{q}_{\parallel}|} \cdot \frac{2}{e^{L|\mathbf{G}_{\parallel} + \mathbf{q}_{\parallel}|} - 1} \quad (4.3.46)$$

$$\cdot \int_{-d/2}^{d/2} \rho_{\mathbf{G}_{\parallel}}(\mathbf{q}_{\parallel}, z', \omega) \cosh((z - z')|\mathbf{G}_{\parallel} + \mathbf{q}_{\parallel}|) dz'$$

$$\approx \frac{4\pi}{|\mathbf{G}_{\parallel} + \mathbf{q}_{\parallel}| \cdot (e^{L|\mathbf{G}_{\parallel} + \mathbf{q}_{\parallel}|} - 1)} \cdot \int_{-d/2}^{d/2} \rho_{\mathbf{G}_{\parallel}}(\mathbf{q}_{\parallel}, z', \omega) dz' \quad (4.3.47)$$

$$= \bar{\rho}_{\mathbf{G}_{\parallel}}(\mathbf{q}_{\parallel}, \omega) \frac{4\pi d}{|\mathbf{G}_{\parallel} + \mathbf{q}_{\parallel}| \cdot (e^{L|\mathbf{G}_{\parallel} + \mathbf{q}_{\parallel}|} - 1)} \quad (4.3.48)$$

Using these two simplified equations, the inverse dielectric function can be formulated from the definition:

$$\varepsilon^{-1}(\mathbf{q}_{\parallel}, \omega, L) = \frac{\delta\Phi^{\text{eff}}}{\delta\Phi^{\text{ext}}} \quad (4.3.49)$$

$$= \frac{\delta \left[\Phi_0^{\text{ext}} + \Phi_0^{\text{inter}}(\mathbf{q}_{\parallel}, \omega) + \Phi_0^{\text{intra}}(\mathbf{q}_{\parallel}, \omega) \right]}{\delta\Phi_0^{\text{ext}}} \quad (4.3.50)$$

Here, the $\mathbf{G}_{\parallel} \neq \mathbf{0}$ components are neglected. This corresponds to the assumption of a homogeneous charge distribution within the layer. In perpendicular direction, they are not ignored, since the real space representation was used here. Introducing the averaged renormalized response function $\bar{R}(\mathbf{q}_{\parallel}, \omega, L) = \frac{\delta\bar{\rho}_0(\mathbf{q}_{\parallel}, \omega, L)}{\delta\Phi_0^{\text{ext}}}$ (L dependence explicitly mentioned) leads to:

$$\varepsilon^{-1}(\mathbf{q}_{\parallel}, \omega, L) = 1 + \frac{2\pi d}{|\mathbf{q}_{\parallel}|} \left(1 + \frac{2}{e^{L|\mathbf{q}_{\parallel}|} - 1} \right) \bar{R}(\mathbf{q}_{\parallel}, \omega, L). \quad (4.3.51)$$

The averaged response function \bar{R} can be expressed via the polarization function $\bar{R}(\mathbf{q}_{\parallel}, \omega, L) = \varepsilon^{-1}(\mathbf{q}_{\parallel}, \omega, L)P(\mathbf{q}_{\parallel}, \omega)$. This is a reformulation of Eq. (4.3.6) where $\varepsilon^{-1}(\omega) = 1 + \mathbf{vP}(\omega) + \mathbf{vP}(\omega)\mathbf{vP}(\omega) + \dots = 1 + \mathbf{vR}(\omega)$.

$$\varepsilon^{-1}(\mathbf{q}_{\parallel}, \omega, L) = \left[1 - \frac{2\pi d}{|\mathbf{q}_{\parallel}|} \left(1 + \frac{2}{e^{L|\mathbf{q}_{\parallel}|} - 1} \right) P(\mathbf{q}_{\parallel}, \omega) \right]^{-1} \quad (4.3.52)$$

In RPA the head element of the 3D renormalized response function is calculated ($\varepsilon^{-1}(\omega) = 1 + \mathbf{vR}(\omega)$). This is defined as:

$$\varepsilon_{00}^{-1}(\mathbf{q}_{\parallel}, \omega, L) = 1 + \frac{4\pi}{\mathbf{q}_{\parallel}^2} R_{00}(\mathbf{q}_{\parallel}, \omega, L) \quad (4.3.53)$$

The 3D response function is connected to the response function of the layer by appropriate scaling with the added vacuum. $R_{00}(\mathbf{q}_{\parallel}, \omega, L) = \frac{d}{L} \bar{R}(\mathbf{q}_{\parallel}, \omega, L)$, therefore:

$$\varepsilon_{00}^{-1}(\mathbf{q}_{\parallel}, \omega, L) = 1 + \frac{4\pi}{\mathbf{q}_{\parallel}^2} \frac{d}{L} \bar{R}(\mathbf{q}_{\parallel}, \omega, L) \quad (4.3.54)$$

Using $\bar{R}(\mathbf{q}_{\parallel}, \omega, L) = \varepsilon^{-1}(\mathbf{q}_{\parallel}, \omega, L) P(\mathbf{q}_{\parallel}, \omega)$ and Eq. (4.3.52) this yields:

$$\varepsilon_{00}^{-1}(\mathbf{q}_{\parallel}, \omega, L) = 1 + \frac{4\pi}{\mathbf{q}_{\parallel}^2} \frac{d}{L} \frac{P(\mathbf{q}_{\parallel}, \omega)}{1 - \frac{2\pi d}{|\mathbf{q}_{\parallel}|} \left(1 + \frac{2}{e^{L|\mathbf{q}_{\parallel}|} - 1}\right) P(\mathbf{q}_{\parallel}, \omega)} \quad (4.3.55)$$

The loss function of interest is the L scaled single monolayer limit ($L \rightarrow \infty$) of the bulk loss function.

$$A(\mathbf{q}_{\parallel}, \omega) = - \lim_{L \rightarrow \infty} L \operatorname{Im} (\varepsilon_{00}^{-1}(\mathbf{q}_{\parallel}, \omega, L)) \quad (4.3.56)$$

$$= - \frac{4\pi d}{\mathbf{q}_{\parallel}^2} \operatorname{Im} \left(\frac{P(\mathbf{q}_{\parallel}, \omega)}{1 - \frac{2\pi d}{|\mathbf{q}_{\parallel}|} P(\mathbf{q}_{\parallel}, \omega)} \right) \quad (4.3.57)$$

Replacing $P(\mathbf{q}_{\parallel}, \omega)$ from Eq. (4.3.55) a result only dependent on the calculated loss function can be formulated ($P(\mathbf{q}_{\parallel}, \omega) = \left[\frac{4\pi}{\mathbf{q}_{\parallel}^2} \frac{d}{L} \frac{1}{\varepsilon_{00}^{-1}(\mathbf{q}_{\parallel}, \omega, L) - 1} + \frac{2\pi d}{|\mathbf{q}_{\parallel}|} \left(1 + \frac{2}{e^{L|\mathbf{q}_{\parallel}|} - 1}\right) \right]^{-1}$).

$$A(\mathbf{q}_{\parallel}, \omega) = - \operatorname{Im} \left(\frac{L}{\frac{1}{\varepsilon_{00}^{-1}(\mathbf{q}_{\parallel}, \omega, L) - 1} + \frac{L|\mathbf{q}_{\parallel}|}{e^{L|\mathbf{q}_{\parallel}|} - 1}} \right) \quad (4.3.58)$$

The result is independent of layer thickness d , which is very good, since this parameter is not uniquely defined in the crystal. The limiting cases of this loss function are

$$\lim_{\mathbf{q}_{\parallel} \rightarrow 0} A(\mathbf{q}_{\parallel}, \omega) = L \operatorname{Im} \varepsilon_{00}(\mathbf{q}_{\parallel}, \omega, L) \quad (4.3.59)$$

$$\text{and } \lim_{L \rightarrow \infty} A(\mathbf{q}_{\parallel}, \omega) = -L \operatorname{Im} \varepsilon_{00}^{-1}(\mathbf{q}_{\parallel}, \omega, L) \quad (\mathbf{q}_{\parallel} > 0). \quad (4.3.60)$$

It is most obvious how well this approach works by looking at the very fast convergence of Eq. (4.3.58) with increasing layer distance (Fig. 4.12). The two limiting cases

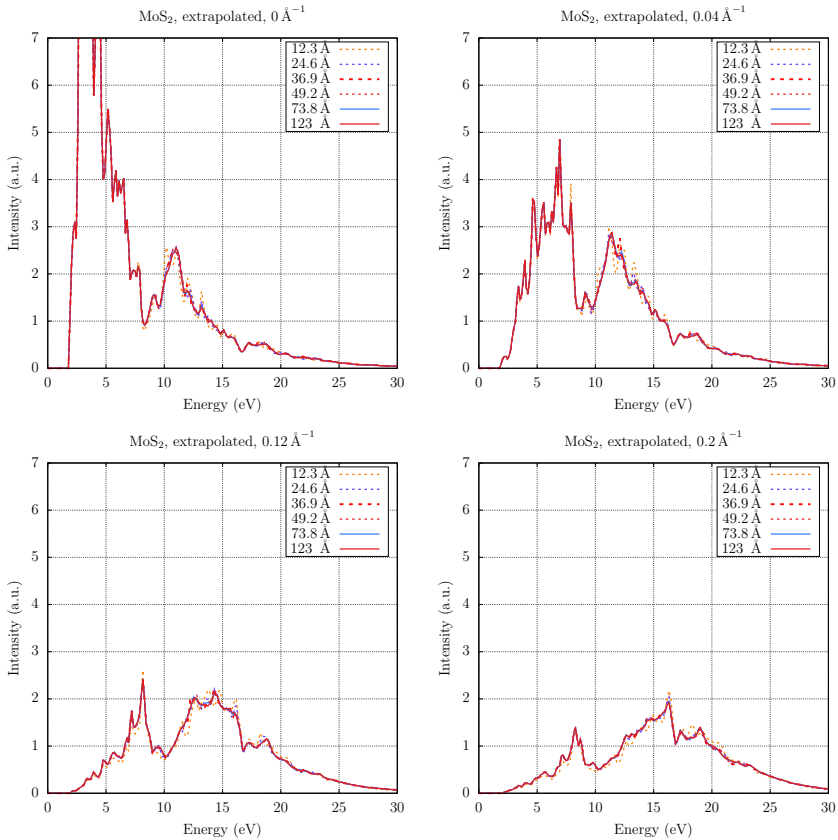


Figure 4.12: Loss function of MoS₂ calculated by extrapolation using Eq. (4.3.58) for different layer distances. A very fast convergence is visible, independent of the momentum transfer (in-plane).

(Eq. (4.3.59) and Eq. (4.3.60)) recover the absorption function ($\text{Im}\varepsilon(\omega)$) and the loss spectrum ($-\text{Im}\frac{1}{\varepsilon(\omega)}$) like it is typically used. This demonstrates nicely that the extrapolated loss function extends the well known way of calculating the loss function. In Fig. 4.13 the convergence of the two limiting cases towards the extrapolated loss function can be observed with increasing layer distance. This behavior has been predicted in Sec. 4.3.1.

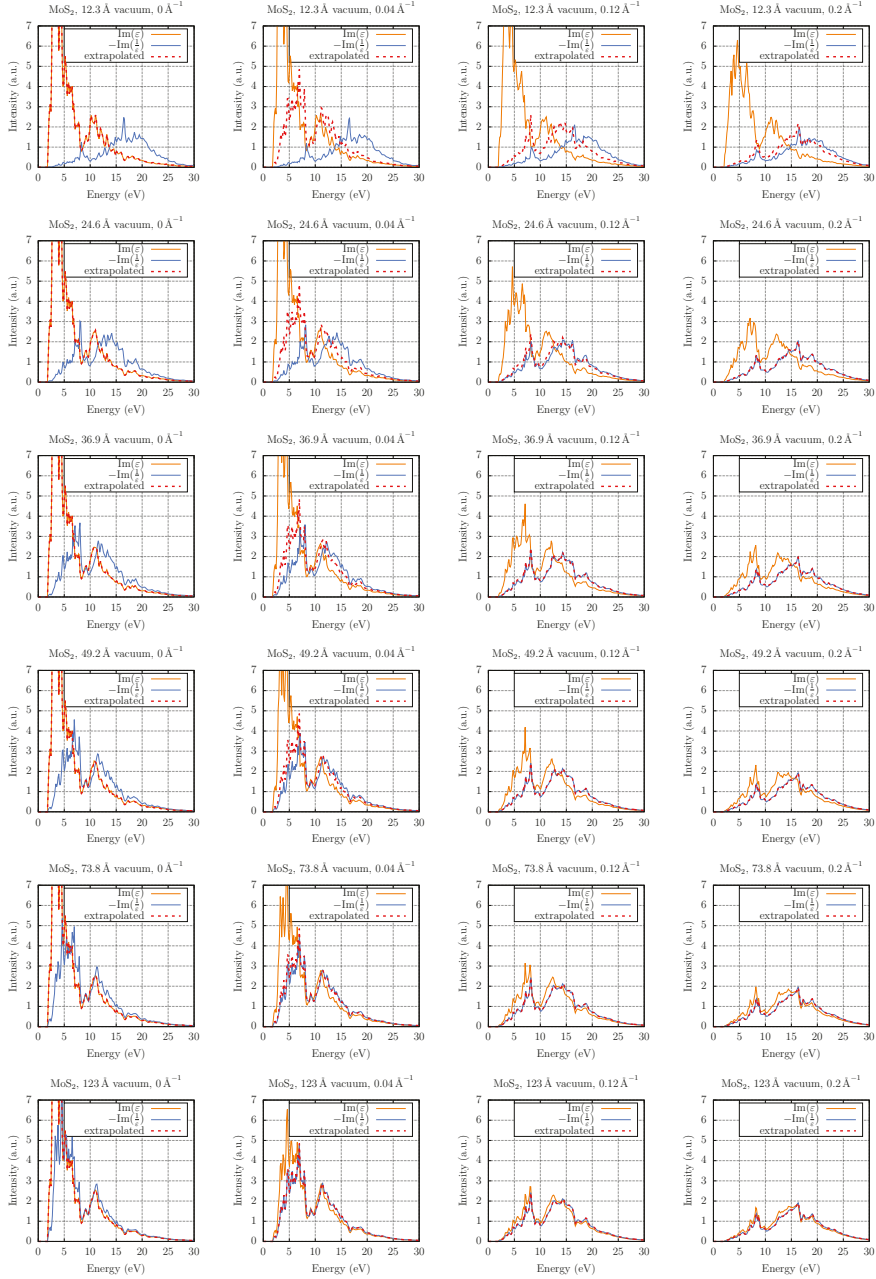


Figure 4.13: Fig. 4.12 shows the explicit convergence of the extrapolated loss function, whereas here the convergence of the the two limiting cases towards the extrapolated loss function with increasing layer distance is shown.

4.4 Momentum dependent EELS

Focusing on the full energy loss equation (Eq. (4.1.18)) there are two momentum dependent terms. The prefactor $\frac{1}{q^2}$ and the dielectric function itself. Fig. 4.14 shows

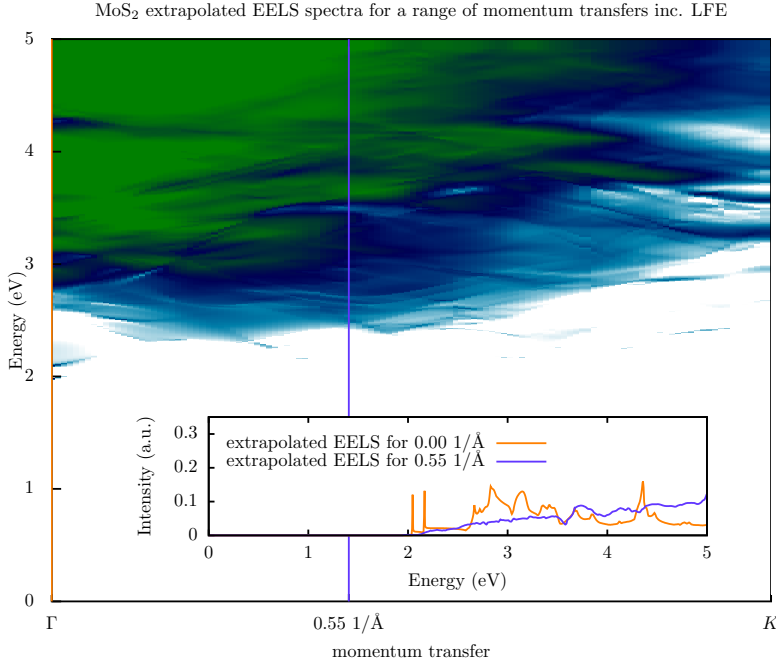


Figure 4.14: Momentum resolved EELS spectra for MoS₂ with a momentum transfer between 0 (Γ) and a momentum transfer of $K = (1/3, 1/3, 0)$. The color darkness (white-blue-green) corresponds to the extrapolated EELS intensity. A layer distance of 24.6 Å is used.

the extrapolated EELS formula Eq. (4.3.58) and its change over different momenta. A clear shift of the main peaks is visible. The following sections are concerned with including the loss function for different momenta in the full energy loss.

In the end, the derived method of including multiple momentum transfers in one spectrum will be combined with the extrapolation method derived in the previous section.

4.4.1 Momentum summation EELS

The treatment of the z -component of the momentum transfer (in the direction of the beam) is interesting and not very intuitive. In reciprocal space, a certain energy loss is connected to one or multiple momentum transfers. In order for the electron to lose energy, the momentum has to be changed (decelerated in the direction of the beam). The electron has a probability to be deflected to a certain angle depending on the momentum transfer occurring. In the classical derivation, it is interesting how starting from a classical starting point one ends up at a possibility distribution (a quantum mechanical concept) (Sec. 4.1). Treating the energy difference along the z -direction allows for all electron excitations with a momentum transfer in the x/y plane of the Brillouin zone (taking into account the dispersion relation of the material) (Eq. (4.1.18)), that itself only contribute marginally to the total energy.

$$\frac{\partial^3 P}{\partial^2 q_{\parallel} \partial \omega} = -\frac{8\pi e^2}{(2\pi)^3 \hbar v^2 \mathbf{q}^2} \text{Im} \frac{1}{\varepsilon(\mathbf{q}, \omega)} \quad (4.4.1)$$

Here the definition of \mathbf{q}_{\parallel} is changed to define parallel as parallel to the plane (for an electron at normal incidence):

$$q^2 = q_{\parallel}^2 + q_z^2 = q_{\parallel}^2 + \left(\frac{\omega}{v}\right)^2 \quad (4.4.2)$$

The momentum in z -direction is calculated by $q_z = \frac{\omega}{v}$ where ω is determined by the energy loss via $E = \hbar\omega$. The speed of the electron has to be calculated in a relativistic way, due to the high energy of the electron. Starting with the total energy $E = m(v) \cdot c^2$ consisting of the kinetic energy E_{kin} and the energy at rest E_0 ($E = E_{\text{kin}} + E_0$), using the relativistic mass of $m(v) = \frac{m_0}{\sqrt{1 - \frac{v^2}{c^2}}}$ one finds the speed. Here c is the speed of light and m_0 the mass at rest.

$$v = c \sqrt{1 - \left(\frac{m_0 c^2}{E_{\text{kin}} + m_0 c^2}\right)^2} \quad (4.4.3)$$

In order to compute the summation, one substitutes the integral by a sum over a finite grid in reciprocal space. This is easily possible by introducing a surface element (dA). The treatment of the Γ point, or to be precise close by since the z -component is not 0, introduces some additional complication, since its weight is very high due to the $\frac{1}{q_{\parallel}^2 + q_z^2}$ prefactor compared to all other points. If the grid is not chosen fine enough, on

the scale of $\frac{\omega}{v}$, the Γ point is not calculated correctly, since it has an extraordinarily high and strongly varying weight that could only be sampled correctly by a very high mesh point density around it. For a typical setup (speed of the electron and energy loss) $\frac{\omega}{v}$ is on the order of 0.00001 1/Bohr, whereas a very small momentum transfer is 0.01 1/Bohr (requiring $100\times$ mesh points in reciprocal space). Therefore, the Γ point should be treated with an integral explicitly. For this approach, the grid for summation has to be fine enough so that the dielectric function between the Γ point and its closest neighbors does not differ significantly. In that case one can assume the dielectric function to be only ω dependent around the Γ point. Thus, the integral can be solved explicitly using polar coordinates. Starting from (4.1.18) the integral can be separated from the sum.

$$\int_{\mathbf{q}'} \frac{4\pi e^2}{(2\pi)^3 \hbar v^2 \mathbf{q}'^2} 2 \operatorname{Im} \frac{1}{\varepsilon(\mathbf{q}', \omega)} d^2 q' \quad (4.4.4)$$

$$\approx \frac{4\pi e^2}{(2\pi)^3 \hbar v^2} \left(\left(\sum_{\mathbf{q}_{\parallel} \neq 0} \frac{1}{\mathbf{q}_{\parallel}^2 + (\frac{\omega}{v})^2} 2 \operatorname{Im} \frac{1}{\varepsilon(\mathbf{q}, \omega)} dA \right) + \int_{q_{\parallel} < q_c} \frac{1}{\mathbf{q}_{\parallel}^2 + (\frac{\omega}{v})^2} 2 \operatorname{Im} \frac{1}{\varepsilon(\mathbf{0}, \omega)} d^2 q_{\parallel} \right) \quad (4.4.5)$$

By introducing polar coordinates (q_{\parallel} and ϕ) and performing the ϕ integration, this can be simplified.

$$= \frac{4\pi e^2}{(2\pi)^3 \hbar v^2} \left(\left(\sum_{\mathbf{q}_{\parallel} \neq 0} \frac{1}{\mathbf{q}_{\parallel}^2 + (\frac{\omega}{v})^2} 2 \operatorname{Im} \frac{1}{\varepsilon(\mathbf{q}, \omega)} dA \right) + 4\pi \operatorname{Im} \frac{1}{\varepsilon(\mathbf{0}, \omega)} \int_0^{|\mathbf{q}_c|} \frac{q_{\parallel}}{q_{\parallel}^2 + (\frac{\omega}{v})^2} dq_{\parallel} \right) \quad (4.4.6)$$

$$= \dots + 2\pi \operatorname{Im} \frac{1}{\varepsilon(\mathbf{0}, \omega)} \left(\ln \left(|\mathbf{q}_c|^2 + \left(\frac{\omega}{v}\right)^2 \right) - \ln \left(\left(\frac{\omega}{v}\right)^2 \right) \right) \quad (4.4.7)$$

q_c has to be chosen depending on the grid. One could think half of the average distance between two grid points would be a reasonable choice, but the correct choice is to make it dependent on the area of the Brillouin zone and total numbers of grid points (evenly spaced grid).

$$\pi \cdot q_c^2 = \frac{|\mathbf{b}_x \times \mathbf{b}_y|}{\text{num}_{\text{qpts}}} \quad (4.4.8)$$

$$q_c = \sqrt{\frac{|\mathbf{b}_x \times \mathbf{b}_y|}{\pi \cdot \text{num}_{\text{qpts}}}} \quad (4.4.9)$$

In the above discussion, ε is always considered to be a single complex number, but, strictly speaking, this is not the case. Especially at the Γ point, where there is no direction given, it is important to consider ε as a tensor quantity. Therefore, the integral should be calculated a little different assuming ε has the entries ε_1 , ε_2 and ε_3 on the diagonal and there are no off-diagonal elements. This means:

$$\varepsilon(\mathbf{0}, \omega) = \begin{pmatrix} \varepsilon_1(\mathbf{0}, \omega) & 0 & 0 \\ 0 & \varepsilon_2(\mathbf{0}, \omega) & 0 \\ 0 & 0 & \varepsilon_3(\mathbf{0}, \omega) \end{pmatrix}$$

$$\frac{4\pi e^2}{(2\pi)^3 \hbar v^2} \left(\left(\sum_{\mathbf{q}_{\parallel} \neq 0} \frac{1}{\mathbf{q}_{\parallel}^2 + (\frac{\omega}{v})^2} 2 \operatorname{Im} \frac{1}{\varepsilon(\mathbf{q}, \omega)} dA \right) + \int_{q_{\parallel} < q_c} \frac{1}{\mathbf{q}_{\parallel}^2 + (\frac{\omega}{v})^2} 2 \operatorname{Im} \frac{1}{\varepsilon(\mathbf{0}, \omega)} d^2 q_{\parallel} \right) \quad (4.4.10)$$

$$= \dots + \int_{q_{\parallel} < q_c} \frac{1}{q_x^2 + q_y^2 + (\frac{\omega}{v})^2} 2 \operatorname{Im} \frac{1}{\frac{1}{q^2} (q_x^2 \varepsilon_1(\mathbf{0}, \omega) + q_y^2 \varepsilon_2(\mathbf{0}, \omega)) + (\frac{\omega}{v})^2 \varepsilon_3(\mathbf{0}, \omega)} dq_x dq_y \quad (4.4.11)$$

$$= \dots + 2 \operatorname{Im} \int_{q_{\parallel} < q_c} \frac{1}{q_x^2 \varepsilon_1(\mathbf{0}, \omega) + q_y^2 \varepsilon_2(\mathbf{0}, \omega) + (\frac{\omega}{v})^2 \varepsilon_3(\mathbf{0}, \omega)} dq_x dq_y \quad (4.4.12)$$

With the assumption $\varepsilon_1 = \varepsilon_2$ the integral can be solved:

$$= \dots + 4\pi \operatorname{Im} \int_0^{|\mathbf{q}_c|} \frac{q_{\parallel}}{q_{\parallel}^2 \varepsilon_1(\mathbf{0}, \omega) + (\frac{\omega}{v})^2 \varepsilon_3(\mathbf{0}, \omega)} dq_{\parallel} \quad (4.4.13)$$

$$= \dots + 2\pi \operatorname{Im} \frac{1}{\varepsilon_1(\mathbf{0}, \omega)} \left(\ln \left(\varepsilon_1(\mathbf{0}, \omega) |\mathbf{q}_c|^2 + \varepsilon_3(\mathbf{0}, \omega) \left(\frac{\omega}{v} \right)^2 \right) - \ln \left(\varepsilon_3(\mathbf{0}, \omega) \left(\frac{\omega}{v} \right)^2 \right) \right) \quad (4.4.14)$$

$$= \dots + 2\pi \operatorname{Im} \frac{1}{\varepsilon_1(\mathbf{0}, \omega)} \left(\ln \left(\frac{\varepsilon_1(\mathbf{0}, \omega) |\mathbf{q}_c|^2}{\varepsilon_3(\mathbf{0}, \omega) \left(\frac{\omega}{v} \right)^2} + 1 \right) \right) \quad (4.4.15)$$

Instead of treating it explicitly, one can also use an approximation around the Γ point $\varepsilon^{-1}(\mathbf{q}) \approx \frac{1}{q^2} \mathbf{q}^T \varepsilon' \mathbf{q}$.

$$\frac{4\pi e^2}{(2\pi)^3 \hbar v^2} \left(\left(\sum_{\mathbf{q}_{\parallel} \neq 0} \frac{1}{q_{\parallel}^2 + (\frac{\omega}{v})^2} 2 \operatorname{Im} \frac{1}{\varepsilon(\mathbf{q}, \omega)} dA \right) + \int_{q_{\parallel} < q_c} \frac{1}{q_{\parallel}^2 + (\frac{\omega}{v})^2} 2 \operatorname{Im} \frac{1}{\varepsilon(\mathbf{0}, \omega)} d^2 q_{\parallel} \right) \quad (4.4.16)$$

$$\approx \dots + \int_{q_{\parallel} < q_c} \frac{1}{q_{\parallel}^2 + (\frac{\omega}{v})^2} 2 \frac{1}{q^2} \operatorname{Im} \mathbf{q}^T \varepsilon'(\mathbf{0}, \omega) \mathbf{q} d^2 q_{\parallel} \quad (4.4.17)$$

$$= \dots + \int_{q_{\parallel} < q_c} \frac{1}{q_x^2 + q_y^2 + (\frac{\omega}{v})^2} 2 \frac{1}{q^2} \operatorname{Im} (q_x^2 \varepsilon'_1(\mathbf{0}, \omega) + q_y^2 \varepsilon'_2(\mathbf{0}, \omega)) + (\frac{\omega}{v})^2 \varepsilon'_3(\mathbf{0}, \omega) dq_x dq_y \quad (4.4.18)$$

$$= \dots + 2 \operatorname{Im} \int_{q_{\parallel} < q_c} \frac{1}{q^4} \left(q_x^2 \varepsilon'_1(\mathbf{0}, \omega) + q_y^2 \varepsilon'_2(\mathbf{0}, \omega) + (\frac{\omega}{v})^2 \varepsilon'_3(\mathbf{0}, \omega) \right) dq_x dq_y \quad (4.4.19)$$

Now introducing polar coordinates and assuming $\varepsilon'_1 = \varepsilon'_2$ gives the following.

$$= \dots + 4\pi \operatorname{Im} \int_0^{q_c} \frac{1}{(q^2 + (\frac{\omega}{v})^2)(q^2 + (\frac{\omega}{v})^2)} \left(q^2 \varepsilon'_1(\mathbf{0}, \omega) + (\frac{\omega}{v})^2 \varepsilon'_3(\mathbf{0}, \omega) \right) q dq \quad (4.4.20)$$

$$= \dots + 4\pi \operatorname{Im} \int_0^{q_c} \frac{q^3 \varepsilon'_1(\mathbf{0}, \omega) + q (\frac{\omega}{v})^2 \varepsilon'_3(\mathbf{0}, \omega)}{q^4 + 2q^2 (\frac{\omega}{v})^2 + (\frac{\omega}{v})^4} dq \quad (4.4.21)$$

This integration can be calculated explicitly, for a simpler notation the dependencies of ε are left out.

$$= \dots + 2\pi \operatorname{Im} \left(\frac{(\frac{\omega}{v})^2 (\varepsilon'_1 - \varepsilon'_3)}{(\frac{\omega}{v})^2 + q_c^2} + \varepsilon'_1 \ln \left((\frac{\omega}{v})^2 + q_c^2 \right) - ((\varepsilon'_1 - \varepsilon'_3) + \varepsilon'_1 \ln \left((\frac{\omega}{v})^2 \right)) \right) \quad (4.4.22)$$

$$= \dots + 2\pi \operatorname{Im} \left(\left(\frac{(\frac{\omega}{v})^2}{(\frac{\omega}{v})^2 + q_c^2} - 1 \right) (\varepsilon'_1 - \varepsilon'_3) + \varepsilon'_1 \ln \left(\frac{(\frac{\omega}{v})^2 + q_c^2}{(\frac{\omega}{v})^2} \right) \right) \quad (4.4.23)$$

With a dimensionless variable $x = \frac{\omega}{q_c v}$, this can be simplified.

$$= \dots + 2\pi \operatorname{Im} \left(\left(\frac{x^2}{x^2 + 1} - 1 \right) (\varepsilon'_1 - \varepsilon'_3) + \varepsilon'_1 \ln \left(\frac{x^2 + 1}{x^2} \right) \right) \quad (4.4.24)$$

$$= \dots + 2\pi \operatorname{Im} \left(\frac{\varepsilon'_3 - \varepsilon'_1}{x^2 + 1} + \varepsilon'_1 \ln \left(\frac{x^2 + 1}{x^2} \right) \right) \quad (4.4.25)$$

Application to monolayers

The above treatment of the prefactor shows how complex it is to handle the Γ point correctly. It was shown before that at the Γ point it is more efficient to use $\text{Im } \varepsilon_{\parallel}$ than $\text{Im } \frac{1}{\varepsilon_{\parallel}}$ because the convergence behavior is significantly faster with increasing layer distance. For the perpendicular component the opposite is true. Here it is best to use $\text{Im } \frac{1}{\varepsilon_{\perp}}$. Equation (4.4.25) already gives the result for a dielectric function of the form $\text{Im } \varepsilon$. Looking at the final result for the Γ point

$$\text{Im} \left(\frac{\varepsilon'_3 - \varepsilon'_1}{x^2 + 1} + \varepsilon'_1 \ln \left(\frac{x^2 + 1}{x^2} \right) \right) \quad (4.4.26)$$

it is possible to analyze this a little further, understanding the factors that have the highest influence.

In Fig. 4.15, the two prefactors for ε'_1 and ε'_3 are shown in terms of x . What is the usual value of x ? For a common setting of fine q -grid sampling ($q_c \approx 10^{-2}$), acceleration voltage of 80 keV and an energy loss of a few electron volts, x is on the order of 10^{-2} . This means, unless looking at a very fine momentum grid or a very high transition energy, ε'_1 dominates the behavior. Furthermore, the plotted prefactor also depends

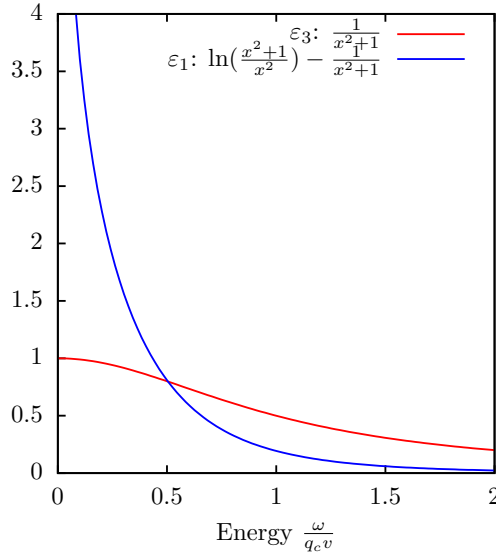


Figure 4.15: Visualization of the prefactor for the in-plane and the out-of-plane component of the dielectric function.

on the mesh density and speed of the electron. With an increasing mesh density the magnitude of the Γ point contribution decreases. For an increasing speed of the electron (acceleration voltage), the contribution of the Γ point increases.

When treating monolayers, the vacuum distance between the layers is a crucial convergence parameter for a correct modeling. Depending on the momentum transfer q a different convergence behavior can be expected. As previously shown for the Γ point, $\text{Im } \varepsilon$ converges by orders of magnitude faster than $\text{Im } \frac{1}{\varepsilon}$, this has also been proven with a simple layer model. But already for small momentum transfers, this is not the case anymore. For large momentum transfers (for instance 0.1 1/Bohr) EELS ($\text{Im } \frac{1}{\varepsilon}$) converges significantly faster than $\text{Im } \varepsilon$. This behavior will be demonstrated using MoS_2 as an example in the following.

As a result of this property, the momentum transfer up to which the energy loss is treated with $\text{Im } \varepsilon$ and from where on $\text{Im } \frac{1}{\varepsilon}$ is used instead has to be carefully chosen. Another possibility is to use a very large layer distance, then most spectra are converged for both. Irrespective of this consideration, the only way to make sure that all spectra are converged is to use the extrapolation scheme (Sec. 4.3.3).

Correct treatment of units

Equation (4.4.25) can be implemented together with the preceding sum. When doing so, special care needs to be taken with the units used. In the ab-initio codes [10], all (reciprocal) length specifications are in terms of the Bohr radius or in internal coordinates, relating to the (reciprocal) lattice vectors. The energy loss is given in eV or Hartree. The speed of the electron is given by the experimental setup in keV (acceleration voltage).

The internal coordinate have to be converted to $\frac{1}{\text{Bohr}}$. Using $\hbar = 6.5821195 \cdot 10^{-16}$ eV·s the energy loss can be converted into an angular frequency by $E = \hbar\omega$ and vice versa. The acceleration voltage has to be converted into the speed of the electron. Due to the very high speed, relativistic corrections need to be taken into account (Eq. (4.4.3)). Using the speed of light c in m/s, $m_0 = m_e$ (in kg) as the rest mass of the electron and E_{kin} as the kinetic energy of the electron in Joule calculated from the acceleration voltage $E_{kin} = \text{acc. voltage(keV)} \cdot \frac{10^3}{1.60218 \cdot 10^{-19}} \frac{\text{J}}{\text{keV}}$.

$$v = c \cdot \left(1 - \left(\frac{m_e \cdot c^2}{E_{kin} + m_e \cdot c^2} \right)^2 \right)^{\frac{1}{2}} \frac{1}{5.29177210903 \cdot 10^{-11} \frac{\text{m}}{\text{Bohr}}} \quad (4.4.27)$$

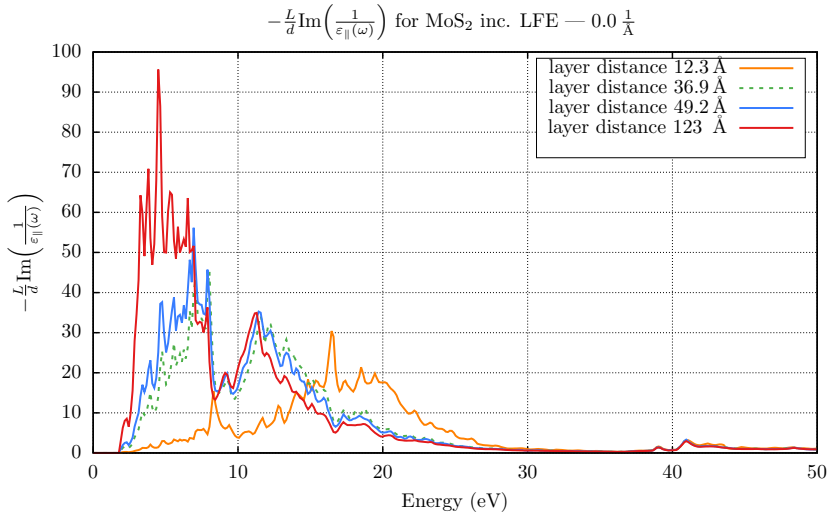
4.4.2 EELS for pristine MoS₂ monolayer with momentum summation

Before showing the summed up spectrum, this section will start with discussing the convergence behavior of the spectra for different momentum transfers, that are included in the summation, with respect to the used vacuum. Without any momentum transfer (Fig. 4.16a and Fig. 4.16b) a fast convergence for the absorption spectrum ($\text{Im } \varepsilon(\omega)$) and a very slow convergence for the loss spectrum (EELS) ($-\text{Im } \frac{1}{\varepsilon(\omega)}$) is found. This has been discussed in detail in Sec. 4.2.3. The two spectra are replotted here for the direct comparison with the spectra for larger momentum transfer. In the simplified layer model (Sec. 4.2), the interaction between the layers is strong due to the long-range Coulomb interaction. For $q \neq 0$ the interlayer interaction becomes weaker, since the charge distribution within one layer screens itself when probed at a distance (like a multipole). If the distance between the layers, corresponding to the unit cell size L , decreases at the same time as q is increased, the total interaction strength does not change. In other words, if the factor $L \cdot q$ does not change, the interaction strength does not change. Therefore, this factor can be used as an indicator for a fast or slow convergence behavior of the loss spectrum. In Fig. 4.17a and Fig. 4.17b, the convergence behavior with a large momentum transfer is shown. The loss function converges very fast with increasing layer distance (Fig. 4.17a). Overall, the criterion for the loss function to be converged is $qL \gg 1$ [47].

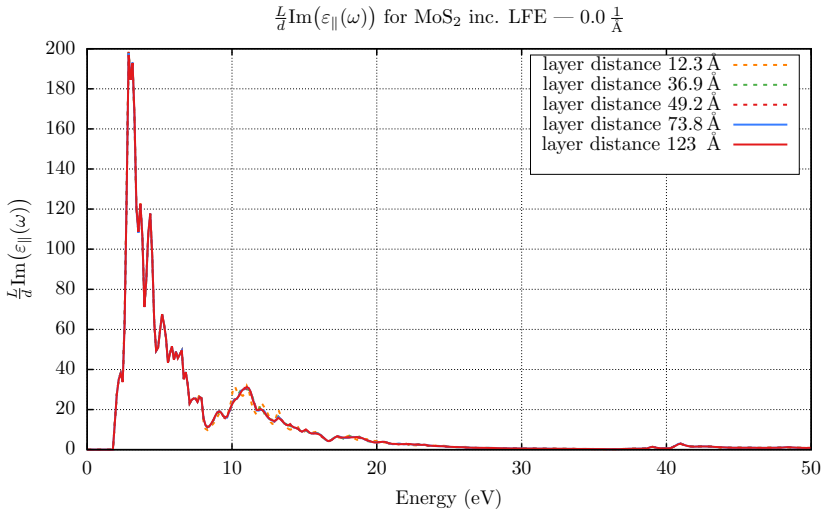
For the absorption spectrum, the opposite is found. It converges very slowly for large momentum transfers. So, the absorption spectrum is converged for $L/q \gg 1$.

In between, neither of the two (absorption spectrum and loss spectrum) is converged. The momentum transfer used in Fig. 4.18a and Fig. 4.18b pictures exactly this case. With increasing layer distance, the spectra in Fig. 4.18a and Fig. 4.18b converge towards the same spectrum. This behavior, predicted in Sec. 4.3.1, is also partly visible for the spectra without momentum transfer and with large momentum transfer. The layer distance required to achieve convergence in these cases is impossible to compute, due to the supercell size, but the direction of the convergence is visible with the here used layer distances.

This finding underlines the fact that for a monolayer either of the two (absorption spectrum or loss spectrum) describes the correct energy loss, if the layer distance is chosen large enough for the spectrum to be converged (Sec. 4.3.1). For completeness the convergence behavior with and without LFE can be found in Sec. D.2.

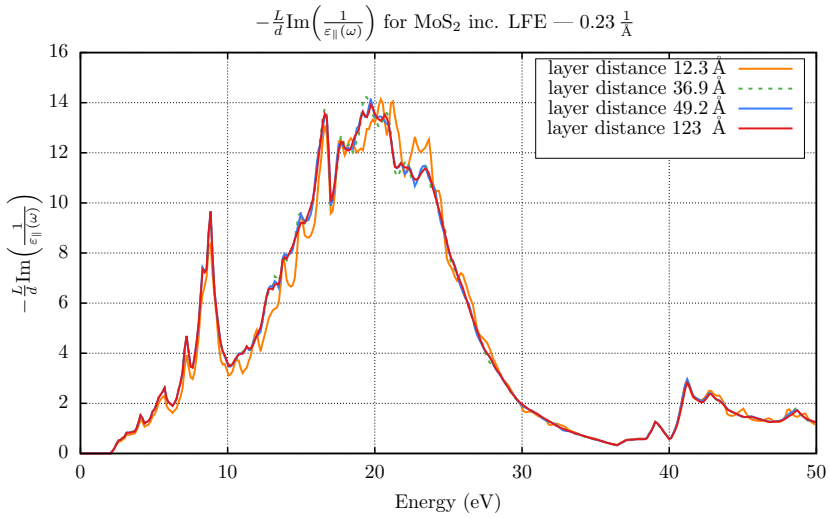


(a) This graph shows EELS for MoS₂ without any momentum transfer projected onto the in-plane direction including LFE calculated for different interlayer distances. A very slow convergence towards the absorption spectrum is visible.

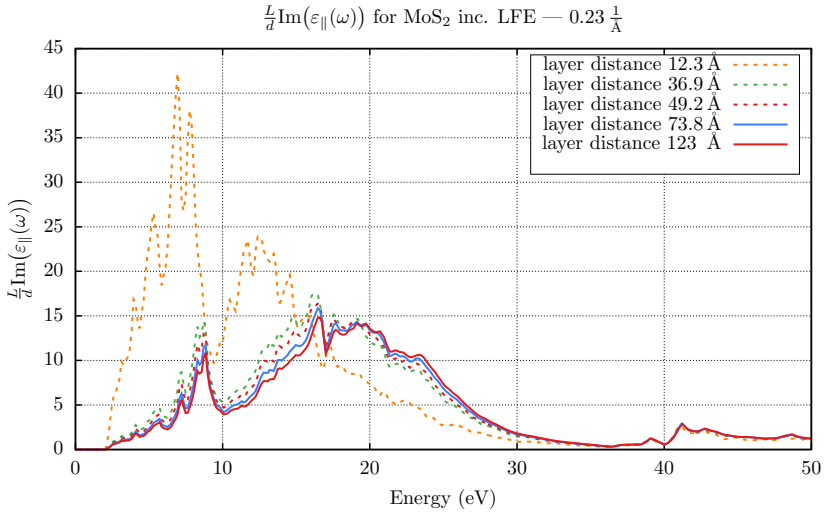


(b) This graph shows the absorption spectrum for MoS₂ without any momentum transfer projected onto the in-plane direction including LFE calculated for different interlayer distances. A very fast convergence is evident. This can be used to simplify calculations.

Figure 4.16: EELS spectrum and absorption spectrum of MoS₂ without momentum transfer

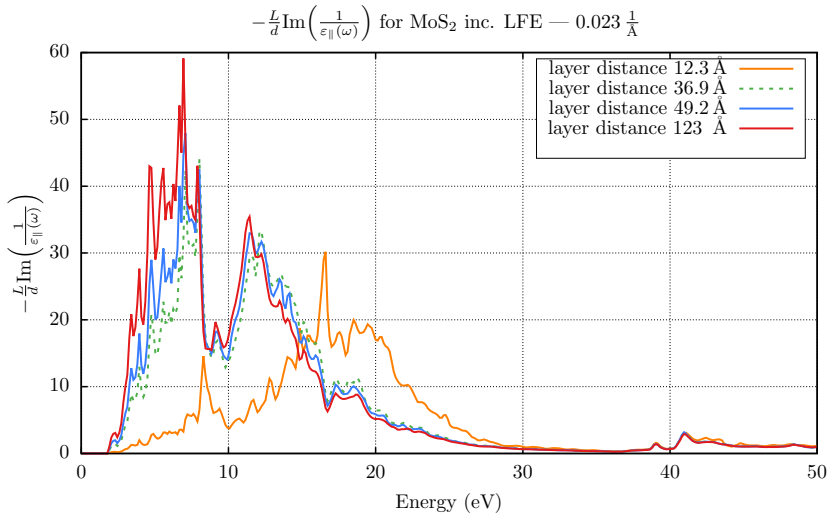


(a) This graph shows EELS for MoS₂ with $0.23 \frac{1}{\text{Å}}$ momentum transfer including LFE calculated for different interlayer distances. A very fast convergence is visible.

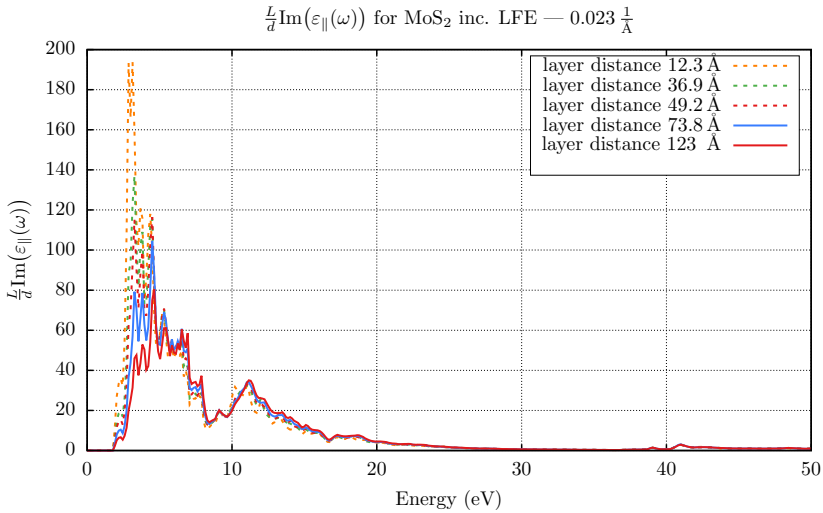


(b) This graph shows the absorption spectrum for MoS₂ with $0.23 \frac{1}{\text{Å}}$ momentum transfer including LFE calculated for different interlayer distances. The convergence is slow.

Figure 4.17: EELS spectrum and absorption spectrum of MoS₂ with $0.23 \frac{1}{\text{Å}}$ momentum transfer



(a) This graph shows EELS for MoS₂ with $0.023\frac{1}{\text{\AA}}$ momentum transfer including LFE calculated for different interlayer distances. A slow convergence is visible.



(b) This graph shows the absorption spectrum for MoS₂ with $0.023\frac{1}{\text{\AA}}$ momentum transfer including LFE calculated for different interlayer distances. The convergence is slow.

Figure 4.18: EELS spectrum and absorption spectrum of MoS₂ with $0.023\frac{1}{\text{\AA}}$ momentum transfer

Summation with different mesh densities

Taking into account the convergence behavior described in the previous section the spectrum at the Γ point is treated as the absorption spectrum, whereas the spectrum at all other momentum transfers is treated as the loss spectrum. This gives a good result already for small layer distances.

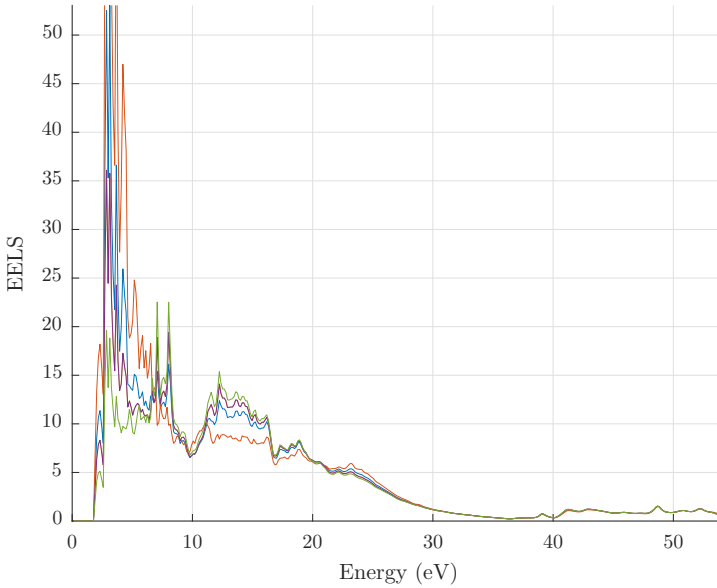


Figure 4.19: Comparison and convergence of different k-point grids with the Γ point treated explicitly (MoS_2). The summation over the full Brillouin zone for a 20×20 (orange), 60×60 (blue), 100×100 (purple) and 180×180 (green) grid are shown.

To achieve a precise result, the layer distance has to be increased until the k-point closest to Γ is converged.

Fig. 4.19 shows the momentum summation for different grid densities. The used grid evenly spans across the first Brillouin zone. Except from the spectrum at the Γ point, all spectra are calculated using the loss function. The spectrum without any in-plane momentum transfer is calculated using the absorption function, due to the before discussed convergence behavior with interlayer distance. The high energy part (25 eV to 50 eV) of the shown curve converges quickly with an increasing density of the summation mesh, whereas the low energy region does not. This is especially evident

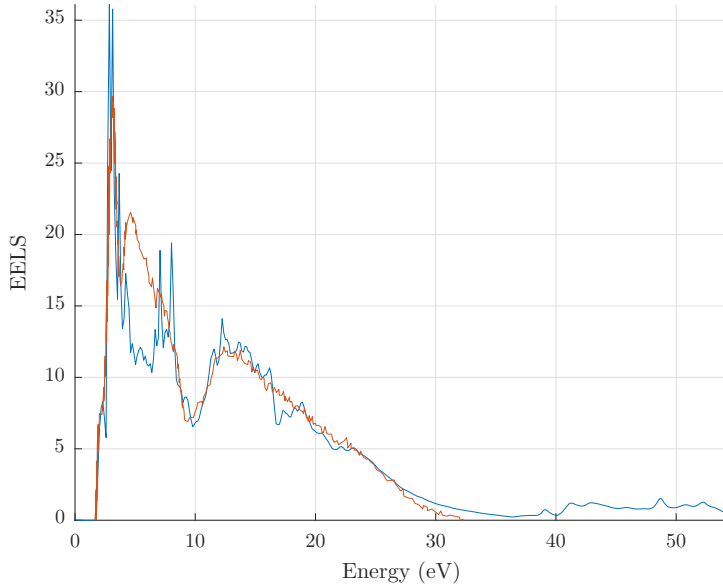


Figure 4.20: Comparison of the experimental spectrum of MoS₂ (orange) recorded by our collaborators from the University of Limerick [53] and the EELS summation (blue) using a 100×100 grid of k-points summed for the full Brillouin zone.

between 0 eV and 10 eV. The reason for the slow convergence is the strongly varying dielectric function around the Γ point that requires a very fine summation mesh to be used. Here, this is especially obvious, since the spectrum for the smallest momentum transfer (not at Γ point) is not converged for the used interlayer distance of 36.9 Å. The finer the mesh is chosen, the smaller this smallest momentum transfer becomes. The smaller the momentum transfer for which the spectrum is calculated using the loss function, the more vacuum would have to be used. When comparing the summed up energy loss to the experimental spectrum (Fig. 4.20), the difference between the two is also due to the spectra, used for the summation, that are not converged with respect to the interlayer distance. Nevertheless, the overall agreement is good, and the only major difference is the lack of intensity between 4 eV and 7 eV. The plot of Fig. 4.18a shows the spectrum for the smallest momentum transfer (not 0) included in the summation (100×100 grid), as used for the comparison. The next challenge is

to make sure that each individual spectrum used for the summation is converged by using a sufficient amount of layer distance.

Mixing different layer distances

The aim is to use a mixture of calculated spectra with different layer distances to achieve a well converged final result for the summation over a range of momentum transfers. So, combining the dataset from the previous section (36.9 \AA , 100×100) with

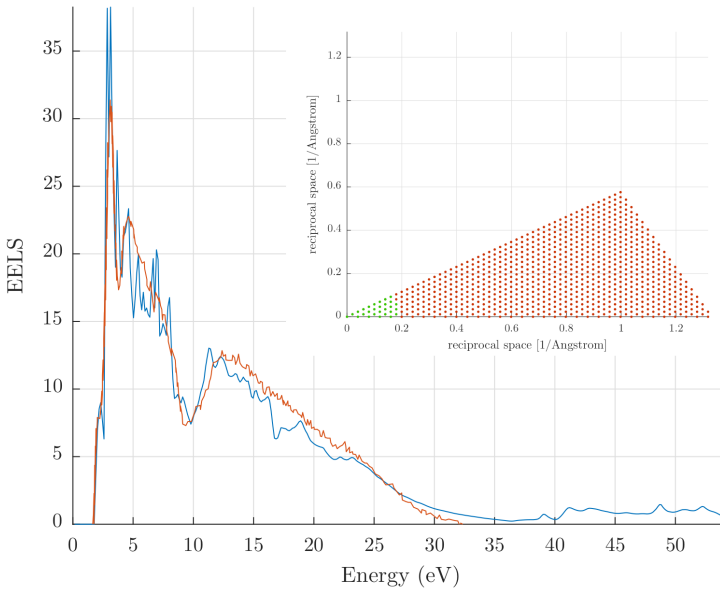


Figure 4.21: Comparison of the experimental spectrum of MoS_2 (orange) recorded by our collaborators from Limerick [53] and the EELS summation (blue) using a combined dataset for different vacuum distances. 100×100 grid of k-points summed for the full Brillouin zone.

a dataset around Γ (to be precise — around $(0,0,\omega/v)$ in reciprocal space) with 123 \AA layer distance, delivers a well converged spectrum along the whole energy range. To combine these two datasets one has to scale the individual contributions according to the added vacuum. For the comparison to experimental findings (Fig. 4.21), the experimental spectrum is scaled in intensity according to the peak around 12 eV and shifted to align the band gap. Fig. 4.21 shows a summed up loss spectrum that has a very good agreement with the experimentally measured one across the whole energy

range. The low energy excitations, as well as the main plasmon peak, are calculated in agreement with the experiment.

The efficiency of the calculation can be further improved by using a fine grid around the Γ point, where the dielectric function is strongly varying, and a coarse grid further away, where the change between different momentum transfers is small. In this case the surface element (for the summation) has to be scaled according to the used grid.

Combining the summation and the extrapolation scheme

Extrapolation to infinite layer distances allows us to achieve a very fast convergence across all momentum transfers and energy ranges (Eq. (4.3.58)). Finally, this will be combined with the summation expression in this chapter (Eq. (4.4.25)). Here, a layer distance of 24.6 Å is sufficient. This scheme for calculating EELS spectra will be used in all following calculations. Fig. 4.22 shows a very favorable agreement between the

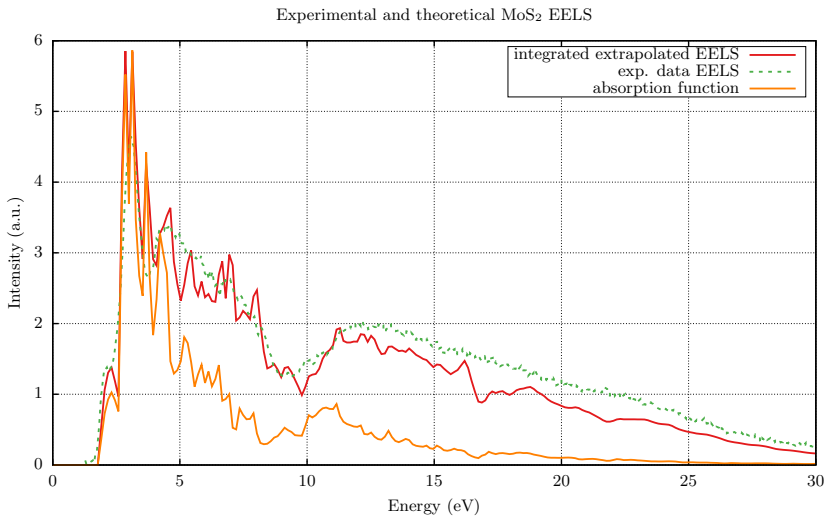
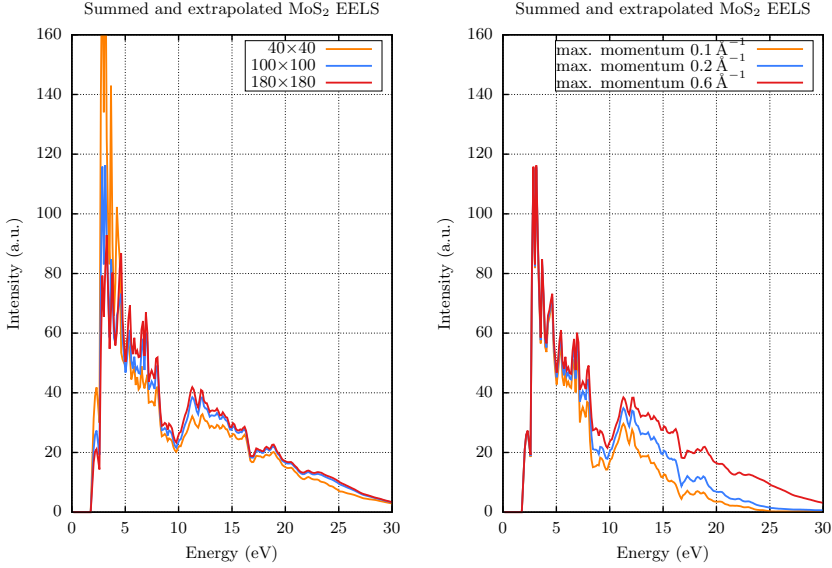


Figure 4.22: Comparison of experimental EELS Data for MoS₂ [53] and the extrapolated and summed loss function for 24.6 Å as well as the absorption function ($\text{Im}(\epsilon)$) without momentum transfer.

summed and extrapolated loss spectrum and the experimental measurement. A significant improvement for the agreement with experiment in comparison to the absorption spectrum (and loss spectrum without momentum transfer Fig. 4.16a) is evident. The summation of multiple momentum transfers depends on the speed of the electrons

used for the individual spectra (Eq. (4.4.4)), the maximum momentum transfer in the summation (Sec. 4.4.1), and the grid density. Fig. 4.23 and Fig. 4.24 show the



(a) Convergence behavior with increasing grid density for the summation. (b) Influence of the maximum momentum transfer in the summed up spectrum on the final result.

Figure 4.23: Impact of (convergence) quantities on the summed and extrapolated loss spectrum of MoS₂.

influence of these three quantities using the MoS₂ monolayer as an example. A layer distance of 36.9 Å is used as well as the extrapolation to infinite layer distance.

In Fig. 4.24 the dependence on the electron velocity is shown without the prefactor of $\frac{1}{v^2}$, since it results in an overall scaling but does not change the peak structure. Fig. 4.24a shows that the impact of different electron velocities is significant in the low energy region. The higher energy region, starting from 15 eV, is only marginally changed. This behavior can be understood from Eq. (4.4.4) — the influence of the out-of-plane momentum transfer, determined by the electron velocity and energy loss, is high for small in-plane momentum transfers, which govern the low energy excitations. Therefore, the impact of the electron speed is mostly visible in the low energy region. Fig. 4.24b shows the same spectra but scaled according to the maximum intensity to focus on the relative change of the peak structures. It shows that the peak around

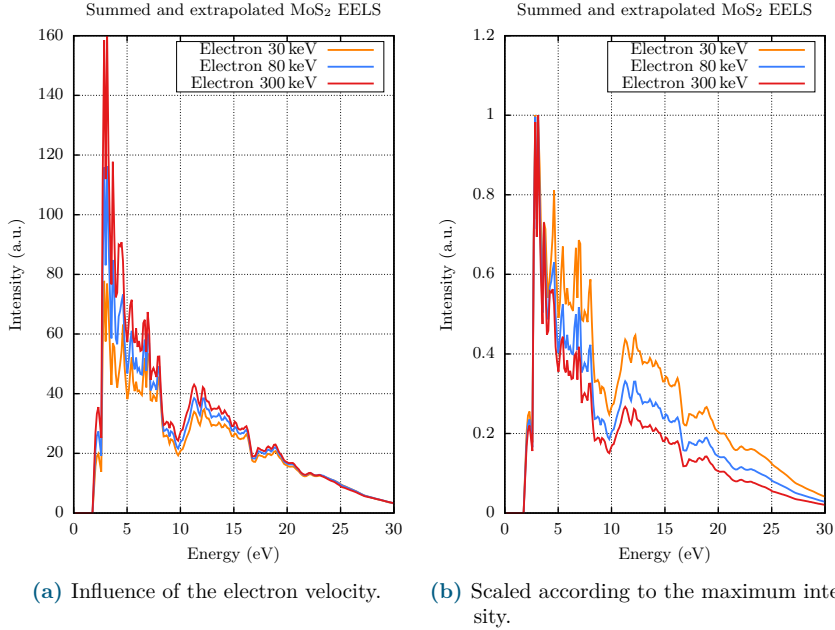


Figure 4.24: Influence of the speed of the electrons on the summed up spectrum — prefactor of $\frac{1}{v^2}$ is left out to focus on the peak structure.

12 eV becomes more pronounced for lower electron velocities, since the impact of large momentum transfers grows in comparison to small momentum transfers. The graph makes clear that the influence of the electron speed is mainly visible in the ratio of the two main excitation peaks, rather than in the overall structure that is nearly unchanged.

4.4.3 Application to other 2D materials

In a further step the combined method of extrapolation to infinite layer distance and summation over multiple momentum transfer will be applied to two other monolayer materials. First graphene, which has no band gap and then hBN, which has a large band gap. So, in combination with the results for MoS₂ (small band gap), the results are verified for a range of monolayer materials. Here, a grid point density for the summation, corresponding to an equidistant 100×100 grid of the 2D Brillouin zone, is used. As the momentum dependent prefactor falls off quickly with increasing momentum transfer, it is sufficient to truncate the set to 20×20 , while leaving the \mathbf{k} -point density unchanged.

Hexagonal boron nitride (hBN)

The absorption function without momentum transfer for hBN (Fig. 4.25, orange curve) shows a shift and missing intensity of the main plasmon peak at 15-25 eV, compared to the experimental spectrum. This difference is resolved when applying the summation

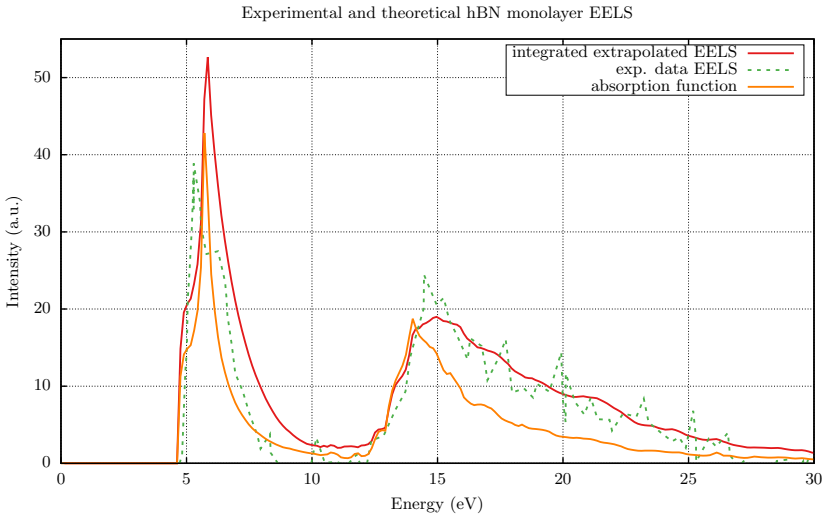


Figure 4.25: Comparison of experimental EELS Data for hBN [54] and the extrapolated and summed loss function as well as the absorption function ($\text{Im}(\varepsilon)$) without momentum transfer.

and extrapolation scheme. All three spectra are scaled in intensity according to the summed curve. The spectrum for each momentum transfer on the grid is added up — the maximum momentum transfer taken into account is $0.5656 \frac{1}{\text{\AA}}$. Taking larger contributions into account has been tested and changes the result only marginally. The calculations are done for a layer distance of 50.35\AA .

Graphene

Comparing the experimental spectrum, the absorption function, and the summed extrapolated loss function the two main peak positions do agree for all three spectra. Only their intensities are different. The correlation between the summed extrapolated loss function and the experimental spectrum is very good. Similar to hBN and MoS_2 , the lack of intensity between the absorption spectrum (15-25 eV) and the experimental spectrum is corrected by the introduced scheme. The maximum momentum transfer

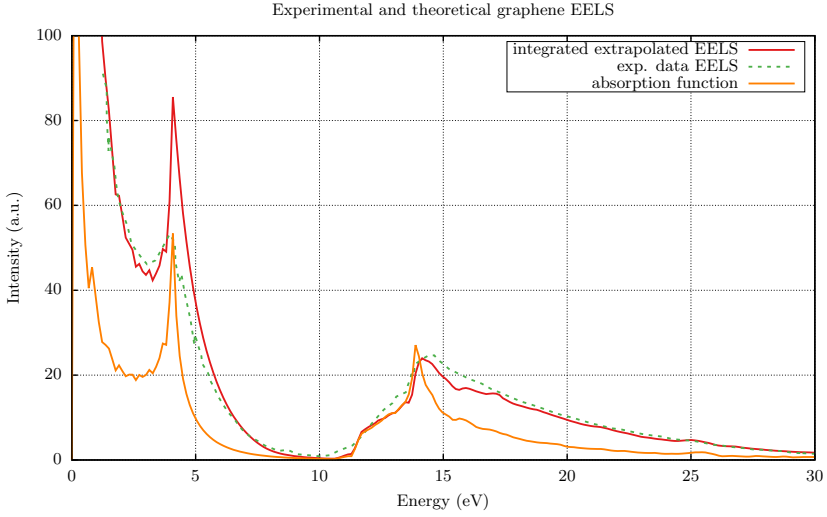


Figure 4.26: Comparison of experimental EELS Data for graphene [55] and the extrapolated and summed loss function as well as the absorption function ($\text{Im}(\varepsilon)$) without momentum transfer.

used for the summation is $0.5752 \frac{1}{\text{\AA}}$. Each spectrum is calculated with a layer distance of 50.95\AA .

EELS calculation for implanted systems

- 5.1 The dielectric function in the supercell approach 131
- 5.2 Tool for visualization 133
- 5.3 EELS signature of defect states 133
- 5.4 Optical transition elements 139

In the following, the developed techniques for extrapolation to infinite layer distances and integration over multiple momentum transfers will be applied to larger systems including defects. First of all, we will make sure that the spectrum calculated for the supercell is actually comparable to the primitive unit cell. This is important for a good comparison of the defect system to the pristine system, that is not necessarily calculated with the same supercell size.

5.1 The dielectric function in the supercell approach

The calculated spectrum for a pristine supercell should in principle be the same as for the pristine unit cell. This can only be achieved, if all computational parameters are well converged or similarly chosen for the two systems. The k-point grid has to be kept constant in density (this means a reduction of the number of k-points in supercell), the energy up to which empty states are included should also stay constant (this means increasing the number of empty states included in the supercell calculation). Also, the grid for summation over multiple momentum transfers has to be adapted similarly to the k-point grid. Most importantly the energy mesh has to be chosen fine enough

for both calculations to be converged, otherwise the structure of the spectrum is not sampled with sufficient accuracy.

In the current implementation, only points in the first Brillouin zone are used. This means that the maximum momentum transfer taken into account is limited. Since the integrated spectrum converges quickly with the maximum momentum included, this is no problem for the sizes of supercells used here. However, in the case of very large supercells this implementation would have to be extended. In Fig. 5.1, the comparison

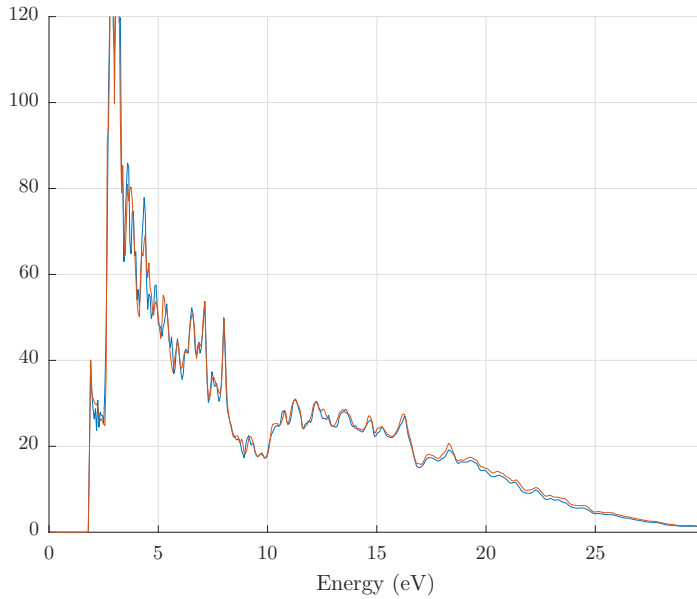


Figure 5.1: Comparison of calculated EELS for MoS₂ in a simple unit cell (dark orange) and in a 3×3 supercell (blue). Special care was taken to converge all computational parameters and the mesh for summation so that the results are comparable. Also, the maximum momentum transfer included in the integration is the same for both cases.

between an EELS calculation in a simple unit cell (orange) and in a 3×3 supercell (blue) is shown. The here used parameter set for integration of momentum transfers corresponds to 25×25 (5×5 in the outer region) k-points for the supercell and 75×75 (15×15 in the outer region) for the primitive cell. Furthermore, the energy mesh on the imaginary axis consists of 400 points between 0 Htr and 5 Htr with an exponentially increasing spacing. The number of empty states is increased from 200 to 1300, this is

roughly compensating the number of additional states due to the larger unit cell - as a result the same maximum energy is used in both setups.

5.2 Tool for visualization

A GUI (graphical user interface) tool based on MATLAB has been designed to fulfill the task of summation for more complex datasets.

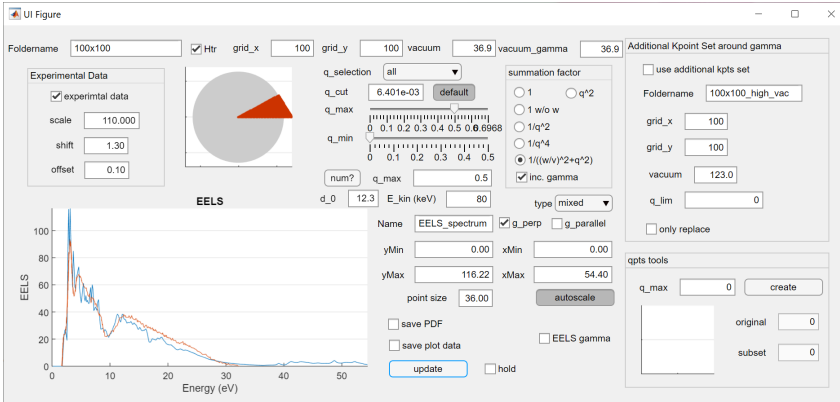


Figure 5.2: Screenshot of the GUI for visualization of EELS spectra. A plotting process of the integrated EELS spectrum of MoS₂ in comparison to the experimental spectrum is shown. In the upper area, a plot of the irreducible wedge (red) and the integration maximum (grey) is visualized.

It allows us to automatically combine datasets with different resolutions and vacuum distances. Furthermore, it allows the selection of the included momentum range, the acceleration voltage, kind of spectrum (absorption spectrum, loss spectrum, extrapolated spectrum), plotting range, and the comparison to experimental datasets. The output is possible as a text file or PDF file ready for presentation. A detailed description with instructions to the download can be found in the appendix (Appx. B).

5.3 EELS signature of defect states

In the following, the developed tool will be used to apply the integration and extrapolation scheme to supercells including defects. Here, a selection of the materials already investigated in Sec. 3.5 will be used to identify the signature of defect states in EELS

spectra. Also, the absorption spectrum is shown where useful to emphasize the effect on the optical properties.

5.3.1 MoS₂+P

In Sec. 3.5.1, a defect state is identified close to the Fermi level (Fig. 3.26). From the

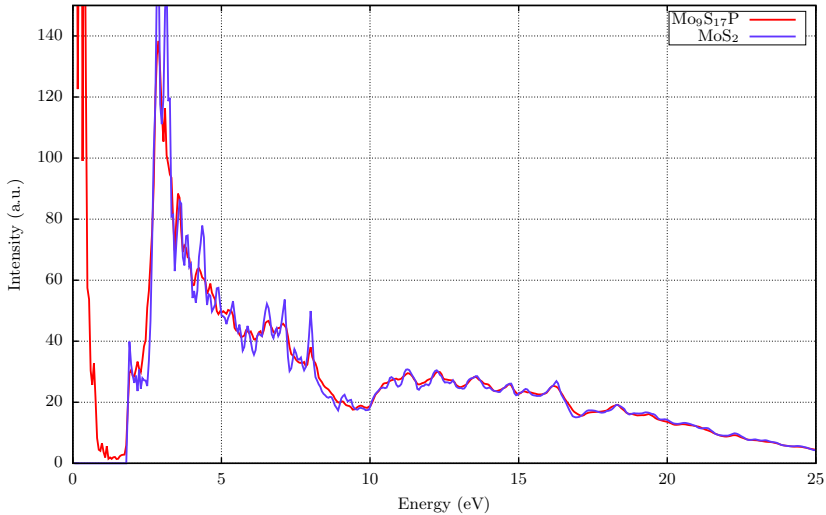


Figure 5.3: Comparison of calculated EELS for MoS₂+P and the pristine MoS₂, both including the extrapolation and integration scheme. Both calculations are done in a 3×3 supercell. The metallic character of the phosphorus implantation is clearly visible.

unfolded band structure itself, one can only see that at a certain energy there is an electronic state, but one cannot be sure which transitions from the conduction band or valence band are possible. Here, the transition elements are evaluated to find exactly this: the possible transitions. To make the comparison as accurate as possible, the defect calculation and the calculation for the pristine system have been performed with exactly the same parameter set in a 3×3 supercell. The comparison could have been done with the primitive cell as well, but since the 3×3 supercell has already been calculated before, it is also used here. In Fig. 5.3, the additional transitions due to the defect states are directly visible. The peaks within the band gap of the pristine MoS₂ are most likely caused by transitions involving the defect level. Also, its metallic character is evident, since for the energy towards 0 the intensity tends to infinity. It

is remarkable that the EELS spectra above the band gap energy (pristine MoS_2) are nearly identical, with only little influence from the defect. The only observation is a smeared out spectrum, due to the distortion of the lattice. This is to be expected, since the avoided crossings, visible for the band structure at higher energies, will cause more possible transitions but not change the overall peak structure.

The same comparison can be made for only the absorption spectrum, so only $\text{Im}(\epsilon)$ at $k = 0$ is plotted. Fig. 5.4 is focused on the very low energy region (below 10 eV),

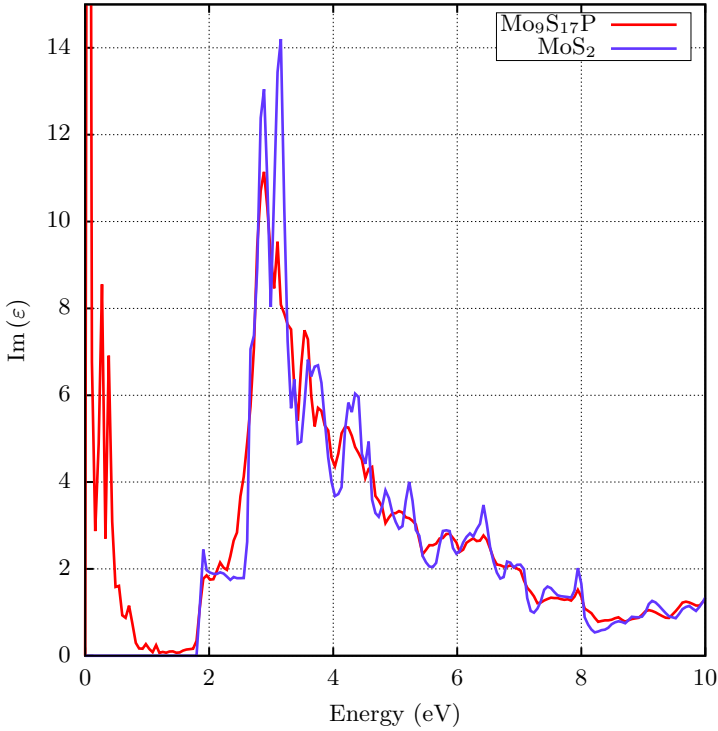


Figure 5.4: Comparison of calculated absorption function for MoS_2+P and the pristine MoS_2 . Both calculation are done in a 3×3 supercell. The metallic character of the phosphorus implantation is clearly visible.

of which the lower half is most relevant to optical transitions. Here, the intensity peaks (below 1 eV) caused by transitions between the defect states and different valence band levels can be seen separately. Overall, the absorption spectrum (Fig. 5.4) looks very similar to the extrapolated and integrated loss spectrum (Fig. 5.3). This, again,

supports the fact that most of the low-energy transitions are already sufficiently shown for this material without including additional momentum transfers in the loss function.

5.3.2 MoS₂+Cr+S

The following chromium defect is described in Sec. 3.5.4 including a band structure plot showing the defect levels within the band gap (Fig. 3.32). The band structure (Fig. 3.31)

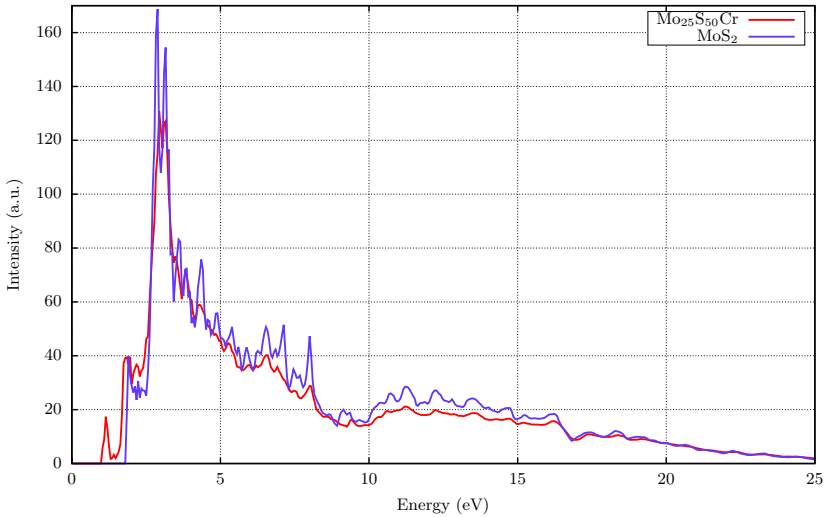


Figure 5.5: Comparison of calculated EELS for MoS₂+S+Cr (5×5 supercell) and the pristine MoS₂ (3×3 supercell). The influence of the defect is clearly visible.

shows two very pronounced defect states, one about 900 meV below the conduction band minimum and another one 200 meV below the conduction band minimum. The shallower defect state actually hybridizes with the host band minimum at the *K* point, therefore reducing the band gap rather than introducing a distinct level. The influence of these defect levels on the loss spectrum (Fig. 5.5) as well as on the absorption spectrum (Fig. 5.6) can be clearly seen as two distinct features. On the one hand, an additional peak at the position of the mid-gap defect state is introduced, on the other hand the first excitation peak of the pristine material is shifted to a lower energy. One should note that for the summed and integrated loss spectrum the maximum momentum transfer taken into account is limited to the first Brillouin zone of the 5×5 supercell. Therefore, the momentum transfer in the pristine calculation (3×3 supercell), has also been limited to the same maximum to allow for the comparison.

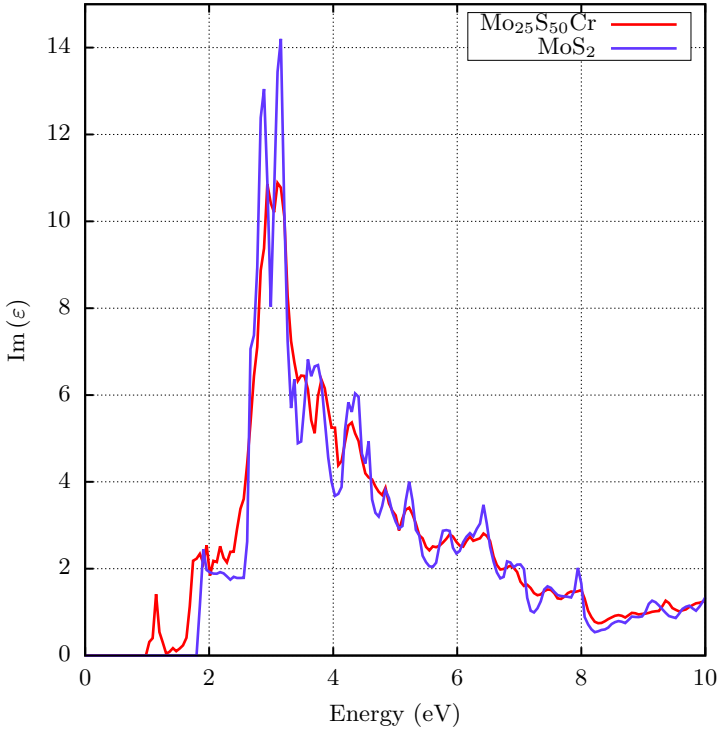


Figure 5.6: Comparison of calculated absorption function for $\text{MoS}_2+\text{S}+\text{Cr}$ (5×5 supercell) and the pristine MoS_2 (3×3 supercell). The influence of the defect is clearly visible.

Without this additional limitation, the two spectra would show a larger discrepancy in the peak around 12 eV. All differences due to the two unit-cell sizes are taken into account: k-point grid, number of empty states etc.

5.3.3 MoSe_2+Cr in several configurations

During the implantation process of a chromium atom into MoSe_2 , the possibility to control the exact position of chromium by the ion energy is limited. Therefore, it is necessary to investigate the final configuration after the implantation. Besides using a TEM and EELS measurements, it is also possible to differentiate the type of defect with photoluminescence measurements. Here, the comparison in Fig. 5.7 of the absorption functions for various chromium in MoSe_2 configurations is supposed to give a guide to

the interpretation of measured data. Fig. 5.7 shows an interstitial chromium atom, a

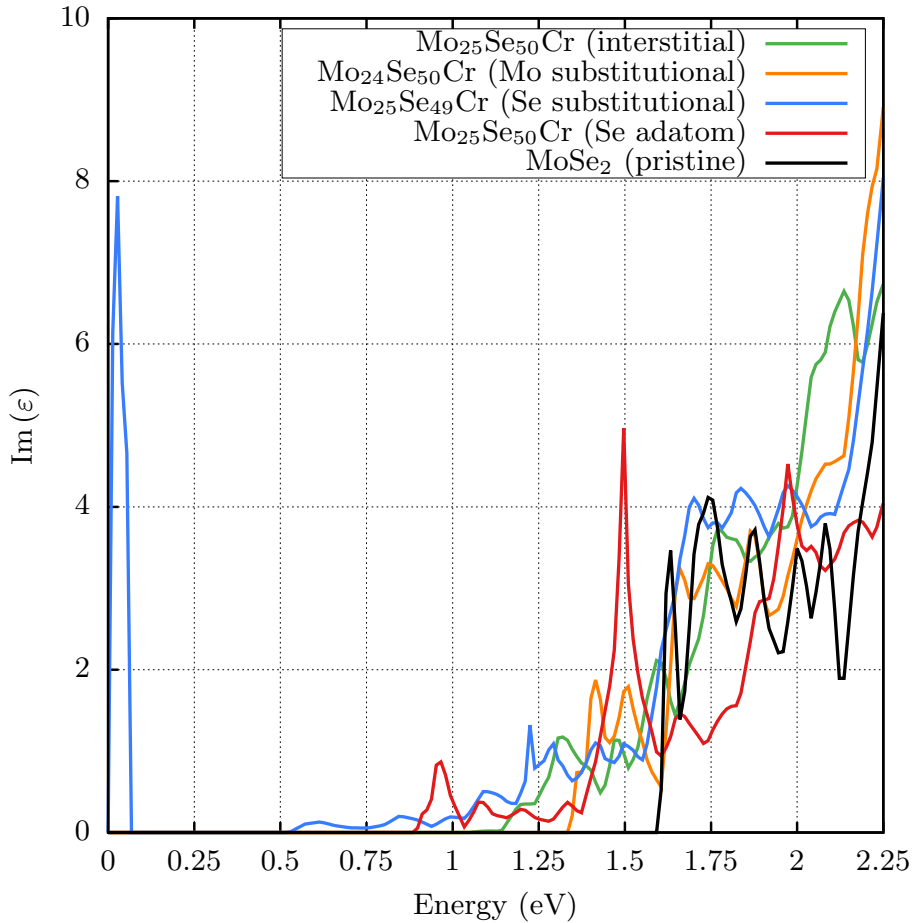


Figure 5.7: Comparison of calculated absorption function for pristine MoSe₂ (5×5 supercell) and MoSe₂+Cr (5×5 supercell) in various positions of the crystal structure (interstitial, Se substitutional, Mo substitutional, and Se substitutional with additional Se). The influence of the different defects is clearly visible.

chromium atom substituting selenium, a chromium atom substituting molybdenum, and a chromium atom substituting selenium with an additional selenium atom on top. The effect of the defect states shown in Sec. 3.5 can be clearly seen. It should be noted, that the DFT calculation preceding the SPEX run of MoSe₂+Cr+Se is,

for computational reasons, calculated with a similar parameter set as the MoSe₂+Cr (interstitial) DFT calculation, which in this case means underconverged parameters. The band structure corresponding to this underconverged parameter set (Sec. C.2) can be found in Fig. D.3. The important defect state has the same energy for both parameter sets.

5.4 Optical transition elements

Until this point, much effort has been put into calculating spectra (EELS and optical). These can be measured in experimental setups, but, when engineering electronic and optical properties by introducing defects, it is also interesting to ask the question of where exactly the possible transitions have their origin.

To calculate the dielectric function possible transitions are "added up" in RPA. Here in Fig. 5.8, the transition elements are shown on top of the band structure. The thickness of each line corresponds to the size of the transition element, with the according color representing the transition energy. The plot is done for direct transitions, so without any momentum transfer. It is not surprising but nice to see this explicitly that the strongest transition is at the K point.

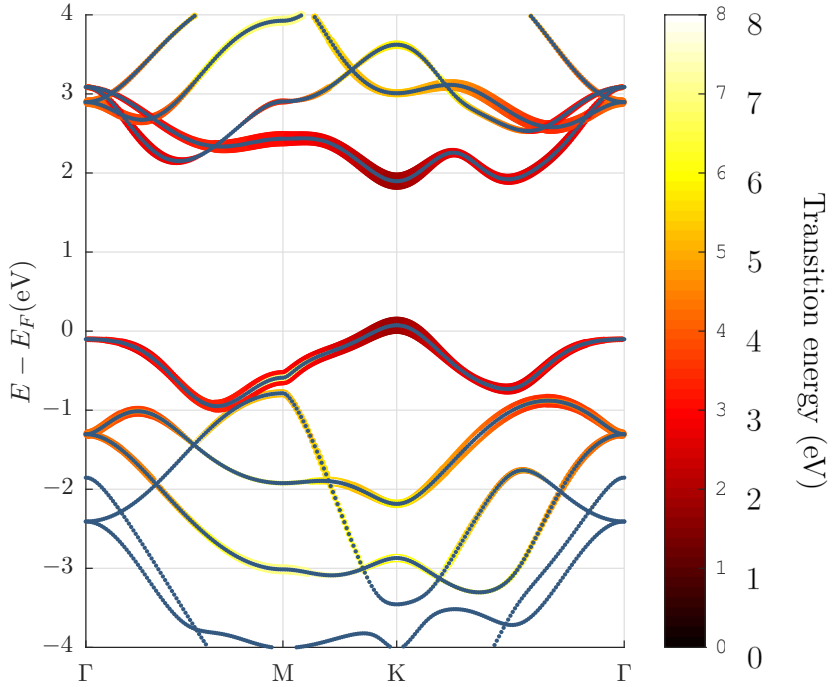


Figure 5.8: The Kohn-Sham band structure of the pristine monolayer MoS₂ is shown in blue. The additional color represents the energy of the transition element. The thickness represents the size of the matrix element (likelihood for this transition). It can be clearly seen that the highest transition probability is at the *K* point.

Conclusions

This work focuses on the investigation of monolayer materials with ab-initio electronic structure methods. Monolayer thick samples of transition-metal dichalcogenides (TMDs) have shown remarkable physical properties like spin-valley locking and a direct band-gap that could be used for single photon emission. To create single photons from a TMD monolayer, the emission has to be confined to a single atomic site under the collection lens, restricting it to one photon at the time. This can be achieved with the aid of suitable defect atoms that locally modify the electronic potential but also preserve the spin-valley locking property in order to control the chirality of the emitted photon. Instead of a single dopant also a small area with a reduced band gap, close to the exciton Bohr radius, can localize the emission. To experimentally evaluate the success of a implantation procedure, spectroscopy methods like electron energy loss spectroscopy (EELS) in a transition electron microscope (TEM) and photoluminescence measurements are applied. Methods in computational solid state physics bring us into the position to predict the electronic characteristic of certain implanted systems, so that only the most promising candidates must be tested experimentally. Therefore, the aim of this work is to develop and apply the required computational methods for the prediction of defect properties in monolayer thick samples.

Aim: Single photon emission

In this work, an unfolding scheme is used to reveal the influence of possible defects on the material within the band structure. Furthermore, a summation and extrapolation method is developed to theoretically predict the spectrum for a two-dimensional material in an EELS experiment.

The calculation of a crystal with a defect, employing a software based on periodic boundary conditions, is performed in a supercell consisting of a defect embedded in

Modeling of defect systems

multiple pristine unit cells. For the calculation of an isolated defect, the supercell is chosen large enough so that the interaction between periodic images of the defect atom is sufficiently suppressed.

Unfolding the supercell band structure

Since the supercell is much larger than the primitive unit cell, the folded band structure of the supercell appears very different from the band structure of the primitive unit cell, even though it describes the same (when calculated without a defect) or a slightly distorted system (when a defect is present). Therefore, an algorithm is developed to unfold the band structure from the small Brillouin zone of the supercell to the large Brillouin zone of the pristine unit cell. In this work, an algorithm by Rubel and coworkers [13] has been extended to the LAPW basis and implemented within the Fleur code [10], which is developed at the Peter Grünberg Institut of the Forschungszentrum Jülich. The implementation allows for the unfolding of supercell band structures in all three dimensions. This means that the unfolding for a bulk system (all three dimensions), as well as a monolayer system (only two dimensions (in-plane)), or a system stacked in one direction (only one dimension) is possible. Additionally, the implementation allows for the unfolding of rotated supercells with respect to the pristine unit cell. This is especially helpful in the case of surface states. Furthermore, the implementation has been extended to the wave functions used in the Fleur code for the calculation of SOC in 2nd variation. For calculations including defects, it is now possible to automatically have the unfolded band structure as an output from the Fleur code.

New insights from unfolded band structures

The unfolded band structure directly compares to the one from experimental measurements. Comparing these two band structures improves the interpretation of measurements, as an identification of measured states is simplified. Besides the importance for experimental comparison, it allows for a significantly better understanding of the calculated band structure. High symmetry points of the pristine unit cell with certain properties (direct band gap, spin-valley locking) can be related to the corresponding high symmetry point of the defect system. This algorithm was applied to a variety of defect systems of interest to the collaboration this thesis is part of: MoS_2 +(Se, P, Cr in various positions of the lattice, and a vacancy), MoSe_2 +(S, P, Cr in various position of the lattice, and a vacancy), and WSe_2 +S.

EELS spectra in simulation

EELS measurements allow us to investigate the possible excitations of a system. This technique is used to verify the type of defect and its suitability for single photon

emission. It is possible to predict the measured spectrum utilizing the random-phase approximation (RPA). The treatment of monolayers with a code that requires 3D periodic boundary conditions requires supercells of empty space modelling the vacuum in the out-of-plane direction, which has to be chosen large enough for the layers to be electronically decoupled.

The energy loss spectrum obtained from the dielectric function calculated with RPA shows a very slow convergence with respect to this interlayer distance due to the long-range Coulomb interaction, therefore requiring very large unit cells. To reduce the computational effort and thus allow for the treatment of larger supercells in lateral direction, the development of an extrapolation scheme to infinite layer distance is necessary. This scheme is based on ideas by Nazarov [52, 56] and re-derived for the present case of the loss function.

Developed extrapolation scheme for EELS

The EELS spectrum that is measured in a TEM includes electrons with a range of momentum transfers, since the electrons are collected in a finite aperture after passing through the probe. This implies that the loss function has to be calculated for all these different momentum transfers and summed accordingly. Here, the treatment of the area around Γ in reciprocal space requires the derivation of an integration formula due to the strongly varying loss function in this region (typically six orders of magnitude). The development of the extrapolation scheme together with the summation scheme puts us in the position to calculate a well converged EELS spectrum comparable to the experimentally measured one.

Adding momentum transfer to the EELS spectrum

This has been demonstrated for the prototypical monolayer materials of MoS₂ (semiconductor), graphene (semimetal), and hexagonal BN (insulator). Especially for MoS₂, the inclusion of these two schemes is necessary to achieve a simulation result that is in agreement with the experiment, in contrast to the spectrum without including momentum transfers. The EELS spectrum is also calculated for the defect systems of MoS₂+P and MoS₂+Cr. Additionally, this method allows for the calculation of a momentum resolved EELS curve with finite resolution, since the limiting momenta for the summation can be chosen according to the experimental setup. The resulting spectra can not only be used to help interpret experimental measurements, but also to predict the influence of certain materials implanted in the system and only investigate

Successful agreement with experimental EELS spectra

the most promising candidates that could facilitate single photon emission.

Two standalone
tools developed

Two standalone tools based on MATLAB have been developed to automatize the unfolding of supercell band structures and the calculation of EELS spectra including the summation and extrapolation scheme. These tools are available as described in Appx. A and Appx. B.

Impact on
method
development
and
understanding
of TMD
monolayer
defects

The main result from this thesis is, on the one hand, the algorithm for unfolding a supercell band structure that allows for a meaningful interpretation and a direct comparison to experiments. On the other hand, the calculation of EELS spectra for monolayer materials has been extended with a momentum summation and extrapolation scheme. This results in a computationally efficient calculation of spectra that are directly comparable to EELS measurements in a TEM as they incorporate all the different momentum transfers included in the experiment. This has been demonstrated for multiple materials among which are graphene, hBN, and MoS₂. It has also been applied to the doped systems of MoS₂+P and MoS₂+Cr.

The presented results have found defect states in MoS₂/MoSe₂+Cr (in various positions of the crystal) that fall into the band gap as well as a local modification of the band gap in MoSe₂+S. These local defects give rise to a reduction of the energy gap, which may be able to trap excitons and thus confine the photon emission in real space. At the same time, these defect atoms seem not to break the spin-valley locking property of the TMD host material, which is necessary to eventually control the polarization of the emitted photon by the spin of the excited electron. Thus, we conclude that these are promising candidates for the construction of electrically driven single photon sources with known polarization.

Further
extensions and
applications

In future research, this work can be extended by including more precise methods like *GW*, which corrects the band energies by including a many-body self-energy, or solving the Bethe-Salpeter equation, adding excitonic contributions to the spectrum. Also, the developed method can be applied to all band structure calculations that include supercells. The calculations of EELS spectra can be further put to use for all systems, especially monolayer materials, where the extrapolation scheme plays an important role.

Tool for plotting band structures

The tool for plotting band structures is written in MATLAB as an app but can be exported as a standalone software. It is publicly available from the git repository for tools in our institute https://github.com/JuDFtteam/mascli-tools/tree/develop/mascli_tools/tools/banddos_tool. It can either be loaded as an app into MATLAB, exported as a standalone software, or edited within MATLAB.

The graphic interface (Fig. A.1) consists of two plotting areas, several optional switches, the input selection, and a button to start the plotting procedure. A description of the most important functions is given below.

Depending on the size of the system to be plotted, it can take several minutes for the file system to scan the whole `banddos.hdf` (can be several GB) file from Fleur and extract the data needed for the plot. The plotting procedure is started with a click on the button "update". The top left area, below the file selection box, shows the atomic structure including a color coded visualization of the atom groups. This is important for the top right area, where additional properties of the band structure can be defined. It is possible to plot only the energy levels connect to the muffin-tin sphere of a certain atom group and thereby analyze the real space properties of parts of the band structure. In addition, also the orbital character of the states can be selected. Since the tool allows for a fast testing of different settings, it is easy to find the orbital character of a certain band, needed as an input to construct Wannier orbitals. In the same area, there is also a "tick-box" to differentiate the contribution of the two different spins along the selected spin quantization axis (in Fleur) in the case of SOC. The "unfold bandstr" button adds the unfolding weights to the plot in order to plot a supercell band structure.

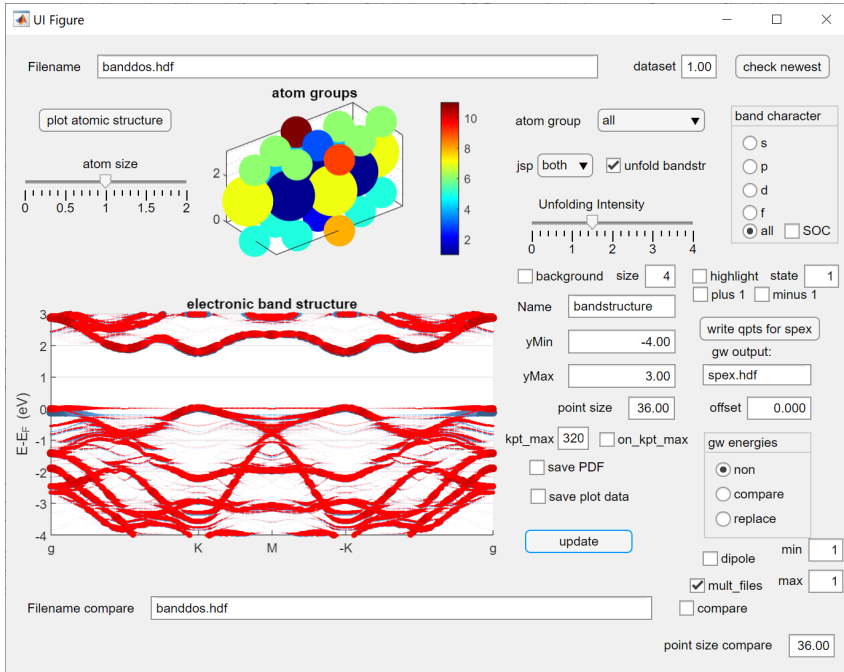


Figure A.1: Screenshot of the GUI for visualization of unfolded band structures. A plotting process of MoS_2 with a P defect is shown. In the upper area, a plot of the atom groups helps to select a projection onto one.

The area to the right of the band structure plot is concerned with the settings for the band structure plot of which most are self-explanatory. There is the option to show the folded band structure in the background and highlight certain states (selected by the band index from Fleur). Also, the point size of the shown plot and the one of the exported plot are selectable. The exported band structure is saved as a PDF file with the correct label for the high symmetry points. Furthermore, it is possible to export the plot as an ordinary text file, so that one can use it for any other plotting tool as an input. In the bottom right corner, there are options to include a band structure file from SPEX in order to compare or replace the energy levels from Fleur. To create the input for this, the option "write qpts for spex" helps to create the needed band path input for SPEX. Finally at the bottom, there is the option to plot a second band structure into the same plot in order to compare it. This can be useful when comparing a defect band structure and a pristine one.

Tool for plotting EELS

For the calculation of EELS spectra the developed methodology of extrapolating to infinite layer distance and summing over multiple momentum transfers is implemented in a standalone MATLAB app. It is available from <https://github.com/>

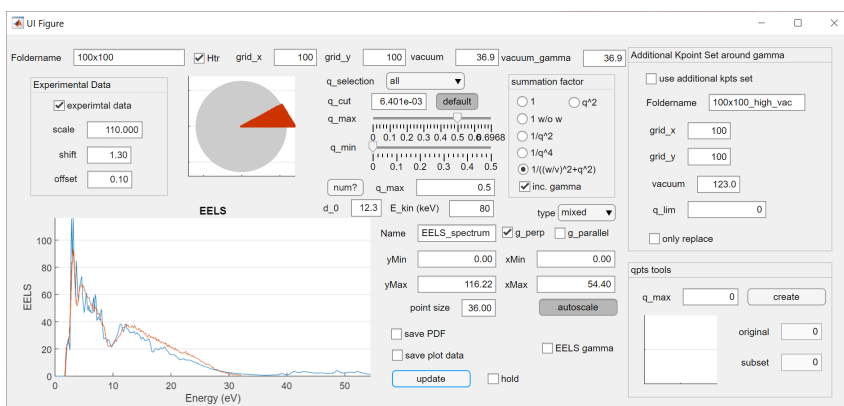


Figure B.1: Screenshot of the GUI for visualization of EELS spectra. A plotting process of the integrated EELS spectrum of MoS_2 in comparison to the experimental spectrum is shown. In the upper area a plot of the irreducible wedge (red) and the integration maximum (grey) is visualized.

`JuDFTteam/masci-tools/tree/develop/masci_tools/tools/EELS_tool` as a MATLAB app installer and as a source file.

This app uses the output from multiple runs of SPEX as an input. The different runs of SPEX calculate the dielectric function for different momentum transfers. The list of

points in reciprocal space that are equally spaced can also be calculated with SPEX. The app contains a feature in the bottom right corner to cut out all mesh points from such a list that exceed a maximum momentum transfer given as input. Furthermore, the app uses the `basis.hdf` file from Fleur as an input to read the information about the crystal cell. At the top of the graphical user interface (Fig. B.1) the information on the input folder and calculation settings are given. The upper plot shows a map of the points in reciprocal space that define the different momentum transfers used. To the left of this plot there are settings to include the results from an experiment as a comparison (`exp_data.txt`). The corresponding curve can be shifted and scaled. In the middle there are settings for the maximum and minimum momentum transfer used for the summation and an option to only plot the result for one certain momentum transfer. Since the speed of the electron influence the loss spectrum, this should also be given as an input in the according field. It is possible to select different summation prefactors, but the one corresponding theory is selected as a default. Also, the setting for including the spectrum at the Γ point in the in-plane direction as $\text{Im}(\varepsilon)$ and in the out-of-plane direction as $\text{Im}(\frac{1}{\varepsilon})$ are selected by default. Instead of using the extrapolation scheme "mixed", there is also the option to just look at the absorption spectrum or the loss spectrum. Similar to the band structure plotting tool, it is possible to set basic parameters for the plot, use a PDF export, or use a text file export. Next to the "update" button there is the option to "hold", keeping multiple runs of the tool visible in the plotting window for comparison.

The tool also allows the usage of an additional k-point set. This can be helpful when combining a fine grid around the Γ point with a coarse grid everywhere else in the Brillouin zone. Either all calculations up to a certain maximum momentum transfer are replaced or just at the points that did exist in the coarse dataset.

Computational parameters

C.1	Self-consistent DFT calculations	150
C.1.1	Crystal structure of pristine systems	150
C.2	EELS calculations	151
C.3	List of materials (supercells)	153
C.3.1	MoS ₂ +P	153
C.3.2	MoS ₂ +Cr (@ Mo)	154
C.3.3	MoS ₂ +Cr (@ S)	157
C.3.4	MoS ₂ +Cr+S	159
C.3.5	MoS ₂ +vacancy	162
C.3.6	MoS ₂ rotated supercell	163
C.3.7	MoSe ₂ +P	163
C.3.8	MoSe ₂ +Cr (@ Mo)	164
C.3.9	MoSe ₂ +Cr (@ S)	167
C.3.10	MoSe ₂ +Cr+Se	169
C.3.11	MoSe ₂ +vacancy	172
C.3.12	MoSe ₂ +Cr (interstitial)	173
C.3.13	MoS ₂ +Se	175
C.3.14	MoSe ₂ +S	177
C.3.15	WSe ₂ +S	179
C.4	Using quantities within the Fleur code	181
C.4.1	Reciprocal lattice vectors	181

C.1 Self-consistent DFT calculations

All calculations in this work require a converged self-consistent DFT run. For a spatial relaxation this is done several times after each change of the atomic positions. For band structure and EELS calculations it serves as a starting point. All DFT calculations have been done with the Fleur code. The default input parameter created by the input generator of the release version MaX 5.0 have been used. In the case of spatial relaxation the muffin-tin radius is adapted automatically by Fleur so that the muffin-tin spheres don't crash. When the calculation is then started with the relaxed positions they are again chosen by default. The band structures are calculated for 320 k-points unless something different is noted. Here, the input file for the input generator of the relaxed pristine MoSe₂ is included as an example.

```
&input film=F cartesian=f symor=t/  
0.5 -0.5 0.0 ! a1  
0.5 0.5 0.0 ! a2  
0.0 0.0 1.0 ! a3  
6.2039733 ! lattice constant  
1.0 -3.0 3.9348 ! scale  
3  
42 0.333333 0.666667 0.125  
34 0.666667 0.333333 -0.00523187248  
34 0.666667 0.333333 0.25523186614  
&factor 1.0 1.0 1. /  
&end /
```

A description of this file format can be found in the Fleur manual at flapw.de. Ch. 1 includes a MoSe₂ bulk and monolayer band structure for demonstrational purpose that is done without spatial relaxation using a lattice constant of $a = 3.2917 \text{ \AA}$. All input files are available upon request.

C.1.1 Crystal structure of pristine systems

For the pristine systems of MoS₂, hBN, and graphene the following unrelaxed structures are used.

MoS₂: The lattice constant of the layered bulk system ($a = 3.15 \text{ \AA}$ [57]) is used. The monolayer consists of a Mo layer sandwiched between two S layers. The bulk structure

is used with additional vacuum in between the layers to construct the monolayer. This layer distance is mentioned next to the respective plots. The sulfur layer is allowed to relax in perpendicular direction up to a residual force of $5 \cdot 10^{-2}$ eV/Å. The relaxed positions of the sulfur layers are at $c(1/4 - z)$ and $c(z - 1/4)$ relative to the Mo layer with the bulk lattice constant $c = 12.3$ Å and the internal lattice parameter $z = 0.124$. This is in good agreement to the experimental and theoretically optimized structure of the bulk phase [58].

hBN: For hBN the monolayer is one atom thin, so relaxation in perpendicular direction does not make sense. The lattice constant of the layered bulk system of $a = 2.504$ Å [59] is used.

graphene: For graphene the monolayer is also one atom thin. The lattice constant of the layered bulk system of $a = 2.462$ Å [60] is used.

C.2 EELS calculations

EELS calculations consist of two sets of parameters. First the parameters for the RPA based dielectric function and then the set of parameters for the integration over multiple momentum transfers. The latter one is mentioned next to the individual plots. The dielectric function is calculated from the polarizability (Eq. (2.3.3)) for which the calculation involves a summation over occupied and unoccupied states and in reciprocal space also k-points. The number of empty states used and the number of k-points depends on the atom type and unit cell size. In reciprocal space the tetrahedron method [61] is used to interpolate between the k-points. Unless noted otherwise, the following parameters were used:

MoS₂: A k-point grid of $12 \times 12 \times 1$ and 190 bands are used.

hBN: A k-point grid of $42 \times 42 \times 1$ and 190 bands are used.

graphene: A k-point grid of $42 \times 42 \times 1$ and 190 bands are used.

MoS₂+Cr+S: A k-point grid of $5 \times 5 \times 1$ and 1800 bands are used.

MoS₂+P: A k-point grid of $8 \times 8 \times 1$ and 1300 bands are used.

MoSe₂+Cr in several configurations A k-point grid of $5 \times 5 \times 1$ and 1800 bands are used for all calculations of this type. Additionally, the DFT calculation (preceding the SPEX run) for MoSe₂+Cr+Se has been done with similar cutoff and convergence parameters as the MoSe₂+Cr (interstitial) DFT calculation (parameters in the Fleur input file: mtSphere radius Se=1.93, mtSphere radius Cr=1.73, mtSphere radius Mo=1.73 (MoSe₂+Cr (interstitial)), mtSphere radius Mo=1.373 (MoSe₂+Cr+Se), Kmax=3.6, and Gmax=10.8)(converged parameter set for MoSe₂+Cr+Se: mtSphere radius Se=1.93, mtSphere radius Cr=1.93, mtSphere radius Mo=2.32, Kmax=4.1, and Gmax=12.3). This increases the comparability and reduced the computational cost.

Additionally, a very fine energy mesh on the imaginary axis has been used as defined with the according graphs. For the analysis of the pristine systems a frequency (ω) mesh between 0 and 2 htr has been employed with an increment of 0.005 htr and a total number of 401 frequency mesh points. Furthermore, two setting to speed up the calculation were used, so that an exemplary input for MoS₂+Cr+S of SPEX looks like the following (description can be found at [17]).

```
#####  
### Input file ###  
#####  
BZ 5 5 1  
JOB DIELEC +:{0:1.1,0.002}/10  
ITERATE SR  
STOREIBZ  
NBAND 1800  
MEM 400000  
SECTION WFPROD
```

```

FFT 6
END
SECTION MBASIS
  OPTIMIZE MB 3.2
END
SECTION SUSCEP
  HILBERT 400 30
END
RESTART 03000
KPT +=(0, .06666, 0)

```

C.3 List of materials (supercells)

In the following the full specification of the unit cells (including the defect systems) is given. The unit cells described are the ones after spatial relaxation, meaning the ones used for the band structure and EELS calculations.

To make usage in other tools and for further research as easy as possible the common XSF format is used. This can be directly copied to several other tools. The relevant part of the format used here is described in the following. The file for MoS₂+P is used as an example:

Following the first two initial lines the lattice vectors are given. Each row corresponds to one primitive vector. The coordinates are given in Angstrom. This block of three rows is followed by the coordinates of the atoms. Starting with the word "PRIMCOORD" and followed by the next line stating the number of atoms (27) and the number (1) that can be ignored. The atoms are defined per row, First the ordering number in the periodic system (42) and then the Cartesian coordinate in Angstrom. If forces on the atoms would be included, these would follow in the same row in Cartesian coordinates in the units of Hartree per Angstrom.

C.3.1 MoS₂+P

```

CRYSTAL
PRIMVEC
4.7249996 -8.1839394 .0000000
4.7249996 8.1839394 .0000000

```

```

.0000000 .0000000 12.2999990
PRIMCOORD
      27  1
42  .0000000 1.8223358 1.5782739
42  -1.5781891 -.9111679 1.5782739
42  1.5781891 -.9111679 1.5782739
15  .0000000 .0000000 -.0048391
16  .0000000 .0000000 3.1535600
42  1.5794465 4.5440658 1.5778761
42  -1.5794465 4.5440658 1.5778761
42  .0000000 7.2797473 1.5778761
16  1.5781468 2.7266448 -.0048654
16  -1.5722703 -2.7300376 -.0048654
16  1.5722703 -2.7300376 -.0048654
16  3.1504171 .0033928 -.0048654
16  -1.5781468 2.7266448 -.0048654
16  -3.1504171 .0033928 -.0048654
16  1.5866501 2.7277299 3.1563438
16  -1.5689583 -2.7379443 3.1563438
16  1.5689583 -2.7379443 3.1563438
16  3.1556085 .0102144 3.1563438
16  -1.5866501 2.7277299 3.1563438
16  -3.1556085 .0102144 3.1563438
42  3.1539076 1.8209094 1.5721834
42  .0000000 -3.6418188 1.5721834
42  -3.1539076 1.8209094 1.5721834
16  .0000000 -5.4559596 -.0093940
16  .0000000 -5.4559596 3.1520273
16  .0000000 5.4559596 .0016686
16  .0000000 5.4559596 3.1500959

```

C.3.2 MoS₂+Cr (@ Mo)

```

CRYSTAL
PRIMVEC

```

7.8749994 -13.6398991 .0000000
7.8749994 13.6398991 .0000000
.0000000 .0000000 12.2999990

PRIMCOORD

75 1

24 .0000000 .0000000 .0000000
16 .0000000 -1.7434048 -1.5278856
16 .0000000 -1.7434048 1.5278856
16 1.5098328 .8717024 -1.5278856
16 1.5098328 .8717024 1.5278856
16 -1.5098328 .8717024 -1.5278856
16 -1.5098328 .8717024 1.5278856
42 1.5639396 2.7197356 .0000000
42 -1.5733903 -2.7142792 .0000000
42 1.5733903 -2.7142792 .0000000
42 3.1373299 -.0054564 .0000000
42 -1.5639396 2.7197356 .0000000
42 -3.1373299 -.0054564 .0000000
42 3.1470079 5.4508060 .0000000
42 -3.1470325 -5.4507918 .0000000
42 3.1470325 -5.4507918 .0000000
42 6.2940405 -.0000142 .0000000
42 -3.1470079 5.4508060 .0000000
42 -6.2940405 -.0000142 .0000000
16 3.1424306 3.6269202 -1.5755363
16 3.1424306 3.6269202 1.5755363
16 -1.5697897 -4.5348848 -1.5755363
16 -1.5697897 -4.5348848 1.5755363
16 1.5697897 -4.5348848 -1.5755363
16 1.5697897 -4.5348848 1.5755363
16 4.7122203 .9079646 -1.5755363
16 4.7122203 .9079646 1.5755363
16 -3.1424306 3.6269202 -1.5755363
16 -3.1424306 3.6269202 1.5755363
16 -4.7122203 .9079646 -1.5755363

16 -4.7122203 .9079646 1.5755363
16 -3.1512584 -7.2738862 -1.5735286
16 -3.1512584 -7.2738862 1.5735286
16 3.1512584 -7.2738862 -1.5735286
16 3.1512584 -7.2738862 1.5735286
16 .0000000 -12.7320258 -1.5735286
16 .0000000 -12.7320258 1.5735286
16 3.1475888 -1.8172613 -1.5792373
16 3.1475888 -1.8172613 1.5792373
16 .0000000 3.6345225 -1.5792373
16 .0000000 3.6345225 1.5792373
16 -3.1475888 -1.8172613 -1.5792373
16 -3.1475888 -1.8172613 1.5792373
42 4.7192556 2.7246635 .0000000
42 .0000000 -5.4493270 .0000000
42 -4.7192556 2.7246635 .0000000
42 -1.5760002 -8.1833619 .0000000
42 .0000000 -10.9130743 .0000000
42 1.5760002 -8.1833619 .0000000
16 -1.5773069 -10.0039246 -1.5733683
16 -1.5773069 -10.0039246 1.5733683
16 .0000000 -7.2719489 -1.5733683
16 .0000000 -7.2719489 1.5733683
16 1.5773069 -10.0039246 -1.5733683
16 1.5773069 -10.0039246 1.5733683
42 4.7230577 -2.7268586 .0000000
42 .0000000 5.4537172 .0000000
42 -4.7230577 -2.7268586 .0000000
16 4.7236395 -4.5458046 -1.5748218
16 4.7236395 -4.5458046 1.5748218
16 6.2986020 -1.8178895 -1.5748218
16 6.2986020 -1.8178895 1.5748218
16 -1.5749625 6.3636941 -1.5748218
16 -1.5749625 6.3636941 1.5748218
16 -6.2986020 -1.8178895 -1.5748218

```

16 -6.2986020 -1.8178895 1.5748218
16 1.5749625 6.3636941 -1.5748218
16 1.5749625 6.3636941 1.5748218
16 -4.7236395 -4.5458046 -1.5748218
16 -4.7236395 -4.5458046 1.5748218
42 -1.5758122 8.1834705 .0000000
42 .0000000 10.9128572 .0000000
42 1.5758122 8.1834705 .0000000
16 .0000000 9.0932660 -1.5747695
16 .0000000 9.0932660 1.5747695

```

C.3.3 MoS₂+Cr (@ S)

CRYSTAL

PRIMVEC

```

7.8749994 -13.6398991 .0000000
7.8749994 13.6398991 .0000000
.0000000 .0000000 12.2999990

```

PRIMCOORD

```

      75  1
42 .0000000 1.8122522 1.6470775
42 -1.5694564 -.9061261 1.6470775
42 1.5694564 -.9061261 1.6470775
24 .0000000 .0000000 -.4273585
16 .0000000 .0000000 3.2016413
42 1.5742650 4.5375309 1.5708930
42 -3.1424845 -3.6321189 1.5708930
42 3.1424845 -3.6321189 1.5708930
42 4.7167495 -.9054119 1.5708930
42 -1.5742650 4.5375309 1.5708930
42 -4.7167495 -.9054119 1.5708930
16 1.5381576 2.6653691 .0100050
16 -1.5391985 -2.6647681 .0100050
16 1.5391985 -2.6647681 .0100050
16 3.0773561 -.0006010 .0100050

```

16 -1.5381576 2.6653691 .0100050
16 -3.0773561 -.0006010 .0100050
16 1.5921029 2.7453984 3.1894756
16 -1.5815333 -2.7515008 3.1894756
16 1.5815333 -2.7515008 3.1894756
16 3.1736362 .0061023 3.1894756
16 -1.5921029 2.7453984 3.1894756
16 -3.1736362 .0061023 3.1894756
42 3.1503231 7.2744261 1.5703433
42 -3.1503231 7.2744261 1.5703433
42 .0000000 12.7309459 1.5703433
16 3.1481226 5.4514014 -.0076351
16 -3.1469908 -5.4520548 -.0076351
16 3.1469908 -5.4520548 -.0076351
16 6.2951134 .0006534 -.0076351
16 -3.1481226 5.4514014 -.0076351
16 -6.2951134 .0006534 -.0076351
16 3.1474952 5.4570633 3.1489367
16 -3.1522078 -5.4543425 3.1489367
16 3.1522078 -5.4543425 3.1489367
16 6.2997031 -.0027208 3.1489367
16 -3.1474952 5.4570633 3.1489367
16 -6.2997031 -.0027208 3.1489367
42 3.1360903 1.8106226 1.5867501
42 .0000000 -3.6212451 1.5867501
42 -3.1360903 1.8106226 1.5867501
42 4.7237481 4.5478335 1.5720132
42 -1.5766653 -6.3648026 1.5720132
42 6.3004133 1.8169691 1.5720132
42 1.5766653 -6.3648026 1.5720132
42 -6.3004133 1.8169691 1.5720132
42 -4.7237481 4.5478335 1.5720132
16 4.7170658 2.7233992 .0016364
16 .0000000 -5.4467984 .0016364
16 -4.7170658 2.7233992 .0016364

```

16 4.7253654 2.7281910 3.1466441
16 .0000000 -5.4563819 3.1466441
16 -4.7253654 2.7281910 3.1466441
16 -1.5743245 -8.1843294 -.0049551
16 .0000000 -10.9111393 -.0049551
16 1.5743245 -8.1843294 -.0049551
16 -1.5762513 -8.1832169 3.1525231
16 .0000000 -10.9133643 3.1525231
16 1.5762513 -8.1832169 3.1525231
16 4.7236528 -2.7272022 -.0045587
16 .0000000 5.4544044 -.0045587
16 -4.7236528 -2.7272022 -.0045587
16 4.7210222 -2.7256834 3.1449317
16 .0000000 5.4513669 3.1449317
16 -4.7210222 -2.7256834 3.1449317
42 .0000000 -9.0932660 1.5747800
42 -1.5752419 10.0027324 1.5736662
42 .0000000 7.2743333 1.5736662
42 1.5752419 10.0027324 1.5736662
16 -1.5745741 8.1841853 -.0045695
16 .0000000 10.9114276 -.0045695
16 1.5745741 8.1841853 -.0045695
16 -1.5759453 8.1833936 3.1525093
16 .0000000 10.9130109 3.1525093
16 1.5759453 8.1833936 3.1525093

```

C.3.4 MoS₂+Cr+S

```

CRYSTAL
PRIMVEC
7.8749994 -13.6398991 .0000000
7.8749994 13.6398991 .0000000
.0000000 .0000000 12.2999990
PRIMCOORD
76 1

```

42 .0000000 1.9545556 1.5290634
42 -1.6926948 -.9772778 1.5290634
42 1.6926948 -.9772778 1.5290634
16 .0000000 .0000000 .1233758
24 .0000000 .0000000 2.9824138
16 .0000000 .0000000 4.9994112
42 1.5926092 4.5597739 1.5636095
42 -3.1525754 -3.6591270 1.5636095
42 3.1525754 -3.6591270 1.5636095
42 4.7451846 -.9006469 1.5636095
42 -1.5926092 4.5597739 1.5636095
42 -4.7451846 -.9006469 1.5636095
16 1.6184567 2.7608798 -.0437766
16 -1.5817637 -2.7820645 -.0437766
16 1.5817637 -2.7820645 -.0437766
16 3.2002204 .0211847 -.0437766
16 -1.6184567 2.7608798 -.0437766
16 -3.2002204 .0211847 -.0437766
16 1.5675339 2.7354523 3.1416291
16 -1.5852043 -2.7252503 3.1416291
16 1.5852043 -2.7252503 3.1416291
16 3.1527381 -.0102020 3.1416291
16 -1.5675339 2.7354523 3.1416291
16 -3.1527381 -.0102020 3.1416291
42 3.1509974 7.2740369 1.5774337
42 -3.1509974 7.2740369 1.5774337
42 .0000000 12.7317244 1.5774337
16 3.1640314 5.4681269 -.0023914
16 -3.1535211 -5.4741950 -.0023914
16 3.1535211 -5.4741950 -.0023914
16 6.3175526 .0060681 -.0023914
16 -3.1640314 5.4681269 -.0023914
16 -6.3175526 .0060681 -.0023914
16 3.1525981 5.4593742 3.1529621
16 -3.1516577 -5.4599171 3.1529621

16 3.1516577 -5.4599171 3.1529621
16 6.3042558 .0005429 3.1529621
16 -3.1525981 5.4593742 3.1529621
16 -6.3042558 .0005429 3.1529621
42 3.1398869 1.8128145 1.5699602
42 .0000000 -3.6256291 1.5699602
42 -3.1398869 1.8128145 1.5699602
42 4.7270325 4.5532152 1.5797134
42 -1.5796838 -6.3703378 1.5797134
42 6.3067163 1.8171226 1.5797134
42 1.5796838 -6.3703378 1.5797134
42 -6.3067163 1.8171226 1.5797134
42 -4.7270325 4.5532152 1.5797134
16 4.7298409 2.7307749 .0186868
16 .0000000 -5.4615499 .0186868
16 -4.7298409 2.7307749 .0186868
16 4.7184387 2.7241919 3.1414907
16 .0000000 -5.4483837 3.1414907
16 -4.7184387 2.7241919 3.1414907
16 -1.5733319 -8.1849025 .0039901
16 .0000000 -10.9099932 .0039901
16 1.5733319 -8.1849025 .0039901
16 -1.5725476 -8.1853553 3.1531597
16 .0000000 -10.9090876 3.1531597
16 1.5725476 -8.1853553 3.1531597
16 4.7304220 -2.7311104 .0040533
16 .0000000 5.4622208 .0040533
16 -4.7304220 -2.7311104 .0040533
16 4.7272322 -2.7292688 3.1357442
16 .0000000 5.4585376 3.1357442
16 -4.7272322 -2.7292688 3.1357442
42 .0000000 -9.0932660 1.5779319
42 -1.5721183 10.0009290 1.5731258
42 .0000000 7.2779401 1.5731258
42 1.5721183 10.0009290 1.5731258

```

16 -1.5754669 8.1836698 .0021744
16 .0000000 10.9124585 .0021744
16 1.5754669 8.1836698 .0021744
16 -1.5735262 8.1847903 3.1476712
16 .0000000 10.9102176 3.1476712
16 1.5735262 8.1847903 3.1476712

```

C.3.5 MoS₂+vacancy

CRYSTAL

PRIMVEC

```

4.7249996 -8.1839394 .0000000
4.7249996 8.1839394 .0000000
.0000000 .0000000 12.2999990

```

PRIMCOORD

```

          26  1
42 .0000000 1.7717995 1.6143630
42 -1.5344233 -.8858997 1.6143630
42 1.5344233 -.8858997 1.6143630
16 .0000000 .0000000 3.1979759
42 1.5742919 4.5470418 1.5443583
42 -1.5742919 4.5470418 1.5443583
42 .0000000 7.2737954 1.5443583
16 1.5432760 2.6629977 .0035067
16 -1.5345856 -2.6680150 .0035067
16 1.5345856 -2.6680150 .0035067
16 3.0778616 .0050174 .0035067
16 -1.5432760 2.6629977 .0035067
16 -3.0778616 .0050174 .0035067
16 1.5529012 2.7377194 3.1506847
16 -1.5944839 -2.7137116 3.1506847
16 1.5944839 -2.7137116 3.1506847
16 3.1473852 -.0240078 3.1506847
16 -1.5529012 2.7377194 3.1506847
16 -3.1473852 -.0240078 3.1506847

```

```

42  3.1279933  1.8059478  1.5799395
42  .0000000  -3.6118955  1.5799395
42  -3.1279933  1.8059478  1.5799395
16  .0000000  -5.4559596  .0186904
16  .0000000  -5.4559596  3.1389256
16  .0000000  5.4559596  -.0389491
16  .0000000  5.4559596  3.1045032

```

C.3.6 MoS₂ rotated supercell

```

SLAB
PRIMVEC
2.7279811  -4.7250019  .0000000
2.7279811  4.7250019  .0000000
.0000000  .0000000  6.6147151
PRIMCOORD
      9  1
42  .0000000  .0000000  .0000000
42  .0000000  -3.1500013  .0000000
42  .0000000  3.1500013  .0000000
16  .9093270  -1.5750006  1.5867936
16  .9093270  1.5750006  1.5867936
16  -1.8186541  .0000000  1.5867936
16  .9093270  -1.5750006  -1.5867936
16  .9093270  1.5750006  -1.5867936
16  -1.8186541  .0000000  -1.5867936

```

C.3.7 MoSe₂+P

```

CRYSTAL
PRIMVEC
4.9245019  -8.5294875  .0000000
4.9245019  8.5294875  .0000000
.0000000  .0000000  12.9179534

```

PRIMCOORD

```
      27  1
42  .0000000  1.8805477  1.6870263
42  -1.6286021  -.9402739  1.6870263
42  1.6286021  -.9402739  1.6870263
15  .0000000  .0000000  .1826497
34  .0000000  .0000000  3.3984910
42  1.6444520  4.7369002  1.6693100
42  -1.6444520  4.7369002  1.6693100
42  .0000000  7.5851746  1.6693100
34  1.6360201  2.8303629  -.0126935
34  -1.6331561  -2.8320164  -.0126935
34  1.6331561  -2.8320164  -.0126935
34  3.2691762  .0016535  -.0126935
34  -1.6360201  2.8303629  -.0126935
34  -3.2691762  .0016535  -.0126935
34  1.6521625  2.8455771  3.3611731
34  -1.6382608  -2.8536032  3.3611731
34  1.6382608  -2.8536032  3.3611731
34  3.2904233  .0080261  3.3611731
34  -1.6521625  2.8455771  3.3611731
34  -3.2904233  .0080261  3.3611731
42  3.2844815  1.8962963  1.6698988
42  .0000000  -3.7925926  1.6698988
42  -3.2844815  1.8962963  1.6698988
34  .0000000  -5.6863250  -.0191125
34  .0000000  -5.6863250  3.3537381
34  .0000000  5.6863250  -.0153052
34  .0000000  5.6863250  3.3487250
```

C.3.8 MoSe₂+Cr (@ Mo)

CRYSTAL

PRIMVEC

8.2075032 -14.2158125 .0000000

8.2075032 14.2158125 .0000000
.0000000 .0000000 12.9179534

PRIMCOORD

75 1

24 .0000000 .0000000 .0000000
34 .0000000 -1.8447116 -1.6437102
34 .0000000 -1.8447116 1.6437102
34 1.5975671 .9223558 -1.6437102
34 1.5975671 .9223558 1.6437102
34 -1.5975671 .9223558 -1.6437102
34 -1.5975671 .9223558 1.6437102
42 1.6365129 2.8467996 .0000000
42 -1.6471443 -2.8406616 .0000000
42 1.6471443 -2.8406616 .0000000
42 3.2836572 -.0061380 .0000000
42 -1.6365129 2.8467996 .0000000
42 -3.2836572 -.0061380 .0000000
42 3.2819834 5.6842360 .0000000
42 -3.2817010 -5.6843990 .0000000
42 3.2817010 -5.6843990 .0000000
42 6.5636844 .0001630 .0000000
42 -3.2819834 5.6842360 .0000000
42 -6.5636844 .0001630 .0000000
34 3.2823204 3.7874156 -1.6843097
34 3.2823204 3.7874156 1.6843097
34 -1.6388379 -4.7362806 -1.6843097
34 -1.6388379 -4.7362806 1.6843097
34 1.6388379 -4.7362806 -1.6843097
34 1.6388379 -4.7362806 1.6843097
34 4.9211583 .9488650 -1.6843097
34 4.9211583 .9488650 1.6843097
34 -3.2823204 3.7874156 -1.6843097
34 -3.2823204 3.7874156 1.6843097
34 -4.9211583 .9488650 -1.6843097
34 -4.9211583 .9488650 1.6843097

34 -3.2838387 -7.5812832 -1.6824295
34 -3.2838387 -7.5812832 1.6824295
34 3.2838387 -7.5812832 -1.6824295
34 3.2838387 -7.5812832 1.6824295
34 .0000000 -13.2690587 -1.6824295
34 .0000000 -13.2690587 1.6824295
34 3.2825109 -1.8951586 -1.6863254
34 3.2825109 -1.8951586 1.6863254
34 .0000000 3.7903171 -1.6863254
34 .0000000 3.7903171 1.6863254
34 -3.2825109 -1.8951586 -1.6863254
34 -3.2825109 -1.8951586 1.6863254
42 4.9226831 2.8421124 .0000000
42 .0000000 -5.6842248 .0000000
42 -4.9226831 2.8421124 .0000000
42 -1.6420668 -8.5291606 .0000000
42 .0000000 -11.3733038 .0000000
42 1.6420668 -8.5291606 .0000000
34 -1.6421230 -10.4252885 -1.6824990
34 -1.6421230 -10.4252885 1.6824990
34 .0000000 -7.5810480 -1.6824990
34 .0000000 -7.5810480 1.6824990
34 1.6421230 -10.4252885 -1.6824990
34 1.6421230 -10.4252885 1.6824990
42 4.9237562 -2.8427320 .0000000
42 .0000000 5.6854639 .0000000
42 -4.9237562 -2.8427320 .0000000
34 4.9242712 -4.7381276 -1.6830970
34 4.9242712 -4.7381276 1.6830970
34 6.5654745 -1.8954801 -1.6830970
34 6.5654745 -1.8954801 1.6830970
34 -1.6412033 6.6336077 -1.6830970
34 -1.6412033 6.6336077 1.6830970
34 -6.5654745 -1.8954801 -1.6830970
34 -6.5654745 -1.8954801 1.6830970

```

34 1.6412033 6.6336077 -1.6830970
34 1.6412033 6.6336077 1.6830970
34 -4.9242712 -4.7381276 -1.6830970
34 -4.9242712 -4.7381276 1.6830970
42 -1.6418266 8.5292993 .0000000
42 .0000000 11.3730264 .0000000
42 1.6418266 8.5292993 .0000000
34 .0000000 9.4772083 -1.6843111
34 .0000000 9.4772083 1.6843111

```

C.3.9 MoSe₂+Cr (@ S)

CRYSTAL

PRIMVEC

```

8.2075032 -14.2158125 .0000000
8.2075032 14.2158125 .0000000
.0000000 .0000000 12.9179534

```

PRIMCOORD

```

      75 1
42 .0000000 1.8691787 1.7458246
42 -1.6187562 -.9345894 1.7458246
42 1.6187562 -.9345894 1.7458246
24 .0000000 .0000000 -.2565957
34 .0000000 .0000000 3.4247798
42 1.6395791 4.7237963 1.6768751
42 -3.2711381 -3.7818153 1.6768751
42 3.2711381 -3.7818153 1.6768751
42 4.9107172 -.9419810 1.6768751
42 -1.6395791 4.7237963 1.6768751
42 -4.9107172 -.9419810 1.6768751
34 1.6026410 2.7750973 .0027772
34 -1.6019843 -2.7754765 .0027772
34 1.6019843 -2.7754765 .0027772
34 3.2046253 .0003791 .0027772
34 -1.6026410 2.7750973 .0027772

```

34 -3.2046253 .0003791 .0027772
34 1.6502324 2.8535372 3.4005854
34 -1.6461195 -2.8559118 3.4005854
34 1.6461195 -2.8559118 3.4005854
34 3.2963519 .0023746 3.4005854
34 -1.6502324 2.8535372 3.4005854
34 -3.2963519 .0023746 3.4005854
42 3.2834088 7.5815314 1.6747089
42 -3.2834088 7.5815314 1.6747089
42 .0000000 13.2685623 1.6747089
34 3.2796208 5.6791937 -.0078908
34 -3.2785157 -5.6798318 -.0078908
34 3.2785157 -5.6798318 -.0078908
34 6.5581365 .0006381 -.0078908
34 -3.2796208 5.6791937 -.0078908
34 -6.5581365 .0006381 -.0078908
34 3.2782798 5.6857935 3.3582757
34 -3.2849018 -5.6819704 3.3582757
34 3.2849018 -5.6819704 3.3582757
34 6.5631816 -.0038232 3.3582757
34 -3.2782798 5.6857935 3.3582757
34 -6.5631816 -.0038232 3.3582757
42 3.2612067 1.8828586 1.6938398
42 .0000000 -3.7657171 1.6938398
42 -3.2612067 1.8828586 1.6938398
42 4.9219898 4.7400984 1.6773091
42 -1.6440507 -6.6326174 1.6773091
42 6.5660405 1.8925190 1.6773091
42 1.6440507 -6.6326174 1.6773091
42 -6.5660405 1.8925190 1.6773091
42 -4.9219898 4.7400984 1.6773091
34 4.9100511 2.8348193 .0068247
34 .0000000 -5.6696386 .0068247
34 -4.9100511 2.8348193 .0068247
34 4.9190656 2.8400238 3.3539329

34 .0000000 -5.6800477 3.3539329
 34 -4.9190656 2.8400238 3.3539329
 34 -1.6408480 -8.5298643 -.0042008
 34 .0000000 -11.3718964 -.0042008
 34 1.6408480 -8.5298643 -.0042008
 34 -1.6435922 -8.5282799 3.3646221
 34 .0000000 -11.3750652 3.3646221
 34 1.6435922 -8.5282799 3.3646221
 34 4.9203226 -2.8407496 -.0036342
 34 .0000000 5.6814991 -.0036342
 34 -4.9203226 -2.8407496 -.0036342
 34 4.9157065 -2.8380845 3.3520482
 34 .0000000 5.6761690 3.3520482
 34 -4.9157065 -2.8380845 3.3520482
 42 .0000000 -9.4772083 1.6819546
 42 -1.6422726 10.4253749 1.6790342
 42 .0000000 7.5808753 1.6790342
 42 1.6422726 10.4253749 1.6790342
 34 -1.6408140 8.5298839 -.0045002
 34 .0000000 11.3718572 -.0045002
 34 1.6408140 8.5298839 -.0045002
 34 -1.6429823 8.5286321 3.3639803
 34 .0000000 11.3743608 3.3639803
 34 1.6429823 8.5286321 3.3639803

C.3.10 MoSe₂+Cr+Se

CRYSTAL

PRIMVEC

8.2075032 -14.2158125 .0000000
 8.2075032 14.2158125 .0000000
 .0000000 .0000000 12.9179534

PRIMCOORD

76 1
 42 .0000000 2.0353505 1.6417547

42 -1.7626653 -1.0176753 1.6417547
42 1.7626653 -1.0176753 1.6417547
34 .0000000 .0000000 .1017407
24 .0000000 .0000000 3.0049323
34 .0000000 .0000000 5.1796562
42 1.6556384 4.7406468 1.6767221
42 -3.2777013 -3.8041483 1.6767221
42 3.2777013 -3.8041483 1.6767221
42 4.9333397 -.9364985 1.6767221
42 -1.6556384 4.7406468 1.6767221
42 -4.9333397 -.9364985 1.6767221
34 1.6815579 2.8652252 -.0453967
34 -1.6405789 -2.8888844 -.0453967
34 1.6405789 -2.8888844 -.0453967
34 3.3221367 .0236592 -.0453967
34 -1.6815579 2.8652252 -.0453967
34 -3.3221367 .0236592 -.0453967
34 1.6290855 2.8380118 3.3765932
34 -1.6432476 -2.8298353 3.3765932
34 1.6432476 -2.8298353 3.3765932
34 3.2723331 -.0081765 3.3765932
34 -1.6290855 2.8380118 3.3765932
34 -3.2723331 -.0081765 3.3765932
42 3.2850654 7.5805750 1.6825630
42 -3.2850654 7.5805750 1.6825630
42 .0000000 13.2704751 1.6825630
34 3.2871886 5.6913047 -.0020772
34 -3.2852202 -5.6924412 -.0020772
34 3.2852202 -5.6924412 -.0020772
34 6.5724088 .0011365 -.0020772
34 -3.2871886 5.6913047 -.0020772
34 -6.5724088 .0011365 -.0020772
34 3.2827930 5.6865405 3.3675879
34 -3.2832920 -5.6862524 3.3675879
34 3.2832920 -5.6862524 3.3675879

34 6.5660851 -.0002881 3.3675879
34 -3.2827930 5.6865405 3.3675879
34 -6.5660851 -.0002881 3.3675879
42 3.2634037 1.8841270 1.6880378
42 .0000000 -3.7682541 1.6880378
42 -3.2634037 1.8841270 1.6880378
42 4.9233673 4.7442765 1.6835794
42 -1.6469803 -6.6358993 1.6835794
42 6.5703476 1.8916229 1.6835794
42 1.6469803 -6.6358993 1.6835794
42 -6.5703476 1.8916229 1.6835794
42 -4.9233673 4.7442765 1.6835794
34 4.9242692 2.8430282 .0132172
34 .0000000 -5.6860563 .0132172
34 -4.9242692 2.8430282 .0132172
34 4.9237843 2.8427482 3.3601825
34 .0000000 -5.6854963 3.3601825
34 -4.9237843 2.8427482 3.3601825
34 -1.6413592 -8.5295691 .0005079
34 .0000000 -11.3724867 .0005079
34 1.6413592 -8.5295691 .0005079
34 -1.6410680 -8.5297373 3.3647332
34 .0000000 -11.3721504 3.3647332
34 1.6410680 -8.5297373 3.3647332
34 4.9251155 -2.8435168 .0034178
34 .0000000 5.6870336 .0034178
34 -4.9251155 -2.8435168 .0034178
34 4.9259121 -2.8439767 3.3606276
34 .0000000 5.6879533 3.3606276
34 -4.9259121 -2.8439767 3.3606276
42 .0000000 -9.4772083 1.6827088
42 -1.6408939 10.4245789 1.6810132
42 .0000000 7.5824673 1.6810132
42 1.6408939 10.4245789 1.6810132
34 -1.6417570 8.5293395 .0008323

```

34 .0000000 11.3729460 .0008323
34 1.6417570 8.5293395 .0008323
34 -1.6414607 8.5295106 3.3628682
34 .0000000 11.3726038 3.3628682
34 1.6414607 8.5295106 3.3628682

```

C.3.11 MoSe₂+vacancy

CRYSTAL

PRIMVEC

```

4.9245019 -8.5294875 .0000000
4.9245019 8.5294875 .0000000
.0000000 .0000000 12.9179534

```

PRIMCOORD

```

      26  1
42 .0000000 1.8095228 1.7275535
42 -1.5670927 -.9047614 1.7275535
42 1.5670927 -.9047614 1.7275535
34 .0000000 .0000000 3.4515029
42 1.6420678 4.7382767 1.6495251
42 -1.6420678 4.7382767 1.6495251
42 .0000000 7.5824216 1.6495251
34 1.5968942 2.7662155 .0019896
34 -1.5971658 -2.7660586 .0019896
34 1.5971658 -2.7660586 .0019896
34 3.1940600 -.0001568 .0019896
34 -1.5968942 2.7662155 .0019896
34 -3.1940600 -.0001568 .0019896
34 1.6136987 2.8474230 3.3583226
34 -1.6590913 -2.8212156 3.3583226
34 1.6590913 -2.8212156 3.3583226
34 3.2727900 -.0262074 3.3583226
34 -1.6136987 2.8474230 3.3583226
34 -3.2727900 -.0262074 3.3583226
42 3.2522038 1.8776607 1.6823171

```

```
42 .0000000 -3.7553214 1.6823171
42 -3.2522038 1.8776607 1.6823171
34 .0000000 -5.6863250 .0185766
34 .0000000 -5.6863250 3.3404669
34 .0000000 5.6863250 -.0398778
34 .0000000 5.6863250 3.3157728
```

C.3.12 MoSe₂+Cr (interstitial)

CRYSTAL

PRIMVEC

```
8.2075032 -14.2158125 .0000000
8.2075032 14.2158125 .0000000
.0000000 .0000000 12.9179534
```

PRIMCOORD

```
76 1
24 -.0003618 -3.7908329 .0028323
42 -.0002284 .0328317 .0004780
34 -.0004554 -1.9165305 -1.6276154
34 -.0004574 -1.9154161 1.6308406
42 1.6470987 2.8453048 -.0001227
34 1.6505158 .9511234 -1.6932449
34 1.6511104 .9514516 1.6931240
42 3.2833388 5.6800280 -.0001842
34 3.2780369 3.7936287 -1.7004305
34 3.2780711 3.7936348 1.7001500
42 -3.3121387 -5.7027283 .0004090
34 -3.2819405 -7.5910866 -1.6930978
34 -3.2820139 -7.5916828 1.6930024
42 -1.9959657 -2.6389498 .0011300
34 -1.6238393 -4.7273919 -1.6272985
34 -1.6249122 -4.7278087 1.6305269
42 1.9952798 -2.6389484 .0011538
34 1.6230941 -4.7274603 -1.6272404
34 1.6241762 -4.7278810 1.6305002
```

42 3.3321839 .0345705 -.0002864
34 3.4423042 -1.8029823 -1.7991192
34 3.4436726 -1.8021572 1.7995157
42 4.9214881 2.8446409 -.0002051
34 4.9504114 .9765370 -1.7039457
34 4.9502186 .9765286 1.7034551
42 -1.6474431 -8.5889046 -.0001467
34 -1.6534499 -10.4611932 -1.7036125
34 -1.6534955 -10.4611348 1.7032473
42 -.0003241 -6.0945610 .0011068
34 -.0001375 -7.7660900 -1.7986199
34 -.0001378 -7.7674540 1.7991483
42 3.3116203 -5.7026648 .0004177
34 3.2817387 -7.5909800 -1.6930747
34 3.2818177 -7.5915828 1.6929869
42 4.9777670 -2.8190395 -.0001916
34 4.9317654 -4.7328077 -1.6935119
34 4.9323677 -4.7324815 1.6933021
42 6.5765394 .0060331 -.0001555
34 6.6030019 -1.8876990 -1.7033762
34 6.6029062 -1.8877087 1.7030331
42 -.0000916 -11.3851851 -.0000837
34 -.0001359 -13.2680632 -1.7012287
34 -.0001313 -13.2680274 1.7010966
42 1.6472235 -8.5887952 -.0001445
34 1.6532917 -10.4610719 -1.7036040
34 1.6533386 -10.4610158 1.7032357
42 -3.2834946 5.6801494 -.0001843
34 -3.2781456 3.7937839 -1.7004451
34 -3.2781778 3.7937871 1.7001629
42 -1.6368060 8.5326434 -.0002141
34 -1.6406528 6.6335932 -1.6928480
34 -1.6407285 6.6336057 1.6925916
42 -.0002261 11.3691853 -.0001146
34 -.0001712 9.4718380 -1.7003212

```

34  -.0001675  9.4717375  1.7000745
42  -6.5768038  .0061408  -.0001587
34  -6.6035025  -1.8875992  -1.7034073
34  -6.6034019  -1.8876066  1.7030563
42  -4.9216547  2.8448064  -.0002073
34  -4.9507115  .9767544  -1.7039730
34  -4.9505113  .9767385  1.7034724
42  -1.6472506  2.8454212  -.0001232
34  -1.6508117  .9512756  -1.6932837
34  -1.6514107  .9516048  1.6931535
42  -.0000627  5.6858637  -.0000520
34  -.0000419  3.7917440  -1.6926661
34  -.0000386  3.7915859  1.6924329
42  1.6364795  8.5326450  -.0002189
34  1.6405435  6.6335538  -1.6928332
34  1.6406211  6.6335719  1.6925749
42  -4.9783005  -2.8189139  -.0002014
34  -4.9322102  -4.7327143  -1.6935255
34  -4.9328060  -4.7323827  1.6933047
42  -3.3325304  .0347960  -.0002963
34  -3.4429267  -1.8027209  -1.7991346
34  -3.4442756  -1.8019058  1.7994967

```

C.3.13 MoS₂+Se

The calculation are performed in the same unit cell for all concentrations. The starting point is always the relaxed unit cell (here already including one defect atom). After adding the according number of defects the cell is converged to a residual force of $5 \cdot 10^{-2}$ eV/Å. The final positions are noted with the according result graphs.

MoS₂+Se (1 out of 9) (unrelaxed)

```

CRYSTAL
PRIMVEC
4.7249996  -8.1839394  .0000000

```

```

4.7249996 8.1839394 .0000000
.0000000 .0000000 24.5999981
PRIMCOORD
      27  1
42 -3.1499998 .0000000 .0000000
42 -1.5749999 -2.7279798 .0000000
16 -3.1499998 -1.8186532 -1.5866999
34 -3.1499998 -1.8186532 1.5866999
42 -1.5749999 2.7279798 .0000000
42 1.5749999 -2.7279798 .0000000
16 -1.5749999 .9093266 -1.5866999
16 .0000000 -1.8186532 -1.5866999
16 -1.5749999 .9093266 1.5866999
16 .0000000 -1.8186532 1.5866999
42 -.0000000 5.4559596 .0000000
16 -.0000000 3.6373064 -1.5866999
16 3.1499998 -1.8186532 -1.5866999
16 -.0000000 3.6373064 1.5866999
16 3.1499998 -1.8186532 1.5866999
16 -1.5749999 -4.5466330 -1.5866999
16 .0000000 -7.2746128 -1.5866999
16 -1.5749999 -4.5466330 1.5866999
16 .0000000 -7.2746128 1.5866999
42 .0000000 .0000000 .0000000
42 1.5749999 2.7279798 .0000000
42 3.1499998 -.0000000 .0000000
16 1.5749999 .9093266 -1.5866999
16 1.5749999 .9093266 1.5866999
42 .0000000 -5.4559596 .0000000
16 1.5749999 -4.5466330 -1.5866999
16 1.5749999 -4.5466330 1.5866999

```

C.3.14 MoSe₂+S

Here two different concentrations are investigated. The relaxed positions for both are given.

MoSe₂+S (1 out of 9)

CRYSTAL

PRIMVEC

4.9245019 -8.5294875 .0000000

4.9245019 8.5294875 .0000000

.0000000 .0000000 12.9179534

PRIMCOORD

27 1

42 .0000000 1.8726945 1.6818588

42 -1.6218010 -.9363472 1.6818588

42 1.6218010 -.9363472 1.6818588

16 .0000000 .0000000 .1697965

34 .0000000 .0000000 3.3970648

42 1.6406554 4.7390922 1.6687896

42 -1.6406554 4.7390922 1.6687896

42 .0000000 7.5807907 1.6687896

34 1.6338552 2.8320263 -.0068463

34 -1.6356791 -2.8309733 -.0068463

34 1.6356791 -2.8309733 -.0068463

34 3.2695343 -.0010530 -.0068463

34 -1.6338552 2.8320263 -.0068463

34 -3.2695343 -.0010530 -.0068463

34 1.6402959 2.8435846 3.3548682

34 -1.6424686 -2.8423303 3.3548682

34 1.6424686 -2.8423303 3.3548682

34 3.2827645 -.0012544 3.3548682

34 -1.6402959 2.8435846 3.3548682

34 -3.2827645 -.0012544 3.3548682

42 3.2824014 1.8950953 1.6737653

42 .0000000 -3.7901907 1.6737653

```
42 -3.2824014 1.8950953 1.6737653
34 .0000000 -5.6863250 -.0069140
34 .0000000 -5.6863250 3.3580554
34 .0000000 5.6863250 -.0123090
34 .0000000 5.6863250 3.3530629
```

MoSe₂+S (3 out of 9)

CRYSTAL

PRIMVEC

```
4.9245019 -8.5294875 .0000000
4.9245019 8.5294875 .0000000
.0000000 .0000000 12.9179534
```

PRIMCOORD

27 1

```
42 .0189744 1.8846477 1.6875129
42 -1.6226655 -.9587561 1.6875129
42 1.6202433 -.9354478 1.6801314
16 -.0033130 .0019127 .1724456
34 -.0005967 .0003445 3.3966590
42 1.6607160 4.7275102 1.6875136
42 -1.6398871 4.7374078 1.6554806
42 .0018428 7.5809675 1.6554806
16 1.6381400 2.8450260 .1720420
16 -1.6447947 -2.8411840 .1720420
34 1.6183919 -2.8297666 -.0132967
34 3.2598456 .0133147 -.0132967
34 -1.6144256 2.8274327 -.0203095
34 -3.2558413 -.0155828 -.0203095
34 1.6408392 2.8434578 3.3967249
34 -1.6420871 -2.8427374 3.3967249
34 1.6450480 -2.8451588 3.3487887
34 3.2865037 -.0020740 3.3487887
34 -1.6445701 2.8448997 3.3425750
34 -3.2860405 .0017895 3.3425750
```

```

42  3.2613206  1.9076617  1.6800893
42  -.0214232 -3.7782174  1.6800893
42  -3.2810040  1.8942885  1.6555041
34  -.0231608 -5.6729531  -.0127504
34  .0034440  -5.6883134  3.3484580
34  .0271344  5.6706589  -.0197378
34  -.0031009  5.6881153  3.3422743

```

C.3.15 WSe₂+S

Here two different concentrations are investigated. The relaxed positions for both are found without SOC. The relaxed positions are then used as a starting point for the calculation including SOC, without further spatial relaxation.

WSe₂+S (1 out of 9)

CRYSTAL

PRIMVEC

```

4.9455019 -8.5658606 .0000000
4.9455019  8.5658606 .0000000
.0000000 .0000000 12.9820049

```

PRIMCOORD

27 1

```

74  .0000000 -3.8065477  1.6823610
74  3.2965670  1.9032738  1.6823610
74  -3.2965670  1.9032738  1.6823610
16  .0000000 .0000000 .1664901
34  .0000000 .0000000  3.4155012
74  1.6294025  -.9407360  1.6924276
74  -1.6294025  -.9407360  1.6924276
74  .0000000  1.8814720  1.6924276
34  1.6395510  2.8424096  -.0071350
34  -1.6418235 -2.8410976  -.0071350
34  1.6418235 -2.8410976  -.0071350
34  3.2813744  -.0013120  -.0071350

```

```

34 -1.6395510 2.8424096 -.0071350
34 -3.2813744 -.0013120 -.0071350
34 1.6483518 2.8569666 3.3714727
34 -1.6500298 -2.8559978 3.3714727
34 1.6500298 -2.8559978 3.3714727
34 3.2983816 -.0009688 3.3714727
34 -1.6483518 2.8569666 3.3714727
34 -3.2983816 -.0009688 3.3714727
74 -1.6484581 4.7588360 1.6760317
74 .0000000 7.6140492 1.6760317
74 1.6484581 4.7588360 1.6760317
34 .0000000 -5.7105737 -.0098245
34 .0000000 -5.7105737 3.3729669
34 .0000000 5.7105737 -.0155297
34 .0000000 5.7105737 3.3653143

```

MoSe₂+S (3 out of 9)

CRYSTAL

PRIMVEC

```

4.9455019 -8.5658606 .0000000
4.9455019 8.5658606 .0000000
.0000000 .0000000 12.9820049

```

PRIMCOORD

27 1

```

74 .0003629 -3.8076480 1.6725497
74 3.2977014 1.9035096 1.6725497
74 -3.2753859 1.8910448 1.6905035
16 -.0185888 .0107322 .1707409
34 -.0027288 .0015755 3.4053183
74 1.6276932 -.9397491 1.6795809
74 -1.6497882 -.9270275 1.6942854
74 -.0220648 1.8922723 1.6942854
34 1.6248397 2.8414063 -.0116493
34 -1.6483103 -2.8278556 -.0116493

```

```

34 1.6493028 -2.8530281 -.0129341
34 3.2954461 -.0018240 -.0129341
16 -1.6474451 2.8328686 .1644873
16 -3.2770586 .0102950 .1644873
34 1.6447501 2.8544383 3.3620553
34 -1.6496410 -2.8516145 3.3620553
34 1.6527777 -2.8567670 3.3572047
34 3.3004217 -.0029640 3.3572047
34 -1.6506849 2.8546729 3.4037020
34 -3.2975618 .0021986 3.4037020
74 -1.6478340 4.7336256 1.6736251
74 .0221449 7.6261140 1.6736251
74 1.6472209 4.7595503 1.6705006
34 .0226456 -5.7236482 -.0143423
34 .0062480 -5.7141810 3.3611070
34 -.0013030 5.7113260 -.0196188
34 -.0033497 5.7125077 3.3531819

```

C.4 Using quantities within the Fleur code

When working with results from Fleur or interpreting certain quantities in an experimental context, the atomic quantities within the Fleur code have to be converted to measurable quantities.

C.4.1 Reciprocal lattice vectors

In Fleur and SPEX the crystal is defined using reciprocal lattice vectors. Here is a quick summary how to convert them from internal coordinates to SI units.

The lattice is given in the input file for the input generator of Fleur using Bohr as a unit. One gives a matrix with each row containing one lattice vector with an additional factor for each column. As an example the MoS₂ monolayer is used, with a vacuum of 12.3Å.

$$\begin{pmatrix} 0.5 & -0.5 & 0 \\ 0.5 & 0.5 & 0 \\ 0 & 0 & 1 \end{pmatrix}$$
 is followed by a row containing the lattice constant of 5.9526 and another row of prefactors (here -3 corresponds to $\sqrt{3}$) for the columns of the matrix.

$(1 \ -3 \ 3.9047)$. This gives a total complete matrix of $\begin{pmatrix} 2.976 & -5.155 & 0 \\ 2.976 & 5.155 & 0 \\ 0 & 0 & 23.24 \end{pmatrix}$, which is in units of Bohr and is saved to the file `basis.hdf` in the entry `cell/amat`. The reciprocal lattice vectors are calculated by

$$b_i = 2\pi \frac{a_j \times a_k}{a_i \cdot (a_j \times a_k)} \quad (a_x \text{ corresponds to the lattice vectors}) \quad (\text{C.4.1})$$

and saved to the same file under `cell/bmat`. Here each column stands for one single reciprocal lattice vector in units of $\frac{1}{\text{Bohr}}$. $\begin{pmatrix} 1.0555 & 1.0555 & 0 \\ -0.6094 & 0.6094 & 0 \\ 0 & 0 & 0.2703 \end{pmatrix}$ So giving the

example of $\begin{pmatrix} 0.1 \\ 0.1 \\ 0 \end{pmatrix}$ in internal reciprocal coordinates, this corresponds to a vector of length $0.211 \frac{1}{\text{Bohr}}$.

Additional Remarks

D.1 Fourier transform 183
 D.2 Additional figures 183

D.1 Fourier transform

The Fourier transforms are defined as the following:

$$f(t) = \frac{1}{2\pi} \int \tilde{f}(\omega) e^{-i\omega t} d\omega \tag{D.1.1}$$

$$\tilde{f}(\omega) = \int f(t) e^{i\omega t} dt \tag{D.1.2}$$

$$f(\mathbf{r}) = \frac{1}{(2\pi)^3} \int \tilde{f}(\mathbf{q}) e^{i\mathbf{q}\mathbf{r}} d\mathbf{q} \tag{D.1.3}$$

$$\tilde{f}(\mathbf{q}) = \int f(\mathbf{r}) e^{-i\mathbf{q}\mathbf{r}} d\mathbf{r} \tag{D.1.4}$$

Therefore the delta function is defined with the following prefactor.

$$\delta(\omega) = \frac{1}{2\pi} \int e^{-i\omega t} dt \tag{D.1.5}$$

$$\delta(\mathbf{q}) = \frac{1}{(2\pi)^3} \int e^{-i\mathbf{q}\mathbf{r}} d\mathbf{r} \tag{D.1.6}$$

D.2 Additional figures

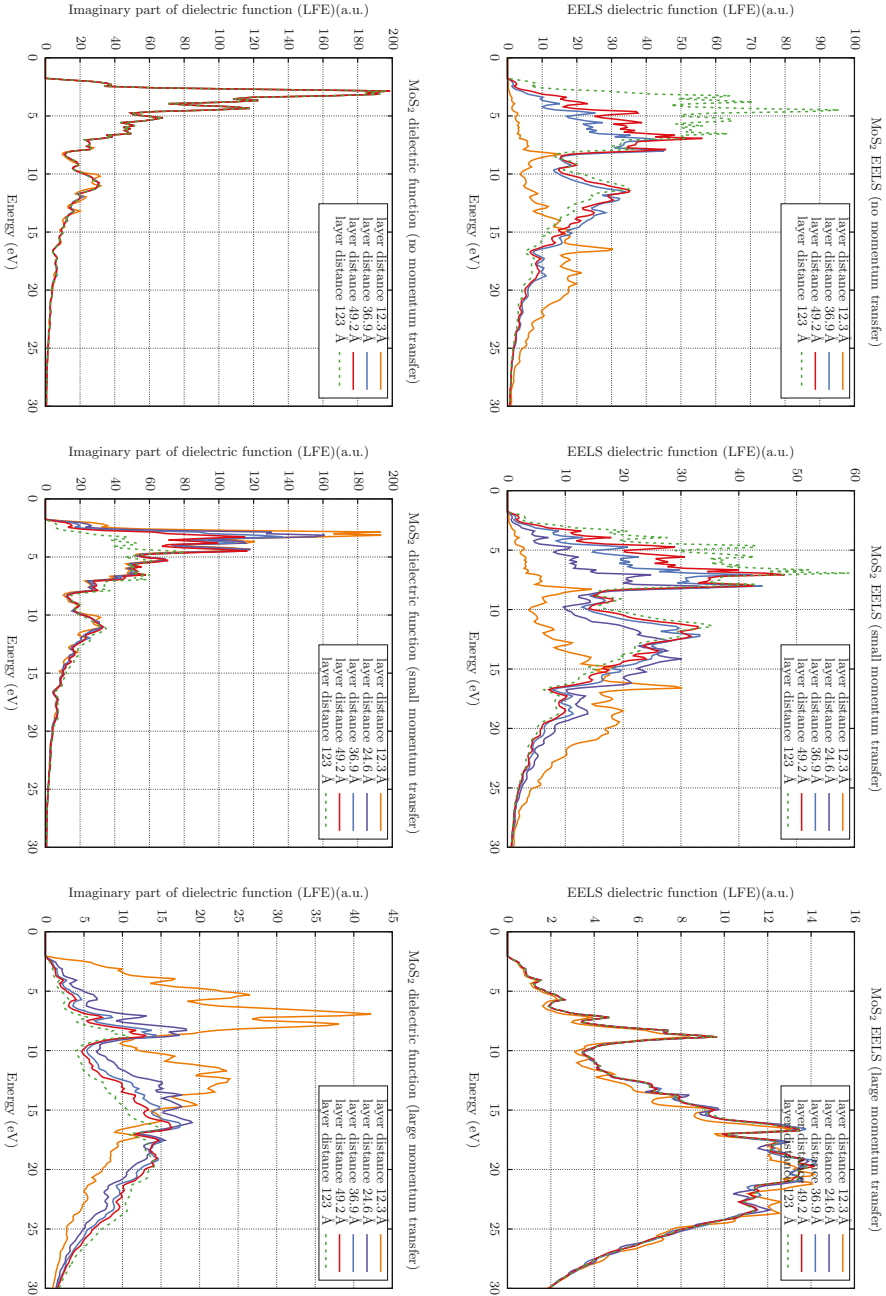


Figure D.1: Convergence behavior with interlayer distance and with momentum transfer (including LFE)

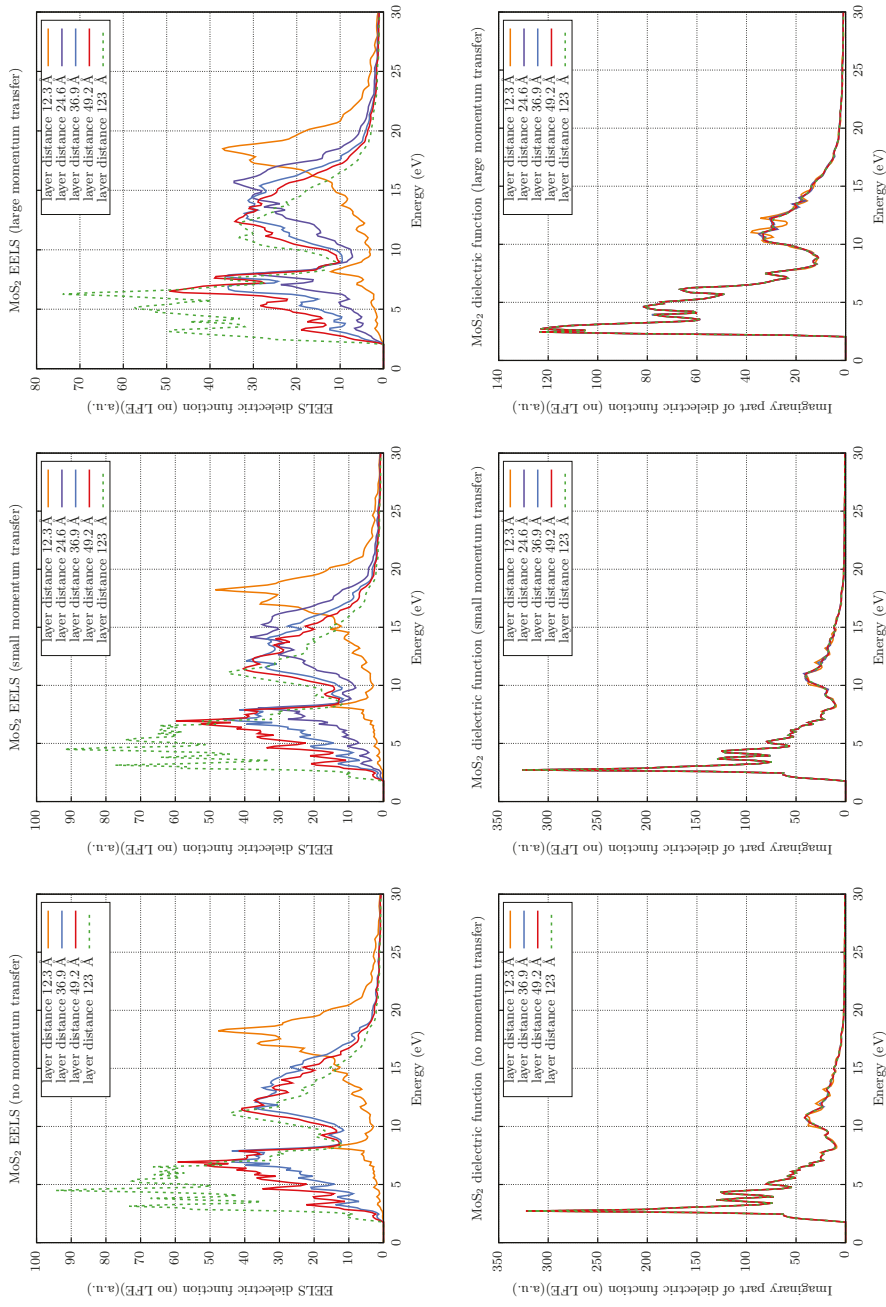


Figure D.2: Convergence behavior with interlayer distance and with momentum transfer (without LFE)

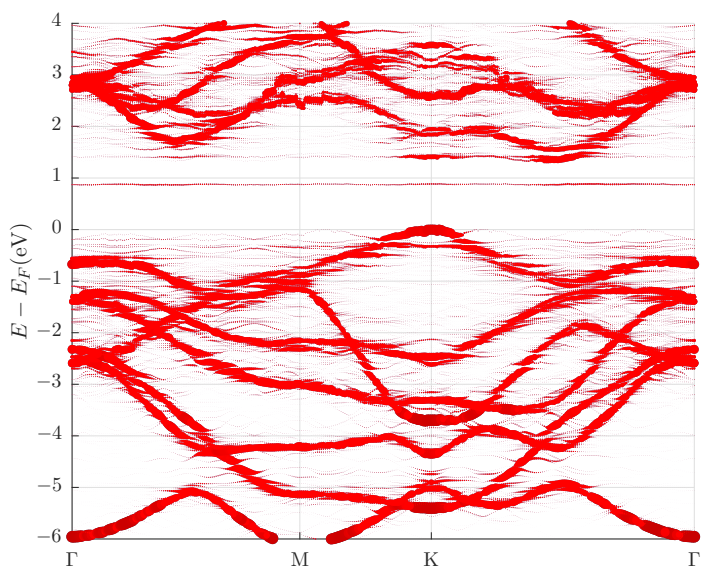


Figure D.3: Unfolded band structure for $\text{MoSe}_2+\text{Cr}+\text{Se}$, calculated in a 5×5 supercell with a similar DFT parameter set as MoSe_2+Cr (interstitial). The defect state within the band gap is clearly visible and not effected by the underconverged parameter set. The calculation includes two spins, which are degenerate due to the lack of SOC. This DFT calculation is used as a starting point for the absorption spectrum of $\text{MoSe}_2+\text{Cr}+\text{Se}$ in Fig. 5.7.

List of scientific contributions

Publications

- E. Moynihan, S. Rost, E. O’Connell, Q. Ramasse, C. Friedrich, U. Bangert. “Plasmons in MoS₂ studied via experimental and theoretical correlation of energy loss spectra.” *Journal of Microscopy* 279, 256–264 (2020) DOI:10.1111/jmi.12900
- M. Hennessy, S. Rost, M. Auge, E. Moynihan, M. Bui, H. Hofsaess, R. M. Wallace. “New single photon sources by optoelectronic tailoring of 2D materials using low energy ion implantation.” *Microscopy and Microanalysis*, 26(S2), 2832-2833 (2021) DOI:10.1017/S143192762002293X
- M. Bui, S. Rost, M. Auge, J. Tu, L. Zhou, I. Aguilera, S. Blügel, M. Ghorbani-Asl, A. Krasheninnikov, A. Hashemi, H. Komsa, L. Jin, L. Kibkalo, E. O’Connell, Q. Ramasse, U. Bangert, H. Hofsäss, D. Grützmacher, and B. Kardynal. “Low energy ion implantation of Se into MoS₂ monolayers.” *npj 2D Materials and Applications* 6, Article number: 42 (2022) DOI:10.1038/s41699-022-00318-4
- S. Rost, S. Blügel, and C. Friedrich. “Efficient calculation of **k**-integrated electron energy loss spectra: application to monolayers of MoS₂, hBN, and graphene.” submitted to: *Physical Review B*

Conference talks

- S. Rost, C. Friedrich, I. Aguilera, B. Kardynal, and S. Blügel. "Analysis of defect states in MoSe₂ and unfolding of defect band structure." Talk at: *ETFS Young Researcher Meeting, Donostia/San Sebastián, Spain, 2 Jun 2019 - 7 Jun 2019*
- S. Rost and C. Friedrich. "Electron Energy Loss Spectroscopy (EELS) for 2D materials." Talk at: *17th ETFS Young Researchers' Meeting, Cagliari, Italy, 6 Sep 2021 - 10 Sep 2021*
- S. Rost and C. Friedrich. "Electron Energy Loss Spectroscopy (EELS) for 2D materials." Talk at: *Discussion Meeting GDR-REST and ETFS, Palaiseau, France, 27 Apr 2022 - 28 Apr 2022*

Oral contributions

- S. Rost. "Band unfolding for supercell calculations." Talk at: *Fleur workshop 2019 (picking flowers) - Tutorial, Forschungszentrum Jülich, Germany, 9 Sep 2019 - 13 Sep 2019*
- S. Rost and C. Friedrich. "Electron Energy Loss Spectroscopy (EELS) for 2D materials." Talk at: *Group Seminar PGI-1, Forschungszentrum Jülich, Germany, 9 Jun 2019*
- S. Rost. "Band unfolding." Talk at: *CECAM workshop "All-electron DFT with Fleur - a Hands-on tutorial", Forschungszentrum Jülich, Germany, 12 Apr 2021 - 16 Apr 2021*

Posters

- S. Rost, C. Friedrich, I. Aguilera, B. Kardynal, and S. Blügel. "MoSe₂+P band structure. Analysis of defect states in MoSe₂ and unfolding of defect band structure." Poster at: *Statussymposium on Functional Macroscopic Systems -*

VolkswagenStiftung, Hannover, Germany, 8 Oct 2018 - 9 Oct 2018

- S. Rost, C. Friedrich, I. Aguilera, B. Kardynal, and S. Blügel. "Analysis of defect states in MoSe₂ and unfolding of defect band structure." Poster at: *Frühjahrstagung der Deutschen Physikalischen Gesellschaft, Regensburg, Germany, 31 Mar 2019 - 5 Apr 2019*
- S. Rost, C. Friedrich, I. Aguilera, B. Kardynal, and S. Blügel. "Analysis of defect states in MoSe₂ and unfolding of defect band structure." Poster at: *JARA-FIT Meeting, Schleiden, Germany, 11 Oct 2019 - 12 Oct 2019*

Bibliography

- [1] *Matter and Light for Quantum Computing*. <https://ml14q.de/>. Accessed: 2022-06-12.
- [2] Nicolas Onofrio, David Guzman, and Alejandro Strachan. “Novel doping alternatives for single-layer transition metal dichalcogenides.” In: *J. Appl. Phys.* 122.18 (2017), p. 185102.
- [3] Charles H. Bennett and Gilles Brassard. “Quantum cryptography: Public key distribution and coin tossing.” In: *Theor. Comput. Sci.* 560 (2014). Theoretical Aspects of Quantum Cryptography – celebrating 30 years of BB84, pp. 7–11.
- [4] Zhiliang Yuan, Beata E. Kardynal, R. Mark Stevenson, Andrew J. Shields, Charlene J. Lobo, Ken Cooper, Neil S. Beattie, David A. Ritchie, and Michael Pepper. “Electrically Driven Single-Photon Source.” In: *Science* 295.5552 (2002), pp. 102–105.
- [5] Christopher J. Ciccarino, Thomas Christensen, Ravishankar Sundararaman, and Prineha Narang. “Dynamics and Spin-Valley Locking Effects in Monolayer Transition Metal Dichalcogenides.” In: *Nano Lett.* 18.9 (2018), pp. 5709–5715.
- [6] Michael Hennessy, Eoghan O’Connell, Stefan Rost, Manuel Auge, Eoin Moynihan, Minh Bui, Hans Hofsaess, Beata Kardynal, and Ursel Bangert. “New Single Photon Sources by Optoelectronic Tailoring of 2D Materials Using Low Energy Ion Implantation.” In: *Microsc. Microanal.* 26.S2 (2020), pp. 2832–2833.
- [7] Zhiliang Yuan, Beata E. Kardynal, R. Mark Stevenson, Andrew J. Shields, Charlene J. Lobo, Ken Cooper, Neil S. Beattie, David A. Ritchie, and Michael Pepper. “Electrically Driven Single-Photon Source.” In: *Science* 295.5552 (2002), pp. 102–105.
- [8] James Hillier and R. F. Baker. “Microanalysis by Means of Electrons.” In: *J. Appl. Phys.* 15.9 (1944), pp. 663–675.

- [9] Peter Schattschneider. *Classical Scattering Theory*. Vienna: Springer Vienna, 1986, pp. 95–96.
- [10] *Jülich FLAPW code family*. <https://www.flapw.de/>. Accessed: 2022-06-12.
- [11] S. Blügel and G. Bihlmayer. *Full-Potential linearized augmented plane-wave method*. Vol. 31. Jülich: Forschungszentrum Jülich, Germany, 1985, pp. 85–129.
- [12] Christoph Friedrich, Stefan Blügel, and Arno Schindlmayr. “Efficient implementation of the GW approximation within the all-electron FLAPW method.” In: *Phys. Rev. B* 81.12 (2010), p. 125102. *ibid.* Friedrich, Blügel, and Schindlmayr [62].
- [13] O. Rubel, A. Bokhanchuk, S. J. Ahmed, and E. Assmann. “Unfolding the band structure of disordered solids: From bound states to high-mobility Kane fermions.” In: *Phys. Rev. B* 90 (11 Sept. 2014), p. 115202.
- [14] Yi Shuang, Shogo Hatayama, Hiroshi Tanimura, Daisuke Ando, Tetsu Ichitsuho, and Yuji Sutou. “Nitrogen doping-induced local structure change in a Cr₂Ge₂Te₆ inverse resistance phase-change material.” In: *Mater. Adv.* 1 (7 2020), pp. 2426–2432.
- [15] J.W. Mayer. “Ion implantation in semiconductors.” In: *1973 International Electron Devices Meeting*. 1973, pp. 3–5.
- [16] M. Uhrmacher and H. Hofsäss. “Ion accelerator facilities at the University of Göttingen.” In: *Nucl. Instrum. Methods Phys. Res. B* 240.1 (2005). Accelerators in Applied Research and Technology, pp. 48–54.
- [17] *SPEX manual*. <https://spex.readthedocs.io/>. Accessed: 2022-06-12.
- [18] P. Hohenberg and W. Kohn. “Inhomogeneous Electron Gas.” In: *Phys. Rev.* 136 (3B Nov. 1964), B864–B871.
- [19] W. Kohn and L. J. Sham. “Self-Consistent Equations Including Exchange and Correlation Effects.” In: *Phys. Rev.* 140 (4A Nov. 1965), A1133–A1138.
- [20] John P. Perdew, Kieron Burke, and Matthias Ernzerhof. “Generalized Gradient Approximation Made Simple.” In: *Phys. Rev. Lett.* 77 (18 Oct. 1996), pp. 3865–3868.
- [21] John P. Perdew, Kieron Burke, and Matthias Ernzerhof. “Generalized Gradient Approximation Made Simple [Phys. Rev. Lett. 77, 3865 (1996)].” In: *Phys. Rev. Lett.* 78 (7 Feb. 1997), pp. 1396–1396.

- [22] John P. Perdew and Karla Schmidt. “Jacob’s ladder of density functional approximations for the exchange-correlation energy.” In: *AIP Conference Proceedings* 577.1 (Aug. 2001), p. 1.
- [23] Gregor Michalick. “The all-electron FLAPW method.” Online Hands-on tutorial 2021 to introduce FLEUR MaXR5.1. 2021.
- [24] David Singh. “Ground-state properties of lanthanum: Treatment of extended-core states.” In: *Phys. Rev. B* 43 (8 Mar. 1991), pp. 6388–6392.
- [25] Stephen L. Adler. “Quantum theory of the dielectric constant in real solids.” In: *Phys. Rev.* 126.2 (Apr. 1962), pp. 413–420.
- [26] Nathan Wiser. “Dielectric Constant with Local Field Effects Included.” In: *Phys. Rev.* 129 (1 Jan. 1963), pp. 62–69.
- [27] Silvana Botti, Arno Schindlmayr, Rodolfo Del Sole, and Lucia Reining. “Time-dependent density-functional theory for extended systems.” In: *Rep. Prog. Phys.* 70.3 (2007), pp. 357–407.
- [28] Akiko Natori. *Lecture Notes: Computational Solid State Physics*. URL: <https://slidetodoc.com/computational-solid-state-physics-5-5-band-offset/>. Last visited on 02.05.2022.
- [29] Audrius Alkauskas, Matthew D. McCluskey, and Chris G. Van De Walle. “Tutorial: Defects in semiconductors - Combining experiment and theory.” In: *J. Appl. Phys.* 119.18 (May 2016), p. 181101.
- [30] R. P. Messmer and G. D. Watkins. “Molecular-Orbital Treatment for Deep Levels in Semiconductors: Substitutional Nitrogen and the Lattice Vacancy in Diamond.” In: *Phys. Rev. B* 7 (6 Mar. 1973), pp. 2568–2590.
- [31] Robert Puig Benyon. “Deep levels in III-V semiconductors and quantum wells at high pressure.” PhD Thesis. University of Surrey, Sept. 1988.
- [32] R. Egerton. *Physical Principles of Electron Microscopy: An Introduction to TEM, SEM, and AEM*. Springer ebook collection / Chemistry and Materials Science 2005-2008. Springer US, 2011.
- [33] W. Heisenberg. “Über den anschaulichen Inhalt der quantentheoretischen Kinetik und Mechanik.” In: *Zeitschrift für Physik* 43.3-4 (Mar. 1927), pp. 172–198.

- [34] P. Wachsmuth, R. Hambach, M. K. Kinyanjui, M. Guzzo, G. Benner, and U. Kaiser. “High-energy collective electronic excitations in free-standing single-layer graphene.” In: *Phys. Rev. B* 88.7 (2013), p. 075433.
- [35] R. F. Egerton. “Limits to the spatial, energy and momentum resolution of electron energy-loss spectroscopy.” In: *Ultramicroscopy* 107.8 (2007), pp. 575–586.
- [36] Li Zhang, Yun Jie Yu, Liu Guo Chen, Yang Luo, Ben Yang, Fan Fang Kong, Gong Chen, Yang Zhang, Qiang Zhang, Yi Luo, Jin Long Yang, Zhen Chao Dong, and J. G. Hou. “Electrically driven single-photon emission from an isolated single molecule.” In: *Nat. Commun.* 8.1 (2017).
- [37] Stefan Hüfner. *Very High Resolution Photoelectron Spectroscopy*. Vol. 715. Jan. 2007.
- [38] Nasser Alidoust, Guang Bian, Su Yang Xu, Raman Sankar, Madhab Neupane, Chang Liu, Ilya Belopolski, Dong Xia Qu, Jonathan D. Denlinger, Fang Cheng Chou, and M. Zahid Hasan. “Observation of monolayer valence band spin-orbit effect and induced quantum well states in MoX_2 .” In: *Nat. Commun.* 5 (2014).
- [39] Hiram J. Conley, Bin Wang, Jed I. Ziegler, Richard F. Haglund, Sokrates T. Pantelides, and Kirill I. Bolotin. “Bandgap Engineering of Strained Monolayer and Bilayer MoS_2 .” In: *Nano Lett.* 13.8 (2013), pp. 3626–3630.
- [40] Minh N. Bui, Stefan Rost, Manuel Auge, Jhih-Sian Tu, Zhou Lanqing, Irene Aguilera, Stefan Blügel, Mahdi Ghorbani-Asl, Arkady V. Krasheninnikov, Arsalan Hashemi, Hannu-Pekka Komsa, Lei Jin, Lidia Kibkalo, Eoghan N. O’Connell, Quentin M. Ramasse, Ursel Bangert, Hans C. Hofsäss, Detlev Grützmacher, and Beata E. Kardynał. “Low-energy Se ion implantation in MoS_2 monolayers.” In: *npj 2D Mater. Appl.* 6.42 (2022).
- [41] Anton Kokalj. “XCrySDen—a new program for displaying crystalline structures and electron densities.” In: *J. Mol. Graph. Model.* 17.3 (1999). Code available from <http://www.xcrysden.org/>, pp. 176–179.
- [42] Matthias Leifgen, Tim Schröder, Friedemann Gädeke, Robert Riemann, Valentin Métillon, Elke Neu, Christian Hepp, Carsten Arend, Christoph Becher, Kristian Lauritsen, and Oliver Benson. “Evaluation of nitrogen- and silicon-vacancy defect centres as single photon sources in quantum key distribution.” In: *New Journal of Physics* 16.2 (Feb. 2014), p. 023021.

- [43] Shuyang Yang, Niels B. M. Schröter, Sergej Schuwalow, Mohana Rajpalk, Keita Ohtani, Peter Krogstrup-Georg, W. Winkler, Jan Gukelberger, Dominik Gresch, Gabriel Aeppli, Roman M. Lutchyn, Vladimir N. Strocov, and Noa Marom. *Electronic structure of InAs and InSb surfaces: density functional theory and angle-resolved photoemission spectroscopy*. 2020.
- [44] P. Nozières and D. Pines. “Electron interaction in solids. Characteristic energy loss spectrum.” In: *Phys. Rev.* 113.5 (1959), pp. 1254–1267.
- [45] R.F. Egerton. *Electron Energy-Loss Spectroscopy in the Electron Microscope*. Springer, Boston, MA, 2011.
- [46] J. Geiger, ed. *Elektronen und Festkörper: Anregungen, Energieverluste, dielektrische Theorie*. Sammlung Vieweg ; deutsch. Braunschweig: Vieweg, 1968, 165 S.
- [47] Ralf Hambach. “Theory and ab-initio calculations of collective excitations in nanostructures: towards spatially-resolved EELS.” Doctoral dissertation. Ecole Polytechnique Palaiseau, Nov. 2010.
- [48] P. Wachsmuth. “Momentum-resolved energy-loss spectroscopy of graphene.” PhD thesis. University Ulm, 2014.
- [49] Stefan Rost, Stefan Blügel, and Christoph Friedrich. “Efficient calculation of \mathbf{k} -integrated electron energy loss spectra: application to monolayers of MoS₂, hBN, and graphene.” In: *Phys. Rev. B* (2022). submitted.
- [50] D.E. Aspnes. “Optical properties of thin films.” In: *Thin Solid Films* 89.3 (Mar. 1982), pp. 249–262.
- [51] Wilfried G. Aulbur, Lars Jönsson, and John W. Wilkins. “Quasiparticle Calculations in Solids.” In: *Solid State Phys.* 54 (2000), pp. 1–218.
- [52] Vladimir Nazarov. “Electronic excitations in quasi-2D crystals: What theoretical quantities are relevant to experiment?” In: *New Journal of Physics* 17 (June 2015).
- [53] Eoin Moynihan, Stefan Rost, Eoghan O’connell, Quentin Ramasse, Christoph Friedrich, and Ursel Bangert. “Plasmons in MoS₂ studied via experimental and theoretical correlation of energy loss spectra.” In: *J. Microsc.* (June 2020), jmi.12900.

- [54] C. T. Pan, R. R. Nair, U. Bangert, Q. Ramasse, R. Jalil, R. Zan, C. R. Seabourne, and A. J. Scott. “Nanoscale electron diffraction and plasmon spectroscopy of single- and few-layer boron nitride.” In: *Phys. Rev. B* 85.4 (Jan. 2012), p. 045440.
- [55] Juan C. Idrobo and Wu Zhou. “A short story of imaging and spectroscopy of two-dimensional materials by scanning transmission electron microscopy.” In: *Ultramicroscopy* 180 (Sept. 2017), pp. 156–162.
- [56] Vladimir U. Nazarov, Fahhad Alharbi, Timothy S. Fisher, and Sabre Kais. “Time-dependent density functional theory of coupled electronic lattice motion in quasi-two-dimensional crystals.” In: *Phys. Rev. B* 89 (19 May 2014), p. 195423.
- [57] Roscoe G. Dickinson and Linus Pauling. “The crystal structure of molybdenite.” In: *J. Am. Chem. Soc.* 45.6 (1923), pp. 1466–1471.
- [58] Alejandro Molina-Sánchez, Kerstin Hummer, and Ludger Wirtz. “Vibrational and optical properties of MoS₂: From monolayer to bulk.” In: *Surf. Sci. Rep.* 70.4 (Dec. 2015), pp. 554–586.
- [59] Erhan Budak and Çetin Bozkurt. “Synthesis of hexagonal boron nitride with the presence of representative metals.” In: *Physica B: Condensed Matter* 405.22 (Nov. 2010), pp. 4702–4705.
- [60] Lucien Boulet-Roblin, Denis Sheptyakov, Philippe Borel, Cécile Tessier, Petr Novák, and Claire Villevieille. “Crystal structure evolution: Via operando neutron diffraction during long-term cycling of a customized 5 v full Li-ion cylindrical cell LiNi_{0.5}Mn_{1.5}O₄ vs. graphite.” In: *J. Mater. Chem. A* 5.48 (Dec. 2017), pp. 25574–25582.
- [61] J. Rath and A. J. Freeman. “Generalized magnetic susceptibilities in metals: Application of the analytic tetrahedron linear energy method to Sc.” In: *Phys. Rev. B* 11 (6 Mar. 1975), pp. 2109–2117.
- [62] Christoph Friedrich, Stefan Blügel, and Arno Schindlmayr. “Erratum: Efficient implementation of the GW approximation within the all-electron FLAPW method (Physical Review B (2010) 81 (125102) DOI: 10.1103/PhysRevB.81.125102).” In: *ibid.* 104.3 (July 2021), p. 039901.

Acknowledgements

Foremost, I would like to thank Prof. Stefan Blügel for his support and supervision. He always had the goal in mind, making sure that everything comes together in the end. After every single meeting with him, he managed to make me feel positive about the future work. My sincere thanks also go to Dr. Christoph Friedrich, there is never a moment for which he does not have a good idea on how to solve a problem. He showed me that questioning every single step, even the ones that seem easy at first, is the key to a successful work. His dedication to a perfect result is incredibly impressive — I hope I have adapted some of it. I am indebted to Prof. Beata Kardynal, who introduced me to the experimental setup, patiently explained every application, and discussed countless results with me. I also would like thank my research group for their warm welcome and support. I am thankful to Dr. Irene Aguilera, she was always patient and willing to give me advice, no matter how much work she had herself. Without the help of Dr. Gregor Michalicek edits to the Fleur code would not have been possible, he always came by the office to make sure I knew how to proceed with the implementation. Furthermore, I would like to acknowledge the insightful discussions during our regular meetings with Prof. Ursel Bangert, Eoin Moynihan, Michael Hennessy, Anoop Chandran, Jörn Stöhler, and Minh Bui. I am grateful to my office mates, Christian Gerhorst and Gideon Müller, for their welcoming atmosphere each day. They never complained about my mood or any question I wanted to discuss. I would like to thank the technical support staff at the PGI-1 for helping out and sharing their experience. I feel in debt to my flatmates, close friends and companions who have coped with a variety of my moods and reminded me of the ability to finish every project.

I am grateful to my parents for supporting me under all circumstances.

This work was partly funded by the project “New single photon sources by engineering monolayer-thick semiconductors on the atomic scale” (Az. 93 427) supported by the “Integration of Molecular Components in Functional Macroscopic System” initiative of the Volkswagen-Stiftung.

I acknowledge the computing time granted through JARA-HPC on the super-computer JURECA at Forschungszentrum Jülich.

Band / Volume 79

Spectromicroscopic investigation of local redox processes in resistive switching transition metal oxides

T. Heisig (2022), vi, 186 pp

ISBN: 978-3-95806-609-0

Band / Volume 80

Integrated Control Electronics for Qubits at Ultra Low TemperatureD.

Nielinger (2022), xviii, 94, xix-xxvi

ISBN: 978-3-95806-631-1

Band / Volume 81

Higher-order correlation analysis in massively parallel recordings in behaving monkey

A. Stella (2022), xiv, 184 pp

ISBN: 978-3-95806-640-3

Band / Volume 82

Denoising with Quantum Machine Learning

J. Pazem (2022), 106 pp

ISBN: 978-3-95806-641-0

Band / Volume 83

Hybrid hydrogels promote physiological functionality of long-term cultured primary neuronal cells in vitro

C. Meeßen (2022), x, 120 pp

ISBN: 978-3-95806-643-4

Band / Volume 84

Surface states and Fermi-level pinning on non-polar binary and ternary (Al,Ga)N surfaces

L. Freter (2022), 137 pp

ISBN: 978-3-95806-644-1

Band / Volume 85

Dynamical and statistical structure of spatially organized neuronal networks

M. Layer (2022), xiii, 167 pp

ISBN: 978-3-95806-651-9

Band / Volume 86

Persistent firing and oscillations in the septo-hippocampal system and their relation to locomotion

K. Korvasová (2022), 111 pp

ISBN: 978-3-95806-654-0

Band / Volume 87

Sol-Gel-Synthese, Tintenstrahldruck und Blitzlampentemperatur von Tantaloxid-Dünnschichten zur pH-Messung

C. D. Beale (2022), xlix, 339 pp

ISBN: 978-3-95806-656-4

Band / Volume 88

Diversity of chiral magnetic solitons

V. Kuchkin (2022), xiv, 155 pp

ISBN: 978-3-95806-665-6

Band / Volume 89

Controlling the electrical properties of oxide heterointerfaces through their interface chemistry

M.-A. Rose (2022), vi, 162 pp

ISBN: 978-3-95806-667-0

Band / Volume 90

Modeling and Suppressing Unwanted Parasitic Interactions in Superconducting Circuits

X. Xu (2022), 123, XVIII pp

ISBN: 978-3-95806-671-7

Band / Volume 91

Activating molecular magnetism by controlled on-surface coordination

I. Cojocariu (2022), xi, 169 pp

ISBN: 978-3-95806-674-8

Band / Volume 92

Computational study of structural and optical properties of two-dimensional transition-metal dichalcogenides with implanted defects

S. H. Rost (2023), xviii, 198 pp

ISBN: 978-3-95806-682-3

Weitere **Schriften des Verlags im Forschungszentrum Jülich** unter
<http://www.zb1.fz-juelich.de/verlagextern1/index.asp>

Information

Band / Volume 92

ISBN 978-3-95806-682-3

Mitglied der Helmholtz-Gemeinschaft

